

2014

Optical characterization of InGaN heterostructures for blue light emitters and vertical cavity lasers: Efficiency and recombination dynamics

Serdal Okur

Serdal Okur, okurs@vcu.edu

Follow this and additional works at: <http://scholarscompass.vcu.edu/etd>

 Part of the [Electronic Devices and Semiconductor Manufacturing Commons](#)

© The Author

Downloaded from

<http://scholarscompass.vcu.edu/etd/3647>

This Dissertation is brought to you for free and open access by the Graduate School at VCU Scholars Compass. It has been accepted for inclusion in Theses and Dissertations by an authorized administrator of VCU Scholars Compass. For more information, please contact libcompass@vcu.edu.

©Serdal Okur 2014

All Rights Reserved

**Optical characterization of InGaN heterostructures for blue light emitters and
vertical cavity lasers: Efficiency and recombination dynamics**

A thesis submitted in partial fulfillment of the requirements for the degree of Doctor of
Philosophy of Electrical and Computer Engineering at Virginia Commonwealth University.

by

Serdal Okur

Bachelor of Science, Ondokuz Mayıs University, 2005

Master of Science, Izmir Institute of Technology, 2009

Director: Ümit Özgür, Associate Professor,

Electrical and Computer Engineering

Virginia Commonwealth University

Richmond, Virginia

Acknowledgements

My first and deepest appreciation must go to my advisor Professor Ümit Özgür. It has been a privilege to have been educated by him. I would like to extend my outmost appreciation to him for his invaluable help, guidance, encouragement and his endless patience as well as his self-sacrifice without which this thesis would not have been possible. I appreciate the efforts that he has made in my personal development as a researcher and numerous discussions required by this study. I am also grateful to Professor Hadis Morkoç for his consistent and valuable effort to me to encourage me during my research, and also his valuable suggestions and constant support. I would also like to acknowledge Dr. Vitaliy Avrutin and Dr. Natalia Izyumskaya for their help and guidance during my research. I am also indebted to Professor Kestutis Jarasiunas for his great suggestions during my studies. It was a great pleasure and memory to have worked with him during his visit to VCU. I am also indebted to Dr. Ryoko Shimada who I benefited from the discussions on vertical cavities during my research. Special thanks go to my colleagues, Daniel Rosales and Professor Bernard Gil from University of Montpellier in addition to Dr. Sebastian Metzner, Professor Frank Bertram and Professor Juergen Christen from University of Magdeburg. Our monthly videoconferences helped me to increase my understanding on optical properties of GaN-based optoelectronic devices. I also want to thank to Professor Shiv Khanna and Professor Michael Reshchikov for their valuable comments and guidance.

I am also grateful to my friends Arda Müftüoğlu and Dr. Koray Dogan Kaya, Dr. Cemil Kayis and Dr. Gunes Aygok for their encouragement and endless support. It was a privilege for me to work with my colleagues at Electrical and Computer Engineering Department; Shopan, Nuri, Fan, Xing Li, Romualdo, Mykyta, Morteza, Barkat, Mahbub and Saikat.

I am very grateful to thank Salih Okur and Nurgul Okur for their invaluable encouragement and support during my whole educational life. I would not be able to reach my goals without them. Last but not least, thanks to my wife Nigar for her constant understanding and love.

TABLE OF CONTENTS

Acknowledgements	ii
List of Tables	vii
List of Figures.....	viii
Abstract	xvi
Chapter 1. Introduction	1
1.1. GaN-based vertical cavities.....	2
1.1.1. Epitaxial lateral overgrowth (ELO)	7
1.1.2. Active region design	8
1.2. Optical characterization of non-polar and semipolar GaN.....	11
1.2.1. Extended defects in nonpolar and semipolar GaN.....	17
1.3. Polariton Lasers	19
1.4. Organization of the thesis.....	26
Chapter 2. Optical investigations of quantum efficiency of InGaN-based active regions....	28
2.1. Quantum Efficiency InGaN multiple quantum wells: Effects of barrier height and thickness	29
2.2. Impact of InGaN double heterostructure active layer design in optical performance	37
2.3. Multi double-heterostructure active regions in InGaN LEDs	42
2.4. The effect of stair-case electron injectors on the electron overflow	50
2.5. A theoretical treatment for injection dependent radiative recombination coefficient for single and multi active layer DH structures.....	55
2.6. Recombination dynamics of InGaN active regions using time-resolved photoluminescence spectroscopy	59
2.6.1. Recombination dynamics in an InGaN epilayer	61

2.6.2. Double heterostructure active regions	69
Chapter 3. Optical investigations of GaN-based blue emitting microcavity structures.....	73
3.1. Optical investigations on hybrid vertical cavities with bottom semiconductor and top dielectric distributed Bragg reflectors (DBRs).....	73
3.2. Optimization and characterization of a vertical cavity with full dielectric distributed Bragg reflectors (DBRs).....	85
Chapter 4. Optical efficiency and carrier dynamics in nonpolar and semipolar GaN and InGaN LEDs	96
4.1. Excitonic effects on recombination dynamics in nonpolar m-plane bulk GaN	97
4.2. Carrier dynamics of nonpolar and semipolar GaN substrates	110
4.3. Impact of extended defects on optical properties of $(1\bar{1}01)$ GaN grown on patterned Silicon.....	121
4.4. Strong carrier localization in basal plane and prismatic stacking faults in semipolar $(11\bar{2}2)$ GaN.....	129
4.5. Microscopic distribution of stacking faults in semipolar $(1\bar{1}01)$ GaN substrates revealed from spatially resolved photoluminescence.....	143
4.6. Optical performance of nonpolar m-plane $(1\bar{1}00)$ GaN layers grown using two-step growth technique	151
4.7. Semipolar $(1\bar{1}01)$ and $(11\bar{2}2)$ InGaN LED performance.....	157
Chapter 5. Summary and Conclusions	164
Chapter 6. Outlook	167
References	170
Appendices.....	181
Appendix A: Determination of IQE from excitation density dependent photoluminescence measurement.....	181
Appendix B: Working principle of a Streak Camera	183

Appendix C: Calculation of temperature dependent radiative and nonradiative lifetimes	185
Curriculum Vitae	186

List of Tables

Table 1: Performance of vertical cavities (with InGaN active region) with chronological order obtained from the selected literature data.	7
Table 2: Polarization selection rules for A, B and C excitons.	16
Table 3: The radiative and nonradiative decay times and amplitude ratios extracted from the fitted biexponential decay parameters and IQE values for the 3 nm, dual 3 nm, 6 nm, dual 6 nm and 11 nm DH LED structures.	72
Table 4: The polarization degree values obtained from excitation dependent PRPL measurements and TRPL measurements for σ -polarization state (267 nm excitation) at 10 K and 300 K.	108
Table 5: Biexponential decay parameters for the room temperature TRPL intensity from c-plane GaN on sapphire and $(1\bar{1}01)$ -plane GaN on Si at two different power levels.	113
Table 6: PL decay times and amplitude ratios obtained from biexponential fits.....	117
Table 7: Longer PL decay times obtained from the biexponential fits.....	120

List of Figures

- Figure 1: Room temperature bandgap energy versus in-plane lattice constant for III-V nitride semiconductors AlN, GaN and InN. Their ternary alloys and visible spectrum energy range are depicted as well. 2
- Figure 2: Schematic of a typical microcavity structure. Squared electric field inside the cavity is shown where an InGaN active region is placed at the antinode of the electric field inside the cavity (red color). 3
- Figure 3: a) Optical gain vs. wavelength characteristics (called the optical gain curve) of a lasing medium. b) Allowed modes and their wavelengths due to stationary EM waves within the optical cavity. c) Gain vs. pump intensity or current density. 5
- Figure 4: Schematic of epitaxial lateral overgrowth technique. The propagation of the threading dislocations is blocked by the mask material. 8
- Figure 5: Schematic illustration of carrier flow in a simple LED structure with flat band consideration. LED structure consists of n-type GaN, InGaN multiple quantum well, AlGaIn electron blocking layer (EBL) and p-type GaN. 10
- Figure 6: Band structures for polar (a) and nonpolar (b) directions. These are not very good figures. The x-axis says growth, instead of thickness, also there is excessive color. Didn't you have simpler figures you prepared?..... 12
- Figure 7: Piezoelectric polarization (left axis) and wavefunction overlap of the electrons and the holes in conduction and valence bands (right axis) in a 3 nm wide $\text{Ga}_{0.75}\text{In}_{0.25}\text{N}$ quantum well.⁴⁴ The crystal angle is defined with respect to the c-axis. For semipolar $(11\bar{2}2)$ and $(10\bar{1}1)$ the angles are 58.4° and 61.7° , respectively. 13
- Figure 8: (a) A representation of crystal structure of wurtzite GaN. (b) Commonly used GaN surface orientations; polar *c*-plane, the nonpolar *a*- and *m*-planes and the semipolar $(11\bar{2}2)$ plane.⁴⁵ 14
- Figure 9: A schematic of the energy band structure and exciton energy levels in wurtzite GaN in an uncoupled hydrogen-like isotropic model.⁴⁶ 16
- Figure 10: Polarization-dependent PL spectra and polarization ratio of an *m*-plane InGaIn/GaN MQWs measured at room temperature. Here, $\phi = 0^\circ$ and 90° represent $E \parallel c$ and $E \perp c$, respectively.⁴⁷ 17
- Figure 11: The atomic arrangement of stacking faults, (a) type-I, (b) type-II, (c) type-III, and (d) extrinsic. The arrows indicate the position of the stacking faults and the black and white circles denote cations and anions, respectively.⁵¹ In your presentation you had better figures. 18

- Figure 12: (a) Atomic model of a prismatic stacking fault and $(11\bar{2}0)$ stacking mismatch boundary (projection onto the (0001)). White and black circles represent Ga atoms (nitrogen atoms are omitted because their projection would overlap with Ga atoms).⁵² (b) Schematic representation of lattice planes and directions for prismatic stacking fault in the (0001) projection.⁵³ 19
- Figure 13: Dispersion of polaritons in a CdTe cavity.⁵⁶ Upper and lower polariton branches are plotted in red, and bare cavity and exciton dispersion curves are given in blue. 21
- Figure 14: Polariton dispersions curves for GaN-based microcavity (a) for different Rabi splitting energies at zero detuning (b) for different detuning energies at 30 meV Rabi splitting. 23
- Figure 15: The operational principles of (a) polariton and (b) conventional laser.⁵⁵ 25
- Figure 16: The conduction band diagrams for the active region designs used in LEDs: (a) coupled MQW (b) uncoupled MQW. Flat band diagrams are shown only for simplicity. 31
- Figure 17: (a) IQE values determined from excitation-dependent PL for LEDs with coupled MQWs. B value was assumed to be $10^{-11} \text{ cm}^3\text{s}^{-1}$ for the calculation of carrier densities. 33
- Figure 18: (a) IQE values determined from excitation-dependent PL for LEDs with uncoupled MQWs. B value was assumed to be $10^{-11} \text{ cm}^3\text{s}^{-1}$ for the calculation of carrier densities. 34
- Figure 19: Relative external quantum efficiencies of uncoupled LEDs as a function of pulsed injection current density (0.1 % duty cycle and 1 kHz frequency). 36
- Figure 20: Flat band conduction band diagram for dual DH-LED structures. 38
- Figure 21: (a) IQE values determined from excitation-dependent PL with various DH thickness by using injection dependent B coefficients (b) IQE values vs. photocurrent density converted from carrier concentration. 39
- Figure 22: Relative external quantum efficiencies of DH structures as a function of pulsed injection current density (0.1 % duty cycle and 1 kHz frequency). The inset shows the normalized resonant PL intensity versus the number of 3 nm DH active regions. ... 41
- Figure 23: (a) PL and (b) EL efficiency of multi-3 nm DHs vs. injected carrier concentration at room temperature. The inset in (b) shows the integrated EL intensity dependence on current density. 46
- Figure 24: Integrated PL intensity as a function of injected carrier density at 15 K (dash-dot line indicates a slope of 1) (a) and 295 K (b); the inset of (b) displays the PL-IQE vs. the number of 3 nm DHs in the active region. 49

- Figure 25: The integrated PL intensity (grey-sold lines indicates slope of 1) with varied SEI thickness as a function of excitation power density for LEDs (a) at 15 K and (b) at 295 K. 52
- Figure 26: The integrated EL efficiencies dependence on current density (grey-sold lines indicates slope of 1) for LEDs with varied SEI thickness. 54
- Figure 27: Calculated B coefficients using squared overlap integrals of electron and hole wave functions (proportional to radiative recombination rate) within the active region as a function of (a) current density calculated using SILVACO ATLAS simulations and (b) injection electrical power density (the product of applied voltages and current densities). 59
- Figure 28: Time-resolved photoluminescence setup used in the temperature or excitation dependent experiments. 61
- Figure 29: PL decay kinetics measured using femtosecond pulses at 375 nm wavelength and various excitation densities I_0 , corresponding to injected carrier densities from $5 \times 10^{16} \text{ cm}^{-3}$ to 10^{18} cm^{-3} 64
- Figure 30: Dependence of time-integrated PL intensity on excitation energy density using femtosecond pulses at 375 nm. The curves can be approximated by a power-function $I_{PL} \propto I_0^\beta$ with slope values β , as indicated on the plot. 65
- Figure 31: DT spectra at various excitation energy densities I_0 (here $I_0=4 \mu\text{J}/\text{cm}^2$). The spectra are taken at 10 ps (a) and 1 ns (b) after photo-excitation by 200 fs duration laser pulses at 375 nm. For comparison, PL spectra at $20 \mu\text{J}/\text{cm}^2$ (375 nm excitation) and $100 \mu\text{J}/\text{cm}^2$ (266 nm excitation) are shown in (a). 66
- Figure 32: Spectrally resolved DT kinetics (a), (b) for two spectral lines which correspond to blue wing of DT at 414nm and PL emission at 425 nm at various excitation energy densities $I_0=10 \mu\text{J}/\text{cm}^2$ (1), $33 \mu\text{J}/\text{cm}^2$ (2), $100 \mu\text{J}/\text{cm}^2$ (3), and $300 \mu\text{J}/\text{cm}^2$ (4). In (c), spectral distribution of the initial DT decay time is plotted for various I_0 68
- Figure 33: TRPL results for 3 nm, dual 3 nm, 6 nm and dual 6 nm DH LEDs for different excitation power densities, 0.08, 0.20 kW/cm^2 and 1.25 kW/cm^2 . TRPL data are fitted with biexponential decay functions $A_1 e^{-t/\tau_i} + A_2 e^{-t/\tau_f}$ to find initial τ_i and final τ_f decay times, which are also indicated in the figures. 70
- Figure 34: Basic schematics of vertical cavity structures: (a) 5λ cavity with $6 \times 2 \text{ nm}$ $\text{In}_{0.01}\text{Ga}_{0.99}\text{N}/\text{In}_{0.15}\text{Ga}_{0.85}\text{N}$ MQW grown on bottom 29 pairs AlN/GaN DBRs grown on $400\mu\text{m}$ thick free-standing GaN (b) 2.5λ cavity with two $6 \times 3 \text{ nm}$ $\text{In}_{0.06}\text{Ga}_{0.94}\text{N}/\text{In}_{0.15}\text{Ga}_{0.85}\text{N}$ DH separated by 132nm (1λ) $\text{In}_{0.01}\text{Ga}_{0.99}\text{N}$ underlying layer grown on bottom 29 pairs AlN/GaN DBRs grown on 2 micron GaN template on sapphire substrate. 75

- Figure 35: (a) Reflectivity and PL spectra for the vertical cavity structure on freestanding GaN (b) The spectrum corresponds to the highest Q-factor measured. 76
- Figure 36: Schematic of angle-resolved photoluminescence setup. 77
- Figure 37: (a) Angle-resolved PL spectra at RT in the range of 0° – 40° for the cavity on free-standing GaN (b) Experimental cavity polariton dispersion curve. 79
- Figure 38: (a) Angle-resolved CL spectra at 5.8K in the range of -14° to 51° for the cavity grown on free-standing GaN. (b) Experimental cavity polariton dispersion curve..... 80
- Figure 39: Calculated fit results for polariton dispersion curves at (a) room and (b) low temperatures. In plane wave vector was obtained using the relation $k_{\parallel} = \frac{\omega}{c} \sin \phi$ 81
- Figure 40: (a) The reflectivity spectrum (black) for the full vertical cavity with DH active region, reflectivity spectrum for the bottom AlN/GaN DBR (red) and photoluminescence spectrum (blue). (b) The spectrum corresponds to the highest Q factor measured. .. 84
- Figure 41: Room temperature NSOM results for the DH active region microcavity structure with bottom semiconductor and top dielectric DBRs (a) height image (b) PL intensity mapping. 85
- Figure 42: Cross sectional SEM images of ELO GaN samples grown with (a) ammonia on/off time 20 s/15 s with TMGa: 20 sccm and (b) ammonia on/off time 20 s/25 s with TMGa: 12 sccm. 86
- Figure 43: Cross sectional SEM images of an ELO layer after ICP etching with ICP/bias power 200/45 W showing wall-like feature on an ELO stripe. 87
- Figure 44: Cross sectional SEM images of an ELO layer (a) before and (b) after ICP etching with ICP/bias power 350/250 W. 88
- Figure 45: (a) Schematic of the full vertical cavity structure. (b) Electric field inside the cavity with respect to distance where an InGaN active region is placed at the antinode of the electric field inside the cavity..... 90
- Figure 46: Reflectivity spectrum of the full cavity structure. Cavity modes are observed around 400 and 412 nm can be clearly seen in inset corresponding to lateral cavity length of $\sim 3\mu\text{m}$ 91
- Figure 47: PL spectra for the full cavity structure (red), half cavity structure (black) and reference sample with no DBRs. The corresponding Q-factors are 500, 60 and 20, respectively. 92
- Figure 48: (a) Oblique view and (b) cross sectional schematics of VCSEL structure with electrical contacts. Red arrows show the electrical injection path, while light green is showing the light output direction. 93

Figure 49: VCSEL devices on the mesa produced after photolithography techniques (without the top deposited layers, (b) the final device shapes with contact layers.	94
Figure 50: I-V characteristics of the full VCSEL structure in (a) linear and (b) logarithmic scales.	95
Figure 51: Temperature dependent PL spectra for σ - and π -polarization states collected using 267 nm excitation wavelength and at an excitation density of $4\mu\text{J}/\text{cm}^2$ for m-plane GaN.	98
Figure 52: a) Excitation intensity dependent σ -polarized PL spectra for m-plane GaN at 10 K and 0° polarizer angle. PL spectra at different polarizer angles for σ -polarization at b) $4\mu\text{J}/\text{cm}^2$, c) $0.4\mu\text{J}/\text{cm}^2$, and d) $0.04\mu\text{J}/\text{cm}^2$	100
Figure 53: Comparison of normalized PL intensities for π - and σ -polarization components, varying with polarization angle in m-plane GaN. The corresponding degree of polarization at 300K is given in the plot.	102
Figure 54: Excitation dependent PL transients for (a) π - and (b) σ -polarization states at 15K. System response of 0.28 ns is also shown in the figures (dashed lines).	102
Figure 55: Temperature dependent π - and σ -polarized PL transients at $4\mu\text{J}/\text{cm}^2$ excitation density.	103
Figure 56: Effective PL lifetimes for the excitation energy densities of $4\mu\text{J}/\text{cm}^2$ and $0.4\mu\text{J}/\text{cm}^2$ obtained using 267 nm excitation wavelength. The solid dashed line represents the PL decay time measured at the lowest excitation density for $0.04\mu\text{J}/\text{cm}^2$ at 15 K.	106
Figure 57: Temperature-dependent radiative and nonradiative PL decay times extracted from time-resolved and photoluminescence results for σ -polarization at $4\mu\text{J}/\text{cm}^2$	107
Figure 58: Temperature dependent effective radiative recombination lifetimes. PRPL measurements were performed under cw HeCd excitation (325 nm wavelength) and TRPL measurements were performed under frequency tripled pulsed Ti:Sapphire excitation (267 nm wavelength)	109
Figure 59: Steady-state room-temperature PL spectra of c-plane GaN films grown on sapphire and (1 100) m-plane and (1101)-oriented GaN layers grown on the Si patterned substrates.	111
Figure 60: Normalized room-temperature TRPL intensity for c-plane GaN on sapphire and (1 $\bar{1}$ 01) oriented GaN on Si measured at an excitation density of $0.09\text{ kW}/\text{cm}^2$. System response is also shown. The red solid lines represent biexponential fits to the data.	113
Figure 61: Cross-sectional SEM images for (a) wide- and (b) narrow-groove pattern (1 $\bar{1}$ 01) GaN samples.	114

- Figure 62: Room-temperature TRPL results for the semipolar and polar GaN samples for the excitation density of 0.32 kW/cm^2 . Numbers indicate values of slow decay component τ_2 . Dashed curve represents the system response of the streak camera..... 115
- Figure 63: Excitation density dependent room-temperature TRPL for (a) polar (0001) nano-ELO GaN film on sapphire and (b) semipolar non-coalesced ($1\bar{1}01$) GaN layer on Si... 117
- Figure 64: Excitation dependent PL transients measured at an excitation wavelength of (a) and (b) 267 and (c) and (d) 353 nm for (a) and (c) the reference c-plane nano-ELO sample and (b) and (d) the semipolar non-coalesced GaN layer. The measurements were performed at room temperature. 119
- Figure 65: Cross-sectional SEM image of the semipolar ($1\bar{1}01$) GaN layers. 122
- Figure 66: (a) Near bandedge steady-state PL spectra at 25K and 295K (D^0X , BSF and PSF are marked in 15 K PL spectra) and (b) temperature-dependent IQE for the semipolar layer. 123
- Figure 67: Temperature-dependent PL spectra between 25 and 115 K. Inset shows energy positions for the D^0X and BSF lines with respect to temperature. 124
- Figure 68. PL transients for NBE peak measured on ^+c - and ^-c -wings of ($1\bar{1}01$) GaN/Si. Red curves represent biexponential fits. The PL decay was measured at room temperature with excitation wavelength of 355 nm: (a) 2 ns and (b) 10 ns time windows..... 125
- Figure 69. PL transients for D^0X , BSF, and PSF spectral lines measured at 15 K and excitation densities of (a) 5 W/cm^2 and (b) 420 W/cm^2 127
- Figure 70: Normalized polarization resolved PL intensity for the semipolar GaN sample for 420 W/cm^2 for the spectral lines D^0X , BSF at low temperature and NBE at room temperature. 128
- Figure 71: Schematic representation of growth procedure for ($11\bar{2}2$) GaN (a) and Crystallographic directions in wurtzite GaN structure (b)..... 132
- Figure 72: Temperature-dependent PL spectra for the semipolar ($11\bar{2}2$) GaN layer. 134
- Figure 73: (a) PL intensity and (b) PL intensity ratio of 3.31 eV SF and I_1 -type BSF with respect to temperature..... 136
- Figure 74: PL decay times for I_1 -type BSF and 3.31 eV SF obtained from biexponential fits of the transients..... 139
- Figure 75: Temperature-dependent radiative and nonradiative decay times extracted from PL decay times. Stars, open circle and full square show radiative, nonradiative and PL decay times, respectively. 141

- Figure 76: Normalized polarization-resolved PL intensity plot for the I_1 -type BSF and 3.31 eV SF at 15 K together with directions for the excitation light wave vector k and the electric field E with respect to selected crystallographic directions in the wurtzite structure. 142
- Figure 77: Top-view (a) AFM and (b) the corresponding room temperature near-band edge emission (integrated between 350-370 nm) NSOM images, (c) 15 K and room temperature PL spectra (red), (d) SEM, and the corresponding 5.8 K (e) CL intensity (integrated between 350-380 nm) and (f) CL peak wavelength images of the wide-groove pattern ($1\bar{1}01$) GaN sample. In (c) the PL spectra for the narrow-groove pattern ($1\bar{1}01$) GaN sample (blue) and a c-plane GaN reference sample (black) are also shown..... 146
- Figure 78: (a) Cross-sectional integrated CL intensity image (350–380 nm) for the wide-groove pattern sample. The dashed lines represent GaN growth boundaries. (b) Cross-sectional schematic of GaN growth from $\text{Si}(\bar{1}11)$ sidewall showing TD propagation (blue lines) and the growth fronts (dashed lines). Note that propagation of the bottom ($1\bar{1}01$) front is the slowest because of limited material supply. 147
- Figure 79: Plan-view (a) SEM and the corresponding 5.8 K (b) CL intensity (350-380 nm) and (c) CL peak wavelength images, and (d) room temperature near-band edge emission NSOM image of the narrow-groove pattern ($1\bar{1}01$) GaN sample. The projection of the c-axis is also indicated on the images. 148
- Figure 80: CL intensity (350–380 nm) and (b) CL peak wavelength images for the narrow-groove pattern sample ($1\bar{1}01$) GaN sample. The solid and dashed lines indicate the Si substrate surface and the GaN stripe cross section, respectively. (c) Cross-sectional schematic of GaN growth from $\text{Si}(\bar{1}11)$ sidewall showing threading dislocation propagation (blue solid lines) and the growth fronts (red dashed lines). 150
- Figure 81: Cross-sectional SEM images of nonpolar m-plane GaN on patterned $\text{Si}(112)$ substrate. 152
- Figure 82: (a) Room-temperature steady-state PL spectra for m-plane GaN layers grown at 30 Torr (blue) and in two steps (30 + 200 Torr) (black). The spectra from polar c-plane GaN nano-ELO sample (green) and ($1\bar{1}01$)GaN semipolar sample (red) are shown for comparison. (b) Low-temperature (15 K) PL spectra for m-plane GaN samples grown at 30 Torr (blue) and in two steps (black). 154
- Figure 83: NSOM maps for (a) near-band edge and (c) yellow emissions. Dashed lines show the boundaries of GaN stripes. The scan area is $20 \times 20 \mu\text{m}$. The spectra were integrated between 350–370 nm for the near bandedge (NBE) intensity maps and above 450 nm for the yellow emission (YE) intensity maps. 156

- Figure 84: Conduction band schematic structure of LED active region grown on $(1\bar{1}01)$ GaN templates on patterned Si substrates (flat band conditions). The underlying $\text{In}_{0.01}\text{GaN}$ layer is used to improve the active region material quality. Similar LED structures were grown on *c*-plane GaN for comparison. 158
- Figure 85: PL spectra for semipolar $(1\bar{1}01)$ InGaN LED structure grown on $(1\bar{1}01)$ GaN on stripe patterned Si substrate measured with an excitation wavelength of 385 nm. PL spectrum for a highly optimized polar *c*-plane LED structure with 80% internal quantum efficiency is shown for comparison..... 159
- Figure 86: Room temperature NSOM maps of semipolar $(1\bar{1}01)$ InGaN/GaN LED structure grown on $(1\bar{1}01)$ GaN templates on stripe patterned Si substrates. (a) Optical reflection image (325 nm wavelength), (b) PL intensity distribution measured with 400 nm high-pass filter. Boundaries of ^+c - and ^-c -wings are indicated with dashed lines..... 160
- Figure 87: PL spectra for semipolar $(11\bar{2}2)$ InGaN LED structure grown on *m*-sapphire substrate measured with an excitation wavelength of 325 nm. PL spectrum for a highly optimized polar *c*-plane LED structure with 80% internal quantum efficiency is shown for comparison..... 162
- Figure 88: Curve fitting results of the generation rate as a function of integrated PL intensity for a *c*-plane LED active layer (with low barrier MQW) on sapphire. The red curve represents the fits obtained using Equation 25..... 183
- Figure 89: Schematic illustration of a Streak camera components and working principle. 184

Abstract

OPTICAL CHARACTERIZATION OF INGAN HETEROSTRUCTURES FOR BLUE LIGHT EMITTERS AND VERTICAL CAVITY LASERS: EFFICIENCY AND RECOMBINATION DYNAMICS

By Serdal Okur, Ph.D.

A thesis submitted in partial fulfillment of the requirements for the degree of Doctor of Philosophy at Virginia Commonwealth University.

Virginia Commonwealth University, 2014.

Major Director: Ümit Özgür, Associate Professor, Electrical and Computer Engineering

This thesis explores radiative efficiencies and recombination dynamics in InGaN-based heterostructures and their applications as active regions in blue light emitters and particularly vertical cavities. The investigations focus on understanding the mechanism of efficiency loss at high injection as well as developing designs to mitigate it, exploring nonpolar and semipolar crystal orientations to improve radiative efficiency, integration of optimized active regions with high reflectivity dielectric mirrors in vertical cavity structures, and achieving strong exciton-photon coupling regime in these microcavities for potential polariton lasing. In regard to active regions, multiple double heterostructure (DH) designs with sufficiently thick staircase electron injection (SEI) layers, which act as electron coolers to reduce the overflow of hot electrons injected into the active region, were found to be more viable to achieve high efficiencies and to mitigate the efficiency loss at high injection. Such active regions were embedded in novel vertical cavity structure designs with full dielectric distributed Bragg reflectors (DBRs) through epitaxial lateral overgrowth (ELO), eliminating the problems associated with semiconductor bottom DBRs having narrow stopbands and the cumbersome substrate removal process. Moreover, the ELO technique

allowed the injection of carriers only through the high quality regions with substantially reduced threading dislocation densities compared to regular GaN templates grown on sapphire.

Reduced electron-hole wavefunction overlap in polar heterostructures was shown to hamper the efficiency of particularly thick active regions (thicker than 3 nm) possessing three-dimensional density of states needed for higher optical output. In addition, excitation density-dependent photoluminescence (PL) measurements showed superior optical quality of double heterostructure (3 nm InGaN wells) active regions compared to quantum wells (2 nm InGaN wells) suggesting a minimum limit for the active region thickness. Therefore, multiple relatively thin but still three dimensional InGaN active regions separated by thin and low barriers were found to be more efficient for InGaN light emitters. Investigations of electroluminescence from light emitting diodes (LEDs) incorporating multi DH InGaN active regions (e.g. quad 3 nm DH) and thick SEIs (two 20 nm-thick InGaN layers with step increase in In content) revealed higher emission intensities compared to LEDs with thinner or no SEI. This indicated that injected electrons were cooled sufficiently with thicker SEI layers and their overflow was greatly reduced resulting in efficient recombination in the active region. Among the structures considered to enhance the quantum efficiency, the multi-DH design with a sufficiently thick SEI layer constitutes a viable approach to achieve high efficiency also in blue lasers.

Owing to its high exciton binding energy, GaN is one of the ideal candidates for microcavities exploiting the strong exciton-photon coupling to realize the mixed quasiparticles called polaritons and achieve ideally thresholdless polariton lasing at room temperature. Angle-resolved PL and cathodoluminescence measurements revealed large Rabi splitting values up to 75 meV indicative of the strong exciton-photon coupling regime in InGaN-based microcavities with bottom semiconductor AlN/GaN and a top dielectric SiO₂/SiN_x DBRs, which exhibited quality

factors as high as 1300. Vertical cavity structures with all dielectric DBRs were also achieved by employing a novel ELO method that allowed integration of a high quality InGaN cavity active region with a dielectric bottom DBR without removal of the substrate while forming a current aperture through the ideally defect-free active region. The full-cavity structures formed as such were shown to exhibit clear cavity modes near 400 and 412 nm in the reflectivity spectrum and quality factors of 500.

Although the polar c-plane orientation has been the main platform for the development of nitride optoelectronics, significant improvement of the electron and hole wavefunction overlap in nonpolar and semipolar InGaN heterostructures makes them highly promising candidates for light emitting devices provided that they can be produced with good crystal quality. To evaluate their true potential and shed light on the limitations put forth by the structural defects, optical processes in several nonpolar and semipolar orientations of GaN and InGaN heterostructures were investigated. Particularly, stacking faults were found to affect significantly the optical properties, substantially influencing the carrier dynamics in nonpolar ($1\bar{1}00$), and semipolar ($1\bar{1}01$) and ($11\bar{2}2$) GaN layers. Carrier trapping/detrapping by stacking faults and carrier transfer between stacking faults and donors were revealed by monitoring the carrier recombination dynamics at different temperatures, while nonradiative recombination was the dominant process at room temperature. Although it is evident that nonpolar ($1\bar{1}00$) GaN and semipolar ($11\bar{2}2$) GaN require further improvement of material quality, steady-state and time-resolved PL measurements support that ($1\bar{1}01$)-oriented GaN templates and InGaN active regions exhibit optical performance comparable to their highly optimized polar c-plane counterparts, and therefore, are promising for vertical cavities and light emitting device applications.

Chapter 1. Introduction

Over the past 30 years, tremendous developments have taken place in optoelectronics, especially devices working in short-wavelength region of the visible spectrum where III-nitride semiconductors (GaN, InN and AlN) have played an important role. Figure 1 shows a plot of bandgap energy versus lattice constant in combination with the visible spectrum for wurtzite InN, GaN and AlN. The bandgap energies of the ternaries (AlGaIn, InGaIn, InAlIn) are given by the expression

$$E_g(A_xB_{1-x}N) = x \cdot E_g(AN) + (1-x) \cdot E_g(BN) - x \cdot (1-x) \cdot b(A_xB_{1-x}N) \quad \text{Equation 1}$$

where A and B represent Ga, In or Al atoms, x represents the composition and $b(ABN)$ represents the bowing parameter for the ternaries reported as 1.4 eV, 0.7 eV and 3.0 eV for InGaIn, AlGaIn and AlInIn, respectively.¹ One can see in Figure 1 that visible spectrum can be easily covered by alloying these nitrides. Development of high efficiency blue light emitting diodes (LEDs) and laser diodes (LDs) have become possible by using InGaIn active regions, and AlGaIn and AlInIn alloys have been utilized for UV emitters as well as power heterostructure field effect transistors.² Despite significant advances, efficiency limiting processes in InGaIn light emitting devices are still not fully understood to date and requires further investigations. Moreover, development of LEDs and LDs based on different crystal orientations for improved optical performance and exploration of new device structures inclusive of those based on vertical cavities utilizing the attractive optical properties of nitrides such as the high exciton binding energy and high optical gain are part of continuing efforts. This thesis specifically focuses on GaN-based vertical cavities and polariton

lasers and the potential of nonpolar and semipolar orientations of GaN for light emitters, which will be briefly introduced below.

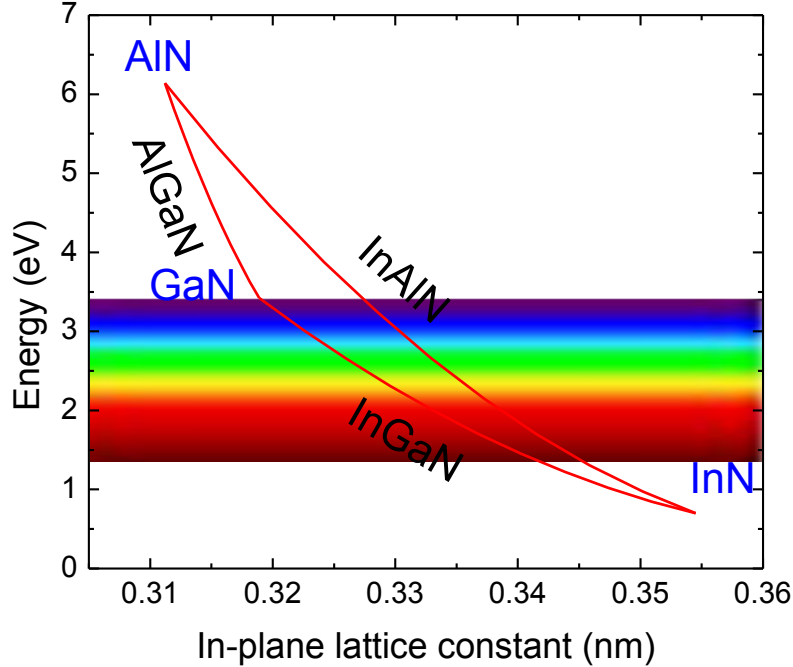


Figure 1: Room temperature bandgap energy versus in-plane lattice constant for III-V nitride semiconductors AlN, GaN and InN. Their ternary alloys and visible spectrum energy range are depicted as well.

1.1. GaN-based vertical cavities

GaN-based vertical cavity lasers have attracted a great deal of interest for prospective use in many applications. This is due to their circular field patterns and to their possibility of dense integration as two-dimensional arrays on the wafer level.^{3,4,5} Optical communications, imaging, optical storage, laser printing/scanning, and signal processing are among the fields vertical cavity lasers can be utilized. As shown in Figure 2, a vertical cavity structure is simply composed of an active cavity medium, bulk or quantum well semiconductor layers, sandwiched between two highly reflective distributed Bragg reflectors (DBRs). DBRs are alternating $\lambda/4$ -thick stacks of dielectric or semiconductor layers, for which high refractive index contrast gives a broad

reflectivity band (stopband) centered at the design wavelength. Higher DBR reflectivity results in higher cavity quality factors and better light confinement in the cavity. Standing-wave pattern of the electric field in the vertical cavity is also shown in **Figure 2** (A $\lambda/2$ thick cavity is depicted). In order to provide good coupling between electrons (or excitons) and photons, the active layers have to be placed at an antinode of electric field pattern in the cavity. The resonance condition for the emission wavelength is given by

$$nL = m \frac{\lambda}{2} \quad \text{Equation 2}$$

where n is the active region refractive index, L is the cavity thickness, m is a positive integer, and λ is the designed emission wavelength. The shortest cavity with the active layers centered on the field antinode can be half wavelength thick, $m = 1$. The cavity depicted in **Figure 2** is for the $m = 1$ case.

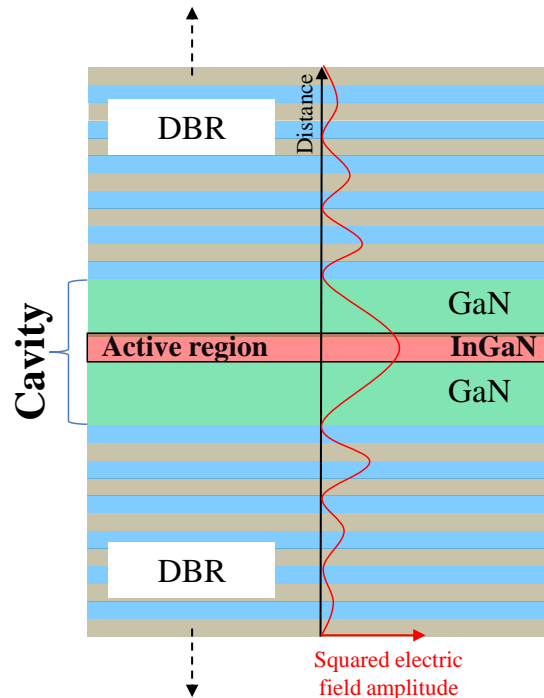


Figure 2: Schematic of a typical microcavity structure. Squared electric field inside the cavity is shown where an InGaN active region is placed at the antinode of the electric field inside the cavity (red color).

Development of blue GaN-based vertical cavity lasers has faced a number of challenges. The integration of high quality InGaN-based active regions with high reflectivity DBRs is one of the most important among those.^{2,6} Semiconductor AlN/GaN DBRs are considered as the natural choice for the DBRs due to simple integration. However, their relatively small refractive index contrast (~ 0.3) necessitates a large number of pairs (>20) to achieve sufficiently high reflectivities. In addition, AlN/GaN DBRs suffer from cracks because of tensile strain with increasing number of pairs. These cracks seriously degrade the reflectivity of the DBRs in addition to quality of the subsequently grown active region. On the other hand, dielectric DBRs provide significant improvements to devices due to their ease of growth, wide stopbands (~ 100 nm) compared to semiconductor AlN/GaN (~ 20 nm) variety, and smaller number of pairs required for high reflectivity if they can be fully integrated with the GaN-based active regions.

Lasing action under optical injection^{7,8,9,10} as well as electrical injection^{11,12,13,14} has been reported at room temperature for InGaN-based blue vertical cavities which are composed of bottom semiconductor/dielectric and top dielectric DBRs. Higher quality factors (Q-factors) result in lower lasing thresholds. However, this is disputed in the literature data for InGaN-based blue vertical cavities. The materials preferences, active region quality, as well as the absorption in the active region, the injected electron density etc. are some of the effects causing the discrepancy in quality factors between the cavities reported. **Figure 3(a)** shows a theoretical representation of a gain profile that has a distribution around the central wavelength, shown in **Figure 3(b)**, which has a strong effect on the quality factor described by $\lambda_0/\Delta\lambda$ where λ_0 is the emission wavelength and $\Delta\lambda$ is the full width of half maximum of the peak. The lasing threshold or gain threshold is characterized by absorption loss and mirror losses. The equation for the lasing threshold for 100% light confinement is given as

$$g_{th} = \bar{\alpha} + \frac{1}{2L} \ln\left(\frac{1}{R_1 R_2}\right) \quad \text{Equation 3}$$

where $\bar{\alpha}$ is the effective absorption loss term (including material absorption, Gaussian beam diffraction and scattering), L is the cavity length, and R_1 and R_2 are the cavity mirror reflectivities. The second term in Equation 3 represents loss due to mirrors. The gain becomes equal to loss at threshold (lasing condition), which is depicted in **Figure 3(c)**.

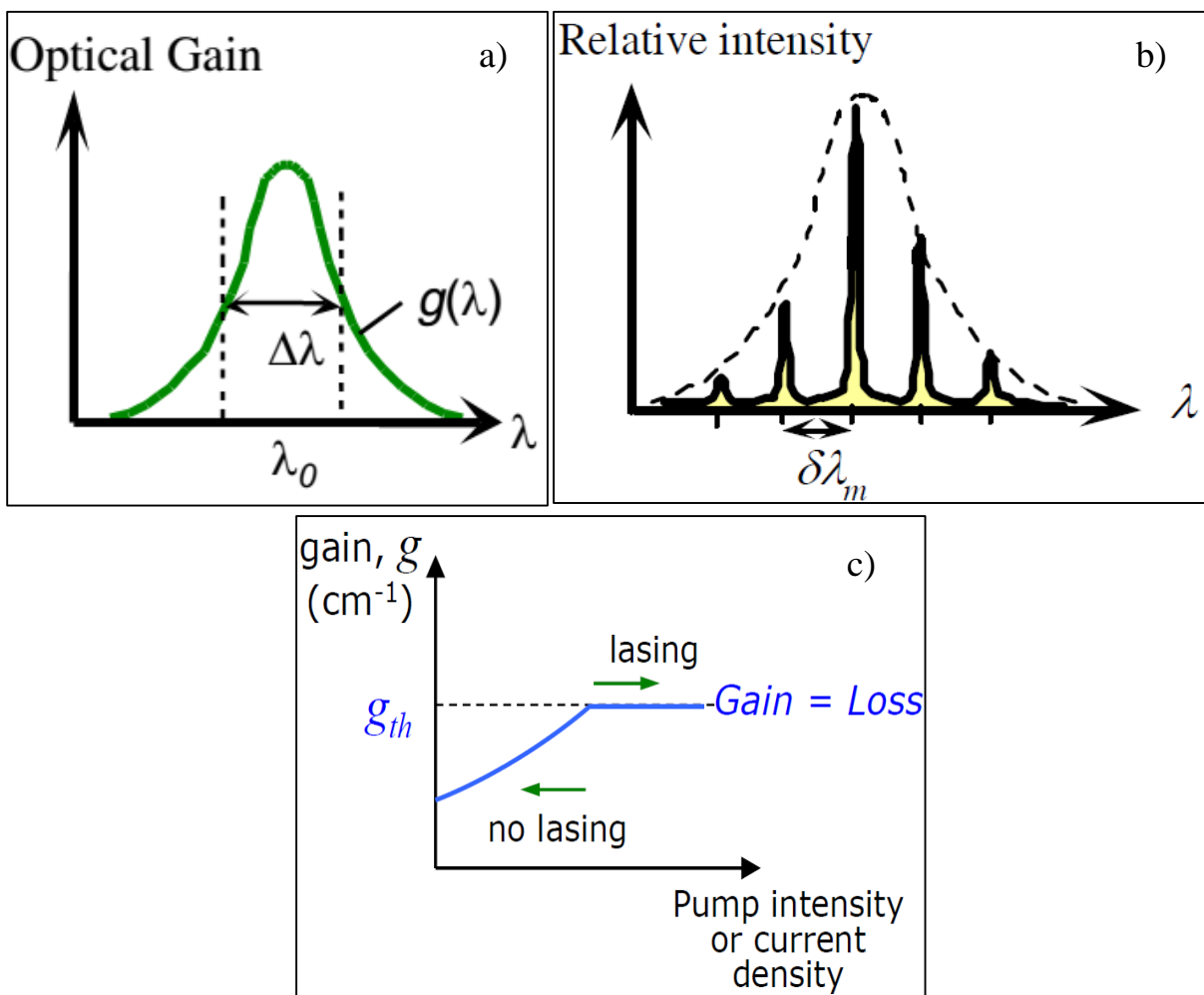


Figure 3: a) Optical gain vs. wavelength characteristics (called the optical gain curve) of a lasing medium. b) Allowed modes and their wavelengths due to stationary EM waves within the optical cavity. c) Gain vs. pump intensity or current density.

With regard to the cavity quality, an emission linewidth of 0.13 nm, corresponding to a Q-factor of 3000, above a 71.5 mJ/cm^2 optical injection threshold has been achieved for a 23.5λ -thick GaN-based cavity sandwiched between $\text{Ta}_2\text{O}_5/\text{SiO}_2$ DBRs.¹⁰ Under electrical injection, an emission linewidth of 0.03 nm (Q-factor 13800) above a threshold current of 1.5 mA has been observed for a 7λ -thick GaN-based cavity sandwiched between $\text{SiO}_2/\text{Nb}_2\text{O}_5$ DBRs.¹³ So far, a Q-factor of 760 has been obtained from a 5λ -thick GaN-based cavity where semiconductor AlN/GaN layers were utilized as bottom DBR with top dielectric $\text{Ta}_2\text{O}_5/\text{SiO}_2$ DBR in the cavity structure, and threshold for lasing action has been observed at 7.8 mJ/cm^2 .¹⁵

Table 1 lists performance parameters of vertical cavities incorporating InGaN MQW active regions with hybrid (semiconductor/dielectric DBRs) and all-dielectric DBRs. In all reports employing all-dielectric DBRs, however, the deposition of the second DBR stack was made possible only after the removal of the substrate. By applying epitaxial lateral overgrowth (ELO) on c-plane sapphire, the need for the substrate removal can be eliminated where the active regions are fabricated entirely on the nearly defect-free laterally grown wing regions. This is conducted to avoid nonradiative centers caused by extended and point defects. One also expects electrical injection to only nearly defect-free active regions grown on ELO wings if ELO technique is well employed with full dielectric DBRs. This also ensures current confinement without any oxidation steps eliminating the substrate removal process.

Table 1: Performance of vertical cavities (with InGaN active region) with chronological order obtained from the selected literature data.

Reference	Cavity Length	Excitation Wavelength (nm)	Bottom DBR	Top DBR	FWHM (nm)	Q-factor	Threshold
Someya 1999 ¹⁶	2.5 λ	399	GaN/AlGaN	ZrO ₂ /SiO ₂	0.8	500	10mJ/cm ²
Tawara 2003 ⁸	4 λ	401	SiO ₂ /ZrO ₂	SiO ₂ /ZrO ₂	0.87	460	5.1mJ/cm ²
Kao 2005 ¹⁷	3 λ	448	AlN/GaN	Ta ₂ O ₅ /SiO ₂	1.4	320	53mJ/cm ²
Wang 2007 ¹⁵	5 λ	448	AlN/GaN	Ta ₂ O ₅ /SiO ₂	0.61	760	7.8mJ/cm ²
Zhang 2008 ¹⁸	12.5 λ	450	SiO ₂ /Ta ₂ O ₅	SiO ₂ /Ta ₂ O ₅	<0.1	-	6.5mJ/cm ²
Zhang 2009 ¹⁰	23.5 λ	397	Ta ₂ O ₅ /SiO ₂	Ta ₂ O ₅ /SiO ₂	0.13	3000	71.5mJ/cm ²
Liu 2013 ¹⁹	-	431	Ta ₂ O ₅ /SiO ₂	Ta ₂ O ₅ /SiO ₂	0.3	1400	3.2mJ/cm ²

1.1.1. Epitaxial lateral overgrowth (ELO)

As explained above, integration of InGaN-based active regions with high reflectivity DBRs is a challenge for vertical cavity structures. Epitaxial lateral overgrowth (ELO) technique will allow one to grow InGaN MQW active regions on nearly defect-free laterally grown wing regions and eliminate cumbersome substrate removal steps. During the growth of GaN on foreign substrates (sapphire, Si or SiC), nearly 10^{10} cm⁻² threading dislocation density is formed due to lattice mismatch. The dislocations start from the interface and propagate vertically through the epitaxial layer up to the surface. One of widely used techniques to reduce the dislocation density is epitaxial lateral overgrowth (ELO). In this technique, a mask material is deposited on top of the first GaN layer. Then a few micrometers wide stripes, windows, are opened in the mask using standard photolithography techniques. Selective GaN epitaxial growth is initiated in the next step, where GaN starts to grow from openings (windows) and laterally extends over the mask material. Consequently, defects still remain in the windows, while nearly defect-free ELO GaN wings are

grown over the mask stripes. This procedure is schematically illustrated in Figure 4. Using this technique the threading dislocation density is reduced down to 10^6 cm^{-2} in the GaN wings.

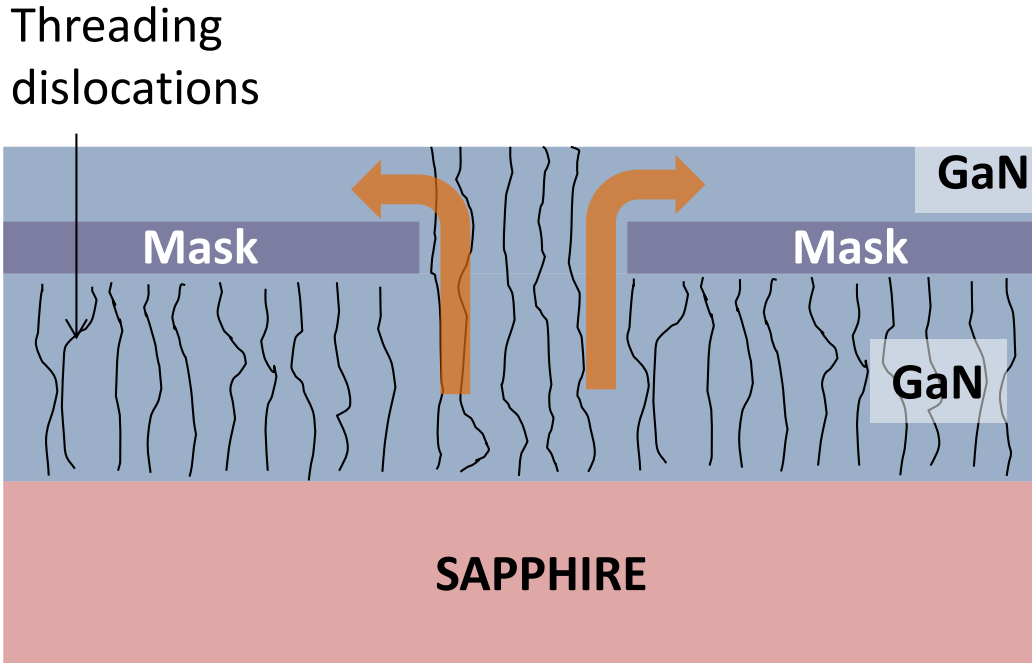


Figure 4: Schematic of epitaxial lateral overgrowth technique. The propagation of the threading dislocations is blocked by the mask material.

1.1.2. Active region design

In order to choose the right active region design for a light emitter one can benefit from extensive studies on InGaN-based active regions used in light emitting diodes (LEDs). As InGaN based LED technology continues to develop and mature, high brightness LEDs retaining high quantum efficiencies at high injection levels ($>100 \text{ A/cm}^2$) have become even more desirable to replace the prevailing incandescent lamps and fluorescent tubes in general lighting. The studies showed that InGaN active regions still face challenges at high current injections for high power LEDs. External quantum efficiency (EQE) of InGaN LEDs peaks at current densities as low as $\sim 5\text{-}10 \text{ A/cm}^2$ and reduces to its half maximum value at as low as $\sim 50\text{-}100 \text{ A/cm}^2$.^{2,20}

In order to better understand this efficiency droop one can analyze the carrier

recombination by using the simplified ABC model assuming no carrier leakage:

$$G = -\frac{dn}{dt} = An + Bn^2 + Cn^3 - \frac{J}{qd} \quad \text{Equation 4}$$

where A, B, and C represent the Shockley–Read–Hall (SRH), radiative recombination, and Auger recombination coefficients, respectively, n is carrier density, and G is recombination rate. The last term in the Eq. 4 represents the contribution from electrical injection where q is the elementary charge, d is the thickness of the active layer, and J is the current density. The assumptions for the simplified ABC model are as following:

- i. injected carrier density is much higher than background carrier density
- ii. electron and hole carrier cross-sections are equal
- iii. trap and Fermi levels are equal

Figure 5 shows a schematic illustration of a simple InGaN active region and carrier flow during the electrical injection. In Figure 5, A, B and C represent the nonradiative, radiative and Auger recombination processes, respectively. As can be seen from Figure 5 some of the injected electrons pass through the active region with their gained kinetic energy while only some of them contribute to the recombination processes. Not all the holes are also contributing the recombination processes due to electron blocking layer as illustrated in Figure 5.

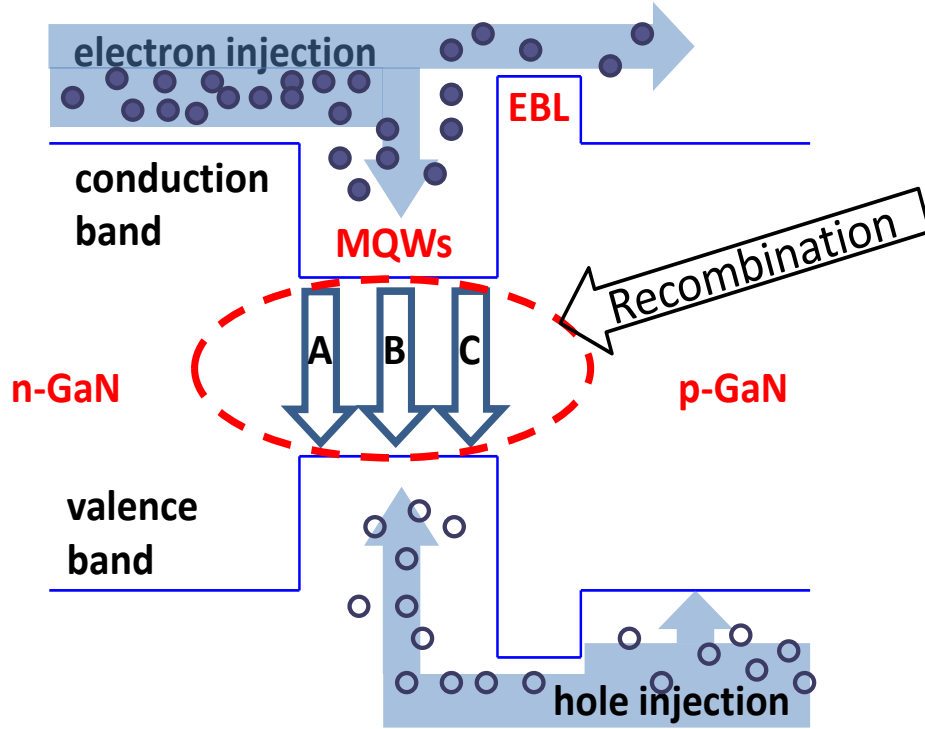


Figure 5: Schematic illustration of carrier flow in a simple LED structure with flat band consideration. LED structure consists of n-type GaN, InGaN multiple quantum well, AlGaIn electron blocking layer (EBL) and p-type GaN.

Shockley-Read-Hall recombination², due to the impurity and defect levels (trap levels) that lie deep within the forbidden band, and Auger recombination² are among the mechanisms limiting the radiative recombination in QWs. Some groups proposed the Auger loss mechanism, energy transfer to another carrier in conduction band, as the main cause for the efficiency droop in InGaIn active regions. The Auger coefficient varies two orders of magnitude among different reports (between 10^{-29} - 10^{-31} $s^{-1}cm^6$).^{21,22,23,24} There is no consensus about the effect of the Auger mechanism on the efficiency drop of nitride-based light emitters yet, which calls for more experimental and theoretical studies. On the other hand, one should also consider the carrier injection, transport, and leakage mechanisms for the efficiency droop. Experiments showed that severe electron overflow results in a substantial electroluminescence (EL) efficiency loss (70% or

more) if no AlGa_N electron blocking layer (EBL) was incorporated²⁵ with InGa_N active regions²⁶. This shows that the carrier leakage must be taken into consideration seriously for the loss mechanism of the injected carriers.^{27,25,28,29} During this process, the injected electrons cross the active region and recombine with the holes outside of the active region. In addition to using the EBL layer, another way to prevent carrier overflow is to use a stair-case electron injector (SEI) right before the InGa_N active region MQWs. SEI is basically multiple InGa_N layers with stepwise increased indium composition inserted before the InGa_N emitting layer. It acts as an electron cooler promoting LO phonon emission to reduce the kinetic energy gained by the injected electrons without hampering hole injection.^{30,31}

It is demonstrated that only the QWs closer to the *p*-Ga_N layer emit light in a typical InGa_N active region due to the poor hole transport.^{32,33,34} Therefore, one may consider using single, but thicker active layer (double heterostructure (DH)) instead of multiple quantum wells in order to obtain more uniform hole concentration across the active region.²² A 9 nm InGa_N-based DH LED provided peak EQE approximately 25% higher than that of a MQW LED [6 period In_{0.15}Ga_{0.85}N (2nm)/In_{0.06}Ga_{0.94}N(3nm)]³⁵ and low efficiency degradation (~10%) was observed at current densities as high as 600 A/cm². Gardner *et al.*²² pointed out that the use of DH active regions provides a lower carrier density compared to a MQW active regions, and therefore, minimizes the effect of Auger nonradiative recombination as well.²²

1.2. Optical characterization of non-polar and semipolar GaN

Most of Ga_N-based light emitting devices use wurtzite (0001)Ga_N orientation due to its well-established technology even though it is electrically polar, which adversely affects the device performance through spontaneous and piezoelectric polarization. Polarization fields cause spatial separation of electron and hole wave functions in active layers and reduce the radiative

recombination rate especially at low injections.^{36,37,38} In contrast, nonpolar orientations have no polarization charge at interfaces. The effect of the piezoelectric field on the PL intensity is higher in low-dimensional systems. In relatively wide quantum wells (2D case), the PL intensity would be higher in nonpolar surfaces compared to polar surfaces since the electron and hole overlap significantly increases due to absence of the piezoelectric polarization field, which is illustrated in Figure 6 for these surfaces.

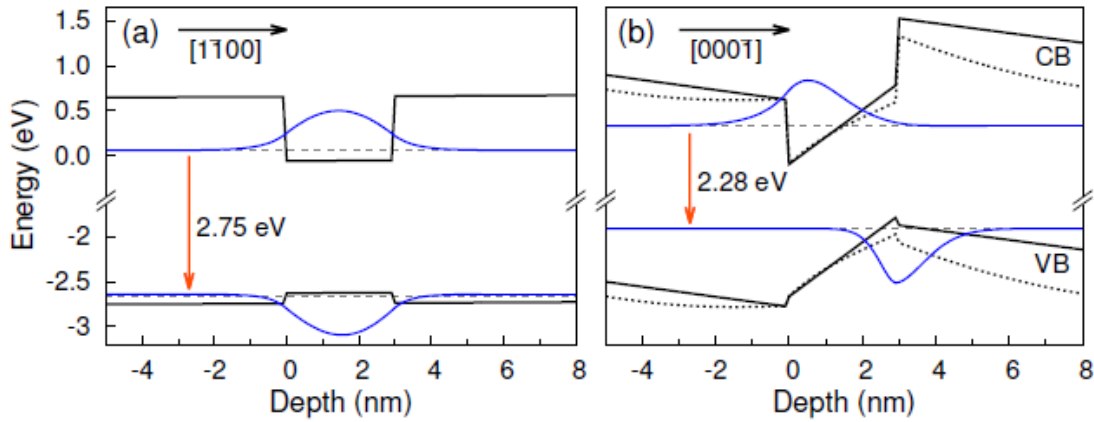


Figure 6: Band structures and electron and hole wavefunctions for nonpolar (a) and polar (b) directions for a 3 nm InGaN quantum well.³⁹

Theoretical calculations⁴⁰ predict that the piezoelectric field across InGaN/GaN heterostructures would be considerably reduced in semipolar orientations as well. **Figure 7** shows piezoelectric polarization and wavefunction overlap of the electrons and the holes in the conduction and valence bands in a 3 nm wide $\text{In}_{0.25}\text{Ga}_{0.75}\text{N}$ single quantum well. It has to be noted that polarization in **Figure 7** is given for a certain composition and thickness considering the strain with respect to GaN. The spontaneous polarization is not included in calculations as well. For a given composition, the net polarization field may vary in thin QWs. It can be seen from **Figure 7** that the electron and hole wavefunction overlap is maximized when the piezoelectric polarization becomes zero for nonpolar orientations (a- and m-orientations) and also at a crystal angle of about 45° tilted from the c-plane. Compared to c-plane, increased electron and hole wavefunctions

overlap and reduced polarization charge are also observable for the semipolar orientations (vertical lines around 60°; $(1\bar{1}01)$, $(11\bar{2}2)$, etc. in **Figure 7**). It has been also shown that the piezoelectric polarization has only a very small dependence on the In or Al percentage in the ternary alloy layers.⁴¹ In agreement with predictions, the electric field across the semipolar InGaN/GaN QWs are weaker than that for the polar c-orientation,^{42,43} but naturally stronger than that for the nonpolar variety.⁴⁴ **Figure 8(b)** shows commonly used polar, nonpolar and semipolar GaN surface orientations in wurtzite GaN structure which are considered here for potential use in light emitting devices. Wurtzite crystal structure of GaN is also schematically represented in **Figure 8(a)** where the hexagonal unit cell is highlighted with bold lines, whilst adjacent atoms are included to highlight the overall hexagonal nature of the structure. Ga–N bonds are shown as dashed lines as well.

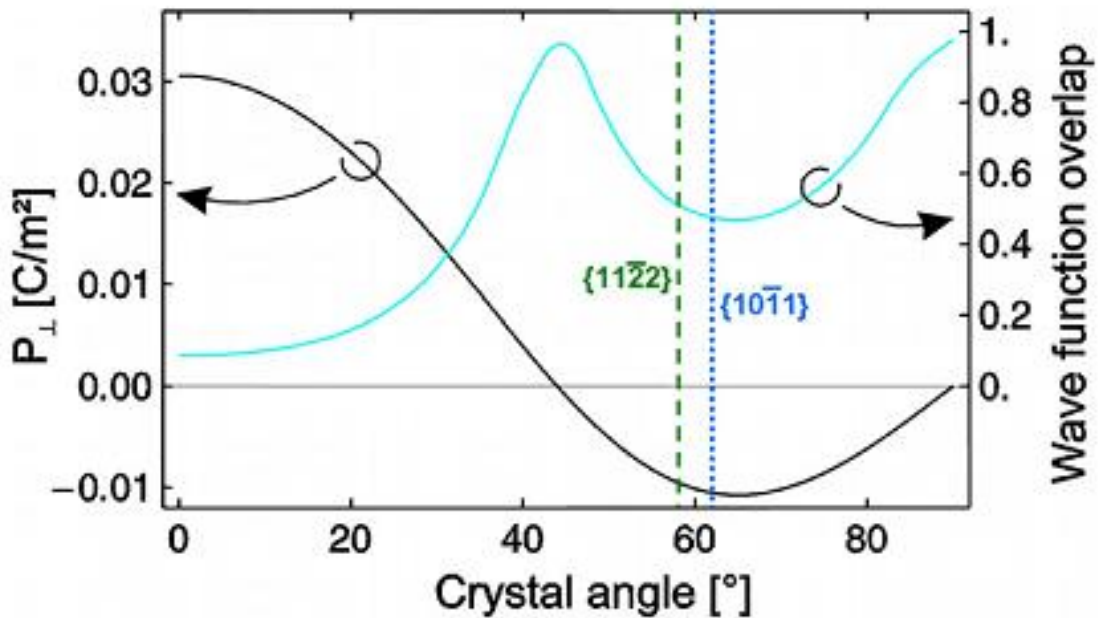


Figure 7: Piezoelectric polarization (left axis) and wavefunction overlap of the electrons and the holes in conduction and valence bands (right axis) in a 3 nm wide $\text{Ga}_{0.75}\text{In}_{0.25}\text{N}$ quantum well.⁴⁵ The crystal angle is defined with respect to the c-axis. For semipolar $(11\bar{2}2)$ and $(10\bar{1}1)$ the angles are 58.4° and 61.7°, respectively.

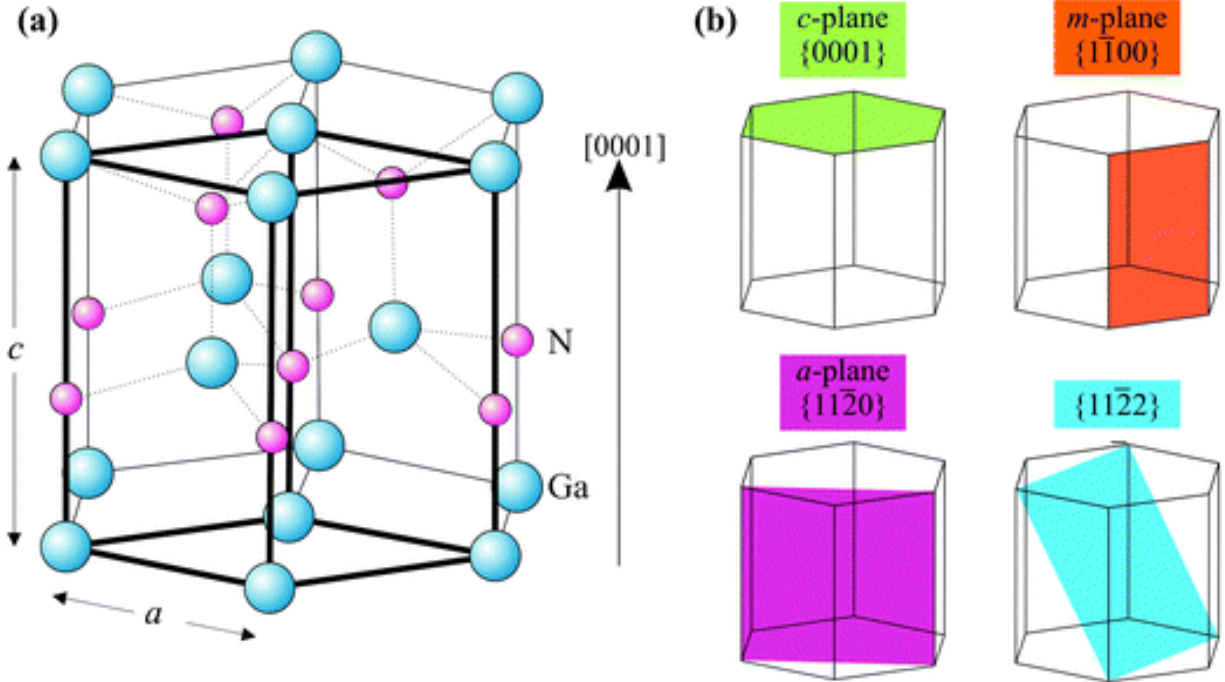


Figure 8: (a) A representation of crystal structure of wurtzite GaN. (b) Commonly used GaN surface orientations; polar c -plane, the nonpolar a - and m -planes and the semipolar $(11\bar{2}2)$ plane.⁴⁶

Another factor affecting the PL intensity in different planes of GaN is the selection rules for the polarization of the excitation source. Polarization selection rules create polarization anisotropy in GaN for both low-dimensional and bulk samples. In wurtzite GaN, optically active exciton states (a bound state of electron and hole attracted to each other by electrostatic force) obey different selection rules primarily due to the complex valence band structure and spin-exchange interaction. The band structure of the A, B, and C excitons for $n=1$ ground states and of $n=2$ excited state of the A exciton obtained in the hydrogen-like isotropic model is shown in Figure 9.⁴⁷ The excitons referred to as the A, B, and C excitons are related to the $\Gamma_9^V - \Gamma_7^C$, $\Gamma_{7upper}^V - \Gamma_7^C$ and $\Gamma_{7lower}^V - \Gamma_7^C$ interband transitions in GaN, respectively. Selection rules for these excitons are given in Table 2. Considering the crystal symmetry, one can easily find that there is no preferential polarization of emission occurring for polar c -plane GaN due to the symmetry in the basal plane.

As can be seen in Table 2 A, B and C excitons are allowed for the light wave vector parallel to c -direction, which is always the case for c -plane GaN in PL measurements. However, when the sample is rotated along the growth direction so that the nonpolar m -plane is parallel to the light wave vector (i.e., light wave vector is normal to c -plane) there is a clear anisotropy observed in the emissions of A, B, and C excitons. In spite of the selection rules one can still observe similar emission intensity from A and B excitons for bulk GaN (assuming homogenous crystal quality) when it is measured in c - and m -directions. This can be done only when the sample is measured with σ -polarized light in the m -direction since A and B exciton transitions are allowed for α - and σ -polarization in both c - and m -directions, respectively. However, in low dimensional systems, such as quantum wells, the excitation power affect the intensities of the excitonic emission lines due to polarization field present in polar direction giving higher emission intensity in nonpolar directions. This should not be mixed with the effect of polarization anisotropy in GaN.

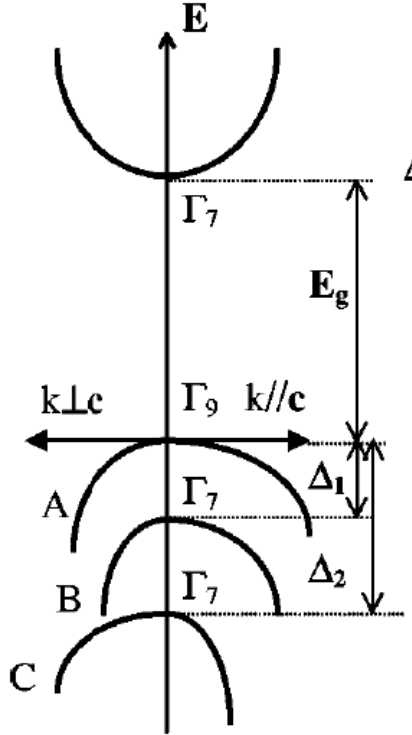


Figure 9: A schematic of the energy band structure and exciton energy levels in wurtzite GaN in an uncoupled hydrogen-like isotropic model.⁴⁷

Table 2: Polarization selection rules for A, B and C excitons.

Polarization	A exciton	B exciton	C exciton
α -polarization ($k \parallel c$ and $E \perp c$)	Allowed	Allowed	Allowed
σ -polarization ($k \perp c$ and $E \perp c$)	Allowed	Allowed	Weak
π -polarization ($k \perp c$ and $E \parallel c$)	Forbidden	Weak	Strong

One example for the polarization anisotropy is given for nonpolar InGaN/GaN multiple quantum well structure in Figure 10. As can be seen from Figure 10 the PL intensity greatly reduced for the different excitation polarization state for the same excitation power density. The excitation whose electric field is parallel to c-direction produces lower PL intensity compared to the excitation with perpendicular electric field component (wave vector is normal to m-plane).

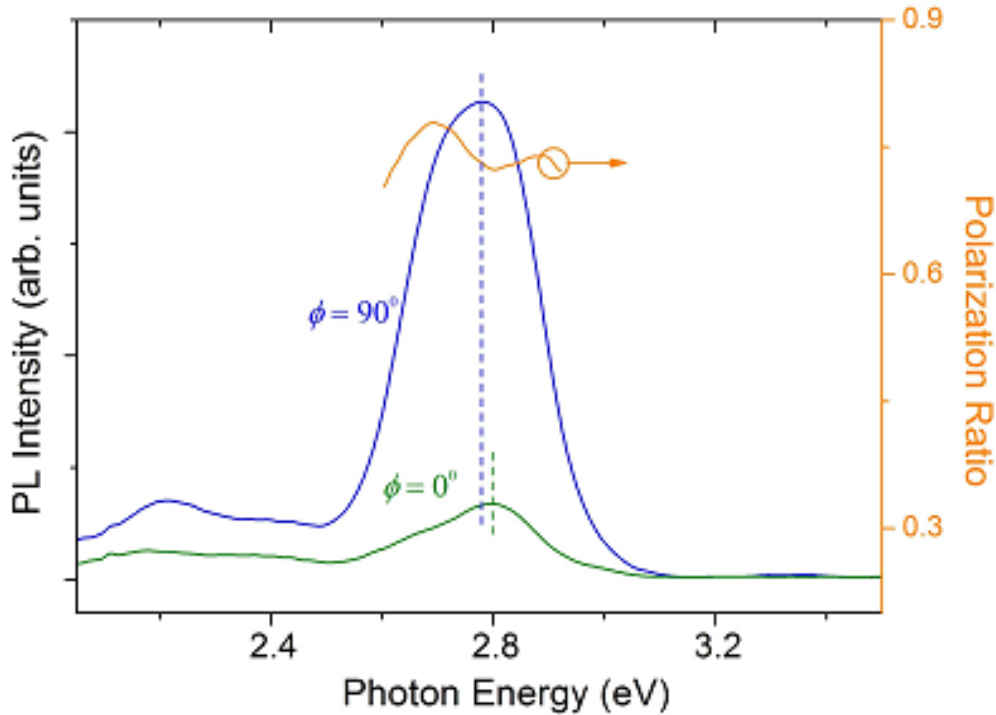


Figure 10: Polarization-dependent PL spectra and polarization ratio of an m-plane InGaN/GaN MQWs measured at room temperature. Here, $\phi = 0^\circ$ and 90° represent $E \parallel c$ and $E \perp c$, respectively.⁴⁸

1.2.1. Extended defects in nonpolar and semipolar GaN

In spite of the observed reduction of the piezoelectric field in semipolar and nonpolar active regions, the crystal quality, and therefore, the efficiency lags behind that of c-plane polar GaN.⁴⁹ High density of extended defects, mainly threading dislocations and stacking faults (SF) emerge during the growth.^{50,51} Stacking faults can form on (0001) basal plane and on $(11\bar{2}0)$ prismatic planes, and develop by slip. In wurtzite GaN, basal plane stacking faults are regarded as very thin zinc-blend segments in a wurtzite matrix and represented as quantum wells with type-II alignment. Electrons are confined in the zinc-blend layer, but with significant spreading of the wave function in the surrounding barrier. Different types of basal plane stacking faults, based on the fault sequence, are depicted in **Figure 11**. In the wurtzite structure, the atoms follow the stacking sequence ...AaBbAaBb... along the [0001] direction, while ...AaBbCcAaBbCc... along the [111]

direction in the zinc-blende structure. Capital letters correspond to Ga atoms and lowercase letters to N atoms. There are four different types of basal plane stacking faults as follows

- a) Type-I stacking faults (I_1): These contain one violation of the stacking rule. For type-I faults two stacking sequences can be considered with equivalent energy. The first where the fault starts on a Bb layer...AaBbCcBb..., and the second where the fault starts on the Aa layer ...AaBbAaCcAaCc....
- b) Type-II stacking faults (I_2): These contain two violations of the stacking rule. The stacking sequence has the fault starting on a Bb layer ...AaBbCcAaCc...
- c) Type-III stacking faults (I_3): These are intrinsic stacking faults in which one of the Aa or Bb layers occupies the wrong Cc position, e.g., ...AaBbAaCcAaBb...
- d) Extrinsic stacking faults (E): These stacking faults have an additional Cc layer inserted in the middle of the normal stacking sequence ...AaBbCcAaBb... .

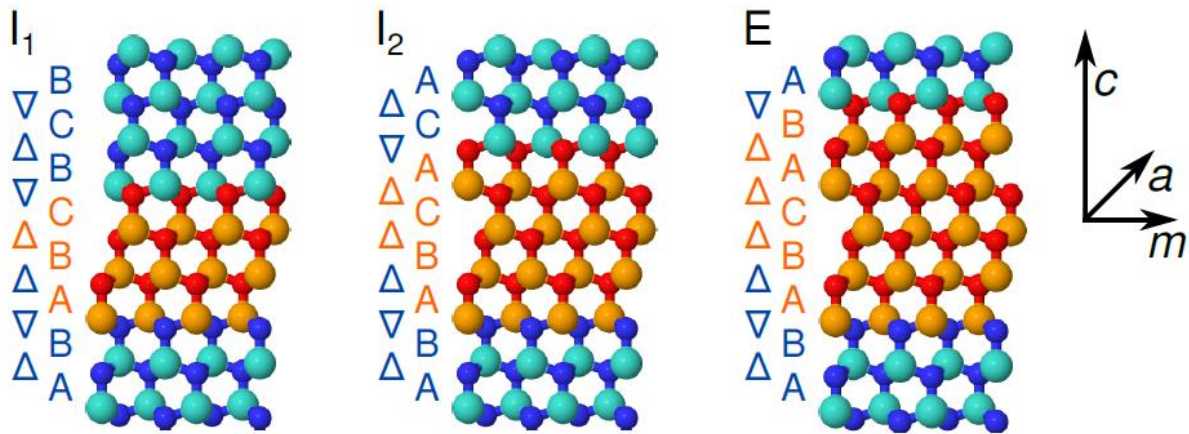


Figure 11: The atomic arrangement of stacking faults, type-I, type-II, and extrinsic basal plane stacking faults. ^{52,53}

It is found that the prismatic stacking faults are attached to basal-plane stacking faults and propagate in the growth direction. The sequential termination of the prismatic faults along the growth direction usually folds into basal-plane faults. It is likely that nucleation of stacking faults

on a prismatic plane are triggered due to the surface structural imperfections at the intersecting basal-plane stacking faults. An atomic model of a prismatic stacking fault projected onto the (0001) plane is depicted in **Figure 12(a)** in addition to a schematic representation of lattice planes and directions for prismatic stacking fault in the (0001) projection in **Figure 12(b)**.

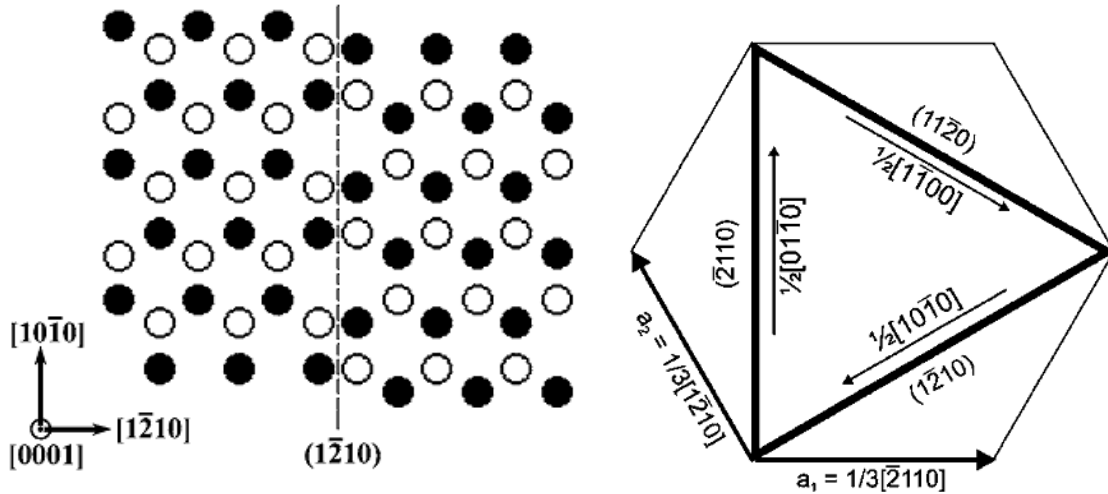


Figure 12: (a) Atomic model of a prismatic stacking fault and $(11\bar{2}0)$ stacking mismatch boundary (projection onto the (0001)). White and black circles represent Ga atoms (nitrogen atoms are omitted because their projection would overlap with Ga atoms).⁵⁴ (b) Schematic representation of lattice planes and directions for prismatic stacking fault in the (0001) projection.⁵⁵

Microscopic mechanisms governing the defect formation as well as effects on the optical quality are not well understood yet. Therefore, comprehensive studies of defect formation in nonpolar and semipolar nitrides and their influence on the optical quality are required for improvement of material quality of active regions and thus device performance.

1.3. Polariton Lasers

Since the first observation of the strong polariton coupling in a gallium arsenide (GaAs) based microcavity⁵⁶ in 1992, the microcavities have attracted a great deal of interest owing to their potential to achieve ultra-low threshold lasers, so-called “polariton laser”, first theoretically

devised by Imamoglu *et al.*⁵⁷ The heart of this phenomenon is the formation of a coherent beam of photons based on a bosonic phase transition toward a condensate. The bosonic condensation can be achieved at densities well below the onset of exciton bleaching, which leads to ultra-low threshold, ideally thresholdless, lasers.

The polaritons are formed due to superposition of excitons and photons having the same energy and momentum, which exhibit an effective mass up to four orders of magnitude smaller than that of excitons. In a microcavity, the exciton-light coupling may lead to either crossing or anticrossing of the real parts of the Eigen-frequencies in the vicinity of the resonance of the excitonic transition in the active region with the bare cavity mode. The system is described by the coupled-oscillator equation:

$$(\omega_x - \omega - i\gamma)(\omega_c - \omega - i\gamma_c) = V^2 \quad \text{Equation 5}$$

where ω_x the exciton resonance frequency, γ is the exciton non-radiative damping rate, $\omega_c - i\gamma_c$ is the complex Eigen-frequency of the cavity mode in the absence of exciton-light coupling, and V is the coupling constant dependent on the exciton oscillator strength and the penetration depth of the Bragg mirrors. The splitting between the cavity modes can be written by $2\sqrt{V^2 - \left(\frac{\gamma - \gamma_c}{2}\right)^2}$

if $\omega_x = \omega_c$. $V < \left|\frac{\gamma - \gamma_c}{2}\right|$ is characterized by crossing of the exciton and photon modes and an increase of the exciton decay rate at the resonance point where the weak-coupling regime holds. This regime is typically used in vertical cavity surface emitting lasers (VCSELs). The strong-coupling satisfies if $V > \left|\frac{\gamma - \gamma_c}{2}\right|$ in which the crossing of real parts of exciton and photon modes takes place. In this regime, two new optical resonances manifest themselves in the spectra known

as upper and lower exciton-polariton branches (UPB and LPB, respectively). A theoretical result is shown in Figure 13 for a CdTe cavity showing newly formed upper and lower polariton branches for -10 meV negative detuning (red color).

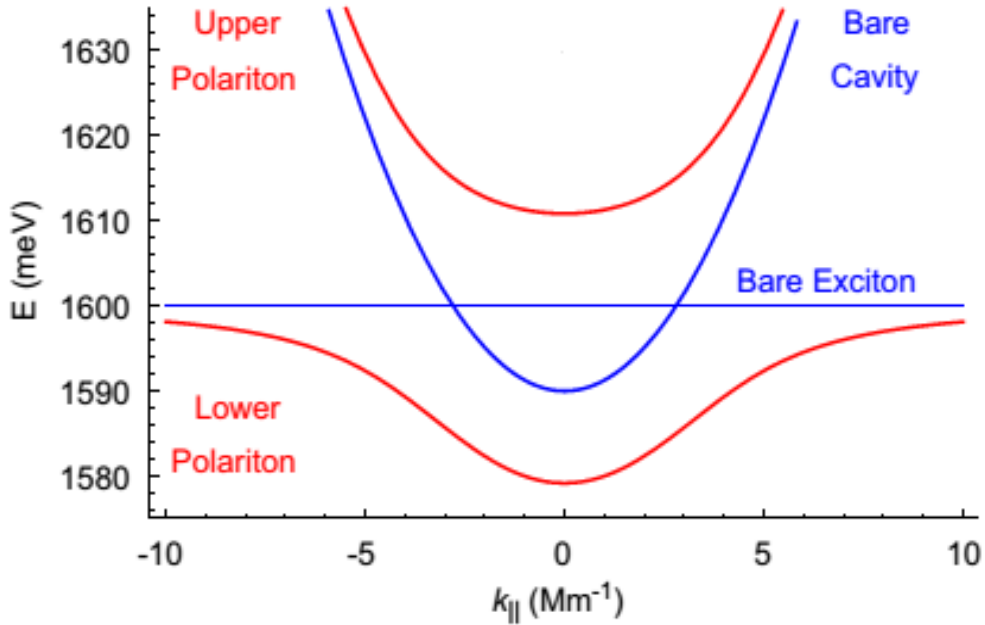


Figure 13: Dispersion of polaritons in a CdTe cavity.⁵⁸ Upper and lower polariton branches are plotted in red, and bare cavity and exciton dispersion curves are given in blue.

In confined structures, an exciton with wave vector k couples to the photon of the same in-plane wave vector ($k_{||}$) because of the absence of in-plane confinement. Momentum is not conserved in z -direction and exciton couples to photons at different k_z whose value is $nz\pi/L$, L being the microcavity length. In this case, Rabi frequency occurs at different frequencies leading to a weak coupling due to fact that one exciton mode couples to a set of photon modes. However, a reversible exchange between exciton and photon modes is established in the strong coupling regime resulting in a much smaller cavity line-width. Differently from the bulk case, photon and exciton dispersions in microcavities are function of in-plane wave vector, $k_{||}$:

$$E_C(k_{\parallel}) = \hbar\omega_C(k_{\parallel}) = E_C(k_{\parallel}=0) + \frac{\hbar^2 k_{\parallel}^2}{2m_{ph}} \quad \text{Equation 6}$$

$$E_X(k_{\parallel}) = \hbar\omega_X(k_{\parallel}) = E_X(k_{\parallel}=0) + \frac{\hbar k_{\parallel}^2}{2M}$$

where M is the sum of the electron and hole effective masses in the QW plane, and m_{ph} is the photonic effective mass described as $m_{ph} = \hbar n_c / cL_c$ which is extremely light when compared to exciton mass. Using the rotating-wave approximation ($E_C - E_X \ll E_C + E_X$) and solving the resulting eigenvalue problem one reaches to energy values of upper (+) and lower (-) polariton modes as⁵⁹

$$E_{+(-)}(k_{\parallel}) = \frac{E_C(k_{\parallel}) + E_X(k_{\parallel})}{2} \pm \frac{1}{2} \sqrt{\left(E_C(k_{\parallel}) - E_X(k_{\parallel})\right)^2 + 4\hbar\Omega_R(k_{\parallel})^2} \quad \text{Equation 7}$$

where coupling Ω_R is given by $\Omega_R(k_{\parallel}) = \frac{\mu}{2\pi a_B^{2D}} \sqrt{\frac{E_X(k_{\parallel})}{\epsilon_b L}}$, μ being exciton dipole. The in-plane

wave-vector is related to the light incidence angle, ϕ , by the relation $k_{\parallel} = \frac{\omega}{c} \sin \phi$. The polariton

dispersion curves can simply be obtained by measuring angular dependences of the resonances.

Angle-resolved reflectivity and photoluminescence techniques are the most commonly used

techniques to restore the polariton dispersion curves for such microcavities. **Figure 14(a)** shows

theoretical polariton dispersion curves in a typical GaN-based microcavity for different Rabi

splitting values at zero detuning. The detuning of bare photon and exciton modes in a microcavity

is described as $\delta = \omega_c - \omega_x$ which is an important parameter strongly affecting the shape of the

polariton dispersion. **Figure 14(b)** shows polariton dispersion curves for different detuning values

at 30 meV Rabi splitting.

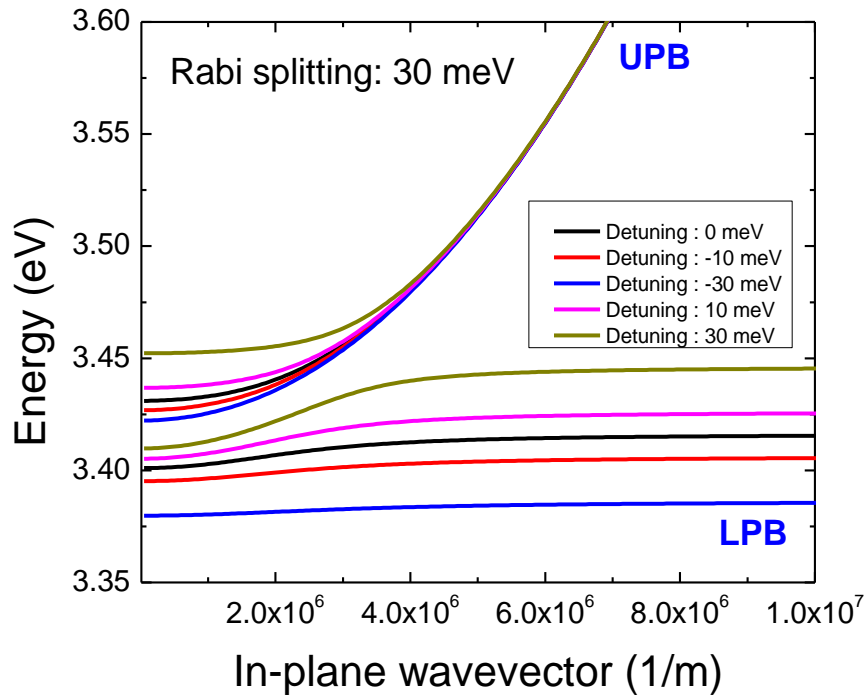
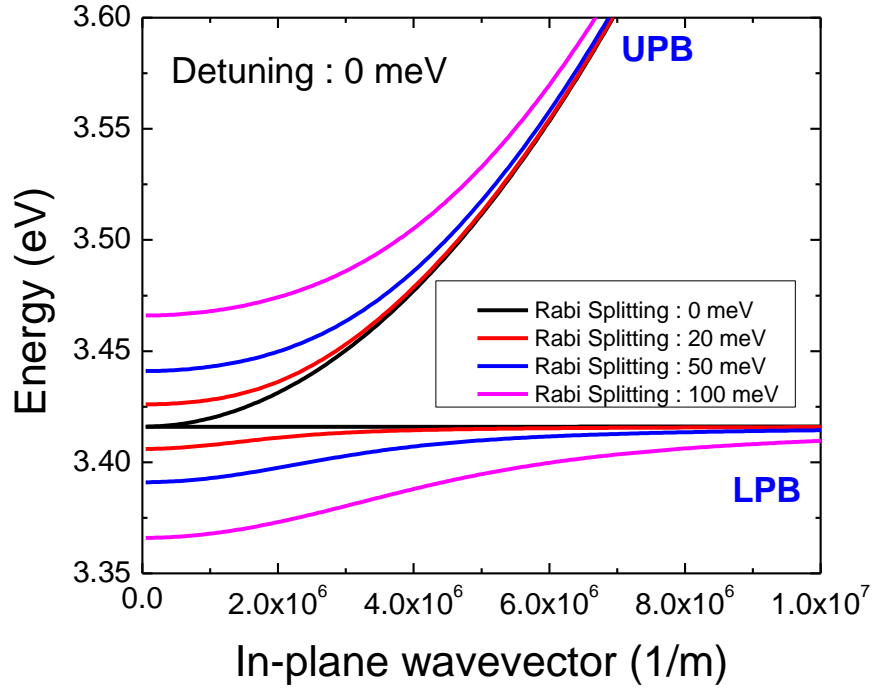


Figure 14: Polariton dispersions curves for GaN-based microcavity (a) for different Rabi splitting energies at zero detuning (b) for different detuning energies at 30 meV Rabi splitting.

As can be seen from **Figure 14** central part (near 0 momentum region) of the lower polariton branch is strongly dominated by an extremely light photon effective mass, while the rest is dominated by a relatively heavy exciton effective mass. This produces the so-called “polariton trap” at $k_{\parallel} = 0$ in the LPB.⁶⁰ The photon emission process is totally different from a photon laser where the lasing results from stimulated emission of photons with an occupation number larger than 1. The quantum degeneracy threshold of polaritons is triggered by the same principle of bosonic final-state stimulation, yet the physical process is different. It is stimulated scattering of massive quasiparticles from nonlasing states at $k_{\parallel} > 0$ into the lasing state at $k_{\parallel} = 0$. The polaritons that reach to polariton trap region (at $k_{\parallel} = 0$) can only thermalize through the internal interactions with each other since the acoustic phonon assisted relaxation is forbidden by energy and momentum conservation laws in this region. The polaritons in the trap region are subject to quantum coherent effects and maintain coherence during their lifetime. The basis for “polariton lasing” is the non-zero minimum of the LPB at $k_{\parallel} = 0$.⁵⁶ The nonlinear increase of the photon flux is an outcome of the leakage of the polaritons via cavity mirrors. Hence the observed threshold of the polariton system requires no electronic population inversion. The difference in the operational principles of a polariton laser and a conventional laser is shown schematically in **Figure 15**. The vacuum Rabi splitting becomes significantly greater than the broadening of both the exciton and the cavity modes when the LPB and UPB anticross. The coupling strength is determined by the exciton oscillator strength and the amplitude of the cavity field. Rabi splitting can be increased by choosing proper and high quality active regions with large exciton oscillator strength. It reaches 4-15 meV⁶¹ in existing GaAs-based microcavities, up to 30 meV⁶² in CdTe based microcavities, up to 50 meV^{63,64} in GaN and ZnO cavities and more than 100 meV⁶⁵ in organic microcavities. With its large oscillator strengths and exciton binding energies at room

temperature (26meV in bulk, >40 meV for InGaN quantum wells), and due to its well-developed growth technology GaN-based active regions are very attractive for strong coupling regime in vertical cavities.

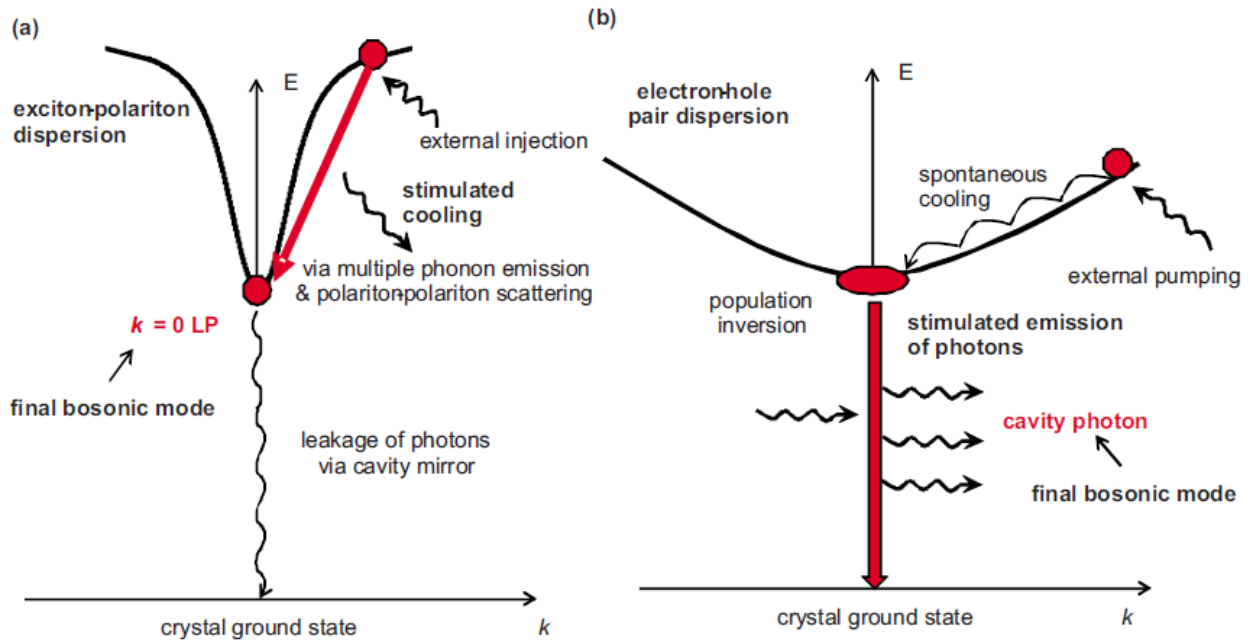


Figure 15: The operational principles of (a) polariton and (b) conventional laser.⁵⁷

Polariton lasing under optical injection for GaN-based vertical cavities has been already reported by several groups in literature.^{66,67} Electrical injection polariton lasing for GaAs-based microcavities has been demonstrated,⁶⁸ while it has not yet been achieved for GaN-based microcavities. One way to obtain polariton lasing under electrical injection is to achieve a better photon confinement in the cavity. This can be done by producing better quality active regions. Consequently, the spontaneous emission will take place in the laser mode which results in a strong increase of the β coefficient (the fraction of spontaneous emission that seeds the lasing process).⁵⁸ The vertical cavities are an example of this trend where a transition from weak coupling (lasing effect only originates from stimulated emission process) to strong coupling regime is seen.⁶⁹ Larger quality factors will allow strong increase of the cavity photon lifetime and a higher β

coefficient. Obtaining high quality GaN-based vertical cavity structures will pave the way for polariton lasing under electrical injection.

1.4. Organization of the thesis

This thesis is a collection of comprehensive results from optical studies focused on InGaN-based blue light emitters in general and vertical cavities in particular, in addition to a detailed investigation of the building blocks mainly polar InGaN active region designs, and nonpolar and semipolar GaN orientations. A set of optical techniques such as photoluminescence (PL), time-resolved PL, angle-resolved PL and reflectivity, polarization-resolved PL, near-field scanning optical microscopy (NSOM), were used to explore the major challenges during the development of the vertical cavity structures and solutions were proposed and some were implemented accordingly. Temperature and excitation power dependent PL and TRPL measurements gave insights about InGaN active region quality as a measure of internal quantum efficiency and radiative/nonradiative PL decay times. These techniques were also used to elucidate the optical quality, recombination dynamics and defect related luminescence in semipolar/nonpolar GaN layers for a prospective use in light emitting devices.

Chapter 2 is dedicated to improvement of the active region quality for the InGaN-based blue light emitting devices by playing with active region components such as staircase electron injector (SEI), electron blocking (EBL) layers, quantum well width, barrier heights as well as understanding of efficiency droop phenomena in the active regions. In addition to theoretical and numerical investigations, optical and electrical measurements were applied to quantify internal and external quantum efficiency (IQE and EQE), respectively, together with time-resolved photoluminescence to better understand the carrier dynamics governed in the carrier recombination processes.

In Chapter 3, optical signatures of strong polariton coupling in a hybrid InGaN-based microcavity obtained from angle-resolved photoluminescence and cathodoluminescence measurements is reported. Having the largest Rabi splitting reported in the literature, 75 meV (promising for ideally thresholdless polariton lasers), the cavity structure consisted of six periods In_{0.15}GaN MQWs with low In_{0.06}GaN barriers and sandwiched between 29.5 pair bottom semiconductor crack-free AlN/GaN and top 13.5 pair SiO₂/SiN_x distributed Bragg reflectors (DBRs). In addition, Chapter 3 reports growth and characterization results of a new type of InGaN-based vertical cavity structure grown on nearly defect-free epitaxial lateral overgrown (ELO) GaN layers utilizing both large stop-band bottom and top dielectric SiO₂/SiN_x DBRs. This new type vertical cavity structure provided solutions to narrow stopband bottom distributed Bragg reflectors (DBRs) and their integration with cavity active region, high quality GaN substrate and InGaN active regions, and cumbersome substrate removal process after top dielectric DBR deposition.

Chapter 4 reports on detailed optical investigations of nonpolar and semipolar GaN layers. These studies extend to the optical quality enhancement, defect analysis, recombination dynamics. Extended defect distributions are studied using spectrally and spatially resolved cathodoluminescence and near field scanning optical microscopy. Also, temperature dependent time-resolved and polarization-resolved PL are used to gain insight into the contributions of excitons and free carriers to the radiative recombination at different temperatures for a nonpolar bulk GaN. In addition, InGaN active regions grown semipolar orientations are investigated and results are presented at the end of Chapter 4. All the results are summarized and overall conclusion are provided in Chapter 5, and the outlook for future studies is discussed in Chapter 6.

Chapter 2. Optical investigations of quantum efficiency of InGaN-based active regions

InGaN is now becoming the first choice in industry for blue light-emitting diodes (LEDs)² due to its high light conversion efficiency. However, it still suffers efficiency droop at high electrical injection levels. The theoretical explanation for the physical origins for the efficiency droop^{21,22,70} have already been discussed in Chapter 1. Carrier overflow is found to be the leading mechanism as the debates about the origins of efficiency droop still continue.^{27,71} One may wisely investigate the active region designs to find possible ways to prevent the efficiency droop, where the active region is constituted of core elements of staircase electron injector (SEI), quantum wells and barriers, and electron blocking layer. One possible approach to prevent the efficiency droop and increase the quantum efficiency might be to increase InGaN active region widths as much as possible maintaining the material quality. For this reason, instead of 2 nm (2-dimensional) quantum well active regions a 3D-like (above 2 nm) double heterostructure (DH) layers can be used for active emitting layer owing to their lower density of states minimizing the Auger recombination effect.²² Earlier reports demonstrated that EBL layer can be safely removed from the active region only if the InGaN SEI layer is maintained in the structure, and the efficiency droop can be significantly reduced.^{72,31} This may inspire one to further investigate the effects of SEI layer on the efficiency droop if the the thicknesses of the InGaN layers in SEI is changed. In this chapter, optical characterization techniques are focused to investigate the efficiency droop mechanism for the InGaN active regions in which the core parameters of their structure are changed. The results are presented and summarized accordingly.

2.1. Quantum Efficiency InGaN multiple quantum wells: Effects of barrier height and thickness

InGaN LED structures with different active region designs are investigated to improve the quantum efficiencies in addition to reduce the electron overflow at high injection current density. In this realm, multiple quantum well (MQW) LED structures with different InGaN barrier heights $\text{In}_{0.06}\text{Ga}_{0.94}\text{N}$ (low barrier, LB) and $\text{In}_{0.01}\text{Ga}_{0.99}\text{N}$ (high barrier, HB) and thicknesses (3 nm and 12 nm) are compared and analyzed. MQWs with 3 nm and 12 nm barriers are called coupled and uncoupled MQWs throughout the thesis, respectively. In addition, the quantum efficiency of uncoupled MQW LED (with only SEI) is compared to that of only EBL. Internal quantum efficiency (IQE) values at different carrier density were measured by resonant photoluminescence excitation power-dependence method.⁷³ The details for this method are given in Appendix A. Being a very straightforward this method provides one a very good comparison for the relative values of internal efficiency of the LEDs investigated, while the exact numbers are still questionable. One may need to rely on some other optical experiments to obtain exact IQE values, which will be discussed in next sections. For this experiment, the excitation wavelength from a frequency doubled Ti:Sapphire laser was set to 385 nm, below the bandgap of the InGaN barriers. Therefore, the photo-excited electron-hole pairs were generated only within the quantum wells while any carrier generation in the barriers was avoided and the carrier distribution was uniform in the active region.^{73,72} Non uniformity in electron and hole distribution was said to be one of the major causes for the efficiency droop in EL observations.⁷⁴

InGaN MQW active region LED structures emitting at ~420 nm (15% In) were grown on ~3.7 μm -thick *n*-type GaN templates on sapphire in a vertical low-pressure metalorganic chemical vapor deposition (MOCVD). The conduction band diagram of the active region designs are given in Figure 16. All the structures contained a 60-nm Si-doped ($2 \times 10^{18} \text{ cm}^{-3}$) $\text{In}_{0.01}\text{Ga}_{0.99}\text{N}$ underlying

layer just beneath the active region or the SEI for improved quality. The SEI consists of two 5-nm InGaN layers (two-layer SEI) with step-increased In composition of 4% and 8%, in the given order, again inserted before the active region. The SEI can in principle be made a continuously graded structure. The steps having potential energy drop equal or more than one LO phonon energy (88 meV) contribute to electron thermalization through electron–LO-phonon interaction. A ~10-nm p -Al_{0.15}Ga_{0.85}N electron blocking layer was deposited on top of the active quantum well region in one particular wafer without SEI for comparison. The LED structure was completed with Mg-doped p -GaN layer of 100-nm thick having $4 \times 10^{17} \text{ cm}^{-3}$ hole density, as determined by Hall measurements on a separate calibration sample. Square mesa pattern ($400 \times 400 \text{ }\mu\text{m}^2$) were formed by conventional lithography and chlorine based Inductively Coupled Plasma (ICP) etching. Ti/Al/Ni/Au (30/100/40/50 nm) metallization annealed at 800 °C for 60 seconds was used for n -type ohmic contacts, and 5-nm/5-nm Ni/Au electrodes served as the semi-transparent p -contacts. Finally, 40/50-nm Ni/Au electrodes were deposited on part of the mesa for contact pads.

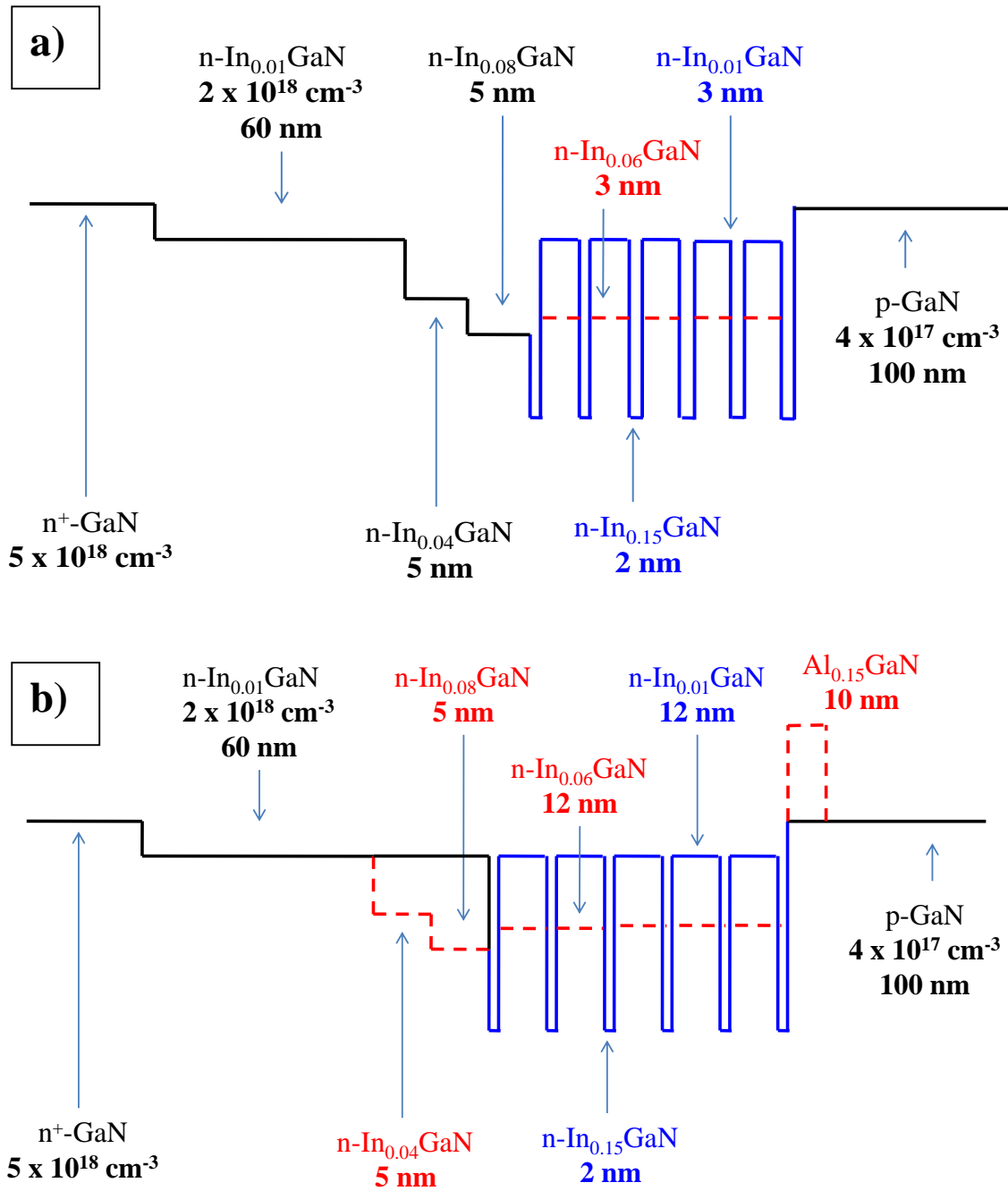


Figure 16: The conduction band diagrams for the active region designs used in LEDs: (a) coupled MQW (b) uncoupled MQW. Flat band diagrams are shown only for simplicity.

Compared to the uncoupled MQW LEDs, the coupled MQW and DH LEDs exhibit lower IQE values and slower rate of increase in the IQE with generated electron (hole) concentration as shown in Figure 17. The low and high barrier coupled MQWs reach the maximum IQE value of 84% and 79% at the carrier density of about $6 \times 10^{18} \text{ cm}^{-3}$, respectively. This appears to bode well for the low InGaN barrier height sample in terms of IQE, most likely due to strain and quality considerations and absorption in the low barrier. The LED structures with coupled MQW active regions either low and high barrier exhibit a much slower rise in the IQE values [80% is reached at the maximum equivalent photocurrent density of 90 A/cm^2] when compared with uncoupled MQWs [80% IQE is reached $\sim 30 \text{ A/cm}^2$, Figure 18], as displayed in Figure 17. IQE values vs. electron density converted from carrier density using rate equation (Equation 8) naturally being resonant optical excitation calls for no carrier leakage:

$$J = qdG = qd(A n + B n^2) \quad \text{Equation 8}$$

where G is the generation rate, n is the carrier density, q is the electron charge, d is the thickness of the active layer, and J is the photo current density. The terms A and B represent Shockley-Read-Hall (SRH) nonradiative recombination and radiative recombination coefficients, respectively. The Auger coefficient C , which we deem small, is neglected here, particularly, at low injection level due to the limitation of laser power during optical measurements. By assuming B to be $10^{-11} \text{ cm}^3 \text{ s}^{-1}$, and fitting the curves, we extracted the A coefficient for the LEDs. Then we converted the carrier density n to photocurrent density by inserting the assumed B and extracted A coefficients into the rate equation.

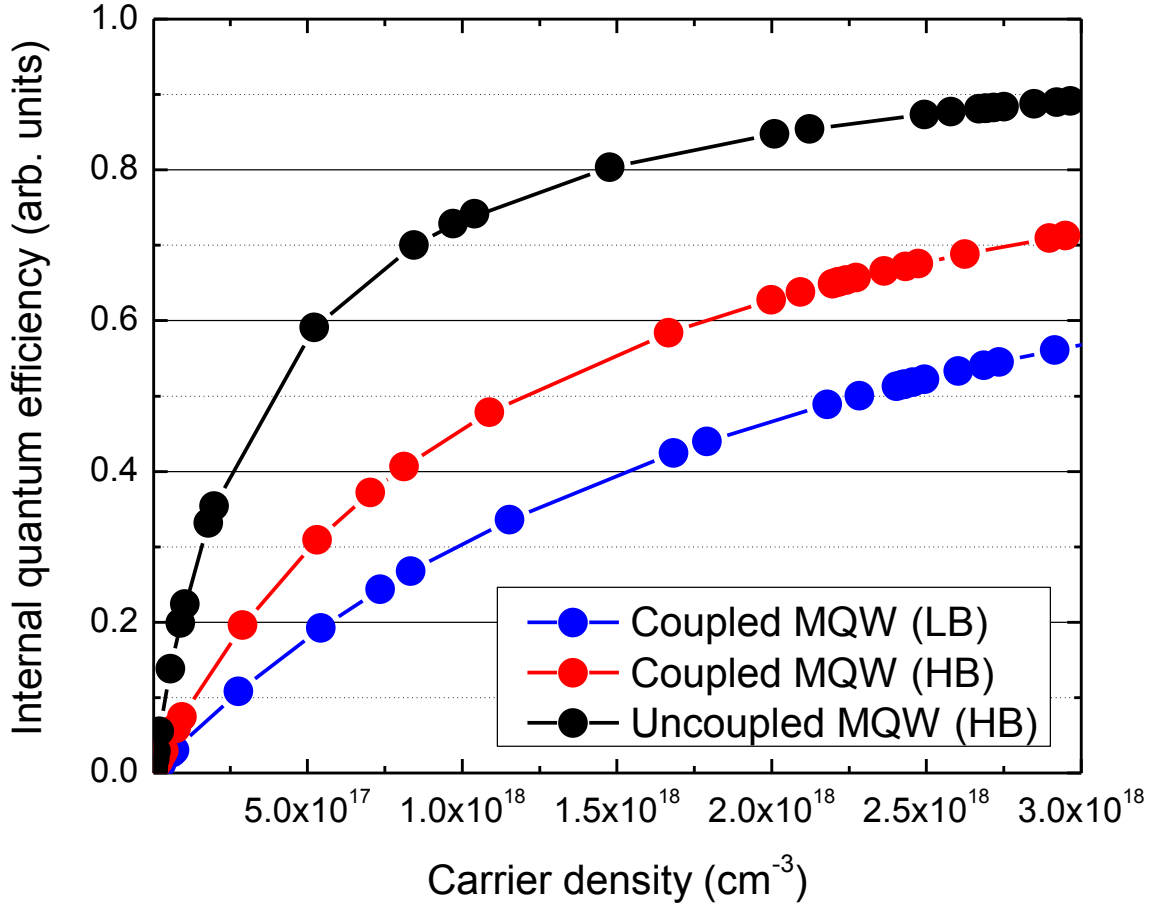


Figure 17: (a) IQE values determined from excitation-dependent PL for LEDs with coupled MQWs. B value was assumed to be $10^{-11} \text{ cm}^3\text{s}^{-1}$ for the calculation of carrier densities.

Figure 18 shows the IQE results for the LED structures with uncoupled MQWs high and low barriers w/ SEI and w/o EBL, uncoupled MQWs high w/o SEI and w/ EBL. The IQE values reached 90% and 93% at a carrier density of $3 \times 10^{18} \text{ cm}^{-3}$ for the high and low barrier uncoupled MQWS (w/ SEI), respectively, and continued to increase for higher carrier densities [Figure 18]. Lowering the InGaN barrier height slightly enhanced the IQE at both low and high carrier densities. The uncoupled MQW w/ EBL and w/o SEI shows about 10% lower IQE values consistently as compared to the MQWs having only SEI. This demonstrates that the IQE value is improved by inserting SEI instead of using EBL. This might be due to the degraded layer crystalline quality by the strain-induced defects in the LED with AlGaIn EBL.

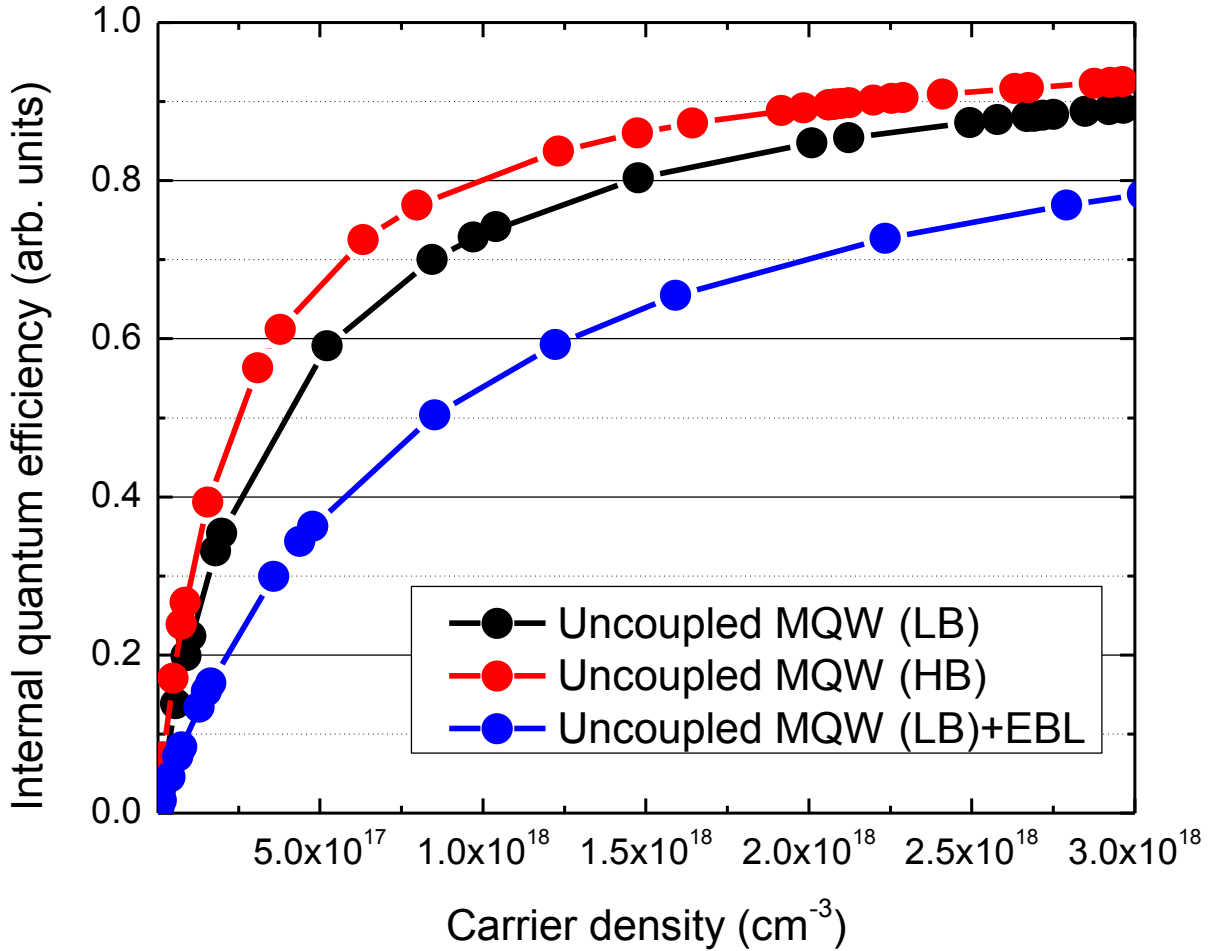


Figure 18: (a) IQE values determined from excitation-dependent PL for LEDs with uncoupled MQWs. B value was assumed to be $10^{-11} \text{ cm}^3\text{s}^{-1}$ for the calculation of carrier densities.

Because resonant excitation assures nearly uniform electron and hole generation in the active region and implies thermal equilibrium for carriers, the efficiency degradation due to the carrier overflow would not be observed. However, it is well known that LEDs exhibit efficiency droop under electrical injection, which is the case in EQE measurements. This means that LEDs having the best IQE values may not necessarily have the best EQE due to possible carrier leakage. To determine the relative EQE, on-wafer pulsed EL measurements (0.1 % duty cycle, 1 kHz) were carried out for all the investigated LEDs with no effort having been made to enhance light extraction. Care was taken to assure the same light collection geometry among all chips. Note that

not all the light emanating from the LED was collected. Figure 19 shows the relative EQE values for the uncoupled MQW structures. Among them, the low barrier uncoupled MQW w/ SEI and w/o EBL exhibited the highest EQE value and reached a maximum at a current density of around 40 A/cm^2 , while the EQE of the high barrier uncoupled MQW w/ SEI and w/o EBL reached the maximum at a same current level ($\sim 40 \text{ A/cm}^2$) but suffers more efficiency degradation in relation to the one with reduced barrier with increasing injection current. As shown in Figure 19, the relative EQE for the low barrier uncoupled MQW is approximately 15% higher than that for the high barrier uncoupled MQW under current density $\sim 600 \text{ A/cm}^2$. It is well known that the hole transport in GaN is compromised due to the large hole effective mass and ensuing low hole mobility ($\sim 5 \text{ cm}^2/\text{Vs}$). The reduced InGaN barrier height ($\text{In}_{0.06}\text{Ga}_{0.99}\text{N}$) in the MQW active regions would help the hole transport and thus reduce the electron overflow induced efficiency degradation at high injection levels as the probability of recombination in the active region would increase with more holes present. Therefore, improved quantum efficiency would be expected with reduced InGaN barriers in MQW-LEDs. As shown in Figure 18, the uncoupled MQW w/ SEI shows 18% higher IQE than the uncoupled MQW w/ EBL but w/o SEI under the carrier density $\sim 2 \times 10^{18} \text{ cm}^{-3}$. This improved IQE with SEI can be attributed to improved crystalline quality due to the absence of any strain induced defects and to more efficient hole injection into the active region, which would have been limited by low hole mobility in AlGaIn layer had we used EBL. Similarly, the uncoupled MQW w/ SEI shows 12% higher peak EQE than the uncoupled MQW w/ EBL w/o SEI at lower injection levels though they tend to converge at higher injection levels, as shown in Figure 19. One can argue then that the efficiency is improved when LEDs use SEI instead of AlGaIn EBL.

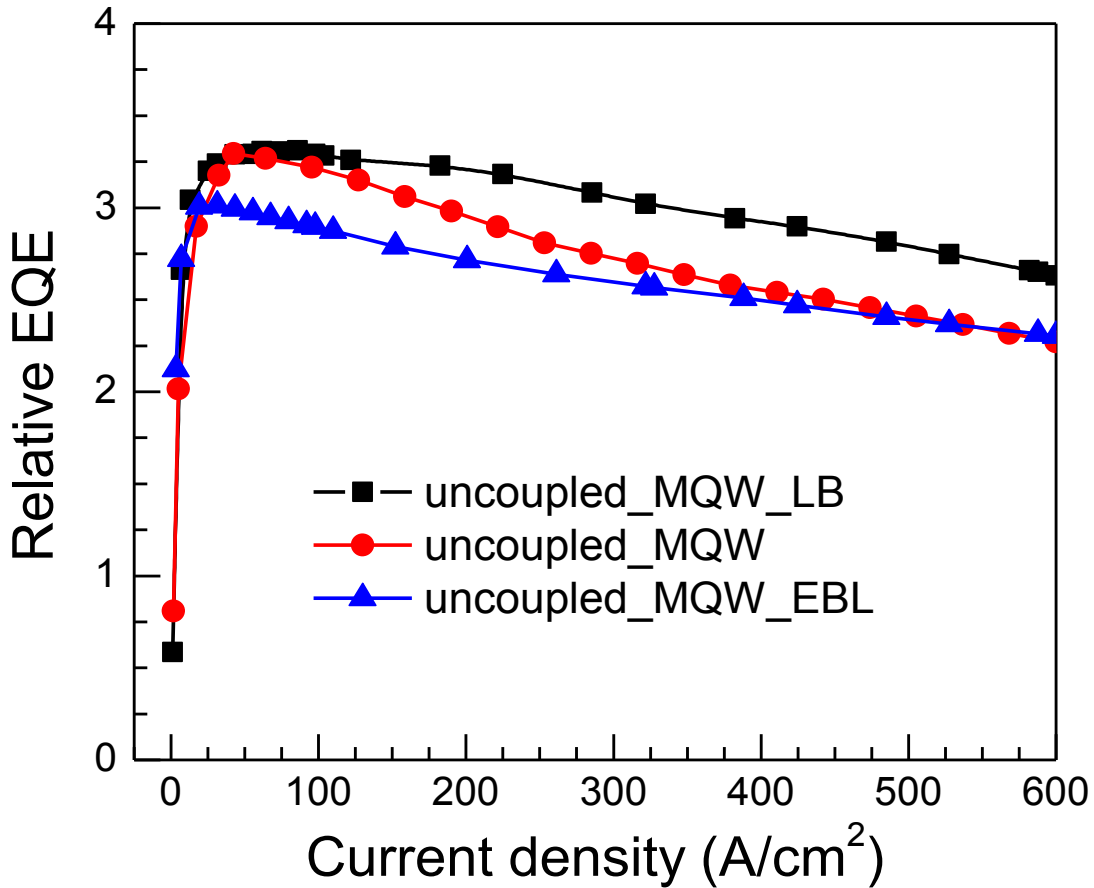


Figure 19: Relative external quantum efficiencies of uncoupled LEDs as a function of pulsed injection current density (0.1 % duty cycle and 1 kHz frequency).

It should be also mentioned that EQE values reach their maximum at current densities ranging from 20-70 A/cm² in the MQW LEDs, depending on the active layer structure. This observation as well is consistent with the IQE data shown in Figure 18. The similarity between the calculated equivalent photocurrent density using the rate equation and the measured electron density suggests that the recombination coefficients A and B reasonably describe the IQE characteristics of LEDs. Also, under low injection levels, any electron overflow can be assumed negligible and thereby there is reasonable correlation between optical measurements and electrical measurements below 30 A/cm².

As a summary, the dependence of both internal and external quantum efficiencies on the induced electron density and injection current density for InGaN based LEDs with coupled and uncoupled MQW active regions are investigated. Wider barrier width (12 nm), namely uncoupled MQW, active region showed better performance in terms of internal quantum efficiency compared to coupled MQW active region (3 nm barrier width). It is also found that the EBL layer can be successfully replaced with SEI in all the LED active layer designs evidenced by ~12% increase in the peak EQE values at low injection levels compared to that with EBL of the same active region.

2.2. Impact of InGaN double heterostructure active layer design in optical performance

InGaN double heterostructure (DH) layers can ensure uniform hole spreading across the active region due to the absence of barriers, unlikely to MQW active regions, and consequently have resulted in quantum efficiencies beyond current densities of $\sim 150 \text{ A/cm}^2$.²² Moreover, DH structure possesses bulk-like 3D density of states (DOS) which can accommodate more free carriers than stepwise DOS in the thin QWs. In this sense, active regions with different DH thicknesses are investigated in a series of optical and electrical measurements. Internal and external quantum efficiency (IQE and EQE) measurements were held to quantify the efficiency of active regions containing either one or more (dual) InGaN DH separated by 3 nm $\text{In}_{0.06}\text{Ga}_{0.94}\text{N}$ barriers. The common procedures to evaluate the IQE involve excitation power dependent PL measurements and comparison of the peak PL efficiencies at low and room temperatures by assuming 100% IQE at low temperature.^{75,76} Excitation dependent (up to $1.1 \times 10^{18} \text{ cm}^{-3}$ injected carrier concentration) PL measurements were performed at both 15 K and 295 K to find more accurate IQE results. The $\text{In}_{0.15}\text{GaN}$ structures (emitting at $\sim 420 \text{ nm}$) were grown on $\sim 3.7 \text{ }\mu\text{m}$ -thick *n*-type GaN templates on sapphire in a MOCVD system. **Figure 20** shows the conduction band diagram for dual DH structures (flat bands shown for simplicity). SEI layer, two 5 nm InGaN

layers with step-increased In compositions of 4% and 8%, is incorporated into all structures. The structures were completed with 100 nm-thick Mg-doped p -GaN layers having $4 \times 10^{17} \text{ cm}^{-3}$ hole density.

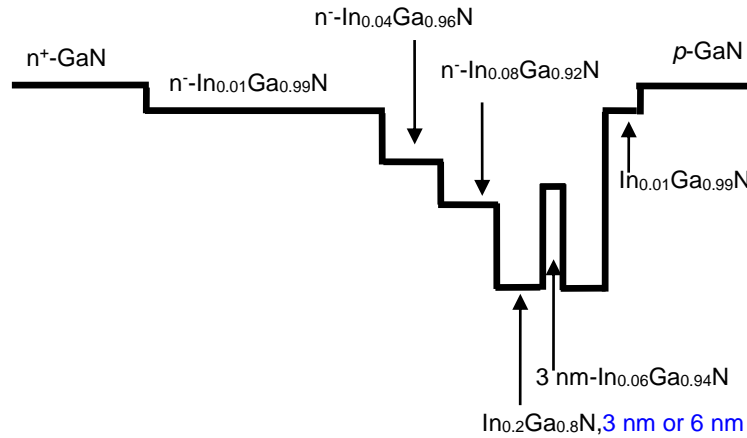


Figure 20: Flat band conduction band diagram for dual DH-LED structures.

Room temperature resonant optical excitation intensity-dependent method⁷³ was used to obtain IQE values versus photo-induced carrier concentration for DH active regions. Injection dependent radiative recombination, B , coefficients⁷⁷ were also used during calculations for an effort to produce more accurate qualitative analysis of the DH active regions. Upper limit of the IQE values were obtained from the low and room temperature PL comparison of the DH active regions, simply assuming 100% IQE at low temperature. The excitation wavelength from a frequency doubled Ti:Sapphire laser was set to 385 nm assuring photo-generation of carriers within the active region only.^{72,78} **Figure 21(a)** shows the IQE values vs. carrier concentration for all the DH structures. The IQE for 3 nm DH reaches above 35% at a carrier concentration of 10^{18} cm^{-3} . When a second DH active region is inserted into active region separated by a 3 nm-thick $\text{In}_{0.06}\text{Ga}_{0.94}\text{N}$ barrier, the IQE increase rate with increasing photocurrent density is slower than that for the single 3 nm DH. For this sample, maximum 35% IQE is reached at a photocurrent density

of $\sim 5.5 \text{ A/cm}^2$ compared to 0.3 A/cm^2 in single 3 nm DH. However, the IQE values are very similar for both structures at high injection levels.

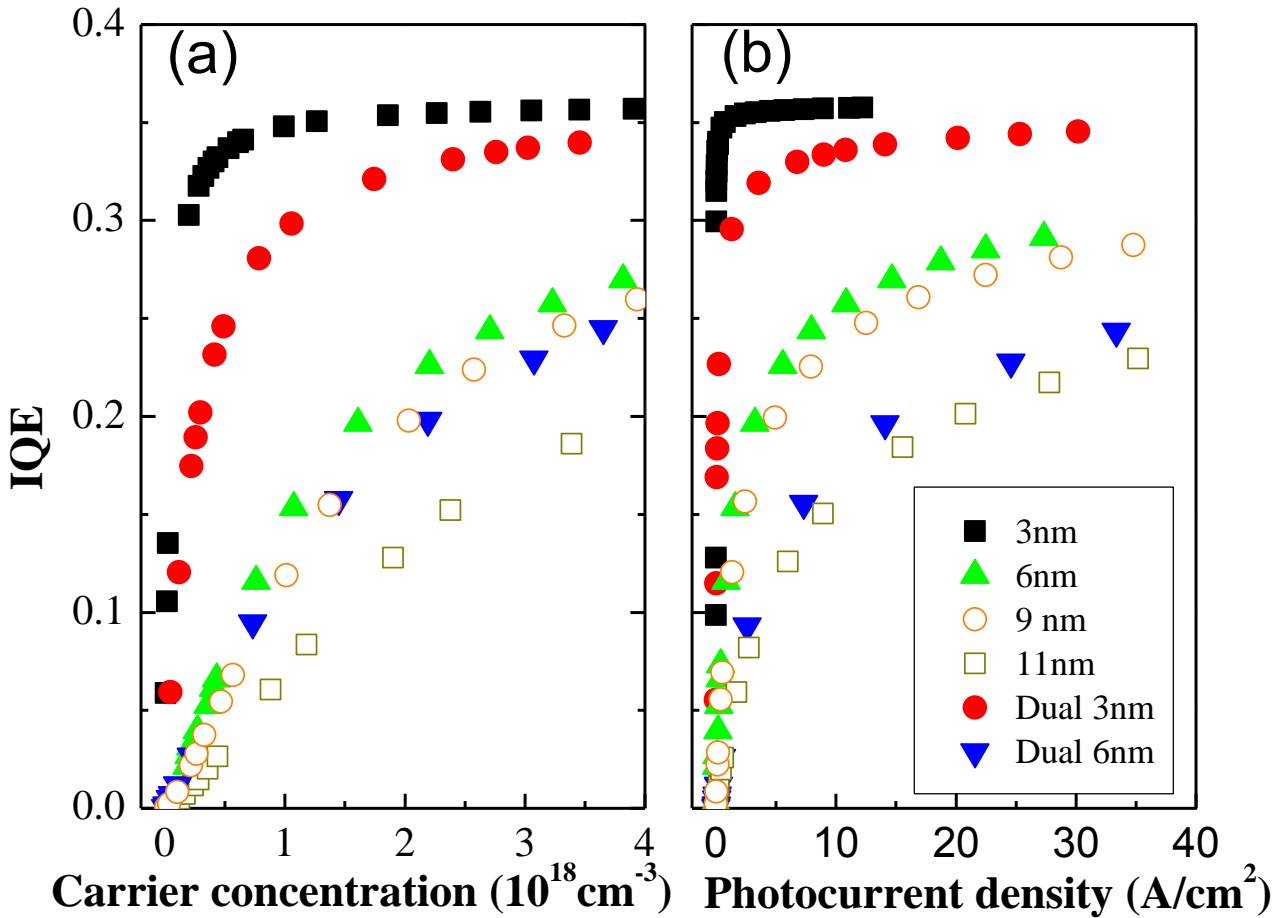


Figure 21: (a) IQE values determined from excitation-dependent PL with various DH thickness by using injection dependent B coefficients (b) IQE values vs. photocurrent density converted from carrier concentration.

When the DH thickness is increased from 3 nm to 6 nm and 9 nm, the IQE and its rate of increase is decreased substantially. IQE for both 6 nm and 9 nm DH LED increases slowly with carrier concentration and reaches 25% at around $3 \times 10^{18} \text{ cm}^{-3}$ carrier density. The single and dual 6 nm DH essentially have quite similar IQE dependence on carrier density, however, the dependence on photocurrent density clearly shows a discrepancy due to increased overall active region thickness (12 nm) for dual 6 nm DH. Further increase in DH thickness (up to 11 nm) resulted in

degradation in IQE and its rate of increase with respect to both carrier concentration and photocurrent density. This is partially due to the degraded layer quality with increasing active region thickness, which stimulates the nonradiative recombination process in the emitting layer, in addition to stronger polarization effects (increased electron and hole wavefunction separation in wider active regions).

In order to determine the relative EQE, pulsed electroluminescence (EL) was carried out for the active regions. **Figure 22** shows the relative EQE values for the structures with various DH thicknesses. The EQE of 3 nm DH exhibited a fast rate of increase with increasing current injection and reached its maximum at $\sim 30 \text{ A/cm}^2$. However, its maximum EQE was only 23% of that of the single 6 nm DH active region, most likely due to lower density of states within the 3 nm InGaN layer compared to 6 nm InGaN layer. When another 3 nm InGaN layer is added, the total EQE values are doubled due to increased active layer volume, which is consistent with resonant PL measurements showing two fold increase in emission intensity for the same excitation power.

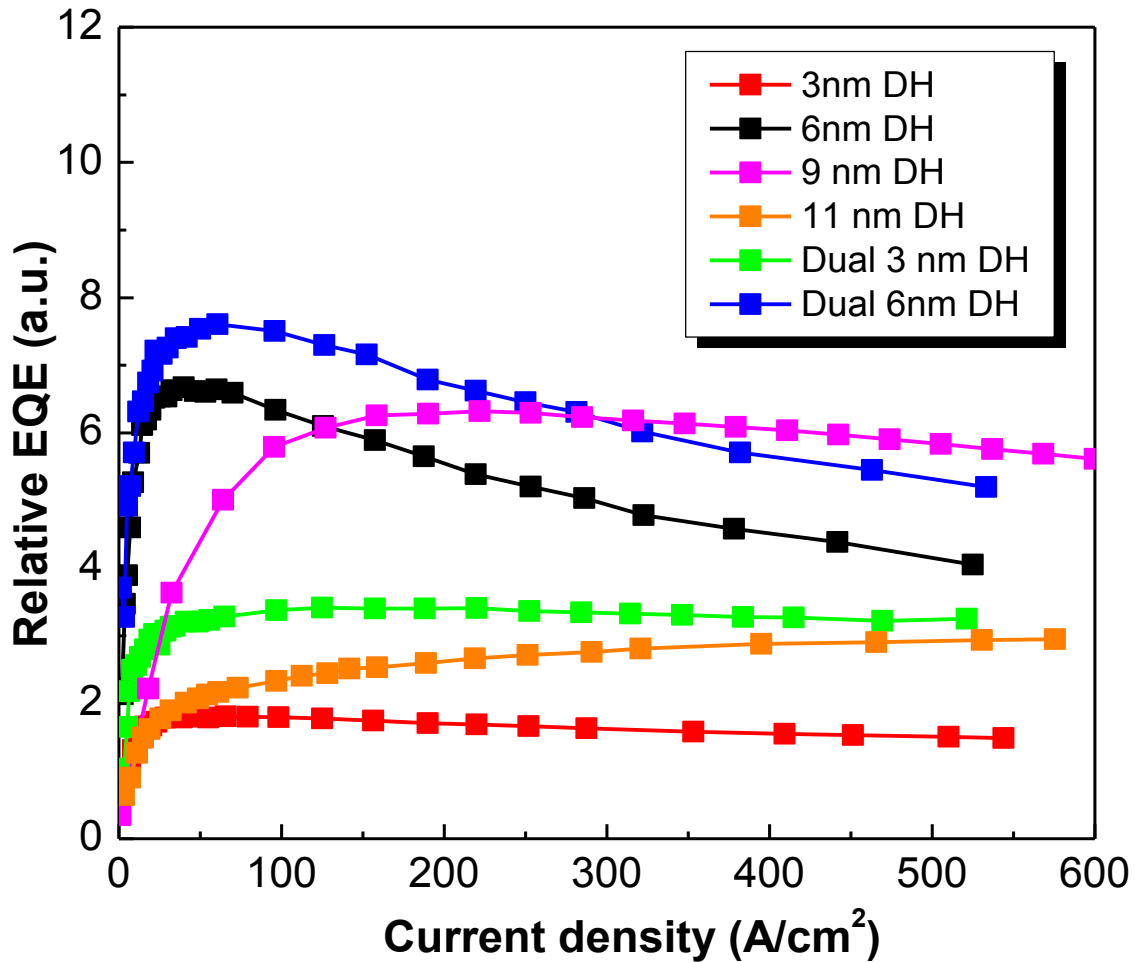


Figure 22: Relative external quantum efficiencies of DH structures as a function of pulsed injection current density (0.1 % duty cycle and 1 kHz frequency). The inset shows the normalized resonant PL intensity versus the number of 3 nm DH active regions.

The maximum relative EQE values for the single 6 nm DH structure were obtained at current density of $\sim 41 \text{ A/cm}^2$, slightly higher than that for the 3 nm DH LEDs. However, single 6 nm DH suffered from large efficiency droop with increasing current density compared to single and dual 3 nm DH structures. The dual 6 nm DH showed $\sim 12\%$ higher peak EQE values and slightly less efficiency droop percentile (reduced by $\sim 30\%$) compared to single 6 nm DH under the same current density. Making an analogy between 3 nm and 6 nm DH LEDs, this results show that the second 6 nm DH layer in dual 6 nm DH structure is inferior to the first single 6 nm DH,

unlikely in the case of 3 nm DH. Increasing the individual layer thickness further to 9 and 11 nm results in deteriorated layer quality and the 11 nm DH LED exhibits much lower EQE values. It must be mentioned that uniform electron and hole generation can be achieved in active region under resonant optical excitation, which prevents the efficiency degradation due to carrier overflow observed under electrical injection. Therefore, active regions exhibiting the highest IQE values may not necessarily display the highest EQE values due to possible carrier leakage.

2.3. Multi double-heterostructure active regions in InGaN LEDs

The degradation of structural quality with increasing thickness and widely separated electron and hole wavefunctions due to the polarization field are among those problems thicker DH active regions face with.^{79,77} Therefore, applying multi-thin DH layers (*i.e.*, 3 nm) in the active regions could be a promising approach to overcome the efficiency reduction at high driving currents.

The *c*-plane InGaN LED structures, emitting at ~425 nm, were grown on ~5 μm -thick *n*-type GaN templates on sapphire substrate in a MOCVD system. An *in situ* SiN_x nanonetwork⁸⁰ was employed to reduce dislocation density in the GaN templates down to mid-10⁸ cm⁻³. The active regions contained one to eight 3 nm-thick In_{0.15}Ga_{0.85}N DH active layers separated by 3 nm In_{0.06}Ga_{0.94}N barriers. All the structures are incorporated a SEI layer for efficient thermalization of hot carriers prior to injection into the active region, and a 60-nm Si-doped (2 \times 10¹⁸ cm⁻³) In_{0.01}Ga_{0.99}N underlying layer for improving the quality of overgrown layers. The SEI consists of two 5 nm InGaN layers with step-increased In compositions of 4% and 8%, inserted in the given order below the active region. The LED structures were completed with 100 nm-thick Mg-doped *p*-GaN layers having 6 \times 10¹⁷ cm⁻³ hole density, as determined by Hall measurements on a separate

calibration sample. The EL efficiencies for the LED structures were measured under the same conditions were also compared.

To evaluate the optical quality of MDHs, excitation power dependent resonant PL measurements were performed with a frequency doubled Ti: Sapphire laser of excitation wavelength 385 nm ensuring photo-injection of carriers only into the LED active regions. Figure 23 depicts PL efficiencies defined as the collected integrated PL intensity normalized to the incident laser power. The injected carrier density was estimated from incident PL power on the samples, but invoking different absorbed laser power for various samples from transmission and reflectance measurements. Notably, the saturated PL efficiencies nearly scaled with the number of DH layers up to 6, showing ~2, 4 and 6.5 fold increase for dual, quad and hex DHs compared to single DH under carrier density 10^{18} cm^{-3} . Saturation of PL efficiency takes place for octa DH LED probably due to the enhanced non-radiative recombination at this active region thickness.

Toward studying the impact of carrier overflow and other carrier transport features, we measured EL efficiencies on-wafer with light output collected primarily normal to the sample surface into an optical fiber (Figure 23). The integrated EL intensities vs. injection current densities are also exhibited in the inset of Figure 23(b). The collected integrated EL intensity, L_{EL} , can be described by a power dependence on the injection current density J as $L_{EL} \propto J^m$, where the power index m reflects an effective rate of recombination processes within a given range of current densities.⁸¹ The superlinear growth of EL intensity ($m \sim 1.4$ for single, ~ 1.3 for dual and quad, and ~ 1.6 for hex, octa DHs) at low currents can be attributed to the impact of nonradiative recombination. Smaller m values suggest lower density of non-radiative recombination centers in single, dual/quad DHs compared to hex/octa DHs. The EL intensity changes nearly linearly at high current levels (see the inset); therefore EL efficiency tends to be constant.

As presented in Figure 23(b), the EL efficiency for the MDH structures with number of DH layers up to 4 increases at a fast rate with current injection and reaches its maximum at ~ 37 A/cm². The observed increase of peak EL efficiencies by 1.6 and 3.5 times that of single 3 nm DH is consistent with data of resonant PL efficiency shown in Figure 23(a). This significant improvement on EL efficiency by increasing the number of 3 nm DH layers (from 1 to 4) indicates that the amount of injected carriers captured by the active region is increased considerably, while further increase of layers introduces more nonradiative recombination centers. Although the inserted SEI layers in the LED structures can effectively reduce electron overflow,³¹ calculations of electron overflow by simply considering the total active region thicknesses of 3, 6 and 12 nm for single, dual, and quad 3 nm DH, respectively, could provide a viable explanation for the substantial EL efficiency discrepancies among the MDHs. Based on the hot electron model demonstrated in³¹, for a current density of ~ 500 A/cm², the percentage (p) of electrons captured by and recombining in the active region for single, dual, and quad 3 nm DH LEDs are 48%, 60%, and 76%, respectively, which translates to 1, 1.39, and 2.1 fold increase in light output varying as $J^m \propto p^m$ ($m \sim 0.92, 0.96, \text{ and } 0.99$ for single, dual and quad 3 nm DHs, respectively). However, experimental EL efficiency data suggests larger increment amount of light output for quad DHs (3.5 fold). This may hint to another mechanism: the formation of localized states by indium composition fluctuation prevents electrons and holes from recombination at threading dislocations and thereby improves the emission efficiency as well as light output power.⁸² The number of localized states increases with increasing number of DHs due to the more pronounced composition fluctuations,⁸³ which could give rise more radiative centers for quad DHs compared to single 3 nm DH. The two joint effects can facilitate the enhancement of EL efficiency in dual and quad DHs. It should be here emphasized that employment of low and thin InGaN barriers is essential for

enhancing hole transport across the active region as we demonstrated in earlier sections. With continuously increasing the number of DHs, the EL efficiency of hex 3 nm DH LED did not scale to ~6 times that of the single 3 nm DH but is slightly larger than that from the quad 3 nm DH, which indicates that the injected holes are mostly consumed in the first four DHs. Further increasing the number of DH layers to 8 lowered the EQE by ~20% compared to the hex 3 nm DH at a current density of 350 A/cm², which is an indicative of the layer quality degradation confirmed by PL measurements conducted at 15 K and 295 K.

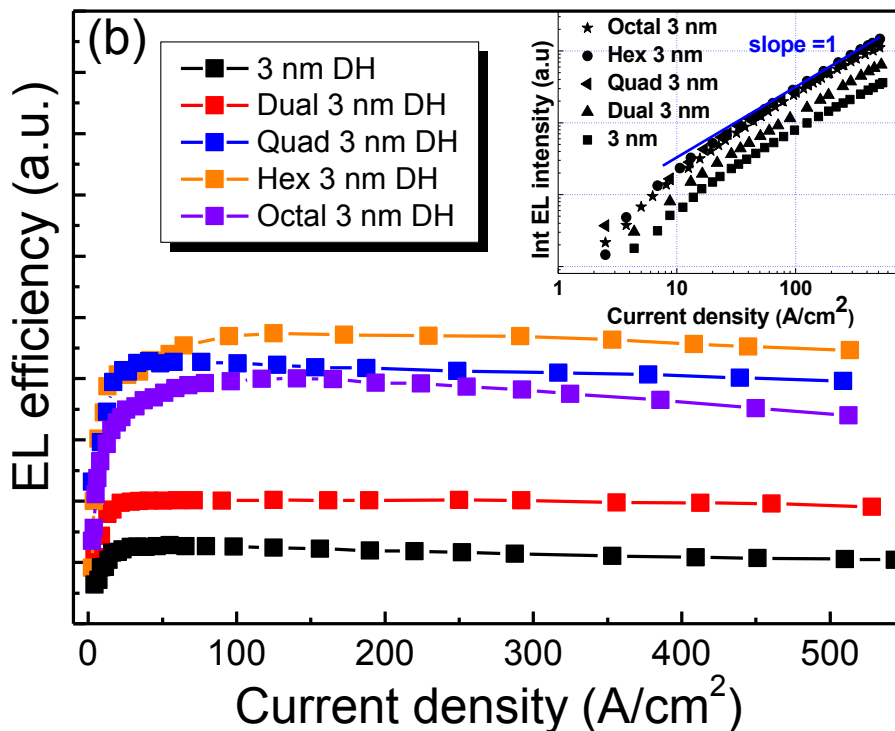
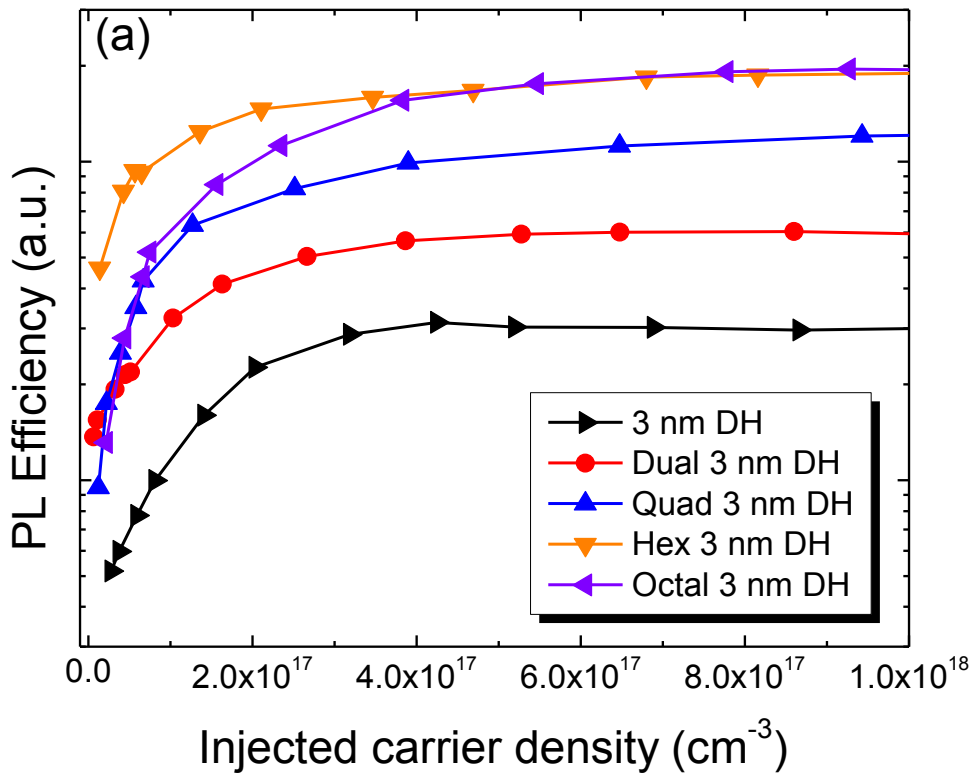


Figure 23: (a) PL and (b) EL efficiency of multi-3 nm DHs vs. injected carrier concentration at room temperature. The inset in (b) shows the integrated EL intensity dependence on current density.

It is worth to note that the EL efficiency for all the DH LEDs except the hex and octal 3 nm DH show negligible degradation with increasing injection current density up to 500 A/cm². Thus the increase of DH layer up to four confirms the optimized DHs solution. In addition, the quad 3 nm DH LED structure outperforms a typical MQW LED having the same total active layer thickness (6×2 nm well) and a slightly thinner single 9 nm-thick DH, which was reported to have 1.25 and 3.8 times higher relative EL efficiency than that of 6 nm and 11 nm-thick DH LEDs, respectively, under current density ~ 300 A/cm².⁷⁷ Therefore, it is apparent that multi-3 nm DH layer design is a superior approach for increasing the active region volume and enhancement of LED external efficiency.

A common procedures to evaluate the IQE involve excitation-dependent PL measurements and comparison of the peak PL efficiencies at low and room temperatures by assuming 100% IQE at low temperature.^{75,76} Excitation dependent (up to 1.1×10^{18} cm⁻³ injected carrier concentration) PL measurements at both 15 K and 295 K are shown in Figure 24. PL-IQE values deduced from the comparison of PL intensities at 15K and 300K are shown in the inset of Figure 24(b) indicating the highest value ~47% for quad 3 nm DHs. Increasing the number of DHs to 6 and 8 weakened the PL-IQE to ~40% and 16%, respectively. It should be noted here that the collected PL intensity is proportional to excitation intensity I_{exc} , *i.e.* $L_{PL} \propto I_{exc}^m$, thus a linear dependence ($m = 1$) for all structures at 15 K indicate that the radiative recombination dominates, $t_{Rad} \ll t_{nonRad}$. Coulomb screening of the quantum confined Stark effect (QCSE) will lead to increase of interband recombination rate $1/t_{rad}(N) \propto BN$, where B is the bimolecular recombination coefficient and N is injected carrier density. The superlinear dependence ($m \approx 1.4 - 1.95$) for low excitation levels at room temperature is attributed to the dominant impact of nonradiative recombination ($m = 2$ in case of constant t_{nonRad}). However, with increasing excitation, this dependence gradually

approaches the linear dependence (at 10^{18} cm^{-3} , $I_{PL} \propto I_{exc}$), thus indicating that carrier lifetime becomes dependent on N . Gradually decrease in slope between 10^{16} and 10^{18} cm^{-3} injection interval reveals strong competition between nonradiative and radiative processes and implies other mechanisms being responsible for lifetime decrease at moderate injections. With gradual filling of deeply localized states, the delocalized carriers (especially holes, as the electron density in the wells is in mid- 10^{17} cm^{-3}) with increased mobility may easily reach defects. Therefore, density of available nonradiative recombination centers increases and leads to enhanced nonradiative rate with respect to lower injections.⁸⁴ Similar hypothesis of density activated defect recombination was proposed recently.⁸⁵ On the other hand, bimolecular recombination rate also increases due to screening of QCSE. The both recombination processes lead to decreasing t_{rad} with excitation; therefore their joint contributions result in gradually decreasing slope value m .

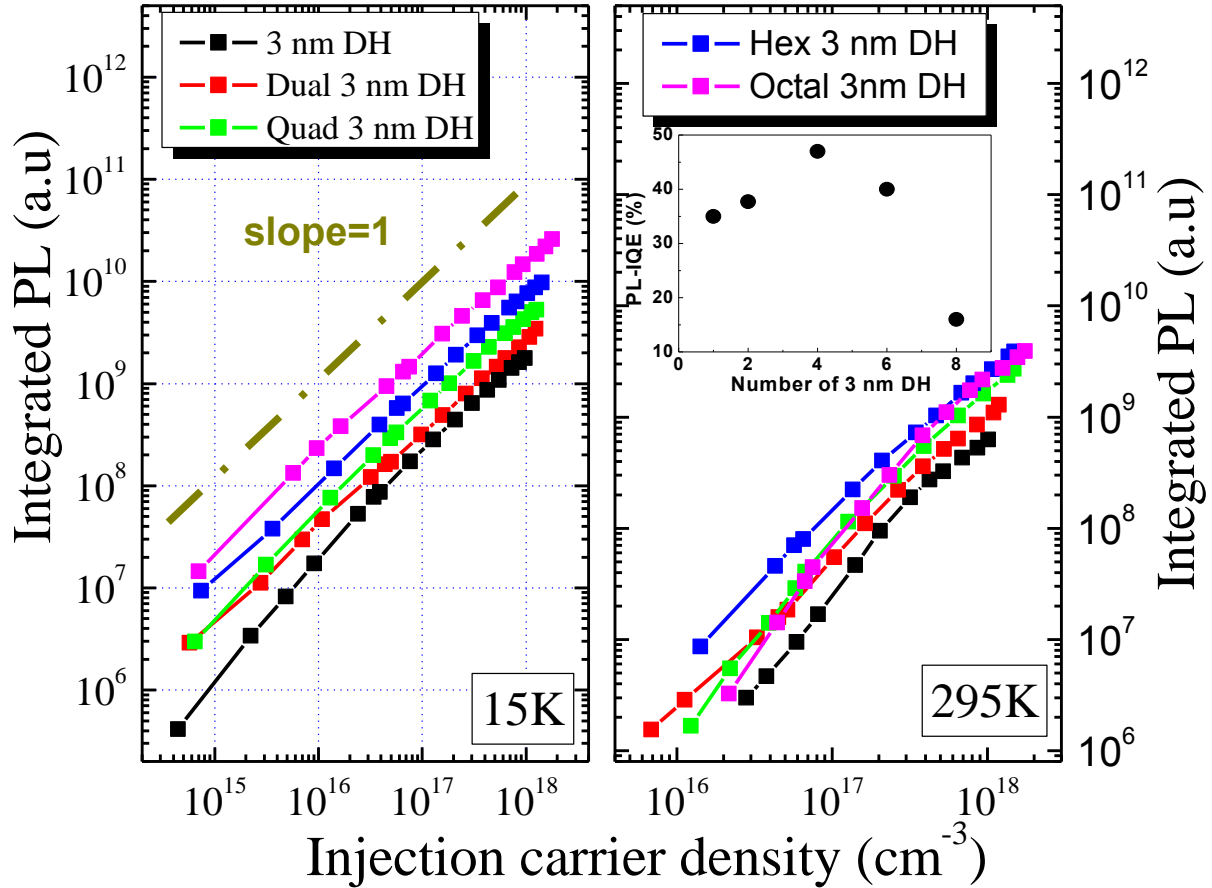


Figure 24: Integrated PL intensity as a function of injected carrier density at 15 K (dash-dot line indicates a slope of 1) (a) and 295 K (b); the inset of (b) displays the PL-IQE vs. the number of 3 nm DHs in the active region.

As a summary, it is demonstrated that incorporating more DH layers (3 nm) separated by the thin and low InGaN barriers is a more efficient way to improve light output from InGaN LEDs. Excitation-dependent PL results indicated that PL efficiency is nearly proportional to the number of DH layers up to 6 at room temperature, suggesting similar quantum efficiency for each DH active layer. Similarly, EL efficiency is also shown to be proportional to the number of DH active layers up to 4 but hex DHs still shows ~20% higher EL efficiency than that of quad DHs at high injection. The proportional increment in EL is attributed to the decreased electron overflow in multi-DH LEDs (e.g., dual and quad 3 nm DHs) as well as higher density of localized states

compared to single 3 nm DH. The absent proportional EL improvement for hex DHs was ascribed to the limited hole transport in each DH layer. Therefore, among the efforts to enhance the quantum efficiency at elevated injection levels, MDH designs can constitute a viable approach to achieve high efficiency and high power LEDs.

2.4. The effect of stair-case electron injectors on the electron overflow

From the previous section (in Figure 24) we saw that, the quad 3 nm DH LED exhibited an IQE of ~47% while 37% for single 3 nm DH. However, the EL efficiency of quad 3 nm DH LED scaled to ~3.5 times higher than that of single 3 nm DH though they tend to be constant at high injection levels, which indicates that more electron overflow in the single 3 nm DH case attributed to the thinner active layer thickness and thereby electrons can be drifted across the active layer without recombining. One way that we can approve our assumption is to reduce electron overflow in the single 3 nm DH by increasing SEI thickness. However, we should note that material quality should not be degraded with increased SEI thickness. SEI thickness is carefully re-designed taking care of material quality in order to reduce the electron overflow. The *c*-plane InGaN LED structures, emitting at ~420 nm, were grown on ~3.7 μm-thick *n*-type GaN templates on sapphire in the MOCVD system. The structures feature various active regions such as variants of DHs, with two-step varied thickness SEI (two InGaN layers with step-increased Indium composition of 4% and 8%). The DH active regions contained single and quad 3 nm In_{0.15}Ga_{0.85}N DH active regions separated by 3 nm In_{0.06}Ga_{0.94}N barriers beneficial for hole transport. All the structures contained a 60-nm Si-doped ($2 \times 10^{18} \text{ cm}^{-3}$) strain relief In_{0.01}Ga_{0.99}N underlying layer below the active region and the SEI for material quality improvement. The LED structures were completed with 100 nm-thick Mg-doped *p*-GaN layers having $6 \times 10^{17} \text{ cm}^{-3}$ hole density. For devices, square mesa patterns ($400 \times 400 \text{ μm}^2$) were formed by conventional photolithography and

chlorine based Inductively Coupled Plasma (ICP) etching. Ti/Al/Ni/Au (30/100/40/50 nm) metallization annealed at 800 °C for 60 seconds was used for *n*-type ohmic contacts, and 5 nm/5nm Ni/Au electrodes served as the semi-transparent *p*-contacts, with 40/50-nm Ni/Au electrodes deposited for *p*-contact pads.

The quad-DH provided an optimum active region design for IQE without induced active region degradation as shown in previous sections. Thus, a quad and single 3 nm DH LEDs with SEI thickness varied from 5 nm to 30 nm per step were taken into investigations for the relationship of the SEI design and efficiency. A quad-DH with gradient-SEI (7-step gradually increase the Indium composition from 4% to 8% with the total thickness 40 nm) was also prepared. The excitation power dependent integrated PL intensity measured at 15 K was shown in Figure 25(a). The linear dependence of PL intensity on excitation power indicates that the radiative recombination dominates. Moreover, the PL intensities show nearly scaled with increasing number of DH layers from 1 to 4. Room temperature PL measurement shown in Figure 25(b) exhibited that with the increase of SEI thickness, the slope of PL efficiency dependence for the quad 3 nm DH at low injection decreases indicating that nonradiative recombination rate and Shockley-Read-Hall (SRH) coefficient decrease. Increasing SEI thickness from 5 nm to 20 nm per step makes considerable improvement of PL intensity up to nearly 10 times improvement at low injection of $0.001\text{kW}/\text{cm}^2$, while it saturated at 30+30 nm-thick SEI or gradient 40 nm-thick SEI. As the excitation density is increased, the slope gradually approaches to 1, indicating strong competition between nonradiative and radiative processes. At high excitation, radiative recombination dominates and the slope tends to be saturate at 1. It is clear that the thicker SEI (SEI thickness lower than the critical thickness) benefits DH quality since it reduces the possible misfit dislocation density and relaxation ratio of InGaN active region. Another possible mechanism for the efficiency

enhancement in the specific positions might be Indium-rich cluster. It is reported that the Indium clusters are free from defects, so that the electrons and holes would be trapped in them with high radiative recombination efficiency, which would result in four DHs emitting uniformly for quad 3 nm DH.^{82,83}

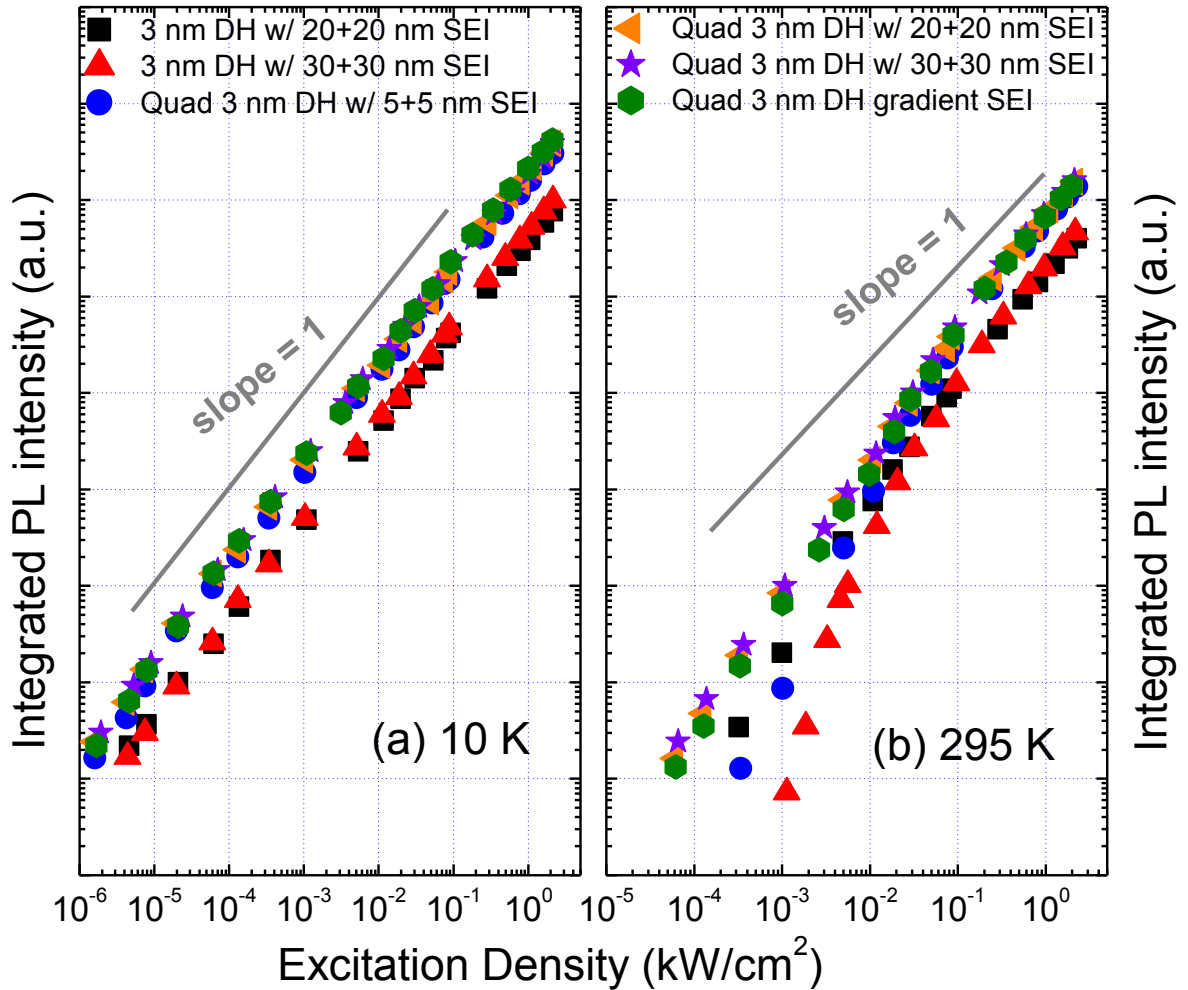


Figure 25: The integrated PL intensity (grey-sold lines indicates slope of 1) with varied SEI thickness as a function of excitation power density for LEDs (a) at 15 K and (b) at 295 K.

Carrier recombination process can be clearly observed through a current injection instead of optical excitation. The integrated EL intensities vs. current injection for varied SEI thickness are shown in Figure 26. The superlinear growth of EL intensities at low current densities is due to

the impact of nonradiative recombination. Smaller slope values suggest lower density of nonradiative recombination centers, and gradient 40 nm SEI shows best quality improvement for the active region. With thicker SEI up to 20+20 nm, the EL efficiency for the single 3 nm DH reaches its maximum at $\sim 32 \text{ A/cm}^2$, showing comparable peak EL efficiency with quad 3 nm DH with the discrepancy around 10%. This significant improvement on EL efficiency of 3 nm DH by increasing SEI thickness (from 5+5 nm to 20+20 nm) indicates that electrons are cooled sufficiently with thicker SEI and electrons overflow are greatly reduced so that most radiative recombination occurs even for a single 3 nm DH. Slight higher EL efficiency for quad 3 nm DH implies that a small amount of holes transport into the front DHs and recombine with electrons. It is noted that 3 nm DH still suffers more visible droop indicating a larger electron overflow through the relatively thinner active region at high injections.

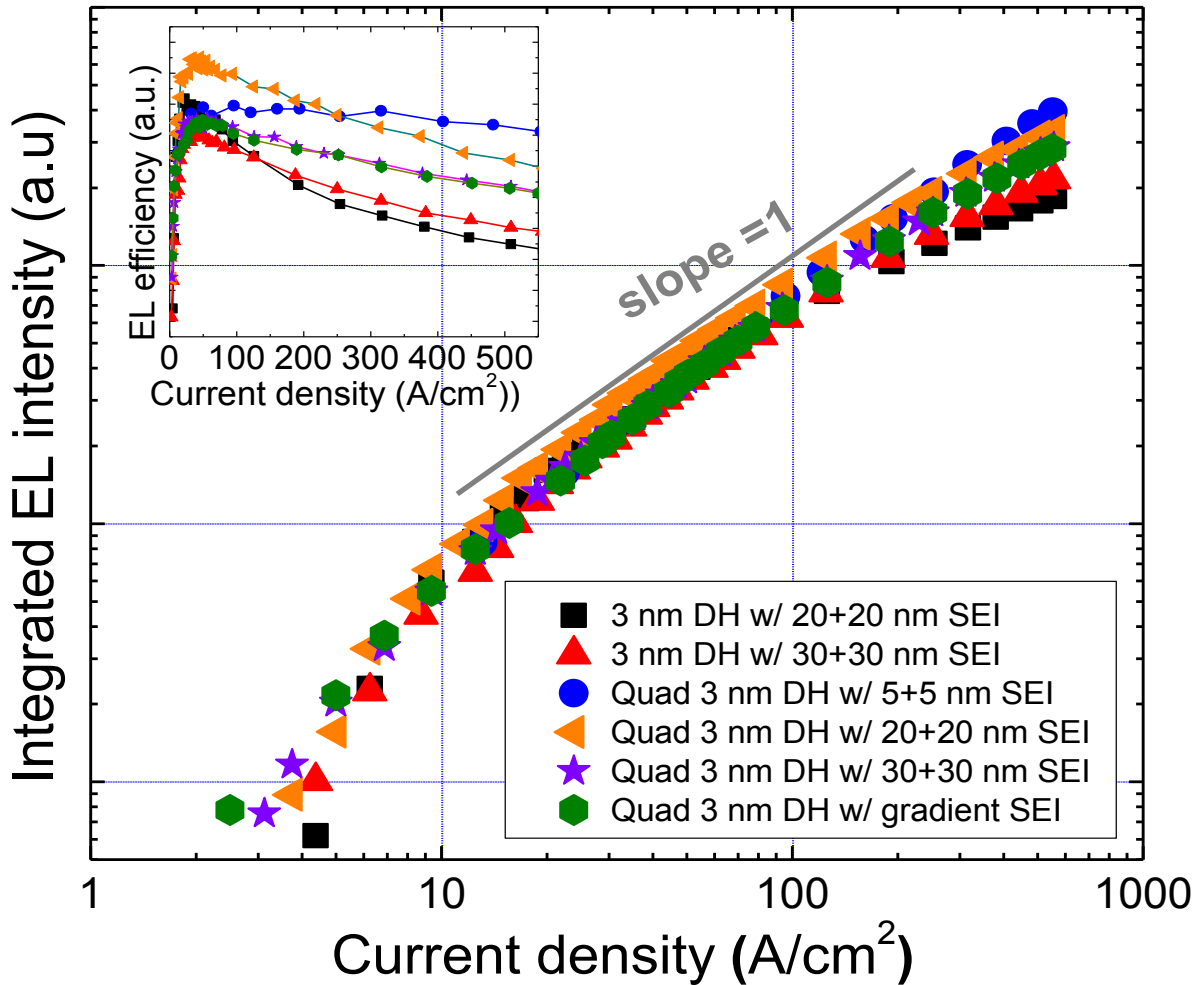


Figure 26: The integrated EL efficiencies dependence on current density (grey-sold lines indicates slope of 1) for LEDs with varied SEI thickness.

As a summary, it is shown that a good design of SEI may play an important role for the efficiency improvement of LEDs. The integrated PL intensity of LEDs employed with 20+20 nm SEI are nearly 10 times higher than that of 5+5 nm at low injection levels. Most importantly, the increased SEI thickness boosted the electron cooler potential and substantially reduced the electron overflow for the single 3 nm DH LED.

2.5. A theoretical treatment for injection dependent radiative recombination coefficient for single and multi active layer DH structures

In the realm of Fermi's Golden Rule, the spontaneous transition rate from a group of initial states i in the conduction band to a group of final states f in the valence band separated by a transition energy $\hbar\omega$ can be expressed as

$$T_{i \rightarrow f} = \frac{2\pi}{\hbar} |H_{fi}|^2 \rho_r(\hbar\omega) F(\hbar\omega) \quad \text{Equation 9}$$

where $\rho_r(\hbar\omega)$ is the reduced density of states, $\hbar\omega$ is the transition energy, $F = f_c(1 - f_v)$ is the Fermi factor given in terms of the Fermi functions for the conduction (f_c) and valence bands (f_v), and H_{fi} is the transition matrix element given by

$$H_{fi} = \langle \Psi_f | H | \Psi_i \rangle = \int \Psi_f^*(r) H(r) \Psi_i(r) d^3r \quad \text{Equation 10}$$

For a system with confinement along the z -direction (growth direction), the wave functions can be expressed using the envelope functions as $\Psi(r) = \psi(z)\phi(r_{xy})$. If the physical interaction operator is independent of the variable z , the matrix element can be simplified to⁸⁶

$$H_{fi} = \left(\frac{eA_0}{2m_0} \right) M \int \psi_f^*(z) \psi_i(z) dz \quad \text{Equation 11}$$

where A_0 is magnitude of the sinusoidal local vector potential, e is the electron charge, m_0 is the free electron mass, and M is the in-plane momentum matrix element. The spontaneous transition rate in Eq. 9 can then be written as

$$T_{i \rightarrow f} = \frac{2\pi}{\hbar} \left(\frac{eA_0}{2m_0} \right)^2 |M|^2 \left| \int \psi_f^*(z) \psi_i(z) dz \right|^2 \rho_r(\hbar\omega) F(\hbar\omega) \quad \text{Equation 12}$$

Eq. 12 indicates that a necessary condition for efficient recombination is the spatial overlap between the electron and hole wave functions (ψ_e and ψ_h) and the radiative recombination rate is

proportional to the squared overlap integral when electrons and holes are confined in the z-direction.

For quantum-confined structures, it has been suggested that low-dimensional equivalents of the bimolecular radiative recombination B coefficient should be introduced to eliminate the artificial dependence of the radiative recombination current on size, such as the active region width in two-dimensional (2D) systems.⁸⁶ For InGaN quantum wells with confinement along the z-direction, defining the spontaneous transition rate as $T_{\text{spont}} = B_{2D} n_{2D} p_{2D}$, where n_{2D} and p_{2D} are the 2D electron and hole densities, respectively, the 2D B coefficient can be expressed in terms of the momentum matrix element in Equation 12⁸⁶

$$B_{2D} = \frac{4\pi n^2}{\epsilon_0 c^3 k_B T} \frac{(\hbar\omega)}{m_e^* m_h^*} \left(\frac{e}{2m_0} \right)^2 \times |M|^2 \left| \int_0^\infty \psi_h^*(z) \psi_e(z) dz \right|^2 \rho_r(\hbar\omega) \quad \text{Equation 13}$$

where n is the refractive index, ϵ_0 is the permittivity of free space, c is the speed of light, $\hbar\omega$ is photon energy, k_{BT} is the thermal energy, and m_e^* and m_h^* are the electron and hole effective masses (obtained using linear interpolation from the binary values for a given In content), respectively. The momentum matrix element M can be obtained from the in-plane interband transition matrix element (for polarization within the plane), $P_{cv} = 2|M|$,⁸⁷ which has been determined from the absorption measurements for binaries InN and GaN.⁸⁸ Using a value of $P_{cv} = 9.6 \times 10^{-20}$ g cm/s obtained from linear interpolation for the required composition, the B_{2D} coefficient was calculated to be 1.8×10^{-4} cm²s⁻¹ for an In_{0.15}Ga_{0.85}N active region assuming full overlap of electron and hole wave functions. In order to make the transition from the 2D to the 3D case to be able to employ the conventional 3D rate equation, the 2D B coefficient should be

multiplied by the active region thickness, L_z . To test this approach and the validity of the 2D approximation, the 3D limit for the B coefficient for $\text{In}_{0.15}\text{Ga}_{0.85}\text{N}$ was also calculated from⁸⁹

$$B_{3D} = \frac{e^2 n}{m_0^2 c^3 h^2} \left(\frac{2\pi h^2}{k_B T} \right)^{3/2} \times M^2 \times \frac{1}{(\bar{m}_x \bar{m}_y \bar{m}_z)^{1/2}} h\omega \quad \text{Equation 14}$$

where $\bar{m}_{x,y,z} = m_{e(x,y,z)} + m_{h(x,y,z)}$. The 3D B coefficient calculated using Equation 14 is $5 \times 10^{-11} \text{ cm}^3 \text{ s}^{-1}$ for $\text{In}_{0.15}\text{Ga}_{0.85}\text{N}$. This value is smaller than that obtained using $B_{2D}L_z$ even for the thinnest active region with $L_z=3\text{nm}$. Therefore, it can be assumed that all the LED structures exhibit 3D behavior but with an electric field along the growth direction reducing the spatial overlap of charge carriers in the active region. Consequently, the injection dependent overlap integral of the electron and hole wave functions should be incorporated into the calculation of the 3D B coefficients using the upper limit for full overlap, $5 \times 10^{-11} \text{ cm}^3/\text{s}$

$$B = (5 \times 10^{-11}) \left[\text{cm}^3 \text{ s}^{-1} \right] \times \left| \int_0^\infty \psi_h^*(z) \psi_e(z) dz \right|^2 \quad \text{Equation 15}$$

The effects of the active region design and the resulting polarization-induced field on the overlap integral and the associated spontaneous recombination rates were investigated at different injection levels. **Figure 27(a)** presents the simulated bimolecular recombination coefficients, B, which are obtained from the transition matrix element and thus the simulated squared overlap integrals of the electron and hole wave functions within the DH active regions.^{90,89} It should be mentioned that the calculated B coefficients may vary slightly based on the material parameters used for a given structure; however, this would not affect the overall conclusions. The calculated B coefficients are also plotted in **Figure 27(b)** as a function of supplied electrical power per unit cross-sectional area, which is the product of injection current density and applied voltage used in

the simulations. It is apparent from **Figure 27(a)** that the B coefficient, instead of being constant as assumed in Ref. ⁷³, depends on the injection current density for a given design, increasing with injection due to screening of the internal fields by free carriers. ⁹¹ Naturally, the B coefficient tends to saturate at high injection levels as the nearly flat band condition is approached.⁹⁰ It is also evident that thinner active layers have relatively larger spatial overlap of the electron and hole wave functions. The single 3 nm DH LED shows 30% higher squared overlap integral value compared to the single 6 nm DH LED at a current density of ~ 300 A/cm². The lower B coefficients in wider active regions are attributed to the increased spatial separation of electrons and holes by the larger contribution of the polarization fields. Moreover, while the dual and the single DH structures exhibit comparable overlap integrals at low injection levels (below 100 A/cm²), the dual DH structures surpass their single DH counterparts as the injection current increases. For example, the dual 3 nm DH LEDs show 15% higher EQEs compared to the single 3 nm DH LEDs at a current density of 500 A/cm². Furthermore, the rate of increase for the B coefficient vs. the current density at low injection levels is reduced with increasing active layer thickness, which is consistent with the experimental IQE and EQE data shown in Figure 18(a) and Figure 19 in earlier sections, respectively.

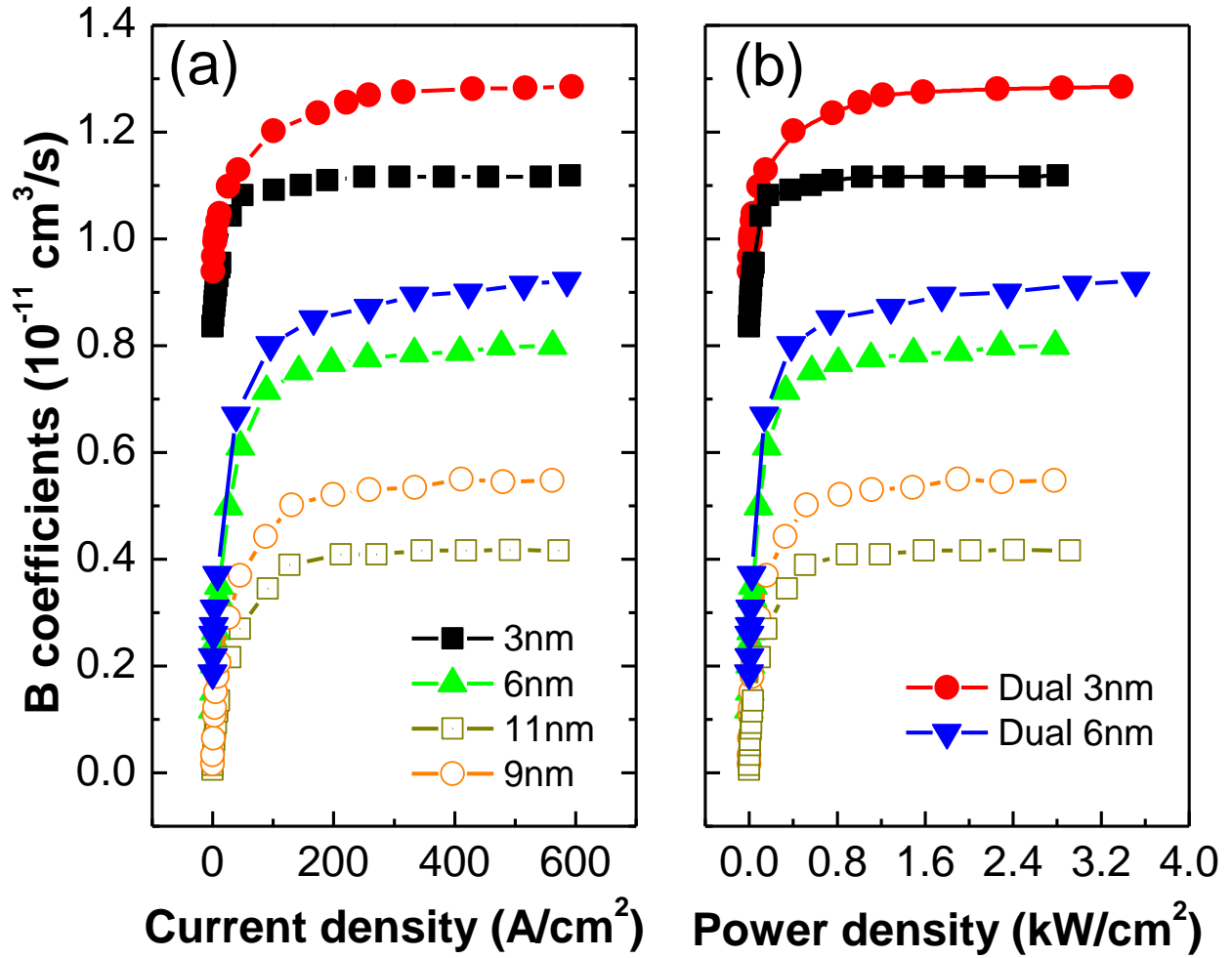


Figure 27: Calculated B coefficients using squared overlap integrals of electron and hole wave functions (proportional to radiative recombination rate) within the active region as a function of (a) current density calculated using SILVACO ATLAS simulations and (b) injection electrical power density (the product of applied voltages and current densities).

2.6. Recombination dynamics of InGaN active regions using time-resolved photoluminescence spectroscopy

Efficiency degradation at high optical injections still remains an object of study. Moreover, carrier recombination dynamics studies in InGaN heterostructures allow insightful information about the recombination processes. Time-resolved photoluminescence (TRPL) is a powerful tool to study materials because the temporal information combined with spectral data can help determine the carrier dynamics involved in optical processes following the sample of interest is

illuminated by a short pulse of light. The short pulse light generates electron-hole pairs that recombine and emit light. The emitted light is composed of set transition energies. As a result, measuring the optical spectrum as a function of time provides the transition energies and their lifetimes. It has mostly been used for monitoring radiative recombination pathways and evaluation of internal quantum efficiency in semiconductor heterostructures.^{92,93,94} It provides easy access to spectral features of emission as the PL decay times vary with injection and temperature because of simultaneous overlapping of different recombination mechanisms (exciton and free carrier, radiative and nonradiative). It is necessary to use a device known as a “Streak camera” since the decay times are on the order of picoseconds or nanoseconds, and the intensity of light emitted can be very weak, which a conventional spectrum analyzer cannot provide the resolution required. The detail about the working principle of a Streak camera can be found in Appendix B. The setup used in the temperature or excitation dependent TRPL experiments in the thesis is illustrated in **Figure 28**. To perform TRPL experiments, the samples under investigation are mounted on a cold finger in the vacuum cell of a closed cycle helium cryostat (operating from 15 K to 350 K), and are illuminated with very fast (150 femtosecond) laser pulses. To obtain the light incident on the sample, first of all, a 532 nm green laser pumps the tunable Ti:Sapphire laser, which can be tuned between 700 and 1000 nm. An ultra-short light, 150 fs, with 80 MHz from Ti:sapphire laser is generated with passive mode locking unit in the laser with nearly 1.4 W light output. Then, the light pass through the doubler/tripler unit, which multiplies the light frequency by either two or three subjected to the nonlinear crystal and nonlinear mixing. The resulting light after doubler/tripler becomes UV or deep UV that may excite GaN and InGaN-based heterostructures. After illuminating the sample with the laser, the optical response is collected by lenses and sent to the spectrograph using an optical fiber, which is connected directly to the input the streak camera.

Photoluminescence measurements are performed using the same optical setup by simply changing the optical beam path replacing the Streak camera with liquid nitrogen cooled Charged-coupled device (CCD) camera. This is illustrated in **Figure 28**.

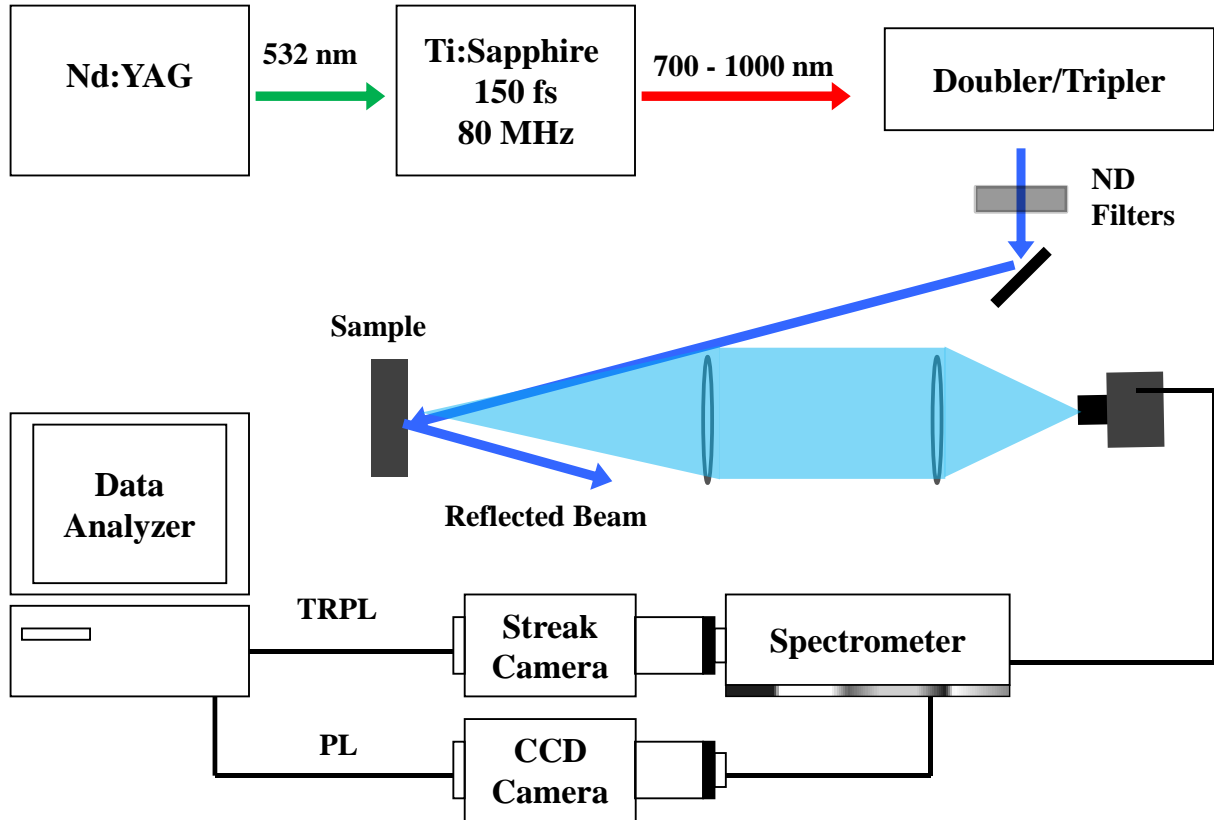


Figure 28: Time-resolved photoluminescence setup used in the temperature or excitation dependent experiments.

2.6.1. Recombination dynamics in an InGaN epilayer

Up to now, studies on InGaN/GaN light-emitting diode structures have been focused predominantly on understanding of “efficiency droop” phenomenon (at both optical and electrical injections) which has been attributed to impact of Auger recombination, carrier delocalization, electron leakage out of active region, and carrier asymmetry.^{20,95} The two former ones may take place under optical injection, while the two latter effects are more important for electrical injection. Most of the studies are focused on the active region with single and multiple InGaN quantum wells

with thicknesses less or equal to 2 nm. It is believed that the carrier recombination dynamics for bulk-like InGaN layer rather 2 nm, two-dimensional, InGaN quantum wells may give insightful information about the processes governed in InGaN heterostructures in addition to help understanding of the efficiency droop.

A 50-nm thick InGaN layer is studied using linear and nonlinear optical techniques to investigate excitation-dependent carrier recombination dynamics. Time-integrated and time-resolved photoluminescence (TRPL) spectroscopy techniques allowed studying PL efficiency as well as PL decay kinetics at various injected carrier densities. By exploring time-resolved differential transmission (DT) spectra, the narrow spectral range accessible by PL was extended well above the lowest band tail states of InGaN alloy. The 50-nm thick $\text{In}_{0.13}\text{Ga}_{0.87}\text{N}$ epilayer was grown on a few-micrometer thick GaN-on-sapphire template by using Aixtron 3x2 Close-Coupled Showerhead reactor at Aixtron in Aachen, Germany. A substrate temperature of 732 °C and a chamber pressure of 200 mbar were used for InGaN growth. An In content of 13% was found in the epilayer based on XRD analysis. The strain state of the InGaN layer was taken into consideration during the simulation of XRD ω -2 θ scan in order to achieve reliable In content. The AFM measurements revealed a surface morphology dominated by terraces with a roughness of 0.8 nm and V-pits with density of about $2.5 \times 10^8 \text{ cm}^{-2}$. The latter value for InGaN is comparable with that in GaN layers, suggesting that not many dislocations are formed at the InGaN/GaN interface which propagate through the InGaN layer and manifest themselves as V-pits on the surface.

Photoluminescence spectroscopy was used with 150 fs pulses at 375 nm wavelength (the 2nd harmonic of an 80 MHz repetition rate Ti-Sapphire laser) for selective excitation of the InGaN layer. PL spectra and transients were measured for injected carrier densities in the range of 10^{16} cm^{-3} to 10^{18} cm^{-3} and data collected using a spectrometer and a streak camera. Another setup

with 20 ps pulse duration at 266 nm (model PL2143, Ekspla) was used to reach higher injections, e.g., up to $5 \times 10^{19} \text{ cm}^{-3}$ at Vilnius University in Lithuania. In this setup, TRPL measurements with 25 ps temporal resolution were performed using a Kerr shutter with toluene. The experimental setup for time-resolved DT is based on a Ti:Sapphire femtosecond amplifier (SuperSpitfire, Spectra Physics) delivering 800 nm pulses of 120 fs duration at 1 kHz repetition rate. The DT technique helps to observe evolution of DT spectra in 380–480 nm range with high temporal resolution.

Room-temperature PL spectra were measured using resonant excitation at 375 nm (150 fs pulses, $I_0 \sim 10 \mu\text{J}/\text{cm}^2$) and at 266 nm (25 ps pulses, $I_0 \sim 100 \mu\text{J}/\text{cm}^2$). The PL line was positioned at 425 nm. PL decay time found to be increasing with increasing injection (**Figure 29**) observed from relatively weak excitation (in the 10^{16} cm^{-3} to 10^{18} cm^{-3} range), indicating a gradual saturation of nonradiative recombination centers. This is also supported by excitation density dependent PL measurements where a change of the power index, β , of PL intensity dependence on excitation density, $I_{PL} \propto I_0^\beta$ is measured. As can be seen in **Figure 30**, β changes from 2.7 to 2 at a carrier density of 10^{17} cm^{-3} at room temperature. The nonradiative carrier lifetime become constant and PL intensity increases quadratically with injection ($\beta=2$) after this point where the trapping centers saturates. The latter β value is indicative of the fact that the injected electron and hole density N_{ep} is larger than the background electron concentration n_0 , thus $N_e = N_p > n_0$ and PL intensity increase follows the relationship $I_{PL} \propto (n_0 + N_e)N_p \propto I_0^2$. The index β changes from ~ 1.5 to 1 at 10 K (see **Figure 30**) at the same carrier density as for room temperature (10^{17} cm^{-3}). Two factors support the argument that radiative recombination is dominant at this temperature:

- (i) The radiative recombination coefficient B essentially increases at low temperatures,

$(B \propto T^{-3/2})^{96}$ and

(ii) Exciton emission dominates due to relatively high exciton binding energy, leading

to $I_{PL} \sim B_{ex} n_{ex}$ (Ref. ⁹⁵) and thus providing the typical $\beta=1$ slope value.

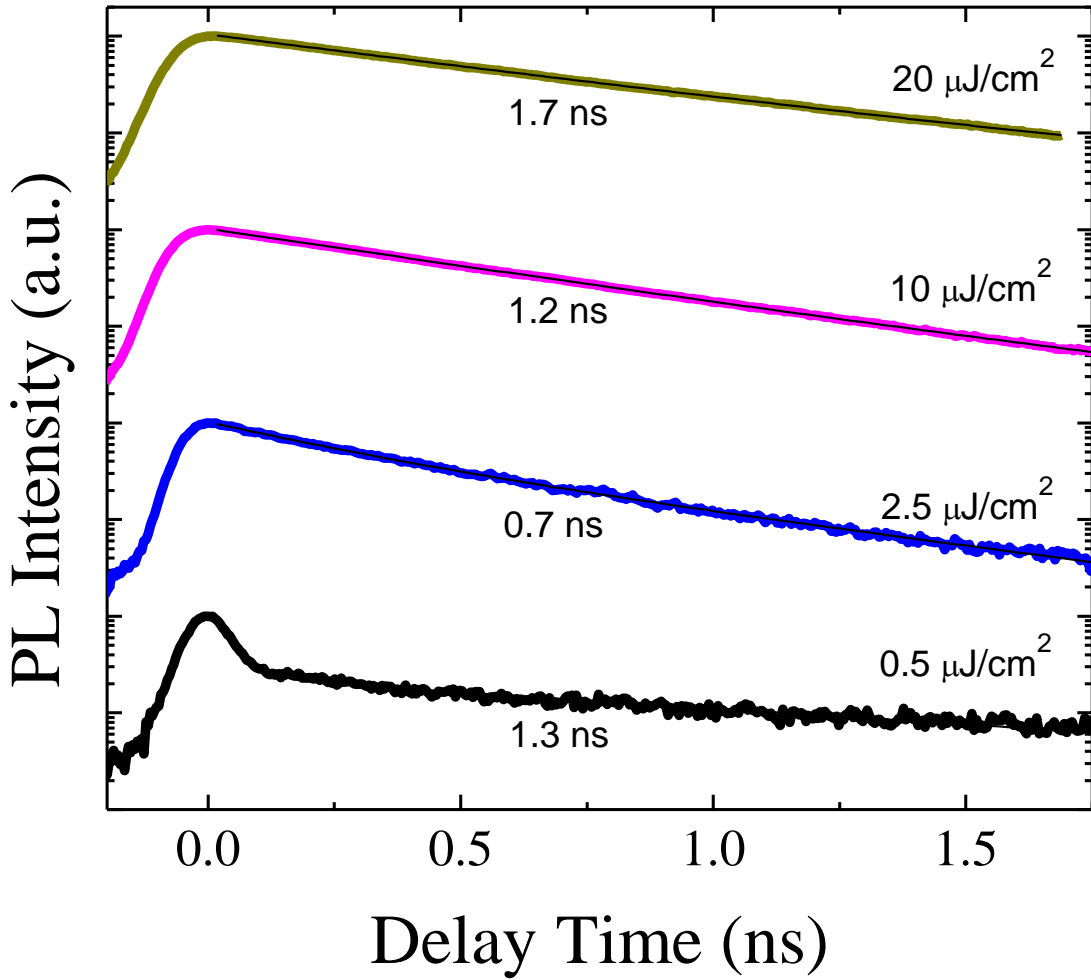


Figure 29: PL decay kinetics measured using femtosecond pulses at 375 nm wavelength and various excitation densities I_0 , corresponding to injected carrier densities from $5 \times 10^{16} \text{ cm}^{-3}$ to 10^{18} cm^{-3} .

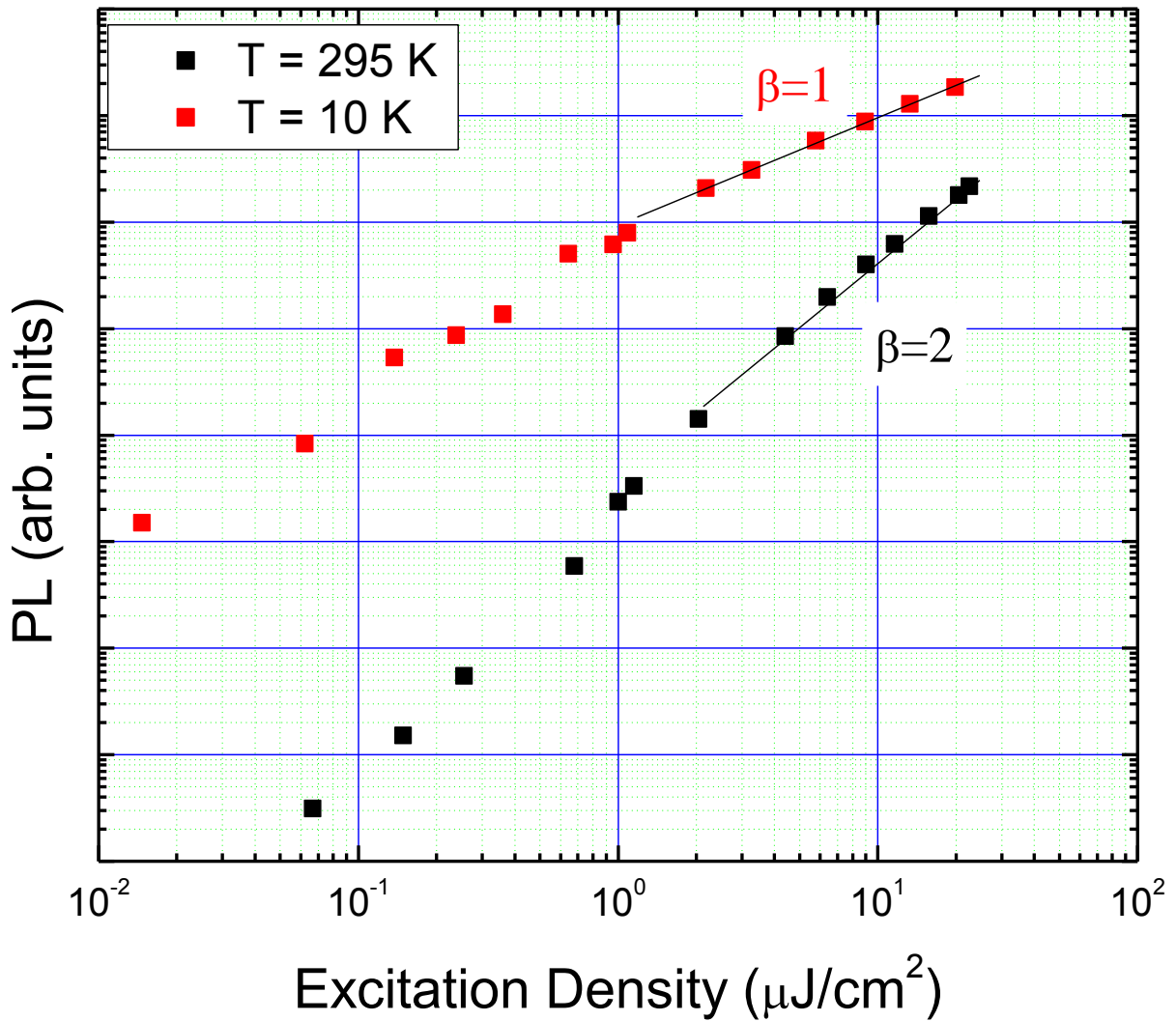


Figure 30: Dependence of time-integrated PL intensity on excitation energy density using femtosecond pulses at 375 nm. The curves can be approximated by a power-function $I_{PL} \propto I_0^\beta$ with slope values β , as indicated on the plot.

Spectrally and temporally resolved DT measurements were performed in a wide spectral range (390 to 440 nm) and excitation ranges (4 to 520 $\mu\text{J}/\text{cm}^2$) in order to explore the full spectral range and determine spectrally dependent relaxation rates. **Figure 31** represents DT spectra measured at 10 ps and 1 ns right after the photo-excitation are presented. PL spectra measured at 20 $\mu\text{J}/\text{cm}^2$ at 375 nm excitation and at 100 $\mu\text{J}/\text{cm}^2$ at 266 nm excitation are shown in **Figure 31** for comparison. As can be seen from **Figure 31**, the DT spectra are blue shifted with respect to those

obtained by PL, which is ascribed to relatively larger density of higher energy states contributing to the absorption bleaching. The FWHM of DT spectra is rather narrow (~ 60 meV), but it broadens towards the blue energy wing due to temporary filling of extended states at higher excitations. The spectral broadening is followed by faster relaxation rates, and the DT spectra become symmetric after 1 ns (Figure 31).

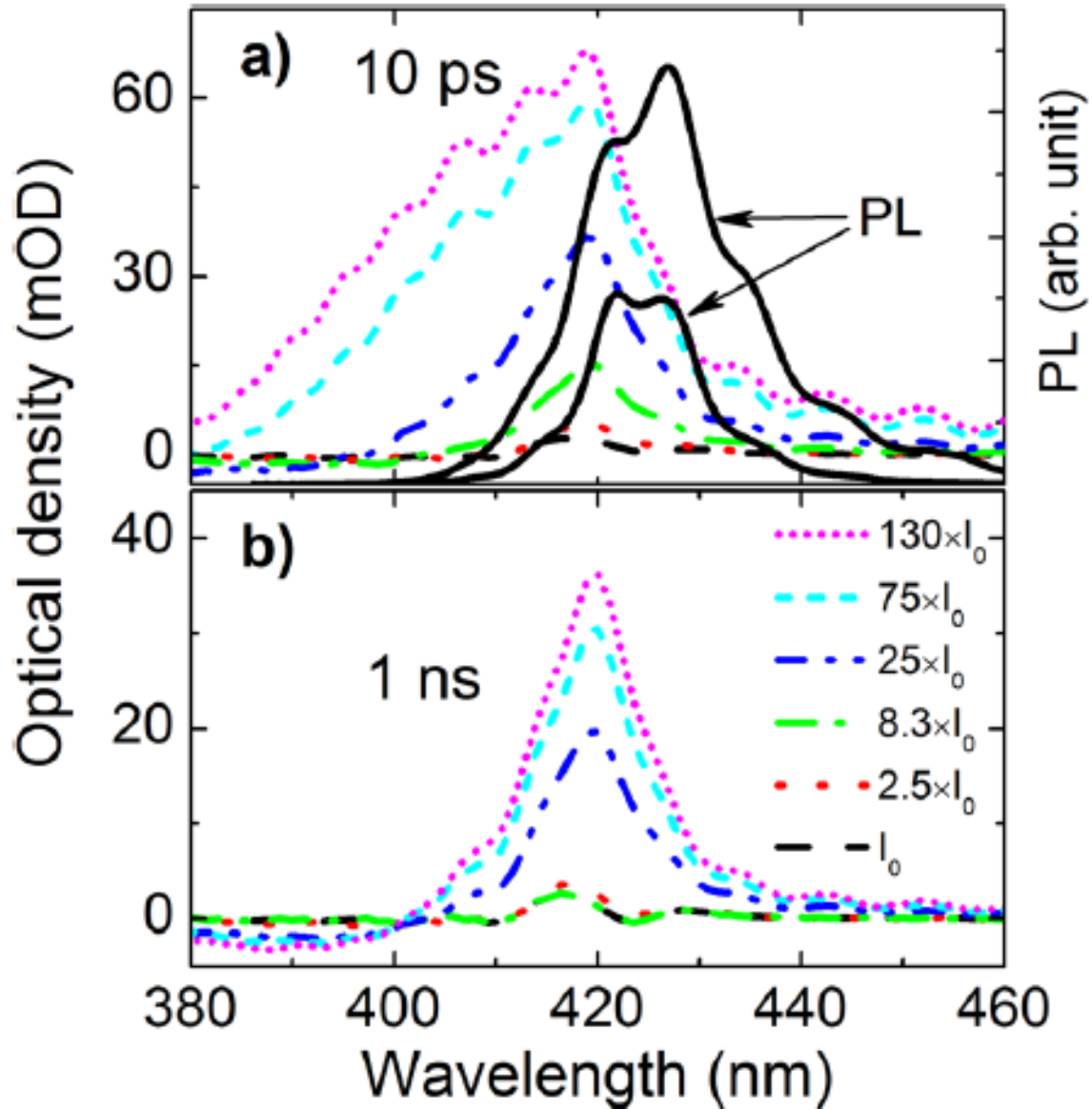


Figure 31: DT spectra at various excitation energy densities I_0 (here $I_0=4 \mu\text{J}/\text{cm}^2$). The spectra are taken at 10 ps (a) and 1 ns (b) after photo-excitation by 200 fs duration laser pulses at 375 nm. For comparison, PL spectra at $20 \mu\text{J}/\text{cm}^2$ (375 nm excitation) and $100 \mu\text{J}/\text{cm}^2$ (266 nm excitation) are shown in (a).

The decay times of DT spectral components as well as their injection dependences were determined from spectrally-resolved DT measurements in order to foster understanding of carrier recombination processes. **Figure 32** provides spectrally resolved DT kinetics for various excitation energy densities (in the range from 10 to 300 $\mu\text{J}/\text{cm}^2$) for two spectral positions, 425 nm (central line of PL peak) and 414 nm (DT blue wing). Fast DT decays are observed at low injection levels in the spectral range of PL, but the decay times get slower and finally saturates with increasing excitation (**Figure 32 b**)), exhibiting 1.5 ns decay time, similarly to PL decay times, see **Figure 29**. The observed long DT decay at the blue wing (**Figure 32 a**)) does not support the common tendency of increasing PL decay rate at the high energy wing. Moreover, the DT decay time at the blue wing decreases with increasing the injection from 30 $\mu\text{J}/\text{cm}^2$ to 100 $\mu\text{J}/\text{cm}^2$. **Figure 32(c)** summarizes the variation of carrier lifetimes in the spectral range from the PL emission band up to absorption edge and their dependence on injected carrier density. It is found that the ~ 415 nm spectral interval (i.e., ~ 70 meV above the PL peak) is more favorable for carrier accumulation at low injections. At low injections, this wing acts as a reservoir for the injected carriers transferred to the lower energy states. At higher injections, the fast recombination rate in this wing consumes the carriers and diminishes their delivery to the PL band most likely due to bandgap renormalization.

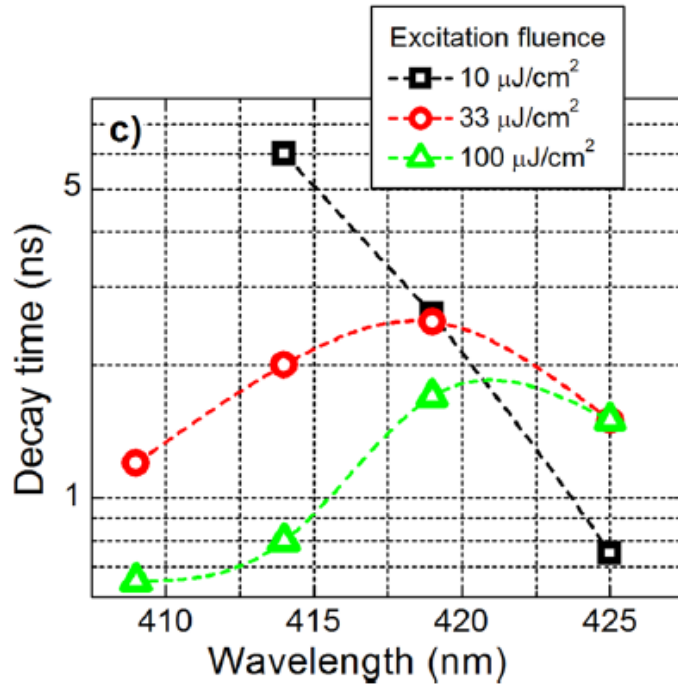
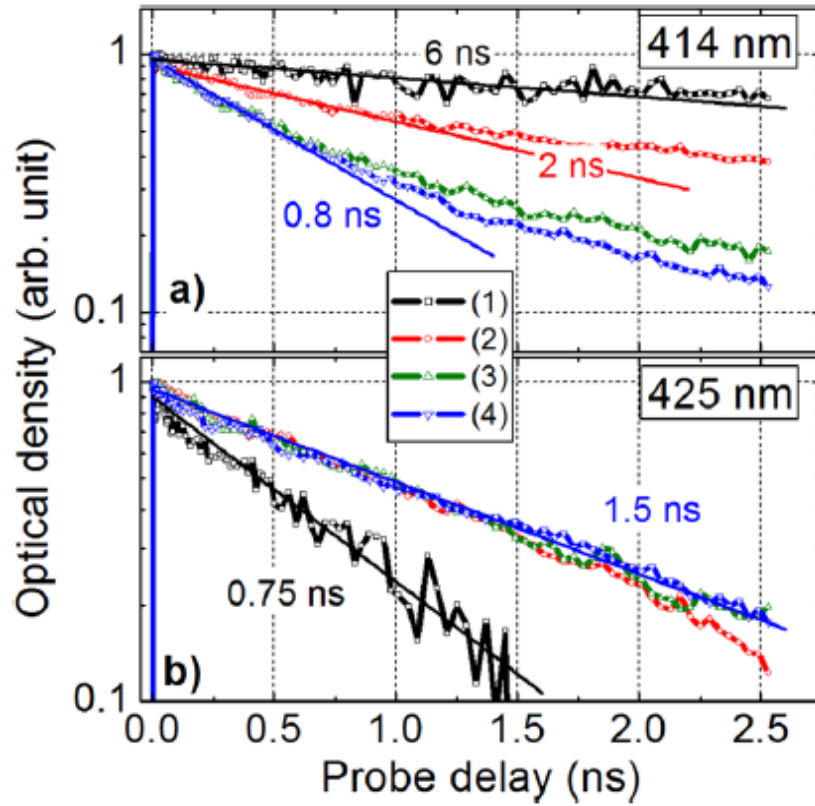


Figure 32: Spectrally resolved DT kinetics (a), (b) for two spectral lines which correspond to blue wing of DT at 414nm and PL emission at 425 nm at various excitation energy densities $I_0=10 \mu\text{J}/\text{cm}^2$ (1), $33 \mu\text{J}/\text{cm}^2$ (2), $100 \mu\text{J}/\text{cm}^2$ (3), and $300 \mu\text{J}/\text{cm}^2$ (4). In (c), spectral distribution of the initial DT decay time is plotted for various I_0 .

Spectral and spatial carrier dynamics are investigated using time-resolved techniques and novel features in carrier recombination dynamics are revealed in an InGaN epilayer. Increase of carrier recombination rate in the spectral interval above the PL emission band (415–420 nm) was attributed to bandgap normalization effect in extended states. It is found that localized states have a strong excitation-dependent impact on radiative emission, resulting in lower PL efficiency as the In composition increases. Similar studies of PL efficiency together with spatial, spectral, and temporal carrier dynamics in InGaN quantum wells may provide deeper understanding of processes leading to saturation of internal quantum efficiency of LEDs.

2.6.2. Double heterostructure active regions

Excitation density dependent TRPL measurements were performed in order to better understand the recombination dynamics for the DH active regions. Resonant excitation (385 nm) from a frequency-doubled Ti:Sapphire laser was used in this experiment. **Figure 33** shows TRPL data for the 3 nm, dual 3 nm, 6 nm and dual 6 nm DH active regions at different excitation power densities: 0.08, 0.20, and 1.25 kW/cm². The other DH structures (9 nm and 11 nm DH not shown) exhibited similar behavior with respect to excitation intensity. In literature, the analysis of PL transients for a variety of InGaN heterostructures, single quantum wells⁹², multiple quantum wells⁹³ and double heterostructures⁹⁴, have been performed using multiple⁹⁷ or stretched exponential⁹⁸ decay functions representing different radiative and nonradiative relaxation pathways. In a recent study, H. Kim *et al*⁹⁹ proposed a method by which radiative and nonradiative decay times and IQE values can be calculated from the TRPL data. The transients were fitted using biexponential decay function $A_1 e^{-t/\tau_i} + A_2 e^{-t/\tau_f}$, where the fast and slow decay components are represented using initial (τ_i) and final (τ_f) decay times, respectively. Based on the carrier rate equation,²⁸ radiative and nonradiative decay times can be approximately estimated using

$\tau_R \gg 2\tau_i\tau_f / (\tau_f - \tau_i)$ and $\tau_{NR} \gg 2\tau_f$, respectively. The initial (fast) decay of the TRPL spectrum is influenced by both radiative and nonradiative recombination rates, whereas the final (slow) decay is only dependent on nonradiative recombination.

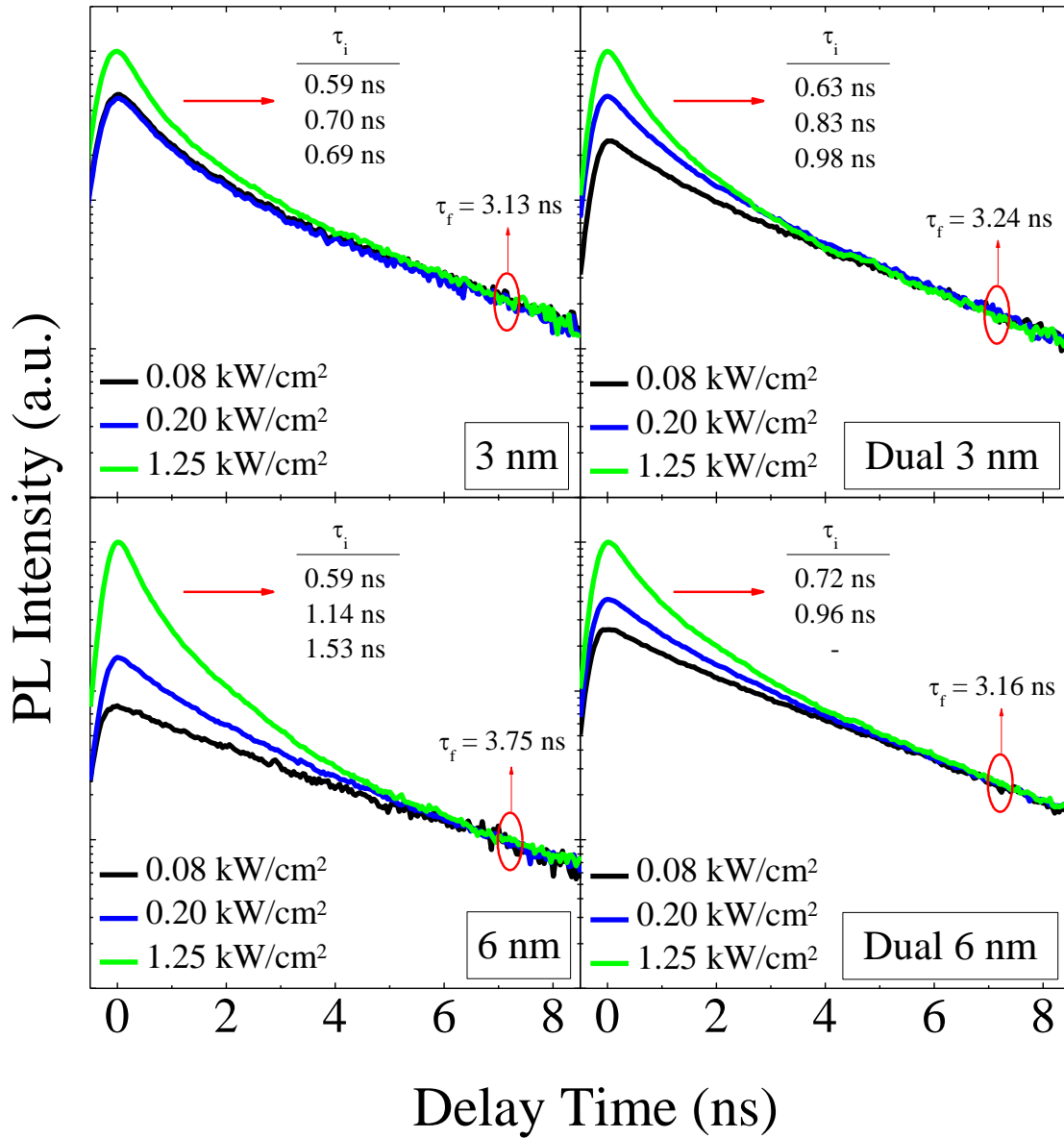


Figure 33: TRPL results for 3 nm, dual 3 nm, 6 nm and dual 6 nm DH LEDs for different excitation power densities, 0.08, 0.20 kW/cm² and 1.25 kW/cm². TRPL data are fitted with biexponential decay functions $A_1e^{-t/\tau_i} + A_2e^{-t/\tau_f}$ to find initial τ_i and final τ_f decay times, which are also indicated in the figures.

The radiative and nonradiative decay times obtained from the biexponential fits for the DH

structures are listed in **Table 3**. As can be seen in **Figure 33**, the initial decay time has a strong dependence on optical excitation power density, decreasing with increasing power, while the final decay time remains nearly constant for the range of excitation power densities used. The decrease of radiative recombination time, τ_R , with increasing excitation power density is attributed to increased electron and hole overlap resulting in faster radiative recombination, which is consistent with earlier observations in single InGaN quantum wells⁹². Furthermore, the final decay time is independent of excitation intensity as the nonradiative recombination centers are fully saturated at high excitation levels. In addition, it is found that the contribution of radiative recombination to the total carrier decay is larger at higher excitation power densities as can be seen from the increasing amplitude fractions (A_1/A_2) of the initial and final decay components with increasing excitation density (Table 2). The single and dual 3 nm DH structures exhibit faster radiative decay times compared to the other DH structures due to better electron and hole wavefunction overlap, which is consistent with the IQE measurements (see Figure 18). Also the initial PL decays at lowest excitation density for 3 nm and dual 3 nm DHs are more apparent compared to those of other DH structures even at low excitation densities, indicating higher radiative efficiency (**Figure 33**).

The IQE values calculated from the measured radiative and nonradiative decay constants using $\eta_{\text{int}} = \tau_{\text{NR}} / (\tau_{\text{NR}} - \tau_R)$ (Ref²⁸) are also listed in **Table 3**. Although these IQE values differ from those shown in **Figure 27** obtained using optical excitation intensity dependent PL measurements (values at the same carrier densities are compared in **Table 3**), they show the same tendency with increasing DH thickness. The differences between the two sets of IQE values are most likely due to the inaccuracy of the materials parameters used, particularly the absolute values of the B coefficients, which neglect any strain relaxation and material degradation with increasing InGaN thickness, and the corresponding carrier densities estimated. To obtain more accurate

quantitative analysis for IQE temperature dependent PL measurements will be done and the results will be compared. However, here the trends observed with increasing DH active layer thickness and increased injection are consistent. In overall, the TRPL data also point out the higher efficiency in thinner (3 nm) DH LEDs, and suggest that increasing the number of 3 nm active regions separated by thin and low barriers would help enhance the EQE while maintaining high IQE.

Table 3: The radiative and nonradiative decay times and amplitude ratios extracted from the fitted biexponential decay parameters and IQE values for the 3 nm, dual 3 nm, 6 nm, dual 6 nm and 11 nm DH LED structures.

DH LED	τ_R [ns]	τ_{NR} [ns]	$\frac{A_1}{A_2}$	IQE (from Figure 27)	IQE (from TRPL using the approach in Ref ²⁸)
0.08 kW/cm ² excitation power density					
3 nm	1.77	6.26	1.84	0.35	0.78
Dual 3 nm	2.81	6.48	0.70	0.27	0.70
6 nm	5.16	7.50	0.22	0.11	0.59
Dual 6 nm	-	6.32	-	0.07	-
11 nm	-	5.86	-	0.05	-
0.20 kW/cm ² excitation power density					
3 nm	1.80	6.26	1.83	0.35	0.78
Dual 3 nm	2.23	6.48	2.09	0.30	0.74
6 nm	3.28	7.50	1.57	0.17	0.70
Dual 6 nm	2.76	6.32	0.88	0.12	0.70
11 nm	3.32	5.86	1.37	0.10	0.64
1.25 kW/cm ² excitation power density					
3 nm	1.45	6.26	3.82	0.36	0.81
Dual 3 nm	1.56	6.48	5.04	0.34	0.81
6 nm	1.40	7.50	9.68	0.26	0.84
Dual 6 nm	1.86	6.32	3.03	0.22	0.77
11 nm	1.67	5.86	9.71	0.21	0.78

Chapter 3. Optical investigations of GaN-based blue emitting microcavity structures

Microcavities possess low lasing thresholds due to their small cavity lengths which are in the order of the wavelength of confined light.¹⁰⁰ In the case of vertical cavity surface emitting laser (VCSEL), the spontaneous emission rate can be controlled and the lasing threshold can be reduced owing to the large optical gain arising from the large joint density of states available in GaN. However, realization of GaN-based blue vertical cavities with high quality InGaN active regions faces major challenges. Integration of active region with the cavity, highly reflective large stop-band bottom distributed Bragg reflector fabrication, current confinement, and cumbersome substrate removal are some of those challenges. Beyond the standard VCSEL, microcavities may lead to a mixed quasi-particle, the polariton, which is half-light and half-matter and possesses unusual dispersion relations. Its genesis lies in the interaction between photons (light) and excitons (matter), which paved the way to polariton lasers. Contrary to the conventional lasers, polariton lasers have no threshold condition (ideally thresholdless) linked to the population inversion. In order to obtain polariton lasing at room temperature it requires a material which excitons actually survive at that temperature. Having 25 meV exciton binding energy, GaN is one of the ideal candidates for achieving low threshold polariton lasing at room temperature.

3.1. Optical investigations on hybrid vertical cavities with bottom semiconductor and top dielectric distributed Bragg reflectors (DBRs)

In regard to active region quality and quantum efficiency, the growth of AlN/GaN DBRs on free-standing GaN may help with reduction of defects and enhance the quality of the vertical cavities in spite of their small stop band widths (~20nm). A vertical cavity structure was grown

using a free-standing GaN substrate utilizing AlN/GaN DBRs. The cavity structure consisted of six periods $\text{In}_{0.15}\text{GaN}$ MQWs with low $\text{In}_{0.06}\text{GaN}$ barriers and sandwiched between 29.5 pair bottom semiconductor crack-free AlN/GaN and top 13.5 pair $\text{SiO}_2/\text{SiN}_x$ distributed Bragg reflectors (DBRs). The vertical cavity structure is schematically depicted in Figure 34(a). Nitride and dielectric DBR layers were grown by MOCVD and PECVD, respectively. In order to achieve crack-free AlN/GaN DBRs favorable for high reflectivity, AlN/GaN superlattice insertion layers were used within the DBRs replacing the GaN quarter-wavelength thick layer every 5 DBR pairs.^{101,102} The cavity length of the this structure is designed to be 5λ centered at 400 nm. The vertical cavity structure was characterized using reflectivity measurements, using a Xe lamp source, and micro photoluminescence (micro-PL) spectroscopy. For low excitation micro-PL, sample was excited normal to the surface from the top DBR side using a HeCd laser (325 nm wavelength) and a long working distance x50 microobjective. The excited area was in the order of $\sim 2 \mu\text{m}$ in diameter. The emission was also collected normal to the surface from the top DBR side.

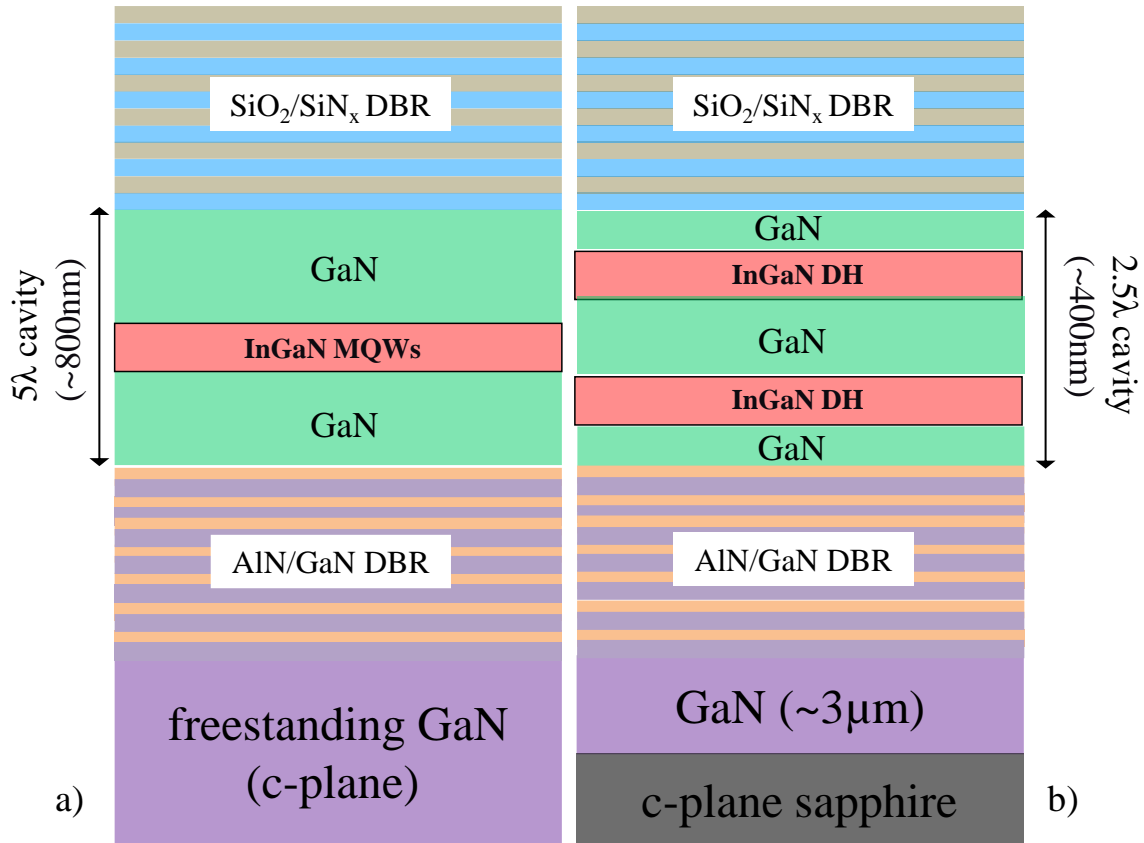


Figure 34: Basic schematics of vertical cavity structures: (a) 5λ cavity with 6×2 nm $\text{In}_{0.01}\text{Ga}_{0.99}\text{N}/\text{In}_{0.15}\text{Ga}_{0.85}\text{N}$ MQW grown on bottom 29 pairs AlN/GaN DBRs grown on $400\mu\text{m}$ thick free-standing GaN (b) 2.5λ cavity with two 6×3 nm $\text{In}_{0.06}\text{Ga}_{0.94}\text{N}/\text{In}_{0.15}\text{Ga}_{0.85}\text{N}$ DH separated by 132nm (1λ) $\text{In}_{0.01}\text{Ga}_{0.99}\text{N}$ underlying layer grown on bottom 29 pairs AlN/GaN DBRs grown on 2 micron GaN template on sapphire substrate.

Figure 35(a) shows the reflectivity and PL spectra for the cavity grown on free-standing GaN. The reflectivity of the crack-free bottom AlN/GaN DBR reached to nearly 98% with stop-band width of ~ 18 nm, while 99% reflectivity is achieved for the top $\text{SiO}_2/\text{SiN}_x$ DBR with a larger stop-band width of ~ 90 nm compared to bottom semiconductor DBR. The full-cavity reflectivity spectrum for the cavity shows a clear dip corresponding to the cavity mode at ~ 400 nm. A cavity Q-factor as high as 300 is deduced from the PL spectrum under low density 325 nm excitation [Figure 35(b)]. Q-factors varied across the wafer due most likely to layer thickness variation and slightly inaccurate positioning of the active region within the cavity. In order to achieve higher Q-

factors, further optimization of the active region quality and positioning in addition to improved interface and thickness control is necessary.

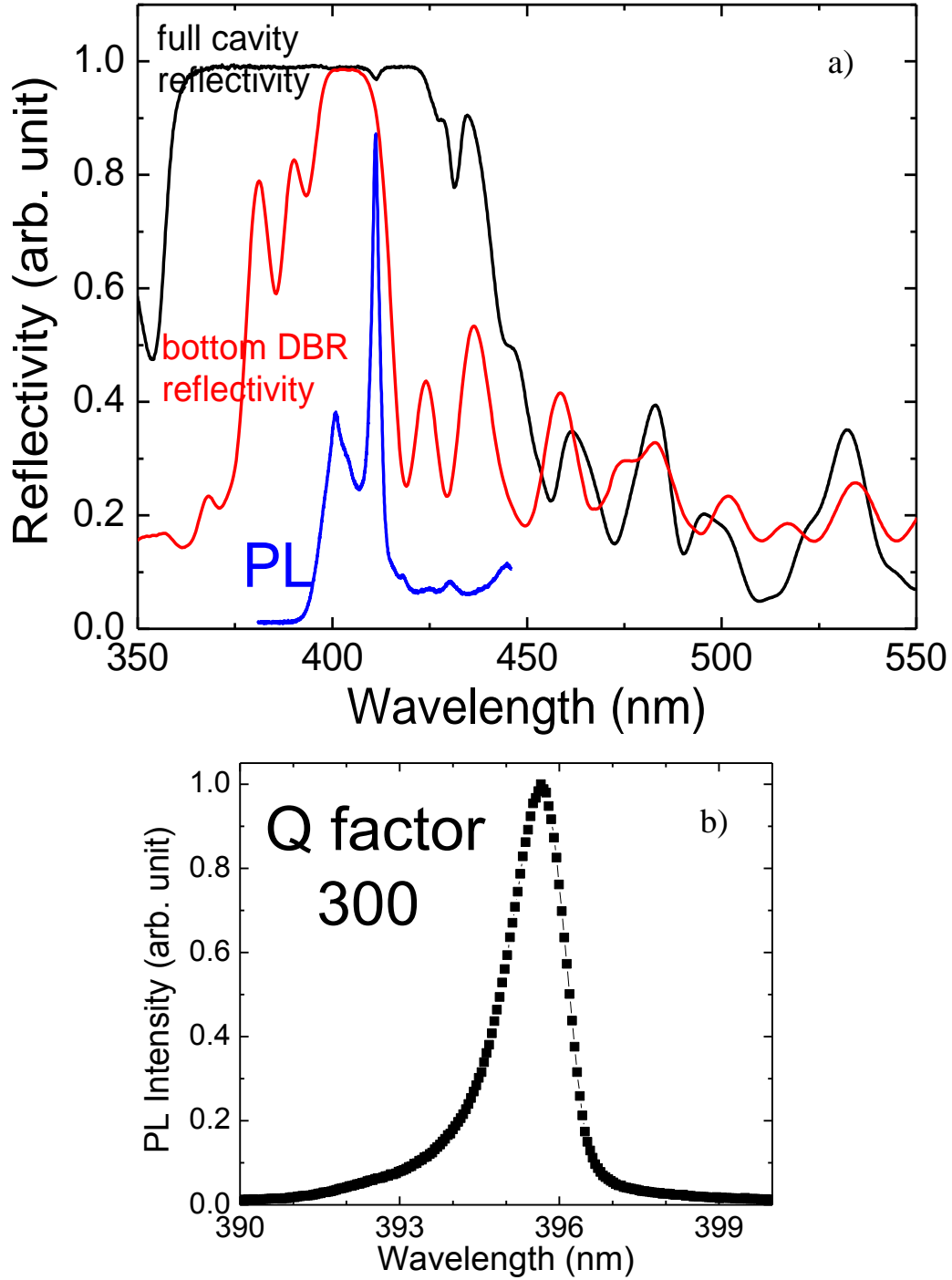


Figure 35: (a) Reflectivity and PL spectra for the vertical cavity structure on freestanding GaN (b) The spectrum corresponds to the highest Q-factor measured.

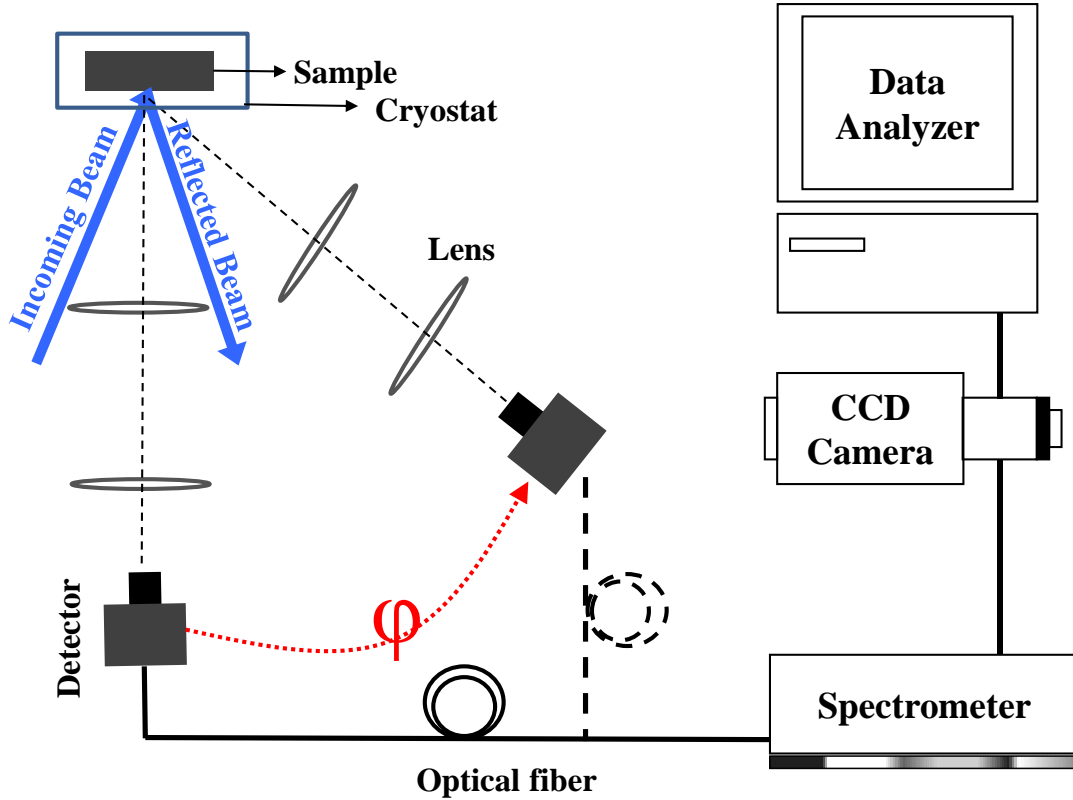


Figure 36: Schematic of angle-resolved photoluminescence setup.

Angle-resolved photoluminescence and cathodoluminescence measurements, which help to trace the polariton modes in microcavities, were conducted at room and low temperature (5.8 K), respectively, for the cavity grown on free-standing GaN. A basic schematic for the angle resolved PL measurement is shown in **Figure 36**. The PL spectra at RT were measured from 0° to 40° , as shown in **Figure 37(a)**. It is clear that the lower polariton mode approaches to the uncoupled exciton mode, and the upper polariton mode is dispersed from the exciton mode to the cavity mode. The experimental cavity polariton dispersion curve shown in **Figure 37(b)** exhibits an anticrossing behavior between the cavity mode and exciton mode when the cavity mode energy crosses the exciton mode. Although the upper polariton branch was weakly resolved in the angle-resolved PL spectra, the anticrossing behavior confirms the strong coupling regime in the microcavity. A vacuum Rabi splitting of 45 meV is estimated at room temperature with a large negative detuning

-70 meV [Figure 39]. Since the stop bandwidth of the bottom DBR is narrow due to relatively low refractive index contrast in semiconductor layers, the upper polariton features are not clear at large angles. However, the strong coupling for this cavity is evidenced at low temperature angle-resolved CL measurement performed by colleagues at University of Magdeburg, and Rabi splitting is found to be 75 meV at 5.8 K (**Figure 38**). The detuning is found to be larger than room temperature value, -110 meV [Figure 39]. Considering the Rabi splitting, one may expect that the oscillator strength of the excitons is larger at low temperatures compared to room temperature leading to stronger exciton photon coupling. This was proved for a (Zn,Mg)(S,Se) microcavity with three (Zn,Cd)Se quantum wells having Rabi-splitting of 17.5 meV at 70 K and 10 meV at 175 K by Kelkar et al.¹⁰³ Also, Tsintzos et al¹⁰⁴ experimentally and theoretically showed that the Rabi splitting decreased with temperature while increasing the number of QWs in the active layer in a GaAs-based microcavity. The largest Rabi splitting energy reported in literature for a GaN-based vertical cavity was 56 meV observed at room temperature from a lattice-matched 3λ GaN/AlGaN QWs cavity system⁶⁴. The Rabi splitting energy of 45 meV at room temperature is quite similar and 75 meV at low temperature for the InGaN microcavity is higher compared to those reported in the literature, conforming strong exciton photon coupling.

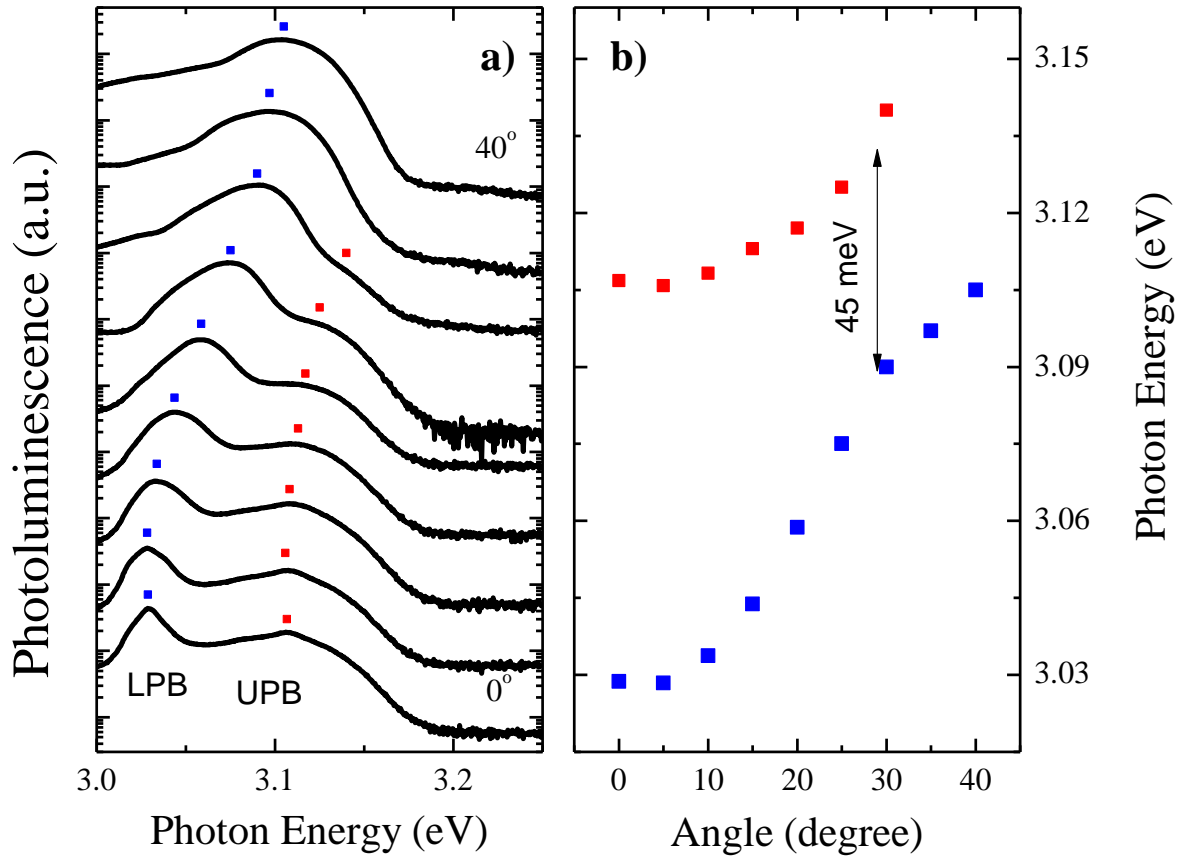


Figure 37: (a) Angle-resolved PL spectra at RT in the range of 0°–40° for the cavity on free-standing GaN (b) Experimental cavity polariton dispersion curve.

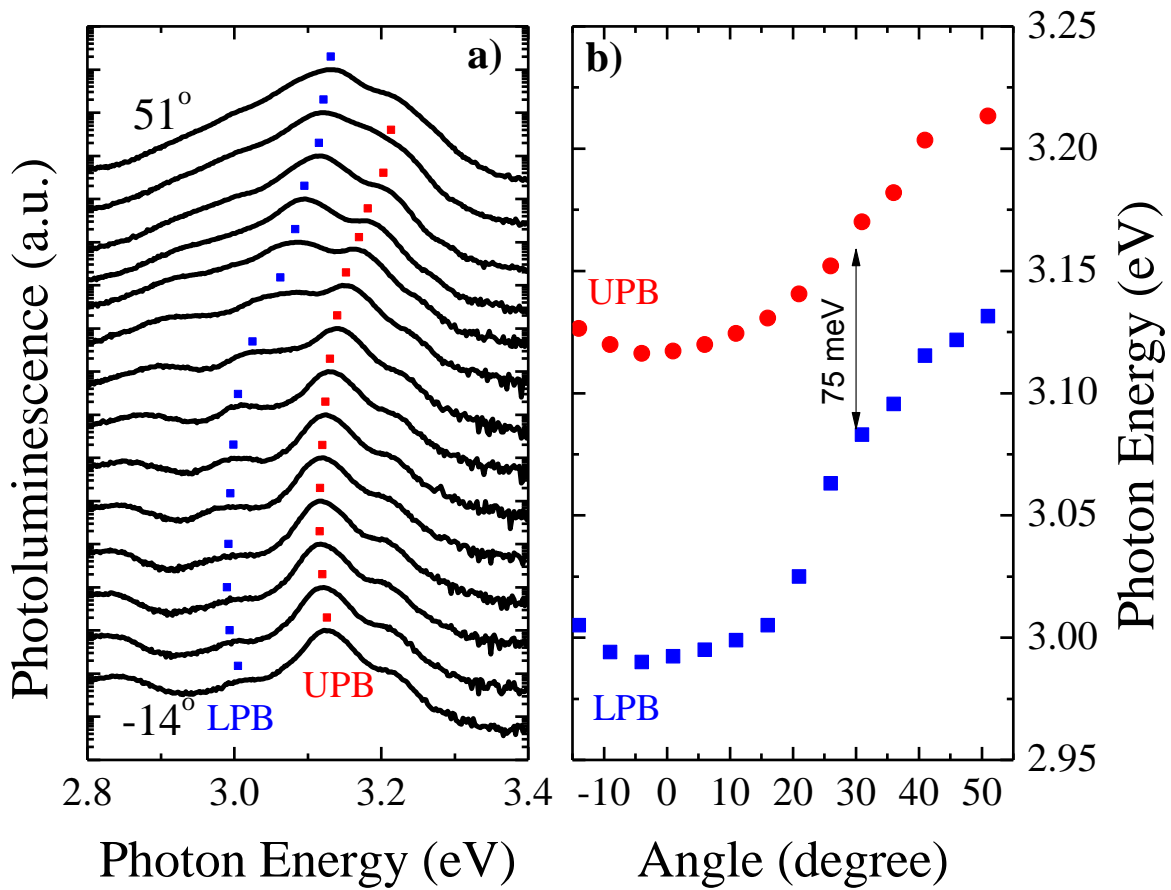


Figure 38: (a) Angle-resolved CL spectra at 5.8K in the range of -14° to 51° for the cavity grown on free-standing GaN. (b) Experimental cavity polariton dispersion curve.

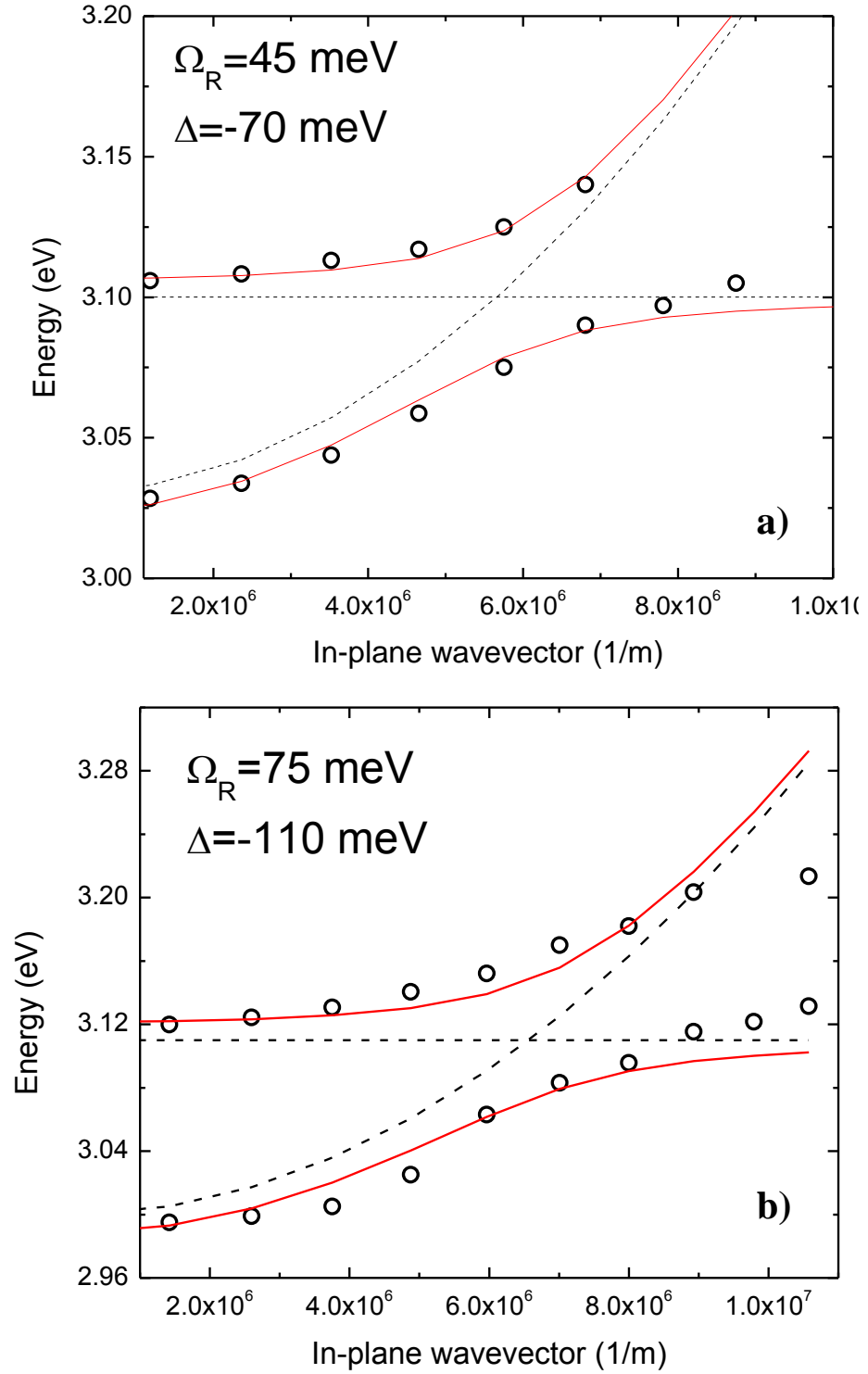


Figure 39: Calculated fitting results for polariton dispersion curves at (a) room and (b) low temperatures. In plane wave vector was obtained using the relation $k_{\parallel} = \frac{\omega}{c} \sin \phi$.

As stated before, better quality active regions are a requirement to increase the exciton photon coupling in microcavities. It is already shown that use of multiple DH active regions is a superior approach for quantum efficiency enhancement compared to MQW or thicker single DH for active regions due to available larger number of states.³⁵ A cavity structure with multi 3 nm DH active region is produced and tested under optical injection, schematically illustrated in Figure 34(b). The structure was designed to have an active region of 2 six periods of 3 nm In_{0.15}GaN DH (with high In_{0.01}GaN barrier) separated by 170 nm (λ) In_{0.01}GaN underlying layer with the effective cavity length 2.5λ at 420 nm. The active region had AlGaIn blocking layer and was sandwiched between 29 pair crack-free bottom AlN/GaN DBRs and highly reflective 13.5 pair top SiO₂/SiN_x DBRs. The bottom AlN/GaN DBRs for the VCSEL was grown on 2 μ m GaN template on sapphire substrate. Reflectivity and PL measurements were performed for the structure in a micro-PL setup. The excitation source for the PL was kept at resonant excitation with the active region, 380nm. The sense of using 2 six periods of 3 nm In_{0.15}GaN DH separated by λ underlying layer was to feed to cavity with more photons to obtain better cavity mode.

Figure 40(a) shows the reflectivity spectrum for the full vertical cavity (black), reflectivity spectrum for the bottom AlN/GaN DBR (red) and photoluminescence spectrum (blue) emitting between top dielectric and bottom semiconductor DBR layers. The reflectivity of the bottom AlN/GaN DBR is approaching to 97-98% with 10-18 nm stop band centered at the wavelength of 435 nm. The reflectivity of the full cavity (completed with a top 13.5 pair SiO₂/SiN_x DBR) peaked at nearly 99.5% with a stop-band width of \sim 90 nm. Figure 40(b) shows the cavity mode peak having a high Q-factor of 1300. However, not all the regions on this sample showed this high Q-factor. The reason was the inhomogeneous thickness variation of the cavity along the wafer. This nonuniform behavior led to inaccurate positioning of the active region within the cavity decreasing

the quality factor. As can be seen in Figure 40, the cavity with the multi DH cavity displays higher Q-factor compared to earlier test cavity grown on free standing GaN with MQW active region. It is apparent that better active region quality has a big impact on the substantial increase in Q-factors (from 300 to 1300) since both vertical cavities have same pairs of bottom semiconductor and top dielectric DBR with similar reflectivities. In order to achieve higher Q-factors, further optimization efforts are needed to be focused on increasing the active region quality and positioning the emission between the top and bottom DBR stop bands by precisely controlling the growth parameters, achieving of sharper cavity interfaces and better thickness control.

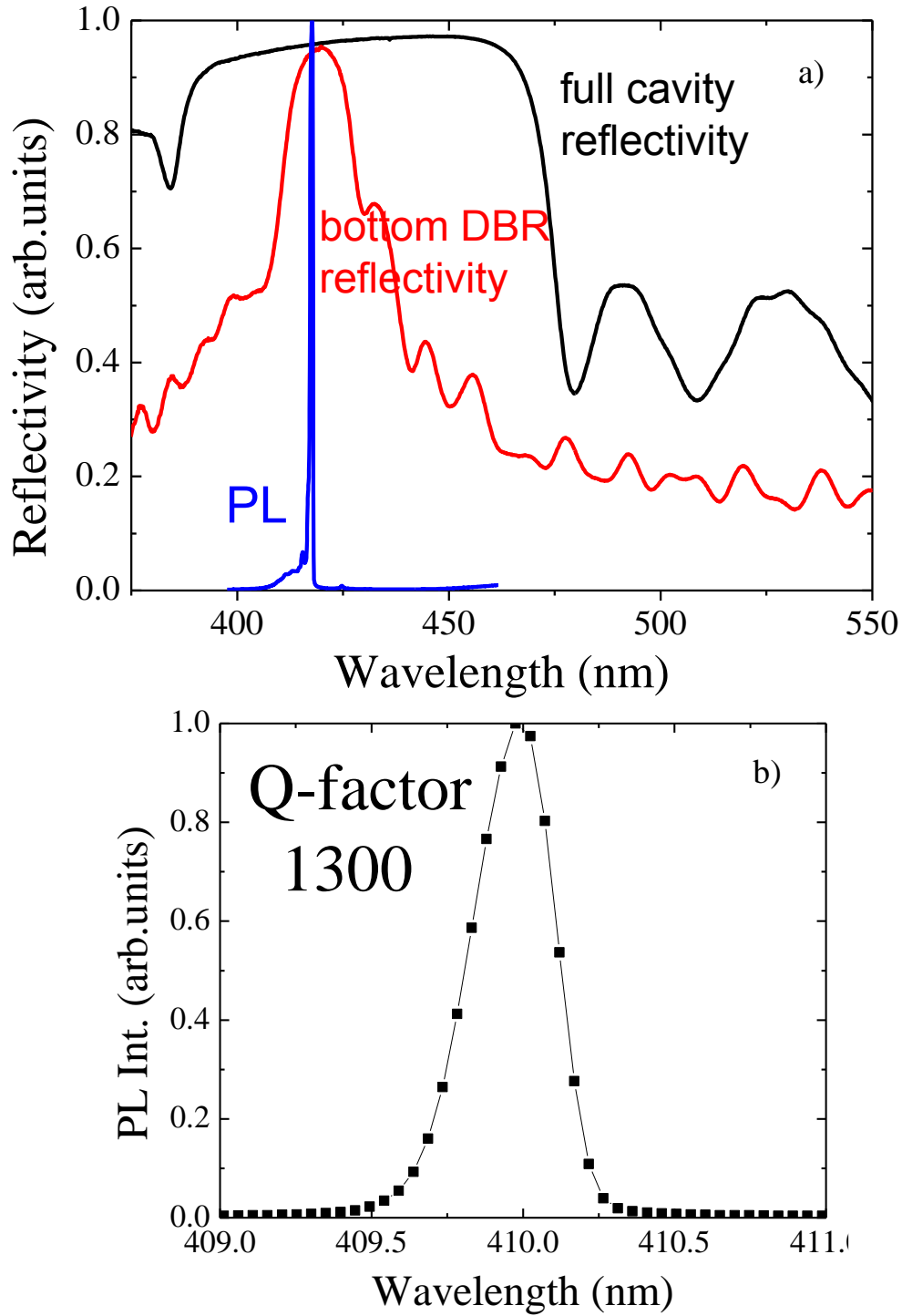


Figure 40: (a) The reflectivity spectrum (black) for the full vertical cavity with DH active region, reflectivity spectrum for the bottom AlN/GaN DBR (red) and photoluminescence spectrum (blue). (b) The spectrum corresponds to the highest Q factor measured.

In order to gain insight into the distribution of active region emission from the full cavity with DH active region, room temperature NSOM was performed (Figure 41). For NSOM measurements, HeCd laser (325 nm wavelength) excitation through a Cr-Al coated optical fiber probe with a 100 nm aperture was used.¹⁰⁵ A low-pass filter (>400 nm) was used to measure the band-edge emission. The PL from the sample surface was collected with a long working distance 50X UV-visible microscope objective and detected by a photomultiplier tube. Figure 41(a) represents the AFM image of the full cavity (13.5 pair top dielectric DBR surface) for the scan area $50 \times 50 \mu\text{m}^2$ while Figure 41(b) represents the corresponding active region emission for the scanned area. The PL emission from the microcavity is found to be nonuniform over the scanned region. The reason might be different structural quality or differences in the cavity length in this region.

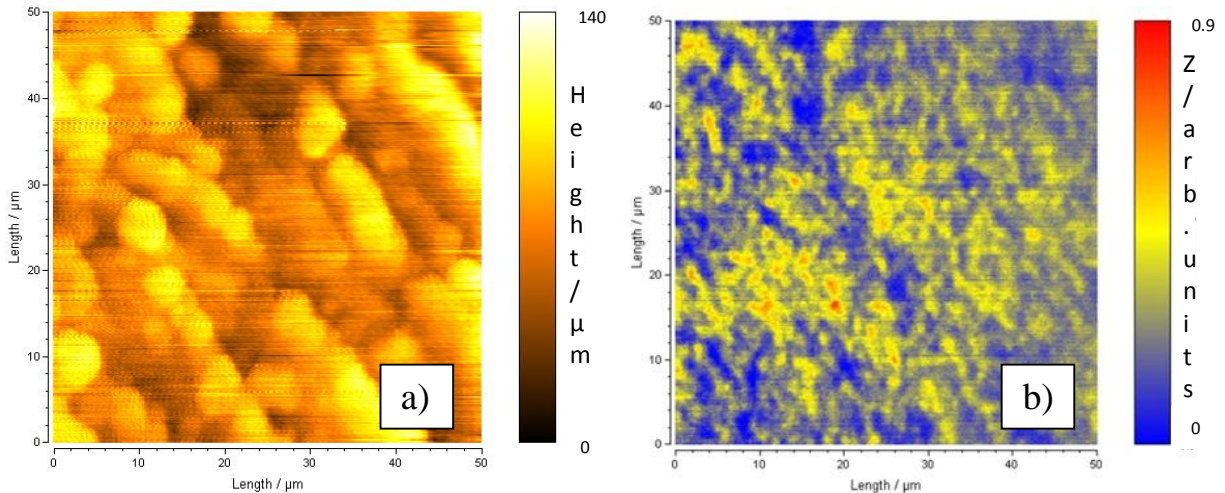


Figure 41: Room temperature NSOM results for the DH active region microcavity structure with bottom semiconductor and top dielectric DBRs (a) height image (b) PL intensity mapping.

3.2. Optimization and characterization of a vertical cavity with full dielectric distributed Bragg reflectors (DBRs)

Epitaxial lateral overgrowth (ELO) of GaN using dielectric DBR masks as the bottom reflector is very helpful to increase the quality of active regions in vertical cavity structures. The

“wing region” (overgrown GaN) would have much lower density of dislocations compared with the window region. In terms of efficiency as well as device application, it is critical to maximize the lateral versus vertical growth ratio and achieve a flat surface and wide enough ELO-GaN wing region. To achieve the goal, NH₃ flow modulation technique in MOCVD growth was employed to enhance the lateral overgrowth, since it could improve the migration of Ga atoms on the (0001) plane of ELO-GaN surface. In this method, interruption of NH₃ flow was inserted for a given time (15, 25, 30 s were test) during growth for every period (20 s) of normal GaN growth, while trimethylgallium (TMGa) flow rate was kept constant. This growth was performed using a growth mask with varied width such as 2, 3 and 4 μm-wide stripe-shaped windows separated by 32, 33 and 34 μm, respectively, and aligned along the GaN $\langle \bar{1}100 \rangle$ direction. The growth parameters such as periods of ammonia on/off time and window size for ELO stripe were optimized to get improvement for L/V growth ratio for ELO-GaN. The L/V ratio is successfully improved for the ELO-GaN from 1 to around 4 after 1.5 hour growth as can be seen from the cross-sectional SEM images in Figure 42.

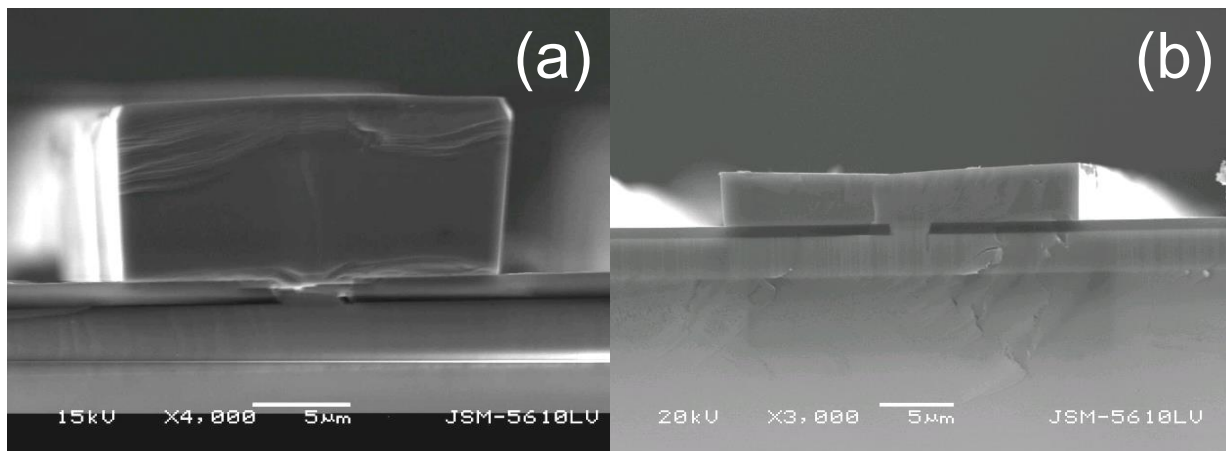


Figure 42: Cross sectional SEM images of ELO GaN samples grown with (a) ammonia on/off time 20 s/15 s with TMGa: 20 sccm and (b) ammonia on/off time 20 s/25 s with TMGa: 12 sccm.

After ELO growth, ICP etching was needed to reduce the ELO thickness in order to obtain proper cavity lengths, 2.5λ chosen in this case, which is about 400 nm. Therefore, it was necessary to investigate the etching conditions to remove the thick GaN layer and achieve smooth ELO-GaN surface. First of all, $\text{Cl}_2/\text{Ar}/\text{SiCl}_4$ gas mixture was used for the ICP plasma etching. The flow rates of Cl_2 , Ar, and SiCl_4 were maintained at 15, 18, and 5 sccm, respectively. The chamber pressure during etching was kept at 0.6 Pa. To verify the results of the dry etching, etched surface morphology and cross sections were examined by SEM. Using ICP/bias power 200/45 W, the ELO stripes were thinned down to around 1.5 μm . However, 4 μm tall wall-like features were appeared at the edges of the ELO wings. This can be clearly seen in **Figure 43**. The formation of these features were concerning that the dielectric material on DBR regions was sputtered during the etching when the chemical component of the etching was relatively large, and the dielectric material was sputtered to the edge of ELO-GaN, acting as the masks in the subsequent etching of GaN.

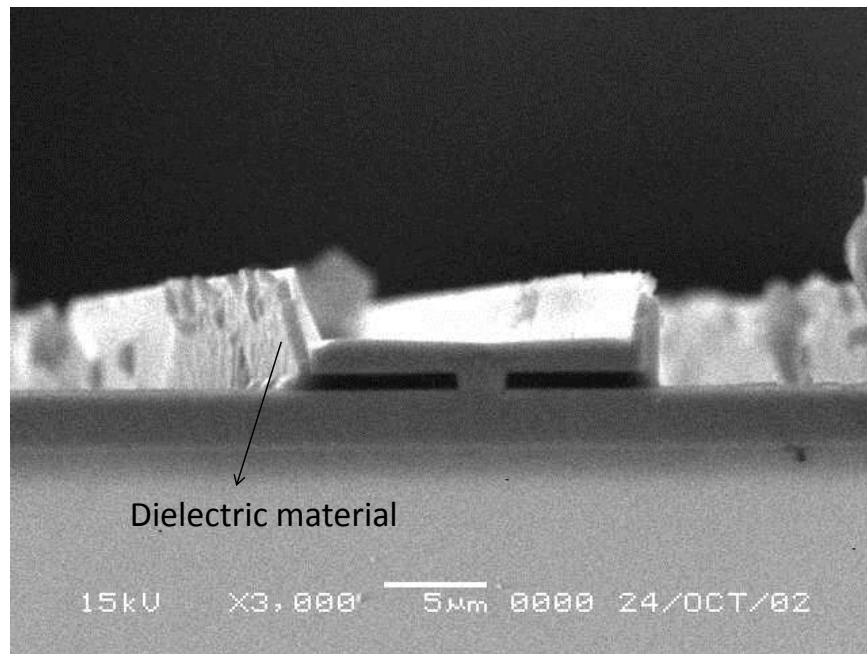


Figure 43: Cross sectional SEM images of an ELO layer after ICP etching with ICP/bias power 200/45 W showing wall-like feature on an ELO stripe.

Later, the ICP/bias powers were increased to 350/250 W and the chamber pressure increased to 0.67 Pa. The Cl₂/Ar gas mixture was kept at 15/25 sccm, and SiCl₄ was removed from the gas mixture as suggested by Kao et al.¹⁰⁶ The cross-sectional SEM images for before and after the ICP etching are shown in Figure 44. For this particular sample, the ELO thickness successfully decreased from 10 μm to a range between 0.4 μm and 1.5 μm. The reason of this variation is the ELO-GaN thickness variation across the wafer during MOCVD growth. The thickness of the ELO layers has an increase from 8.5 to 10 μm from one side of the sample to another side. Because of high physical component of the etching the dielectric DBR in addition to the GaN layer between the stripes were also etched. Since the VCSEL structure is grown only on ELO-GaN wings, etching of these layers does not have an effect.

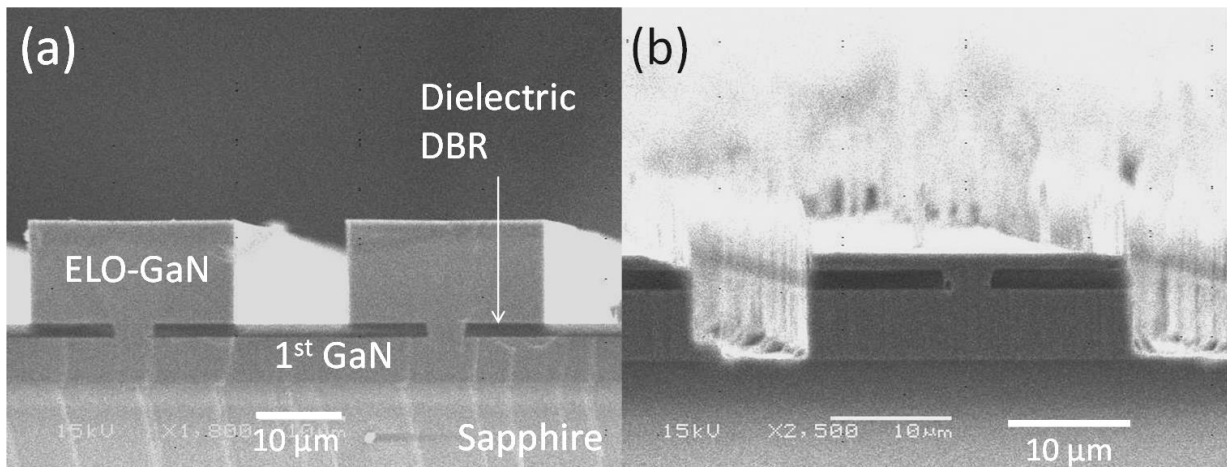


Figure 44: Cross sectional SEM images of an ELO layer (a) before and (b) after ICP etching with ICP/bias power 350/250 W.

After reducing the ELO GaN thickness down to 400 nm (around the center of the sample) using ICP etching the sample was loaded into the MOCVD chamber and subjected to an *in situ* H₂ treatment at high temperature (930 °C) to remove the residual etching damage. As stated before, better quality active region is a requirement to increase the exciton-photon coupling in microcavities. Since the multiple DH active regions have exhibited a superior approach for

quantum efficiency enhancement and better quality compared to MQW, a multi 3 nm DH active region was grown on ELO-GaN layers and tested under optical injection [Figure 47]. The cavity active region was designed to have 2 six periods of 3 nm InGaN DH (with high In_{0.01}GaN barrier) separated by 160 nm (λ) In_{0.01}GaN underlying layer where the designed wavelength was 410 nm. The reason for using 2 six periods of 3 nm In_{0.15}GaN DH separated by λ underlying layer was to feed to cavity more photons to obtain better cavity mode. In addition to vertical cavity sample a test sample was simultaneously grown on c-plane GaN on sapphire substrate in order to compare the optical quality of the vertical cavity active region. PL measurements were performed for the formed half cavity structure together with the test sample in a micro-PL setup. The HeCd laser emitting at 325 nm was used for excitation source for the PL measurement. Later, to form the full cavity structure, a top 13.5 pair SiO₂/SiN_x DBR is deposited using PECVD technique. It should be mentioned here that a SiO₂ layer with a photolithography procedure following p-type GaN growth are grown for the full structure before the top dielectric DBR deposition. The SiO₂ layer here ensures the electrical injection goes through InGaN active region grown on defect free ELO layers, as will be described below in Figure 48(b)). A basic schematic of the full vertical cavity structure is given in Figure 45(a). Figure 45(b) also illustrates the multi-DH positions with respect to cavity length. It can be seen that these active layers are designed to place on electric field antinodes in the cavity in order to maximize the cavity emission. However, due to the thickness variation of the ELO-GaN layers beneath the active regions, the placement of the active regions within the cavity varies across the sample. Further optimization to form homogeneous ELO GaN layers is needed for better optimized vertical cavity structures.

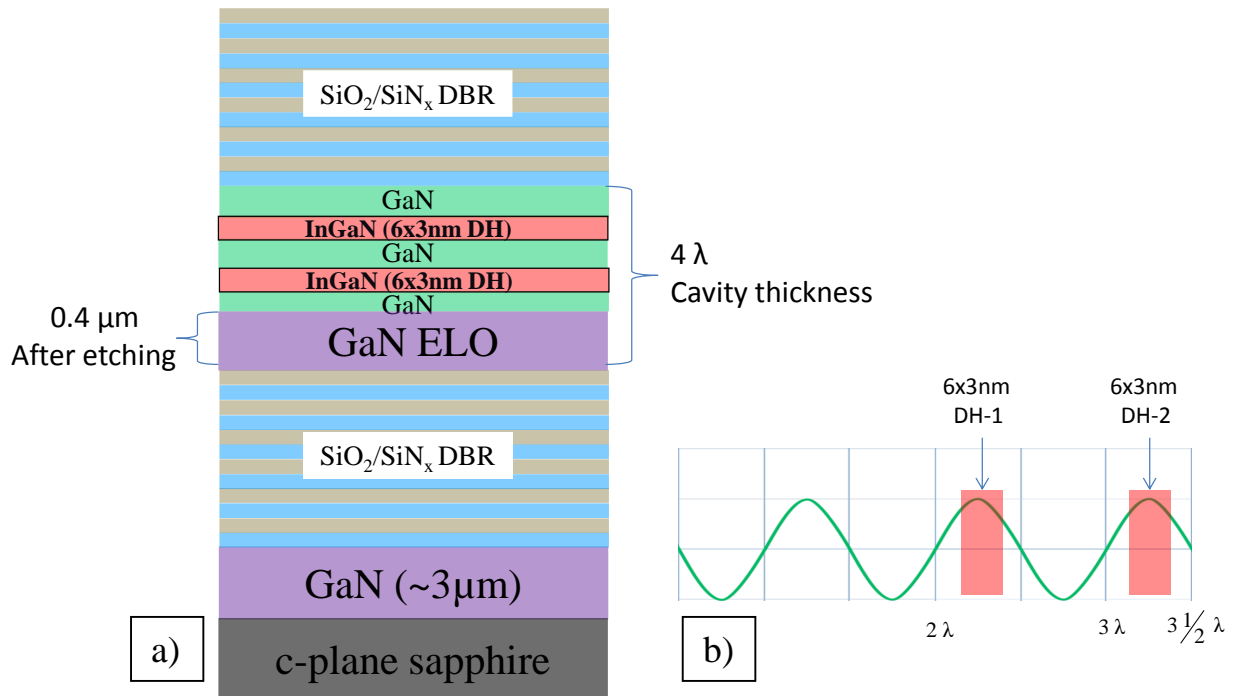


Figure 45: (a) Schematic of the full vertical cavity structure. (b) Electric field inside the cavity with respect to distance where an InGaN active region is placed at the antinode of the electric field inside the cavity.

The full cavity structure was characterized using reflectivity (Xe lamp source) and micro photoluminescence (PL) spectroscopy. For micro-PL, samples were excited normal to the surface from the top DBR side using a HeCd laser (325 nm wavelength) and a long working distance x50 microobjective. The excited area was in the order of $\sim 2 \mu\text{m}$ in diameter. The 325 nm excitation ensured to excite the active region outside of the top DBR stop band where its high energy side ends at 350 nm (**Figure 47**). The emission was also collected normal to the surface from the top DBR side. Figure 46 show the reflectivity spectrum for the full cavity structure. As can be seen from Figure 46, 99% reflectivity is achieved for the top $\text{SiO}_2/\text{SiN}_x$ DBR with a stop-band width of $\sim 80 \text{ nm}$, which is much larger compared to semiconductor AlN/GaN DBRs ($\sim 20 \text{ nm}$). The full-cavity reflectivity spectrum showed clear dips corresponding to the cavity modes at $\sim 400 \text{ nm}$ and $\sim 412 \text{ nm}$.

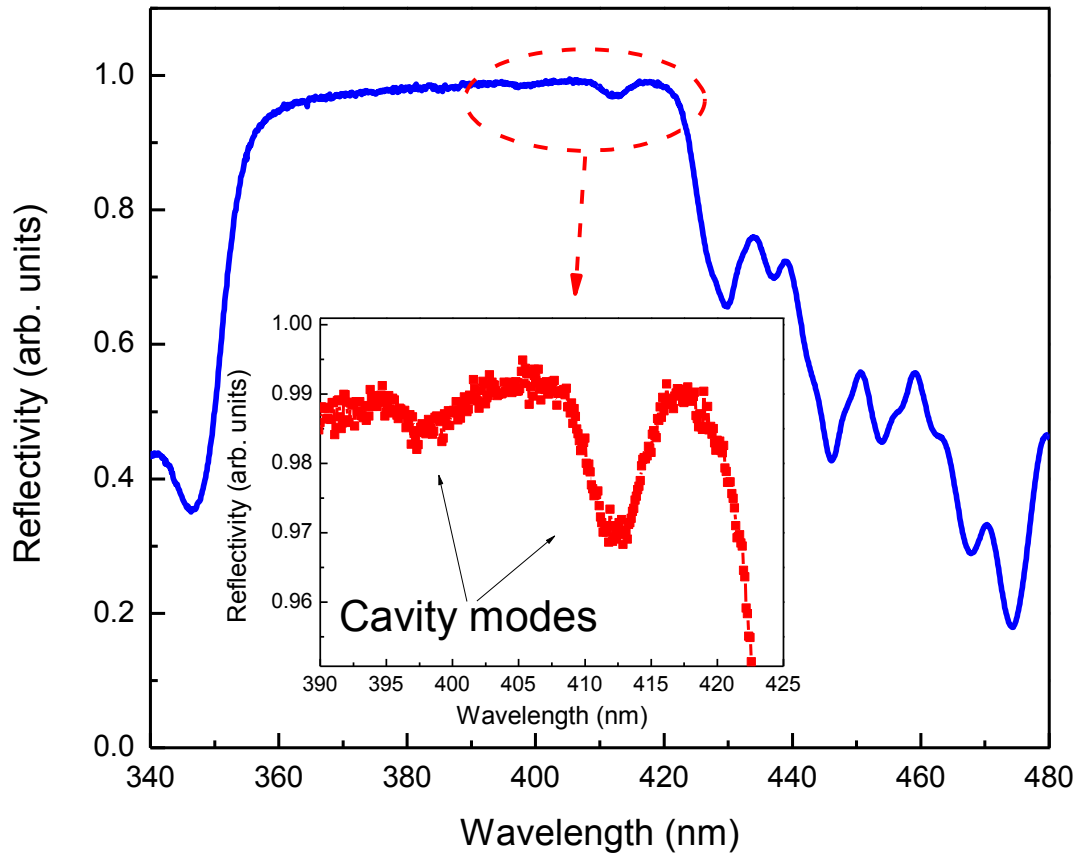


Figure 46: Reflectivity spectrum of the full cavity structure (Micro-objective is used in the measurement). Cavity modes are observed around 400 and 412 nm can be clearly seen in inset corresponding to lateral cavity length of $\sim 3\mu\text{m}$.

Figure 47 shows the PL spectra for the full cavity structure, half cavity structure and reference sample. The Q-factor of the reference sample is found to be 20 which is 3 times smaller than obtained from the half cavity. It can be clearly seen that the bottom dielectric DBR had an influence for the Q-factor increase for the half cavity structure. Q-factor from the full cavity structure, 500, was found to be substantially increased after the deposition of the top dielectric DBR. The result proves the obtained high quality of the full cavity structure and is very promising for the electrical operation.

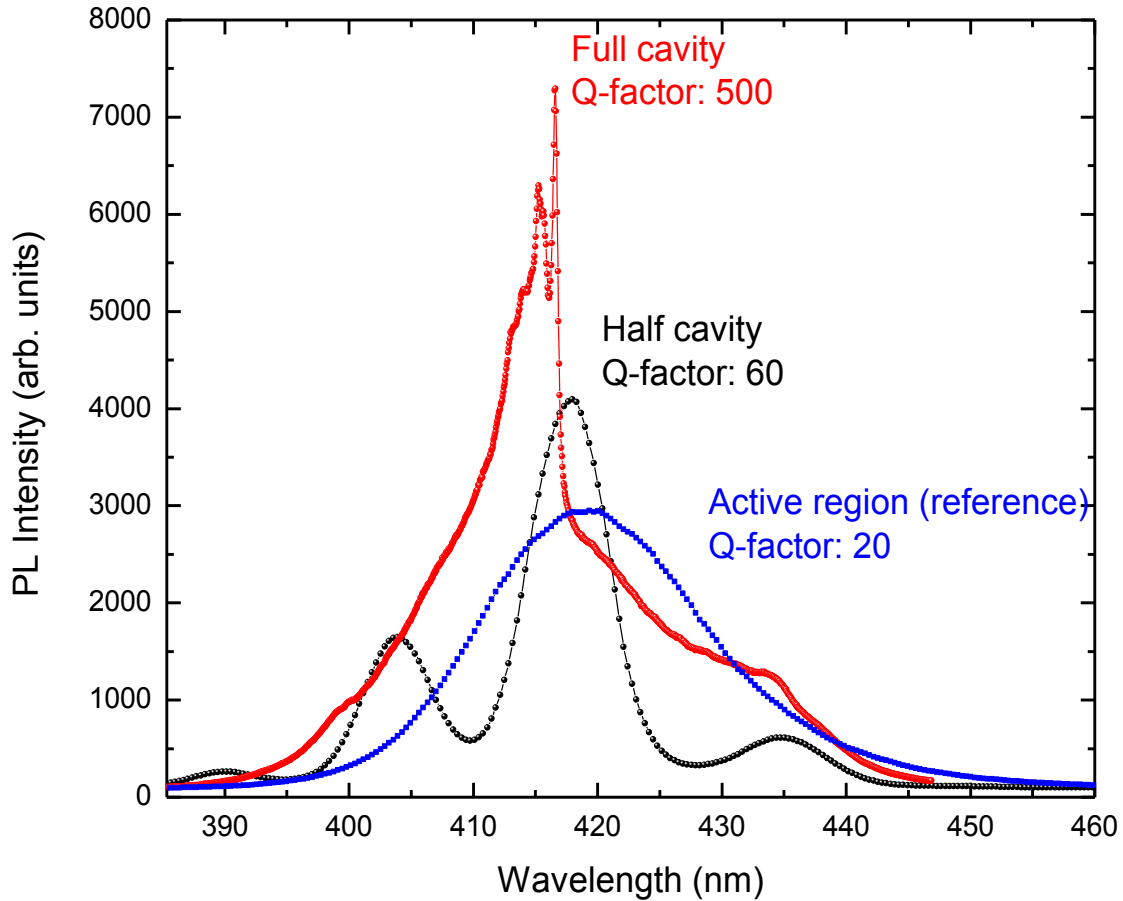


Figure 47: PL spectra for the full cavity structure (red), half cavity structure (black) and reference sample with no DBRs. The corresponding Q-factors are 500, 60 and 20, respectively.

Photolithography techniques were used with different masks in order to form the electrical contacts for the vertical cavity structure following with e-beam metal deposition. Metallization was performed after exposing the n-GaN and p-GaN layers using ICP dry etching. Ti/Al/Ni/Au (30/100/40/50 nm) and Ni/Au (20/50 nm) were deposited for n- and p-contacts, respectively. As a result, the current in the final device structure were allowed to flow only through the nearly defect-free active region formed entirely on the laterally grown wing. The final form of the vertical cavity with n- and p-contacts is schematically illustrated in Figure 48. Figure 48 (a) shows oblique view, while Figure 48(b) shows cross sectional schematics of the VCSEL structure with electrical contacts. The current paths are illustrated with red arrows and the emitted light with light green

color in Figure 48(b). The most significant aspect that differentiates the ELO method employed here from others reported in literature for cavities with all dielectric DBRs is the absence of the need for cumbersome substrate removal, in addition to the naturally formed nearly defect-free active regions and current confinement without the need for any oxidation steps. It should also be mentioned that the ELO method employed here is applicable to DBRs based on not only $\text{SiO}_2/\text{SiN}_x$ DBRs, but also other stable and high optical band-gap dielectrics inclusive of Al_2O_3 , ZrO_2 , and Ta_2O_5 , which may be explored for further improvement in vertical cavity performance.

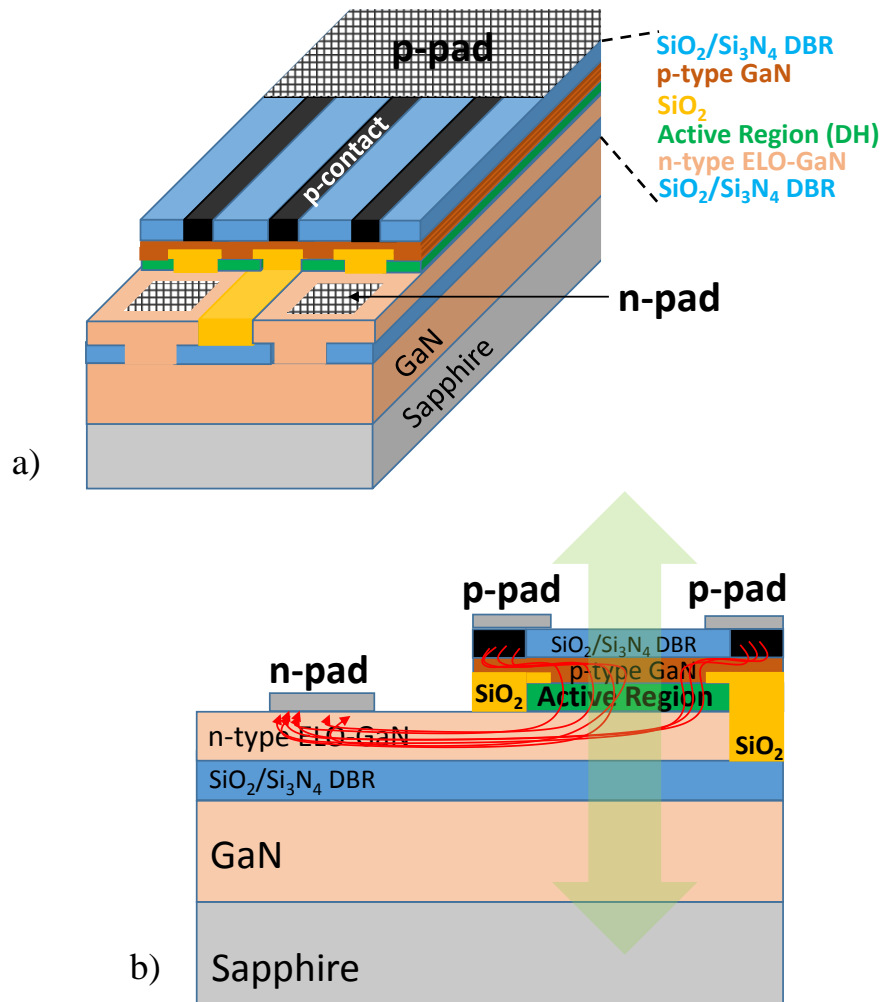


Figure 48: (a) Oblique view and (b) cross sectional schematics of VCSEL structure with electrical contacts. Red arrows show the electrical injection path, while light green is showing the light output direction.

The mask designs to produce the vertical cavity devices with different sizes using photolithography and e-beam deposition techniques are shown in Figure 49. Figure 49(a) is illustrating the mask patterns on the mesa in more detail without showing the top deposited layers, while Figure 49(b) shows the final device shapes with contact layers. The devices are prepared by changing mask patterns in the dimensions of 540X540, 200X200, 20X40, 40X20, 20X20, 20X10 μm^2 as clearly seen in Figure 49(a). The actual device sizes, in other words the active emitting area, are shown in black stripes in Figure 49(b), each of which are grown on nearly defect free single ELO GaN wings. P-contacts (Ni/Au) can be seen at the end of the ELO wings with net-like features on each device in Figure 49(b). N-contacts (Ti/Al/Ni/Au) deposited on etched ELO wings are not distinguishable from Figure 49 (b).

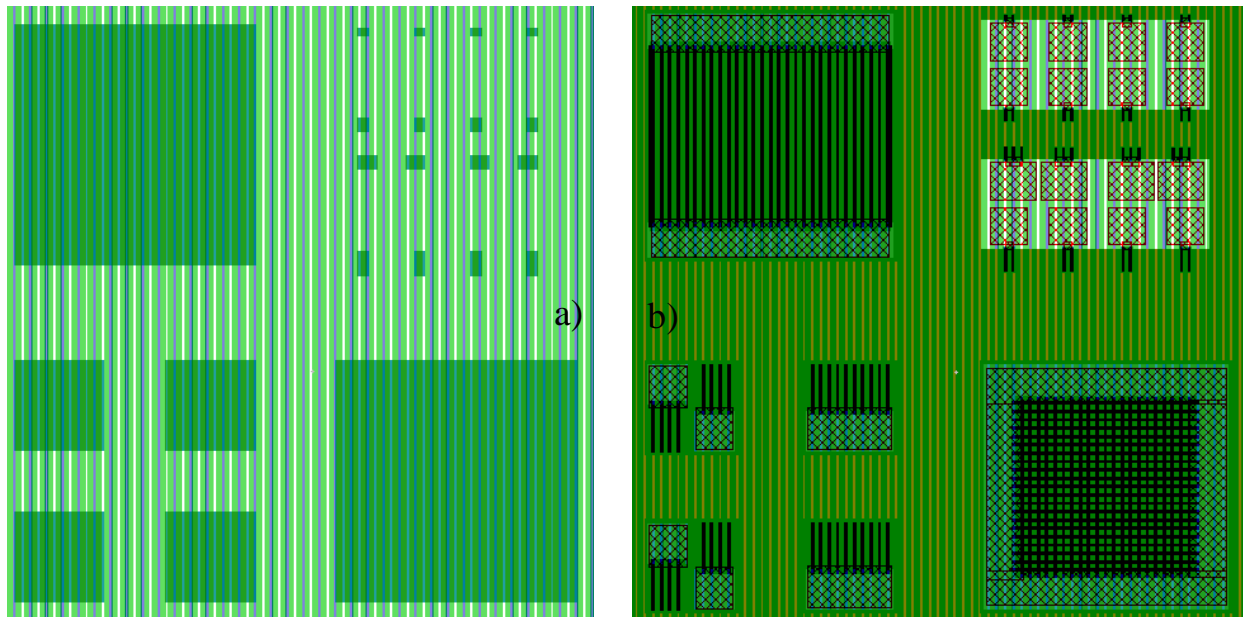


Figure 49: VCSEL devices on the mesa produced after photolithography techniques (without the top deposited layers, (b) the final device shapes with contact layers.

Figure 50 shows the I-V characteristics of a medium size device (200X200 μm^2) in linear and log scales. The forward current level was found to be small (0.1 mA @ 6 V) due to the large resistance contribution from the thick p-GaN layer (100 nm). However, fabrication issues having

to do with the full contiguity of the metal layer are at least partially, if not nearly fully, responsible for these observations. Further reduction of the p-GaN layer thickness in addition to improving the fabrication procedures may lead to lasing in these devices under electrical injection.

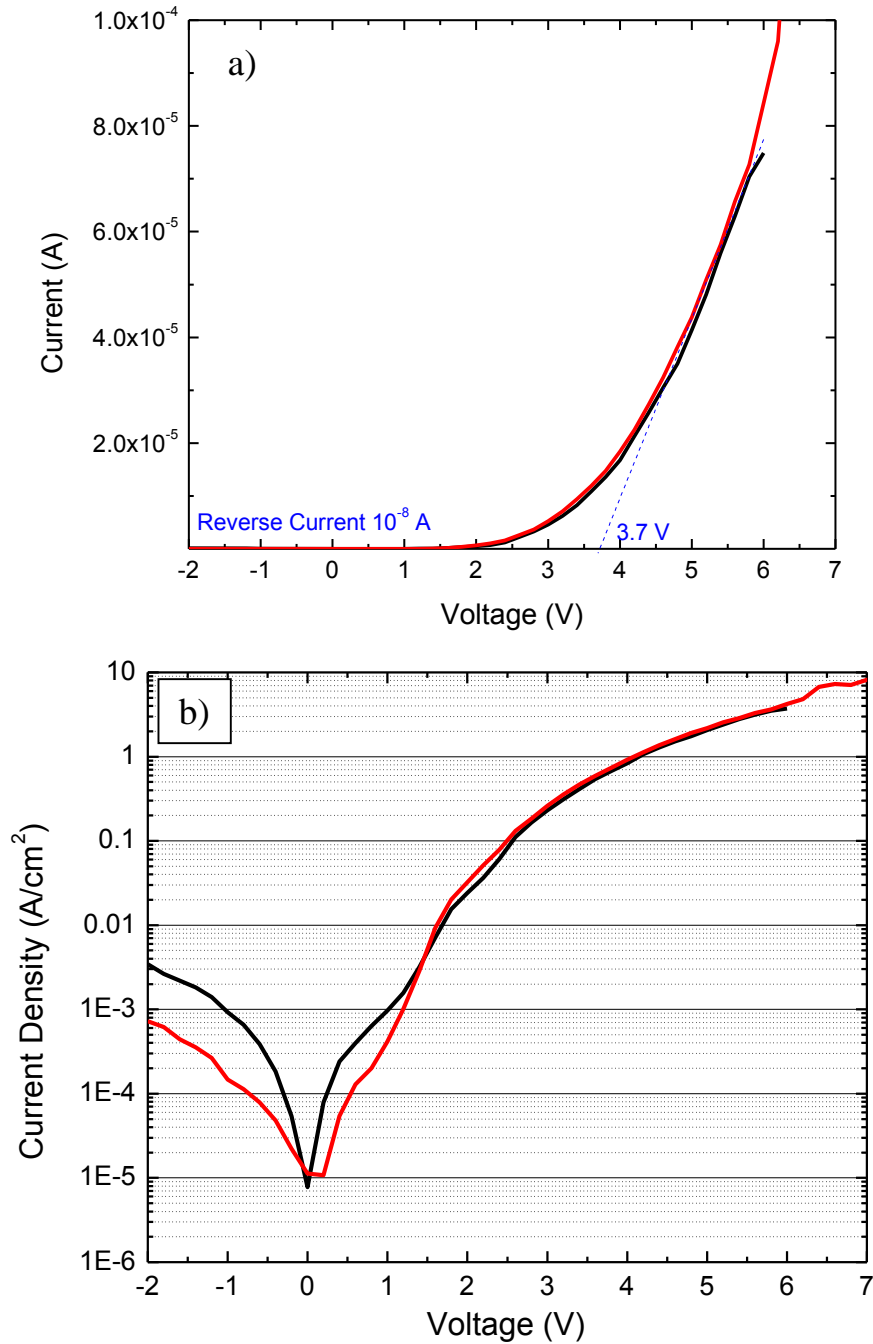


Figure 50: I-V characteristics of the full VCSEL structure in (a) linear and (b) logarithmic scales.

Chapter 4. Optical efficiency and carrier dynamics in nonpolar and semipolar GaN and InGaN LEDs

Carrier recombination dynamics may give useful information about GaN substrates for various electronic transitions and recombination rate of the carriers, etc. Above band-gap (single-photon) excitation¹⁰⁷ is the first choice for the investigation of the carrier dynamics in GaN, while two-photon excitation at below band-gap have advantageous aspects over the above band-gap excitation,¹⁰⁸ but has not been fully utilized in general. For the single-photon excitation, the high absorption coefficient of GaN ($\sim 10^5 \text{ cm}^{-1}$) results in high photo-generated carrier densities within the first a couple of hundred nanometer thick surface region with carrier densities up to 10^{19} cm^{-3} . Time-resolved techniques provide easy access to spectral features of emission as the PL transients vary with injection and temperature because of simultaneous overlapping of different recombination mechanisms, such as exciton and free carrier, radiative and nonradiative recombination processes. In recent years, defects, especially extended defects are also found to be affecting the recombination dynamics involving with the other processes mentioned above.^{109,110} These reports are mainly from nonpolar and semipolar GaN substrates in which the material quality greatly suffers from the extended defects, such as basal-plane and prismatic stacking faults.^{53,55} Clearly, the reported studies for carrier recombination dynamics inspires further investigations of the optical processes by complementary techniques, in order to delineate the role of excitons, nonradiative and radiative decays as well as defects.

4.1. Excitonic effects on recombination dynamics in nonpolar m-plane bulk GaN

Having very close binding energy to the room temperature thermal energy, 25 meV, excitons play an important role in recombination dynamics in GaN. However, identifying their exact contribution is rather challenging. This is because optical techniques such as steady-state or time-resolved photoluminescence are limited to observe excitons in GaN at elevated temperatures. One needs to rely on indirect observations to resolve the excitonic effects, such as the polarization of luminescence and the relevant selection rules. Knowing the polarization degree of exciton emission, one can separate the contribution of excitons to the radiative recombination from that of free carriers at different temperatures. For polar c-plane GaN thin films and substrates,^{78,111,112} monitoring the polarization along the c-axis ($E \parallel c$, π -polarization) is challenging;¹¹³ therefore, non-polar m-plane GaN is more suitable for investigation of the polarization degree of emission^{114,115,116}

In order to reveal the contributions from excitons and free carriers in a wide temperature range (15-350 K), polarization and temperature dependent time-resolved photoluminescence (TRPL) measurements were performed in a bulk m-plane GaN with the excitation beam polarized parallel or perpendicular to the c-axis of the crystal. In addition, polarization-resolved photoluminescence (PRPL) measurements were used to quantify the degree of polarization depending on the exciton populations in the mixed free carrier/exciton system at different excitation densities and temperatures.

The freestanding m-plane wurtzite GaN sample (450 μm thick) was sliced from a c-axis oriented boule grown by hydride vapor phase epitaxy (HVPE) on sapphire and then separated from the substrate by a laser lift-off technique. For TRPL and PRPL measurements a frequency tripled Ti:Sapphire laser (267 nm wavelength) and a continuous wave (cw) HeCd laser (325 nm

wavelength) were used for excitation. The sample was mounted in a closed-cycle Helium cryostat for time-integrated PL spectra and time-resolved PL decay measurements in 15-300 K range, using Hamamatsu streak camera. The optical experiments were performed with the light wave vector $k \perp c$ and the electric field parallel ($E \parallel c$) or perpendicular ($E \perp c$) to the c -axis of the wurtzite GaN (π - or σ -polarization, respectively). A linear polarization analyzer was used to resolve the polarization state of the PL.

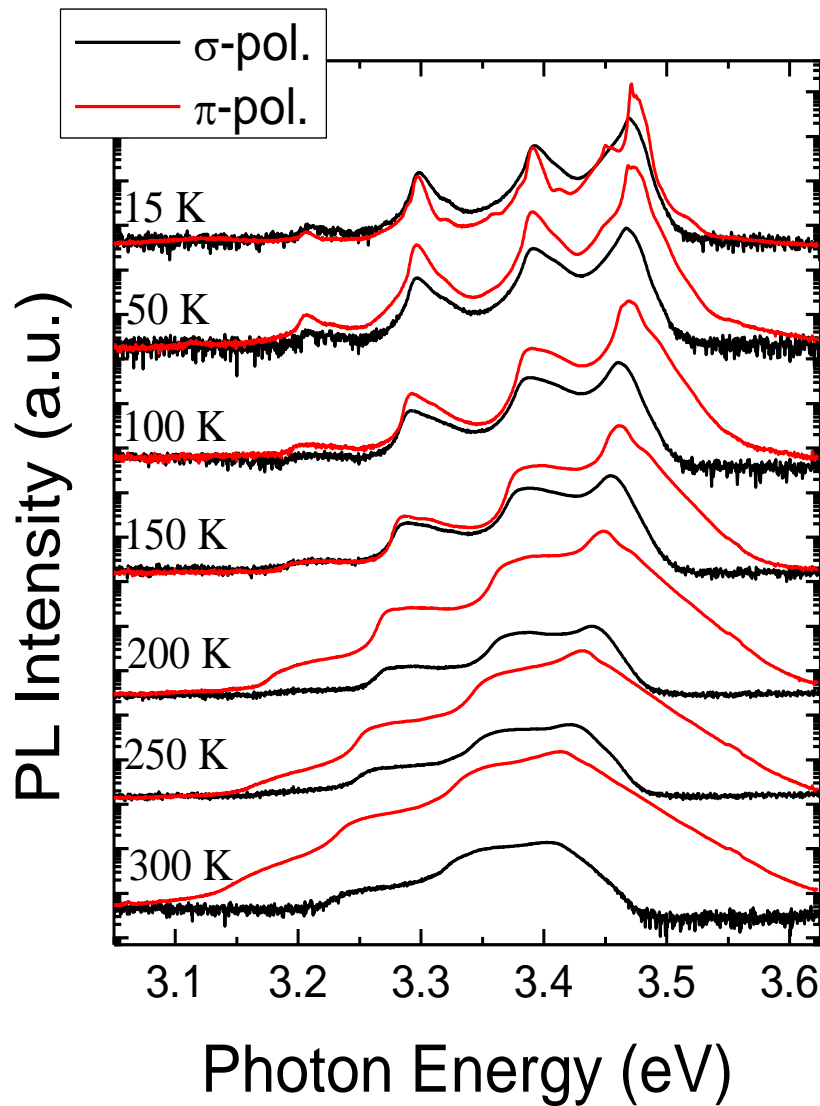


Figure 51: Temperature dependent PL spectra for σ - and π -polarization states collected using 267 nm excitation wavelength and at an excitation density of $4\mu\text{J}/\text{cm}^2$ for m -plane GaN.

Figure 51 shows the temperature dependent PL spectra for m-GaN measured for σ - and π -polarization states at excitation density of $4 \mu\text{J}/\text{cm}^2$. The PL spectra at 15 K for σ -polarization shows very broad near band edge emission (NBE) peaking at 3.465 eV; in contrast, sharp donor bound exciton (DX) lines (~ 2 meV FWHM) at 3.471 (DX_A) and 3.475 (DX_B), and a broad free exciton (FX) line at 3.478 eV are observed for π -polarization. In PL spectra, LO phonon replicas are also seen as shoulders of the main peak at lower energies. The broad peak without fine excitonic features in the 300K PL spectra for σ -polarization has its origins in strong exciton screening.¹¹⁷

Figure 52(a to c) shows low temperature σ -polarized component of PL spectra at different excitation densities. As evident from **Figure 52(a)**, decrease of excitation density reduces the broadening, and fine exciton structure appears in the spectra as a result of reduced exciton screening. The disappearance of the DX_A with increasing polarizer angle (0 degree corresponds to light polarization parallel to the c-axis) observed in **Figure 52(c)** and **Figure 52(d)** confirms a degree of polarization of 1 for DX_A. The polarization degree of photoluminescence is defined as $(I_h - I_l)/(I_h + I_l)$, where I_h and I_l represent the highest and the lowest PL intensities of the polarization components (occurring at polarizer angles of 0 and 90 degrees, respectively in **Figure 52**), respectively. The degree of polarization for the near band edge emission (NBE) peak at excitation density of $4 \mu\text{J}/\text{cm}^2$ decrease to 0.46 (**Figure 52(b)**) primarily due to the dissociation of excitons to free carriers resulting from screening of Coulomb interaction at high excitation densities. It is understood that the polarization degree is determined by the populations of the free carriers and excitons at different excitation densities, where the former species do not have any preferred polarization state.

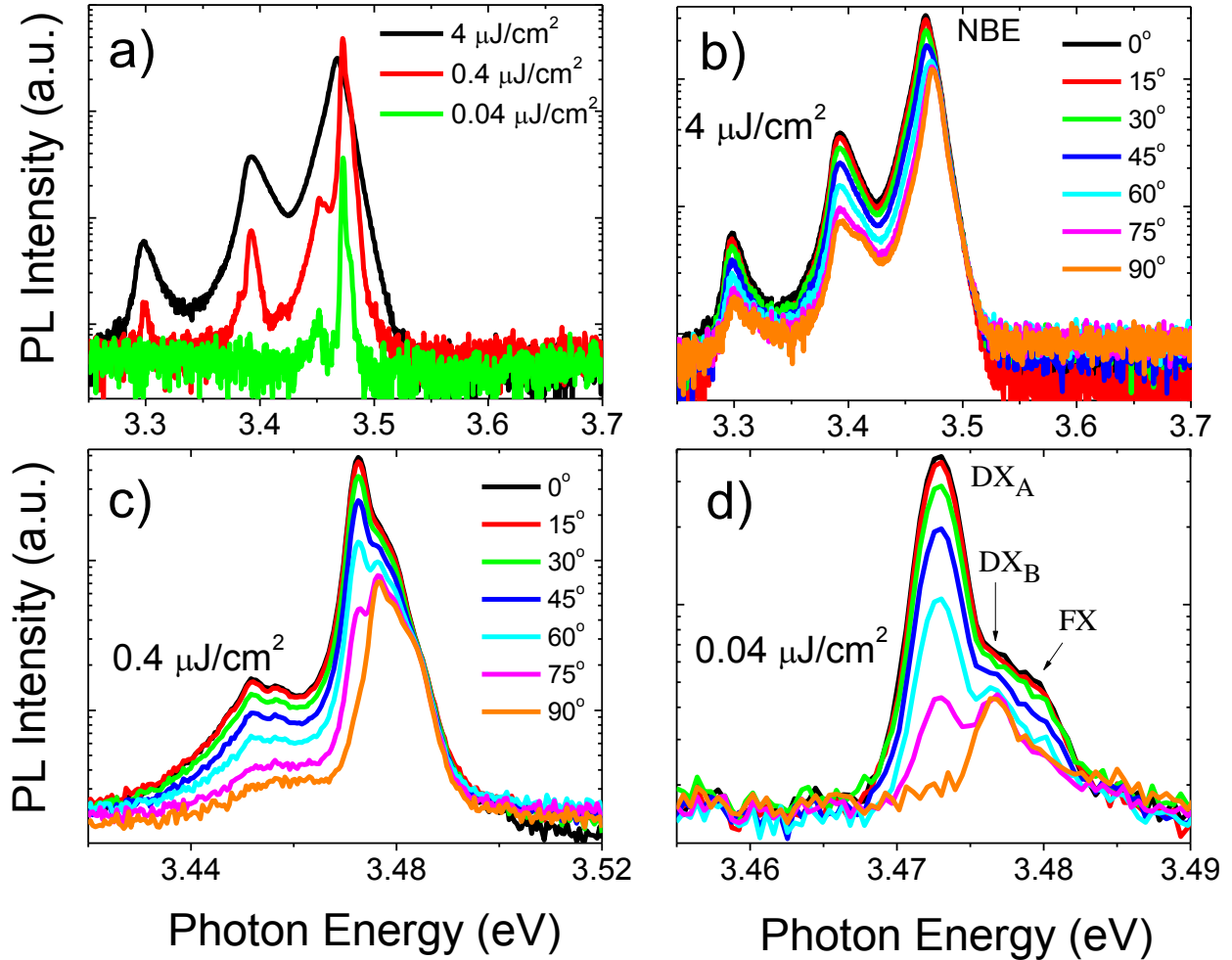


Figure 52: a) Excitation intensity dependent σ -polarized PL spectra for m-plane GaN at 10 K and 0° polarizer angle. PL spectra at different polarizer angles for σ -polarization at b) $4 \mu\text{J}/\text{cm}^2$, c) $0.4 \mu\text{J}/\text{cm}^2$, and d) $0.04 \mu\text{J}/\text{cm}^2$.

Similarly, degree of polarization for NBE was measured at room temperature for two excitation energy densities. The variation of PL intensity with respect to the polarization angle (**Figure 53**) was used to calculate the degree of polarization for σ - and π -polarization states. These values for the σ - and π -polarization states are equal to 0.22 and 0.11, respectively at higher excitations ($4 \mu\text{J}/\text{cm}^2$) and increases up to 0.28 and 0.30, respectively, at $0.4 \mu\text{J}/\text{cm}^2$. The difference in the degree values for σ - and π -polarizations at $4 \mu\text{J}/\text{cm}^2$ is primarily due to selection rules producing different exciton concentrations for different polarization states. For example, both A

and B exciton states are strong for σ -polarization state while only C exciton state is strong for the π -polarization state. The room temperature PRPL results show that the degree of polarization varies with intensity of the excitation. The increase in the degree of polarization for $0.4 \mu\text{J}/\text{cm}^2$ compared to $4 \mu\text{J}/\text{cm}^2$ is a result of reduced exciton screening that is still effective at room temperature. These results suggest that excitons still survive and therefore would enhance the radiative recombination rate in GaN at room temperature.

To investigate the impact of polarization state to PL decay, time-resolved photoluminescence (TRPL) measurements were performed at 15 K for π - and σ -polarization states, at various excitation energy densities. As shown in Figure 54(a,b), the PL transients for different polarization components exhibit similar exponential decay, while the decay times became twice longer at higher excitations. The latter effect may have different genesis, and one of the reasons may be increased ratio of free carriers to excitons. The PL decay time of ~ 0.7 ns at the lowest excitation density is supposed to be of radiative origin, as in the latter case the exciton density is below 10^{16} cm^{-3} and only excitons dominate in the mixed exciton-free carrier system. Nevertheless, estimation of exciton radiative time at 15 K for exciton density of 10^{16} cm^{-3} leads to value of $\tau_{\text{Rad}} = 1/\text{BN}_{\text{ex}} = 30$ ns assuming that the radiative coefficient of excitons $B = 2 \times 10^{-11} \text{ cm}^3/\text{s}$ at 300 K⁸⁹ increases by 90 times at 15 K according to relationship $B \propto 1/T^{3/2}$. This discrepancy requires considering different factors which may compete with radiative decay and make the initial PL decay time so fast at lowest injections. Therefore, the decrease in the degree of polarization with increasing excitation is not unambiguously and quantitatively reflected in the increasing PL decay times. Nevertheless, a search for correlation between excitation-dependent degree of polarization for NBE and its decay rate needs only normalized ratios.

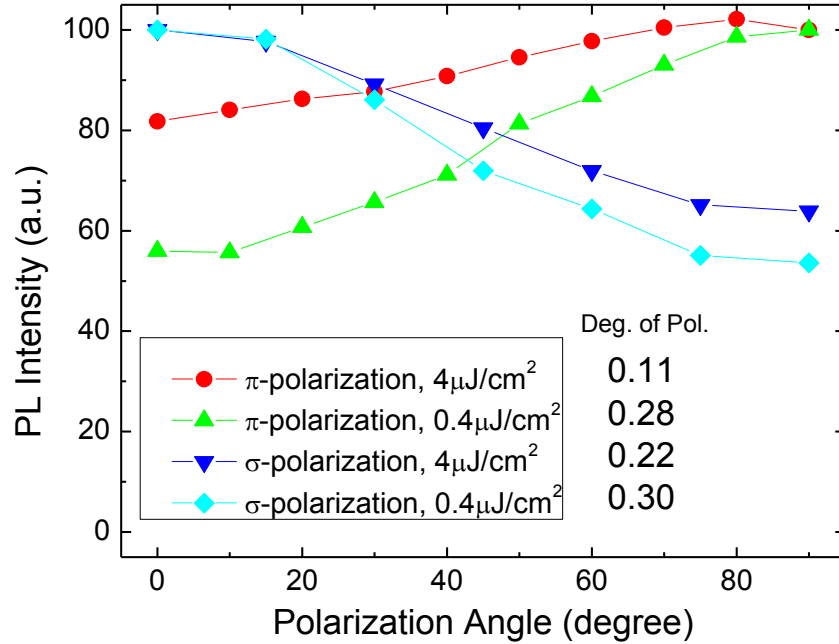


Figure 53: Comparison of normalized PL intensities for π - and σ -polarization components, varying with polarization angle in m-plane GaN. The corresponding degree of polarization at 300K is given in the plot.

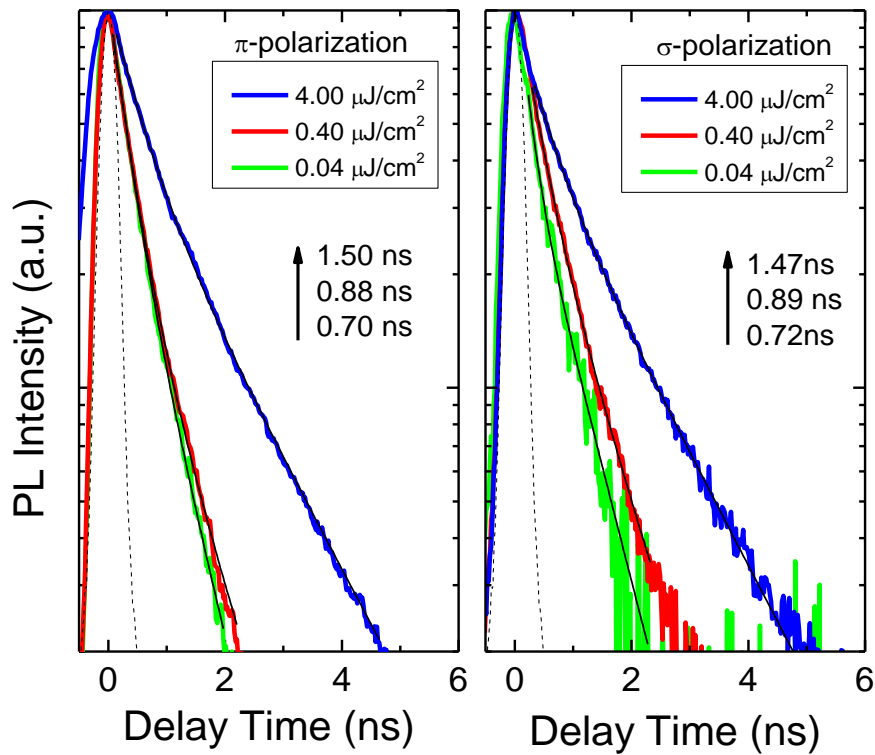


Figure 54: Excitation dependent PL transients for (a) π - and (b) σ -polarization states at 15K. System response of 0.28 ns is also shown in the figures (dashed lines).

The recombination dynamics were further investigated at different temperatures which simply correspond to different exciton populations. Figure 55(a,b) show the temperature dependent PL transients (π - and σ -polarization states) in 15 K to 350 K range at $4 \mu\text{J}/\text{cm}^2$ excitation energy density. TRPL spectra exhibit an initial fast decay followed by a longer and temperature dependent decay, which correspond to the effective PL lifetime of the mixed exciton-free carriers system. The shorter decay may be attributed to the surface recombination, which has been observed in other works^{118,119} and/or to the diffusion of free carriers away from the surface¹²⁰.

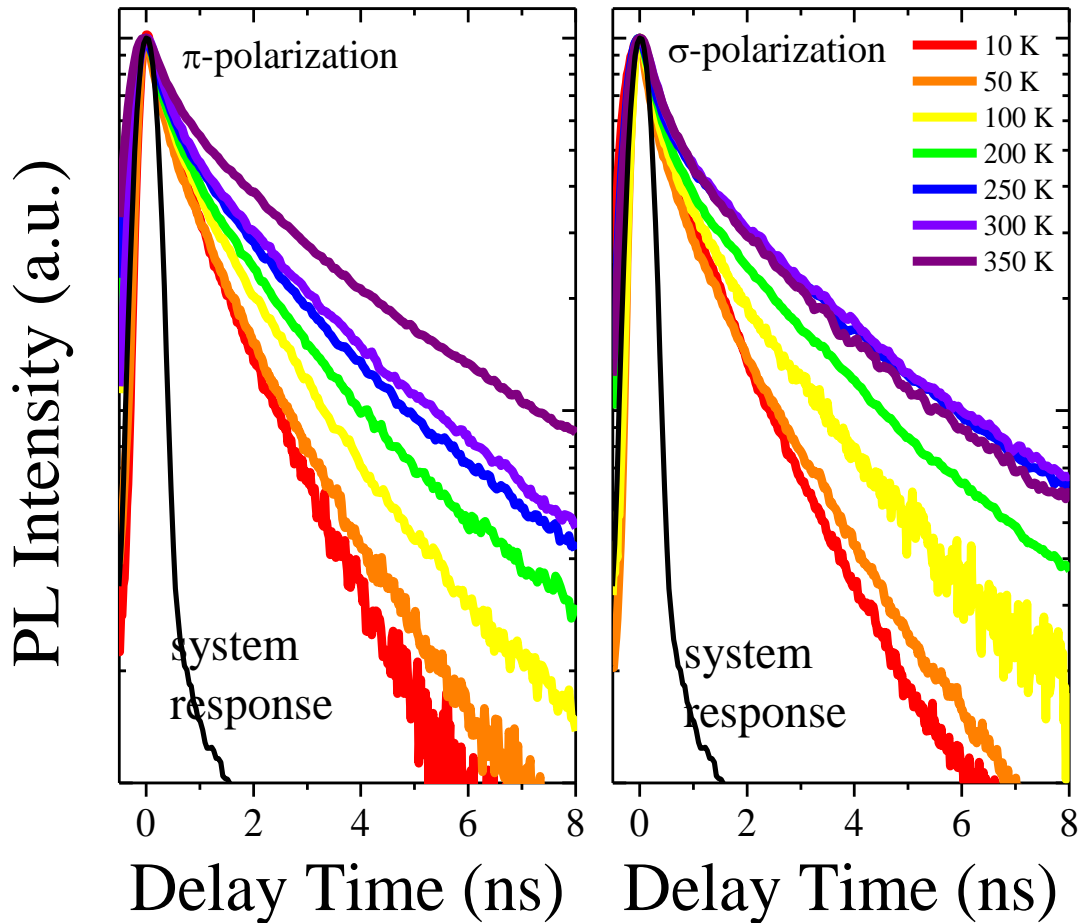


Figure 55: Temperature dependent π - and σ -polarized PL transients at $4 \mu\text{J}/\text{cm}^2$ excitation density.

The effective PL lifetimes obtained from bi-exponential fits to the data in Figure 55 are plotted in Figure 56 as a function of temperature at excitation densities of $0.4 \mu\text{J}/\text{cm}^2$ and $4 \mu\text{J}/\text{cm}^2$.

At low temperatures the PL lifetime is mainly determined by excitons while it increases with increasing temperature due to contribution of free carriers resulting from dissociation of excitons. It is observed that the PL lifetimes at the excitation energy density of $0.4 \mu\text{J}/\text{cm}^2$ are always faster than those at $4 \mu\text{J}/\text{cm}^2$ implying that at lower excitation density there is more excitonic recombination due to less effective exciton screening. This tendency is consistent with the fact that the radiative lifetimes of free excitons are nearly one order of magnitude less than those of free carriers in the nitrides at the same temperature⁸⁹. On the other hand, modeling of carrier dynamics in m-GaN¹⁰⁷ revealed fast initial PL decay transients of 5-6 ns at room temperature in spite that *a priori* known nonradiative carrier lifetime in the m-GaN was of 40-50 ns¹²⁰. This discrepancy having origin in carrier diffusivity may have even stronger impact at lower temperatures, therefore the genesis of the initial fast decay in the set of curves in Figure 55 must be considered very carefully.

Obtaining radiative lifetimes separately for free carriers and excitons from the time-resolved PL measurements at different temperature and excitation density levels is very complicated. The factors affecting the PL decay time such as impact of excitation density on surface band bending and the resulting change in diffusion/drift as well as recombination rates have to be identified. Consequently, variety of reasons may contribute to the total excited carrier density and the radiative recombination rate, which are substantially affected by excitation density and temperature due to screening of the excitons and their thermal dissociation. Therefore, knowledge of radiative decay times of excitons and free carriers together with degree of polarization may give insight about the instantaneous populations of excitons and free carriers at certain conditions since the radiative lifetime is inversely proportional to radiative recombination coefficient times the carrier concentration, $\tau = 1/B\Delta n$, where $B(T) \propto T^{-3/2}$. In the meantime, one

can separate the total radiative lifetime from the nonradiative lifetime for a temperature range by measuring both time-decays and PL intensities. This technique is given in Appendix C. Figure 57 shows extracted radiative and nonradiative lifetime for the σ -polarization measured at $4 \mu\text{J}/\text{cm}^2$ excitation density. As can be seen from Figure 57 the radiative lifetime dominates the PL decay time at low temperatures and increases with temperature by power of 1.33 which is very close to theoretical value for bulk samples, 1.5. It should be also mentioned that that the radiative lifetime at room temperature, 26 ns, is also very consistent with value calculated for the radiative lifetime, 20 ns using the $\tau_{\text{Rad}} = 1/\text{BN}$ for the injected carrier density $\sim 10^{18} \text{ cm}^{-3}$ corresponding to σ -polarization and assuming that the radiative recombination coefficient $B = 5 \times 10^{-11} \text{ cm}^3/\text{s}$ at 300 K.

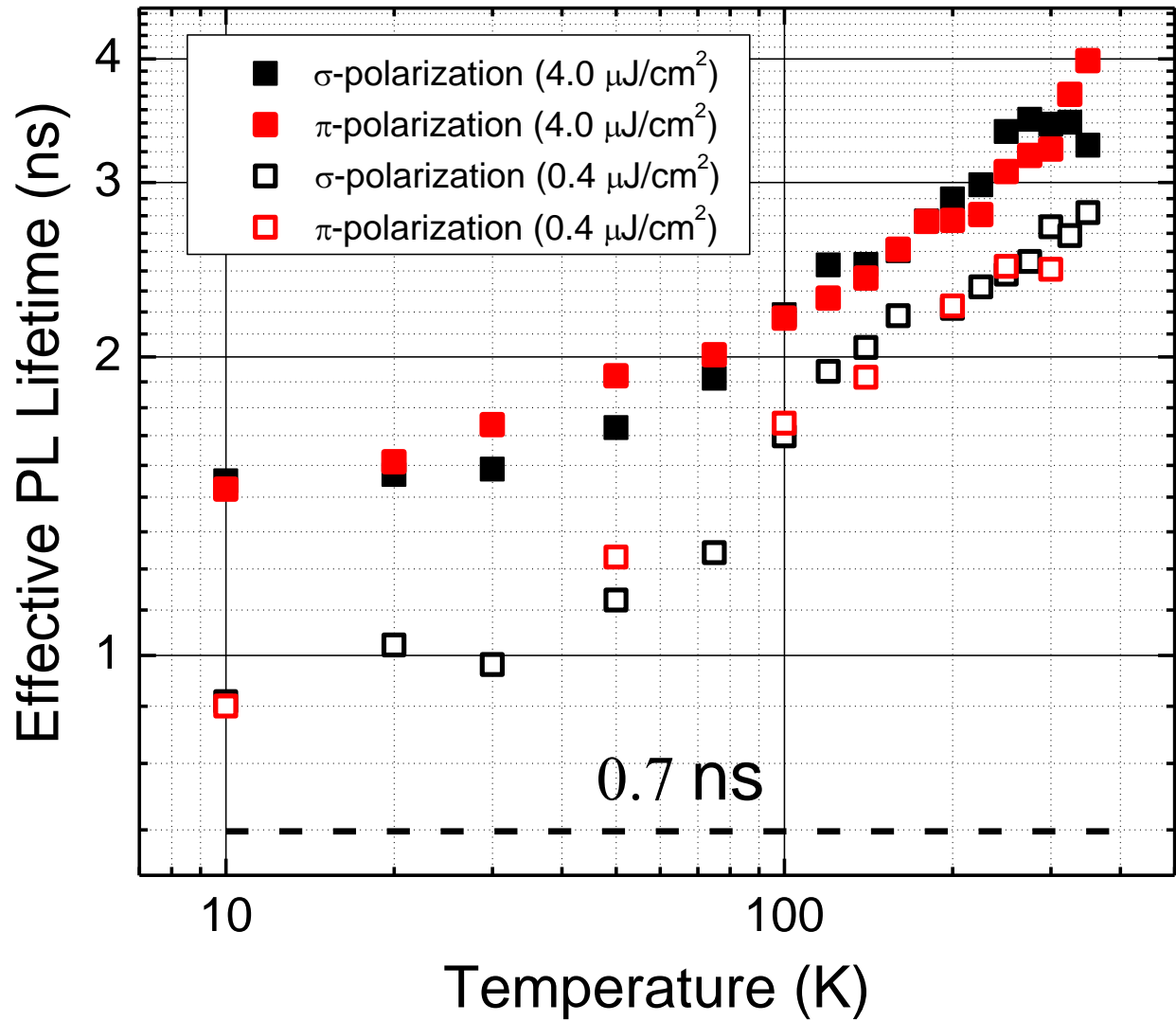


Figure 56: Effective PL lifetimes for the excitation energy densities of $4 \mu\text{J}/\text{cm}^2$ and $0.4 \mu\text{J}/\text{cm}^2$ obtained using 267 nm excitation wavelength. The solid dashed line represents the PL decay time measured at the lowest excitation density for $0.04 \mu\text{J}/\text{cm}^2$ at 15 K.

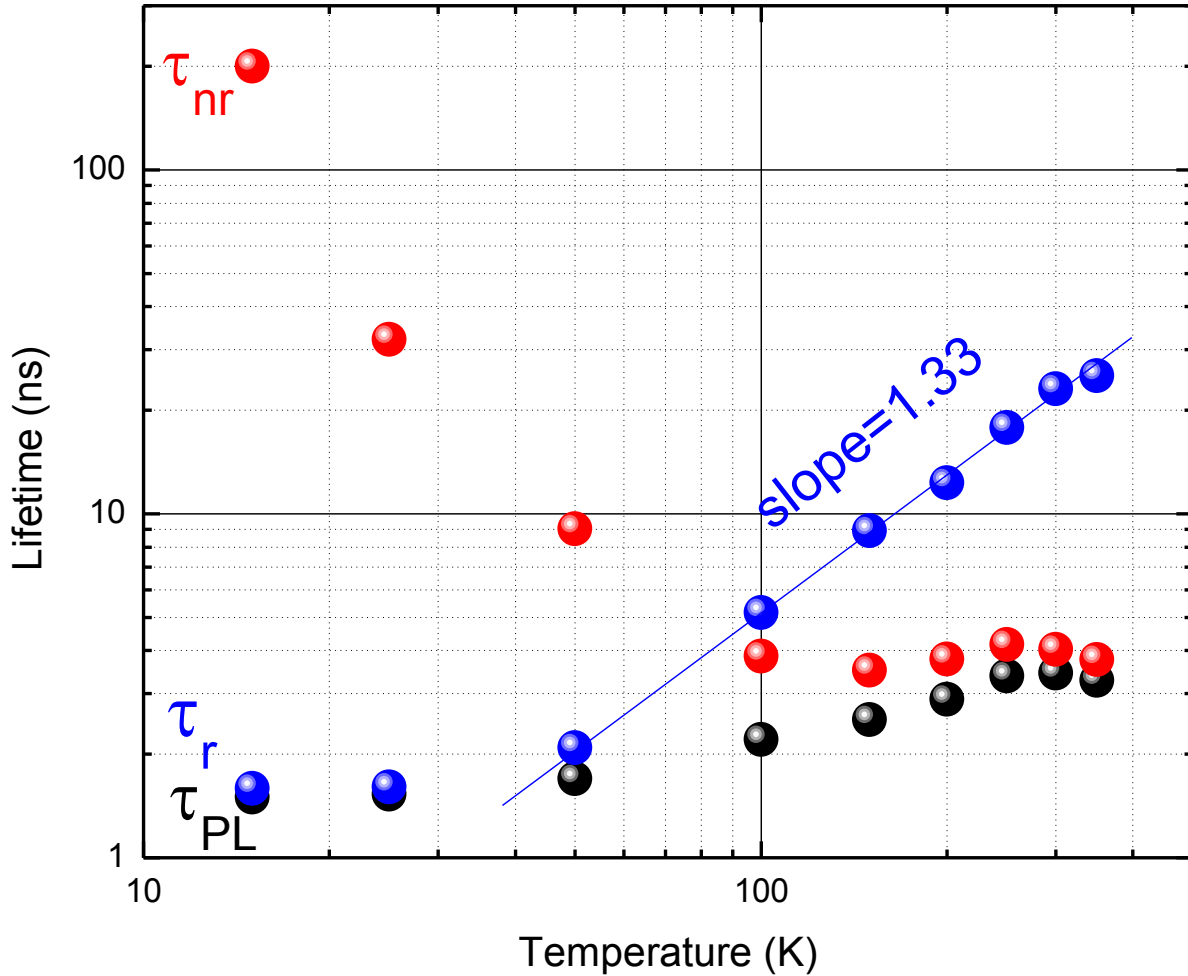


Figure 57: Temperature-dependent radiative and nonradiative PL decay times extracted from time-resolved and photoluminescence results for σ -polarization at $4 \mu\text{J}/\text{cm}^2$.

To have a complete picture on free carrier and exciton contributions to recombination, **Table 4** list the polarization degree values obtained from excitation dependent PRPL and TRPL measurements (267 nm wavelength) for σ -polarization state at low (15 K) and room (295 K) temperatures. In order to determine the polarization degree from the TRPL, the excitonic PL lifetime (0.72 ns and 0.70 ns for π - and σ -polarization, respectively) is divided by the effective PL lifetime representing the mixed exciton-free carrier system. Polarization degree further investigated by temperature dependent PRPL measurements using CW HeCd (325 nm excitation wavelength) laser for excitation density corresponding to $0.32 \text{ kW}/\text{cm}^2$ and compared with values obtained from PL

lifetimes for π - and σ -polarization states. **Figure 58** shows this comparison. The polarization degree due to the different exciton and free carriers populations is sensitive to excitation density and temperature while the excitonic PL lifetime corresponds to unity degree of polarization. The degree of polarization results obtained from TRPL data correlate very well with those from temperature dependent PRPL measurements for the excitation density 0.32 kW/cm^2 for the 325 nm excitation wavelength (**Figure 58**).

These results show that both TRPL and PRPL spectroscopy techniques can be successfully employed to identify accurately the contributions of excitons and free carriers to recombination dynamics in GaN and that the excitons in GaN may have considerable contribution to recombination at room temperature. In order to assess the information, first of all, the true excitonic PL lifetime has to be found comparing the excitation dependent PRPL and TRPL measurements at 15 K. Then, simply dividing the effective PL lifetime one can reach degree of polarization. The exact concentration of excitons and free carriers in the mixed exciton-free carrier system can only be obtained knowing the radiative recombination coefficients for both exciton and free carriers at the temperatures employed as well as additional factors affecting the PL lifetime, such as band bending and diffusion etc.

Table 4: The polarization degree values obtained from excitation dependent PRPL measurements and TRPL measurements for σ -polarization state (267 nm excitation) at 10 K and 300 K.

Excitation density ($\mu\text{J/cm}^2$)	PRPL	TRPL
10 K		
0.04	0.98	1.00
0.40	0.74	0.78
4.00	0.43	0.46
300 K		
0.04	-	-
0.40	0.30	0.27
4.00	0.22	0.21

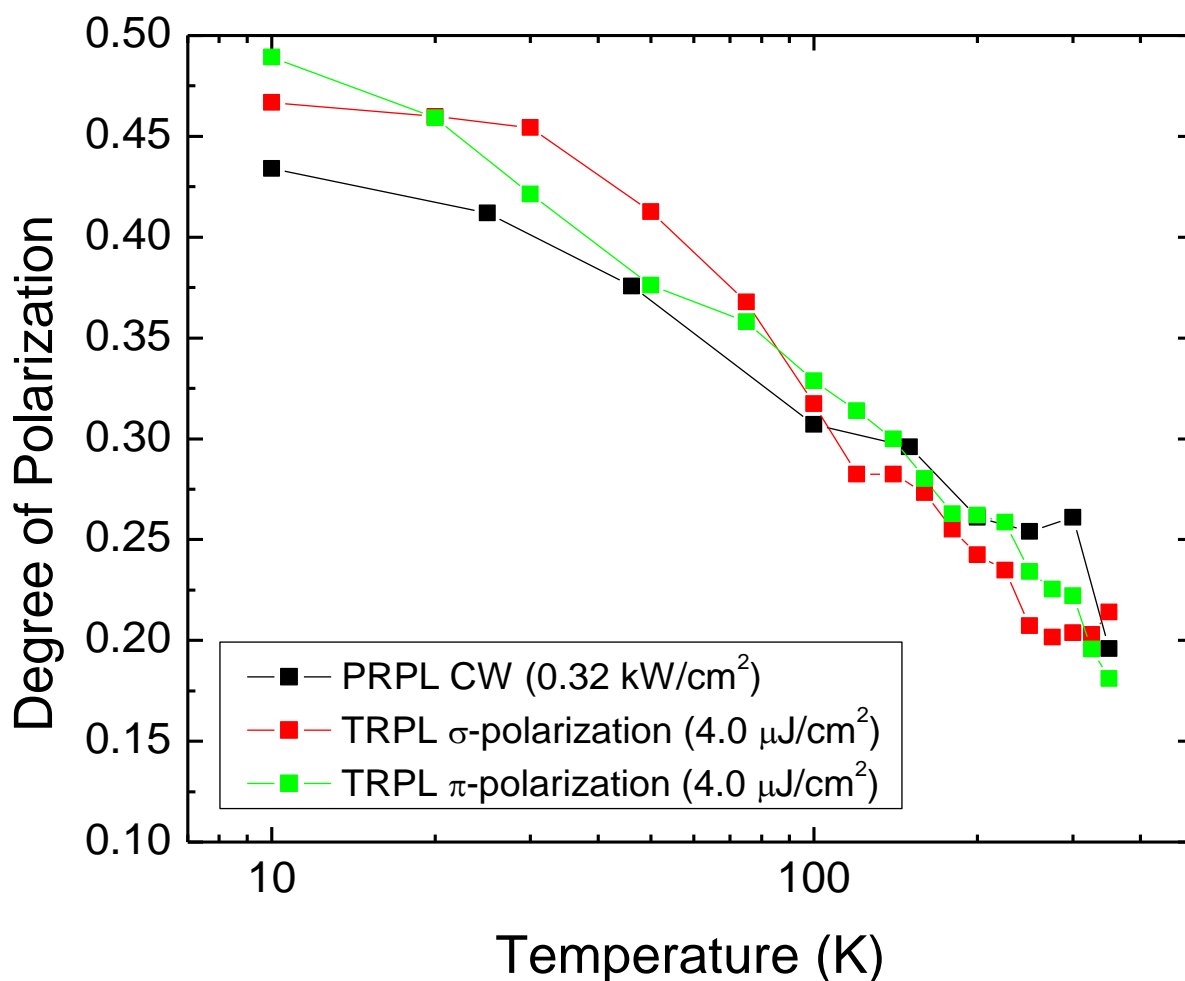


Figure 58: Temperature dependent degree of polarization obtained from PRPL and TRPL. PRPL measurements were performed under cw HeCd excitation (325 nm wavelength) and TRPL measurements were performed under frequency tripled pulsed Ti:Sapphire excitation (267 nm wavelength).

In summary, polarization- and time-resolved PL spectroscopy are used to gain insight into the contributions of excitons and free carriers to the radiative recombination at different temperatures. It is found that as the free carrier population increases by increasing both excitation density (by screening the excitons) and temperature (by dissociation of excitons) radiative recombination rate and degree of polarization are strongly affected. The effective exciton PL decay time was found to be ~ 0.7 ns in low excitation density TRPL measurements at 15 K and its ratio to the effective PL decay time was used to quantify the degree of polarization at different excitation

densities and temperatures for the mixed exciton-free carrier system. The very good agreement between the polarization degree for the PL at different temperatures obtained from both TRPL and PRPL techniques shows that knowing the polarization degree and the radiative recombination lifetime in m-plane GaN one can successfully quantify the contributions of free carriers and excitons to radiative recombination.

4.2. Carrier dynamics of nonpolar and semipolar GaN substrates

As already mentioned earlier GaN-based active regions grown on nonpolar and semipolar GaN substrates have prospective use in light emitting devices due to larger wavefunction overlap of electrons and the holes in active regions increasing the quantum efficiency compared to polar c-plane GaN. In this sense, a series of optical measurements were performed to investigate the quality of nonpolar m-plane ($1\bar{1}00$) and semipolar ($1\bar{1}01$) GaN grown on patterned Si(112) and Si(001) substrates, respectively, in MOCVD. Optical quality was characterized by steady-state micro-PL measurements using HeCd laser of 325 nm excitation wavelength. The spot size of the laser beam was nearly 2 micrometer and power density was 22 MW/cm². Carrier dynamics was studied by time-resolved photoluminescence (TRPL) performed using a frequency-tripled Ti:Sapphire laser with excitation wavelength 267 nm. A c-plane (0001) GaN film grown on a sapphire substrate under conditions optimized for high optical quality was measured as a reference. **Figure 59** compares the room temperature PL spectra from the c-plane GaN film on sapphire, nonpolar m-plane ($1\bar{1}00$) and semipolar ($1\bar{1}01$) GaN layers. One can see that PL intensity of ($1\bar{1}01$)-oriented GaN is comparable to that of the c-plane layer grown on sapphire. The PL intensity of nonpolar GaN layer is rather weak, which can be explained by the fact that the layer

was grown under low pressure and low ammonia flow rate which favors carbon incorporation and deteriorates radiative recombination efficiency.

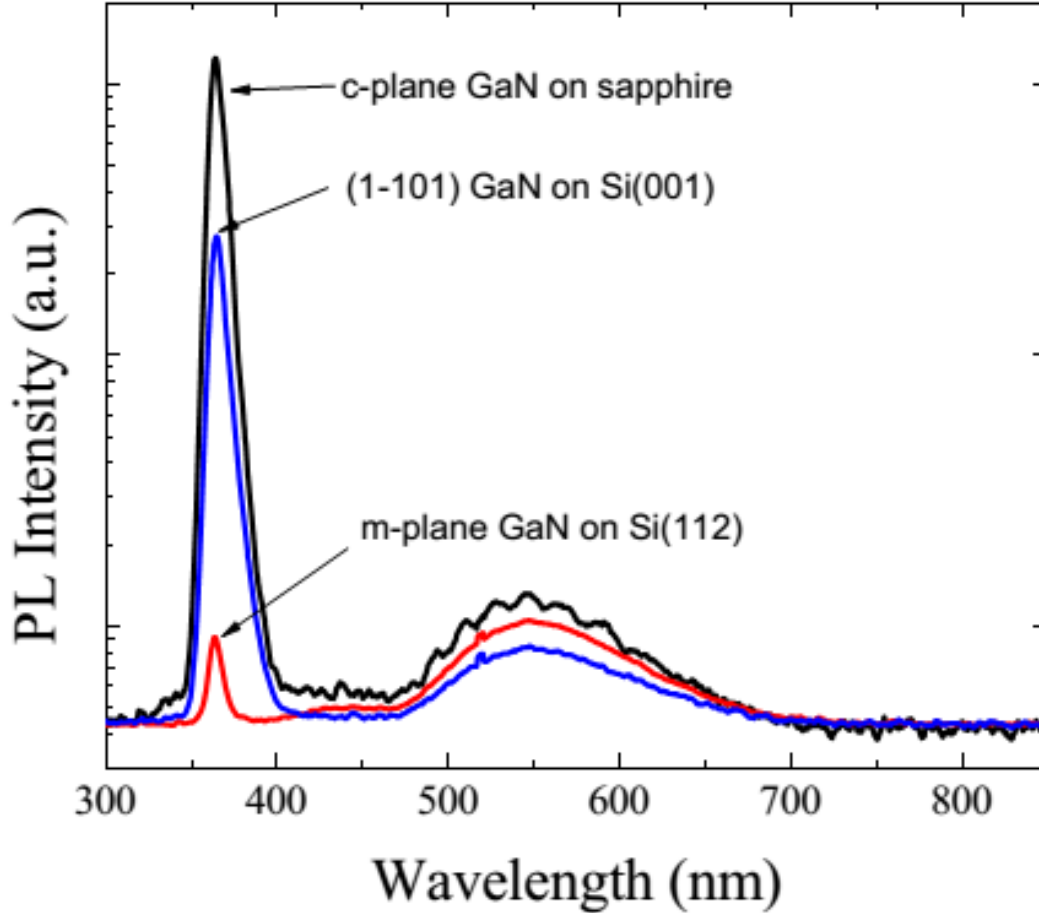


Figure 59: Steady-state room-temperature PL spectra of c-plane GaN films grown on sapphire and (1 100) m-plane and (1101)-oriented GaN layers grown on the Si patterned substrates.

Normalized TRPL data were fit using a biexponential decay function $A_1e^{-t/\tau_1} + A_2e^{-t/\tau_2}$, where A_1 and A_2 are the amplitudes of the slow and fast decay components with representative time constant τ_1 and τ_2 , respectively. **Figure 60** compares the PL transients for c-plane GaN on sapphire and $(1\bar{1}01)$ GaN on Si(001) obtained at an excitation density of 0.09 kW/cm², and **Table 5** lists the fitting parameters for c-plane and $(1\bar{1}01)$ GaN layers. As can be seen from Table 3, the fast and slow decay time constants τ_1 and τ_2 for the two samples are very

similar; however, the amplitude ratio A_1/A_2 varies significantly. The four times smaller A_1/A_2 value observed at an excitation density of 0.90 W/cm^2 , for the $(1\bar{1}01)$ -oriented GaN layer is indicative of a larger proportion of nonradiative centers in the $(1\bar{1}01)$ GaN layer as compared to the c-plane GaN, as the fast decaying component is representative of the nonradiative decay. These results are consistent with the more intense steady state PL observed from the c-GaN layer, as shown in **Figure 59**. As can be seen from **Table 5**, changing the injected power density has little effect on the time constants, whereas the fraction A_1/A_2 increases nearly 2 times for both samples with an order of reduction in the excitation density. This excitation density dependence may be indicative of enhanced carrier-carrier scattering at higher optical injection density. TRPL decays measured for m-plane GaN are within the system resolution ($\sim 30 \text{ ps}$); and therefore, are not presented here, but show that the optical quality of the photo-excited top portions of these m-plane layers need to be improved significantly.

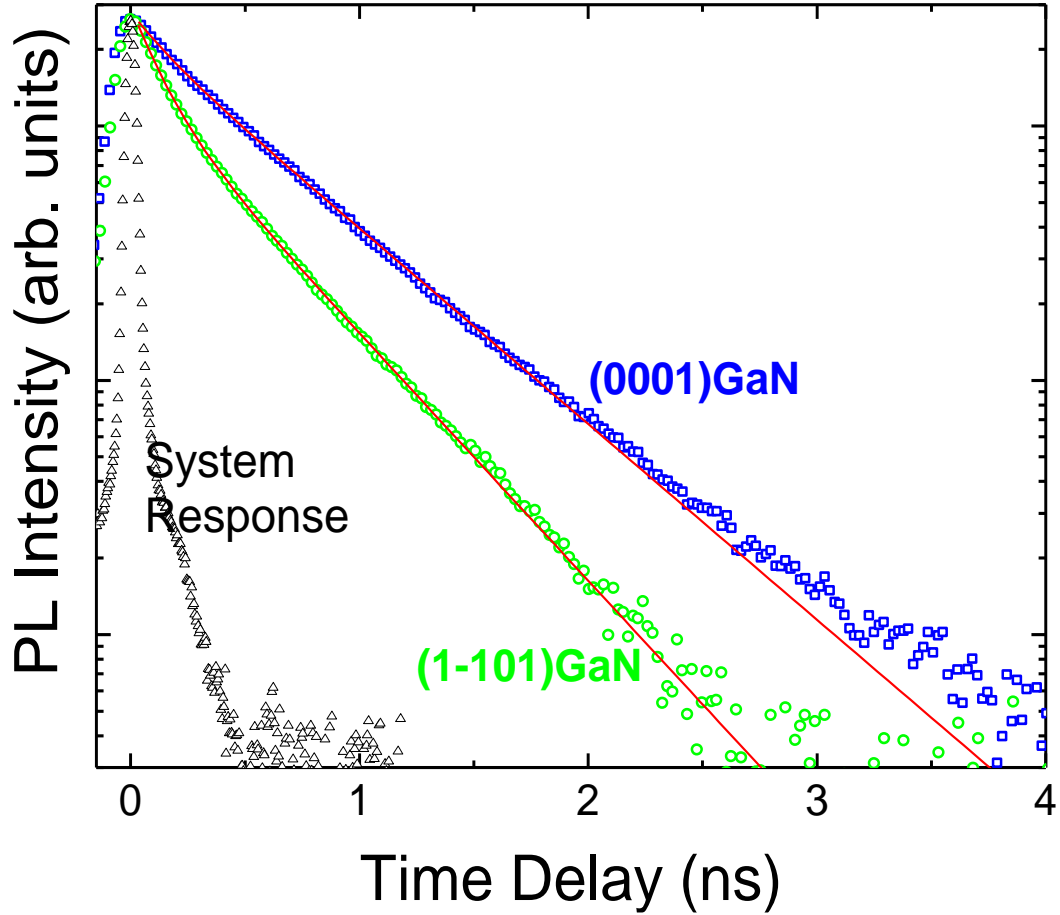


Figure 60: Normalized room-temperature TRPL intensity for c-plane GaN on sapphire and $(1\bar{1}01)$ oriented GaN on Si measured at an excitation density of 0.09 kW/cm^2 . System response is also shown. The red solid lines represent biexponential fits to the data.

Table 5: Biexponential decay parameters for the room temperature TRPL intensity from c-plane GaN on sapphire and $(1\bar{1}01)$ -plane GaN on Si at two different power levels.

Sample	Power Density (kW/cm^2)	τ_1 (ns)	τ_2 (ns)	A_1/A_2
(0001) GaN on Sapphire	0.90	0.58	0.11	2.26
	0.09	0.56	0.15	4.78
$(1\bar{1}01)$ GaN on Si	0.90	0.50	0.12	0.53
	0.09	0.45	0.12	0.94

Since the optical quality of semipolar $(1\bar{1}01)$ GaN was found to be comparable to c-plane GaN layers, additional semipolar $(1\bar{1}01)$ GaN layers were grown on patterned Si(001) substrates in MOCVD with coalesced and noncoalesced geometries, and optical properties were further investigated using PL and TRPL techniques. Si(001) substrates offcut by 7° toward the Si<110> direction were patterned to form grooves of either 3 or 10 μm width, from here and on referred to as the narrow- or wide-groove patterns, respectively, separated by 3 μm terraces. The wide groove pattern (3 μm x 10 μm) did not allow physical contact of the growing GaN stripe with the opposing Si(111) facet, whereas the narrow groove pattern (3 μm x 3 μm) promoted such physical contact and results in a fully coalesced layer. The cross-sectional SEM images are shown in Figure 61. For simplicity, the part of the GaN stripe adjacent to the \bar{c} -wing will hereafter be referred to as \bar{c} -side; and the remaining part, as +c-side, as indicated in Figure 61.

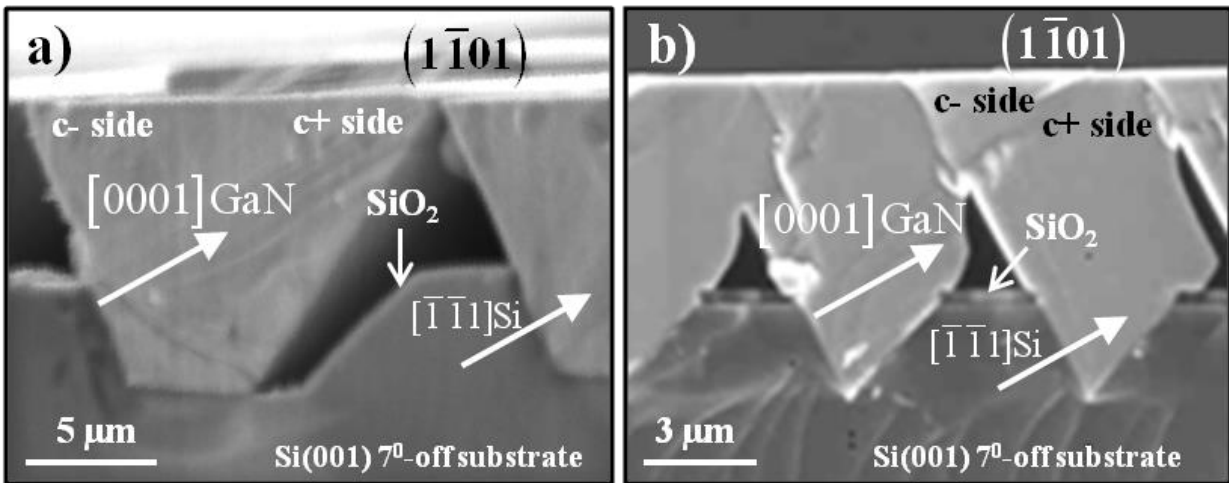


Figure 61: Cross-sectional SEM images for (a) wide- and (b) narrow-groove pattern $(1\bar{1}01)$ GaN samples.

Figure 62 shows PL transients for the coalesced and non-coalesced $(1\bar{1}01)$ GaN layers. For reference, Figure 62 displays also the data for a c-plane GaN on sapphire template and a c-plane GaN layer grown on the state-of-art GaN templates using in situ epitaxial lateral overgrowth (ELO)

with a SiN_x nano-network mask that blocks dislocation propagation (referred to as nano-ELO layer).⁸⁰ The normalized TRPL data were fit by using the bi-exponential decay function. The slow decay component, representative of the radiative recombination, for the non-coalesced layer is as long as 1.50 ns, which is substantially longer than that for the conventional c-plane GaN layer on sapphire (0.62 ns) and even longer than that of the state-of-the-art nano-ELO GaN layer (1.16 ns). This long slow decay constant is indicative of high optical quality of the noncoalesced layer and lower density of extended and point defects compared to coalesced layer. Note that slow decay component for the coalesced layer is substantially shorter (0.20 ns). This must be primarily due to higher dislocation density in addition to point and extended defects present in the coalesced layers.

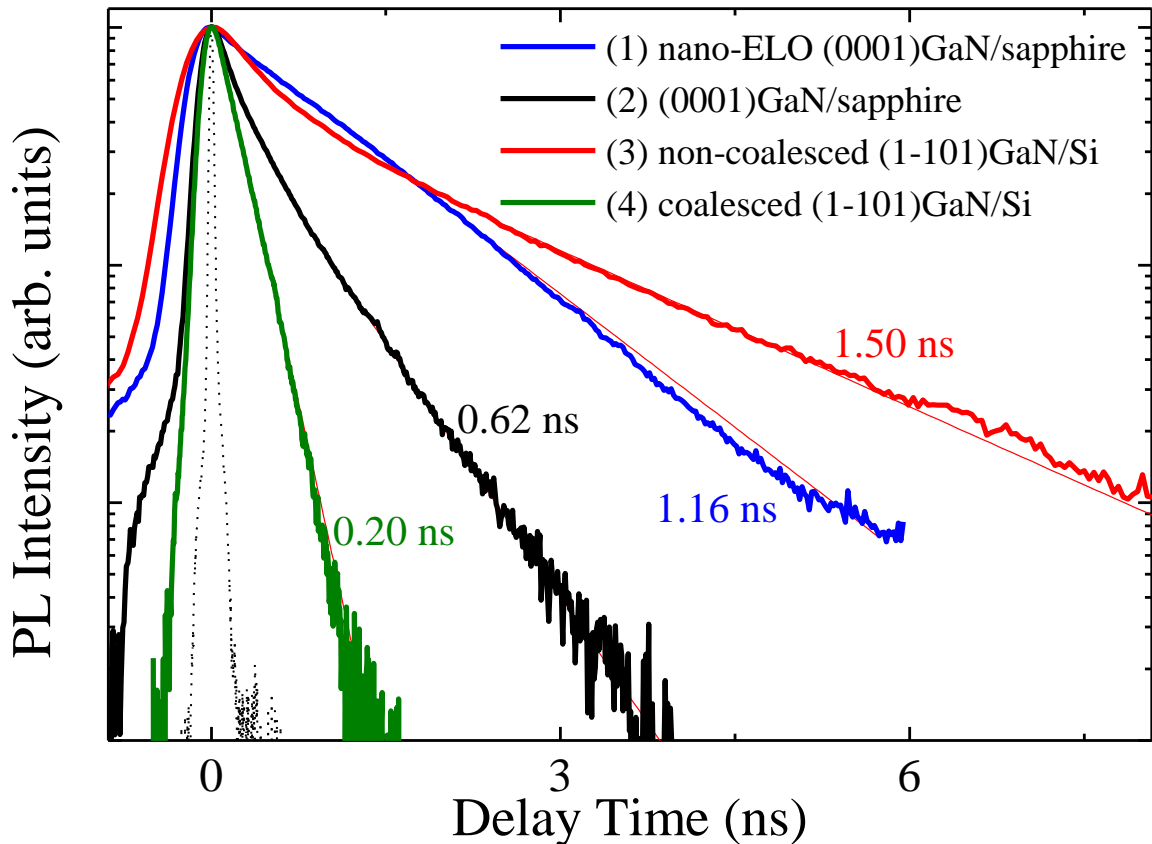


Figure 62: Room-temperature TRPL results for the semipolar and polar GaN samples for the excitation density of 0.32 kW/cm². Numbers indicate values of slow decay component τ_2 . Dashed curve represents the system response of the streak camera.

Figure 63(a) and (b) show room-temperature excitation density dependent TRPL for the c-plane nano-ELO GaN and non-coalesced semipolar (1 $\bar{1}$ 01) GaN on Si(001) layers, respectively. **Table 6** lists the biexponential fitting parameters for the PL transients for various excitation power densities. As seen from Figure 63 and **Table 6**, the fast component of the PL transients, τ_1 , representative of the nonradiative recombination, is virtually independent of the excitation power density for both polar and semipolar GaN, while the slow decay component for both layers becomes longer with increasing excitation power density. However, the amplitude ratio A_1/A_2 for the polar and semipolar GaN samples varies with the excitation power density in different ways. For the polar GaN, the amplitude ratio A_1/A_2 decreases rapidly with increasing excitation power density, and the TRPL shows virtually single-exponential decay for the highest excitation power densities of 0.25 and 0.32 kW/cm². For the semipolar film, the amplitude ratio A_1/A_2 reduces only slightly with increasing excitation power density. This implies that the polar nano-ELO GaN contains relatively low concentration of nonradiative centers (point and/or extended defects); therefore, the nonradiative and the radiative recombination channels compete at low excitations, but radiative recombination become dominant at high excitation density due to limited number of nonradiative centers. To the contrary, within the excitation area, the number of nonradiative centers in semipolar GaN is larger; therefore the nonradiative recombination channel contributes substantially even at high excitation power densities. In the case of semipolar GaN, regions with very different structural quality contribute to the TRPL signal: high quality ⁺c-wing regions, probably responsible for the long slow decay components τ_2 , together with the portions of ⁺c-wings close to the GaN/Si(111) interface by possibly high dislocation density and highly defective ⁻c-wings, contributing to nonradiative decay that is mainly responsible for the fast decay components

τ_1 . It is apparent from the data in Figure 63(b) that the contribution from defects present in the lower quality regions is essential even at high excitation densities.

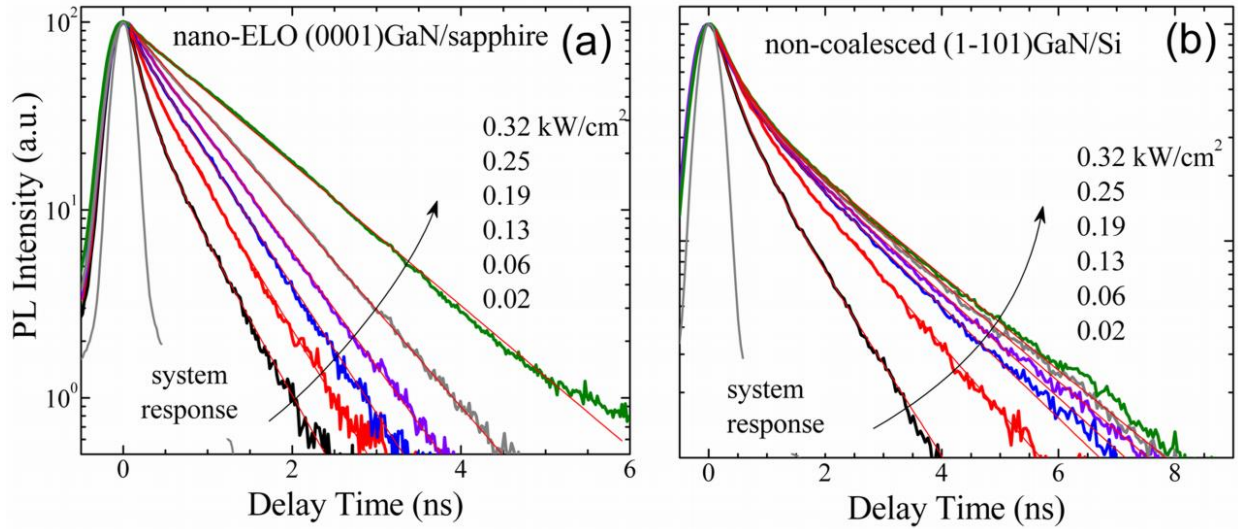


Figure 63: Excitation density dependent room-temperature TRPL for (a) polar (0001) nano-ELO GaN film on sapphire and (b) semipolar non-coalesced ($1\bar{1}01$) GaN layer on Si.

Table 6: PL decay times and amplitude ratios obtained from biexponential fits.

Excitation (kW/cm ²)	τ_1 (ns)	τ_2 (ns)	A_1/A_2	τ_1 (ns)	τ_2 (ns)	A_1/A_2
	polar <i>c</i> -plane nano-ELO film			(1-101) non-coalesced layer		
0.02	0.16	0.54	2.02	0.33	1.03	1.38
0.06	0.19	0.58	0.65	0.38	1.42	1.12
0.13	0.15	0.64	0.22	0.38	1.68	1.10
0.19	0.16	0.71	0.15	0.38	1.80	1.11
0.25	-	0.84	-	0.39	1.90	1.17
0.32	-	1.15	0	0.40	1.98	1.19

To shed light on the contribution from near-surface region and deeper portion of the layers to carrier dynamics in polar *c*-plane and semipolar ($1\bar{1}01$) GaN films, time-resolved PL with different excitation wavelengths, 267 and 353 nm have been studied. Those excitation energies

provided different excitation depths, about 50 nm and 100 nm, respectively. Figure 64 shows excitation-density dependent TRPL for non-coalesced semipolar $(1\bar{1}01)$ GaN and c-plane nano-ELO GaN layers measured at room temperature with excitation wavelengths of 267 and 353 nm. Table 7 lists the biexponential fitting parameters for the PL transients for various excitation power densities. As seen from Table 7, the longer PL decay times for the polar GaN measured with two different excitation wavelengths are comparable at the lowest excitation density of $0.08 \mu\text{J}/\text{cm}^2$, increase with rising excitation density in the very similar way, and finally reach the same value of 1.20 ns at $5.50 \mu\text{J}/\text{cm}^2$. To the contrary, the slow decay time for the semipolar sample measured with an excitation wavelength of 267 nm behaves differently with increasing excitation density as compared to the data obtained with 353 nm. At the lowest excitation density of $0.08 \mu\text{J}/\text{cm}^2$, the longer PL decay times are essentially the same for the both wavelengths; however, the decay times measured with the excitation at 353 nm increase much slower with excitation density as compared to those obtained with excitation $\lambda=267$ nm. At the highest excitation density of $5.50 \mu\text{J}/\text{cm}^2$ employed here, the longer PL decay times for $\lambda=353$ nm reaches only a half of that measured with $\lambda=267$ nm. These findings can be explained as follows. At low excitation, mainly the near-surface area contributes to the observed decay times for the both wavelength because of the strong band bending. However, when the excitation density increases, the carriers penetrate deeper into the sample volume with larger penetration depth for the longer wavelength. This implies that the near-surface layer of $(1\bar{1}01)$ GaN are relatively free from nonradiative centers (point and/or extended defects), while deeper region of the semipolar film contains more point and/or extended defects having a stronger effect on the longer PL decay time than in the case of 267 nm excitation. Most likely, free carriers generated with the longer wavelength reach the region containing threading dislocations propagating in $+c$ direction from the Si(111)/GaN interface. However, these results

indicate that the optical quality of the near-surface area of the semipolar GaN grown on the patterned Si is comparable to that of the thick polar GaN fabricated by nano-ELO technique.

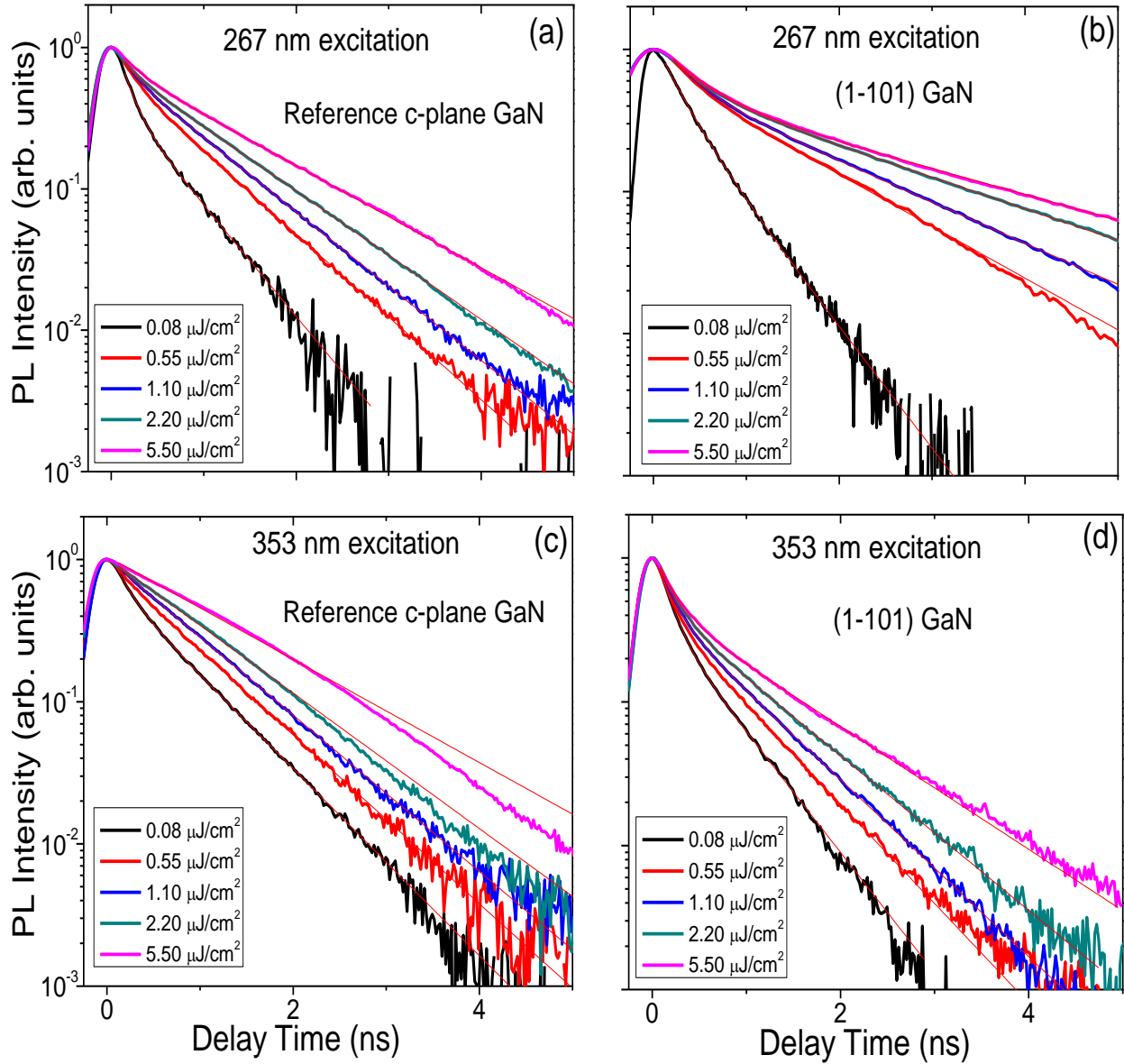


Figure 64: Excitation dependent PL transients measured at an excitation wavelength of (a) and (b) 267 and (c) and (d) 353 nm for (a) and (c) the reference c-plane nano-ELO sample and (b) and (d) the semipolar non-coalesced GaN layer. The measurements were performed at room temperature.

Table 7: Longer PL decay times obtained from the biexponential fits.

Excitation (kW/cm ²)	267 nm	353 nm	267 nm	353 nm
	polar c-plane nanoELO film		(1-101)GaN semipolar noncoalesced layer	
0.08	0.55	0.66	0.51	0.52
0.55	0.74	0.73	1.19	0.63
1.10	0.83	0.79	1.50	0.71
2.20	0.96	0.91	1.96	0.81
5.50	1.20	1.20	2.38	1.02

In summary, optical properties of polar c-plane (sapphire substrate), nonpolar m-plane, and semipolar ($1\bar{1}01$) GaN layers grown by MOCVD on patterned (001) Si substrates were examined by a series of steady-state and time-resolved PL at different excitation energy and densities. It is found that PL intensity of ($1\bar{1}01$)-oriented GaN layer is comparable to that of the c-plane layer grown on sapphire and much higher than nonpolar. The longer PL decay times for the non-coalesced ($1\bar{1}01$)-oriented GaN layer is as long as 1.50 ns, which is substantially longer than that for the conventional c-plane GaN layer on sapphire (0.62 ns) and even longer than that of the state-of-the-art nano-ELO GaN layer (1.16 ns). Excitation density dependent TRPL results revealed that the polar nano-ELO GaN contains relatively low concentration of nonradiative centers (point and/or extended defects), while the number of nonradiative centers in semipolar GaN is found larger than the nonradiative recombination channel contributes substantially at high excitation power densities. Excitation energy dependent TRPL data indicate that the near-surface of semipolar ($1\bar{1}01$) GaN layer is relatively free from nonradiative centers (point and/or extended defects), while deeper region of the film (beyond of ~ 100 nm in depth) contains more defects giving shorter decay times.

4.3. Impact of extended defects on optical properties of (1 $\bar{1}01$) GaN grown on patterned Silicon

Attainment of high quality nonpolar and semipolar GaN is a challenging task for the growers because large densities of extended defects (such as threading dislocations (TDs) and stacking faults (SFs)) emerge during the growth due to lattice mismatch between GaN and substrate materials used.^{121,122,123} Despite the observed high quantum efficiencies^{124,125} point and extended defects are still of major concern in semipolar GaN due to their negative impact on optical quality.^{109,110} It is therefore important to understand the effects introduced by defects observing their influence. Steady-state and time-resolved photoluminescence (PL) techniques, combined with microPL, in addition to polarization-resolved photoluminescence, were used at low and room temperatures to investigate effects of defects in semipolar (1 $\bar{1}01$) GaN layers.

Semipolar (1 $\bar{1}01$) GaN layers were grown on patterned Si substrates by metal-organic chemical vapor deposition (MOCVD) using trimethylgallium (TMGa) and NH₃ as sources of Ga and N with mass flow rates of 8 sccm and 3500 sccm, respectively, at a chamber pressure of 200 Torr and a temperature of 1040°C. Si(001) substrate with an offcut by 7° toward the Si<110> direction were patterned to form grooves of 10 μm width separated by 3 μm terraces. The patterning procedure and initiation of GaN growth on the Si(111) facets exposed within the grooves have been described elsewhere.¹²⁶ Time- and polarization-resolved photoluminescence (TRPL and PRPL) were measured at 15 K and 295 K to investigate the optical quality and effects of defects on carrier dynamics and polarization. Frequency-tripled Ti:Sapphire laser excitation (267 nm) with a pulse width of 150 fs was used as the excitation source for these measurements. The pattern (3 μm x 10 μm) for the semipolar GaN is chosen to prevent the coalescence of the growing wings. Furthermore, this pattern does not allow physical contact of the growing GaN

stripe with the opposing Si(111) facet. For simplicity, the part of the GaN stripe adjacent to the c-wing will hereafter be referred to as \bar{c} -side; and the remaining part, as c^+ -side, as indicated in cross-sectional SEM image in Figure 65. In order to analyze the optical quality, photoluminescence from the semipolar GaN was collected at low (15 K) and room temperatures (295 K). Figure 66(a) and (b) show the steady-state PL spectra measured at 15 K and 295 K and the internal quantum efficiency (IQE), respectively. The 3.416 eV and 3.336 eV peaks of the 25 K spectrum in **Figure 66(a)** are associated with BSFs and prismatic stacking faults (PSFs), respectively.¹²⁷ The presence of a high density of defects is evident from the rapid decrease of the IQE from the assumed 100% at 15 K to 4% at 100 K and to 1% at room temperature.

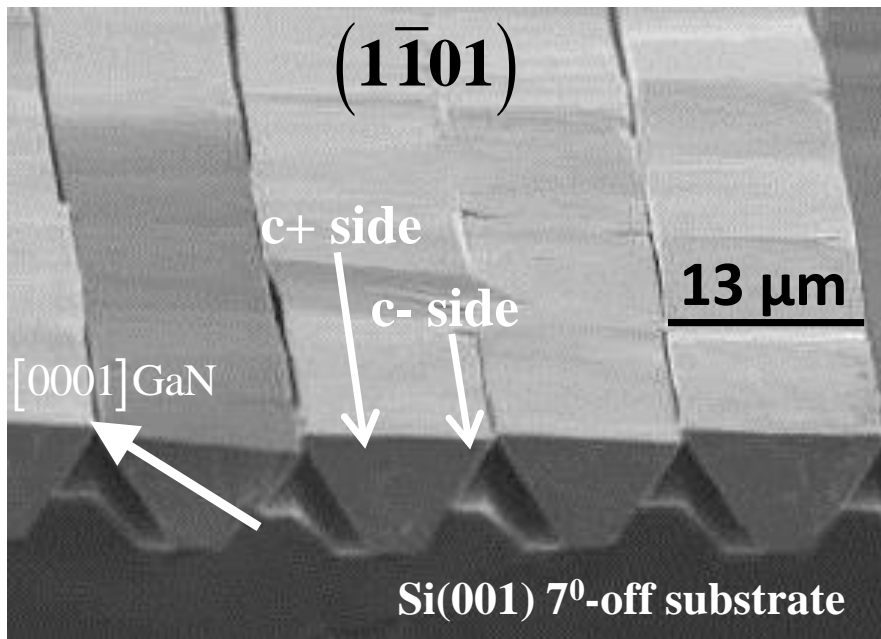


Figure 65: Cross-sectional SEM image of the semipolar $(1\bar{1}01)$ GaN layers.

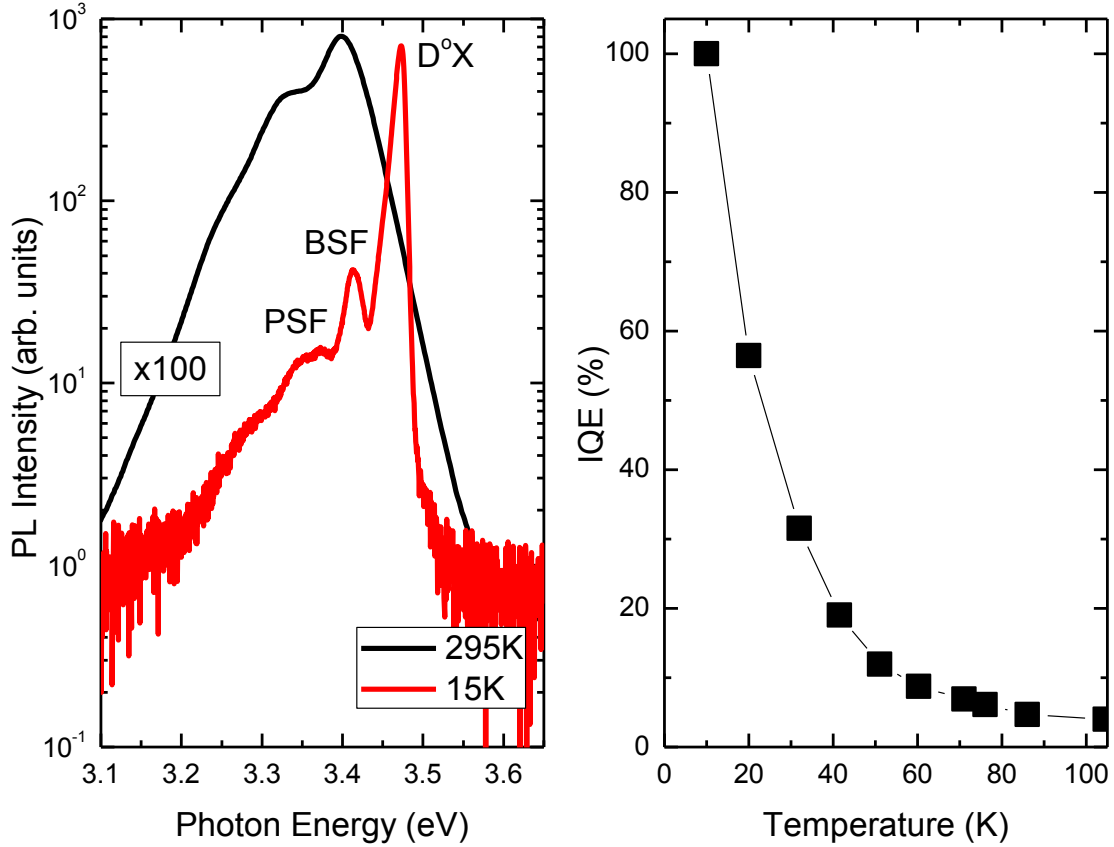


Figure 66: (a) Near bandedge steady-state PL spectra at 25K and 295K (D^0X , BSF and PSF are marked in 15 K PL spectra) and (b) temperature-dependent IQE for the semipolar layer.

In order to explore the optical behavior of the stacking faults in detail, peak positions of the donor bound exciton and basal plane stacking fault emission with respect to temperature were evaluated in large area steady-state PL measurements. Figure 67 shows temperature-dependent PL spectra from 15 to 115 K, where the BSF line vanishes. The change of the peak energy positions for donor bound exciton and BSF lines by varying temperature are illustrated in the inset of Figure 67 obtained by deconvolution of the spectra. Varshni's empirical formula, $E(T) = E(0) - \alpha T^2 / (T + \beta)$, was used to fit the temperature dependence of the donor bound exciton line, providing $E(0) = 3.473$ eV, $\alpha = 0.9$ meV/K and $\beta = \sim 800$ K. These values are in very good agreement with those in the literature except for $E(0)$, which is 5 meV red shifted from the

reported 3.478 eV value for polar GaN. This red-shift in PL suggests that the semipolar layers are relaxed.

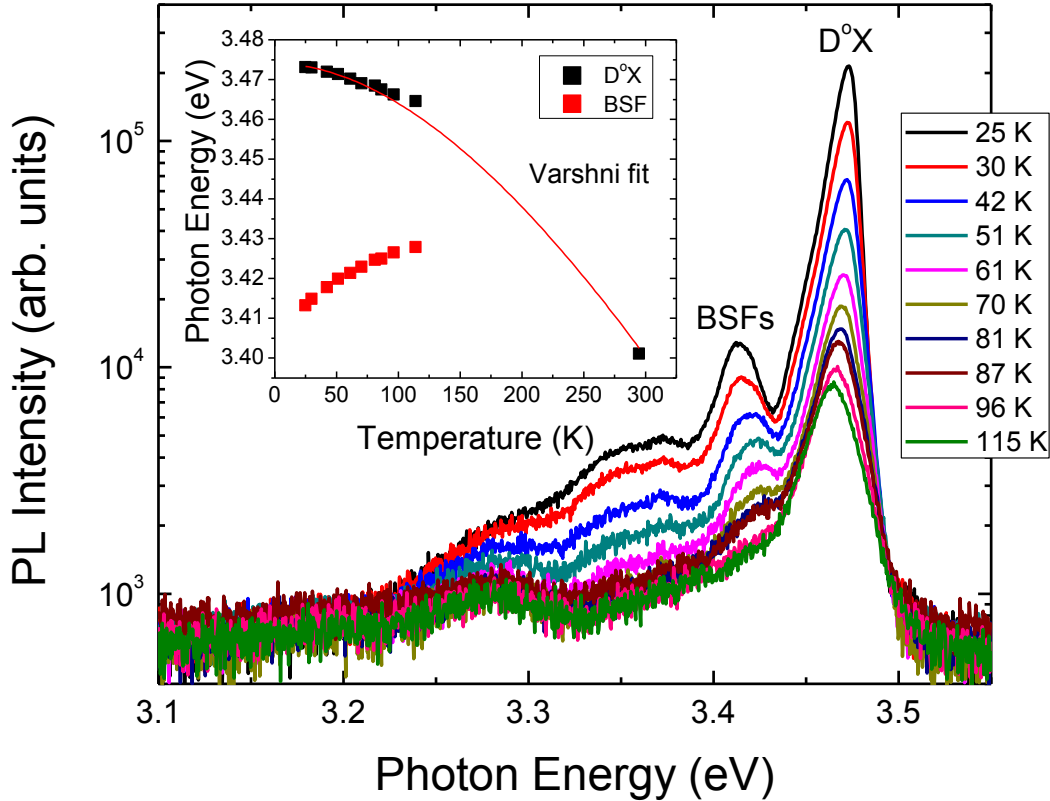


Figure 67: Temperature-dependent PL spectra between 25 and 115 K. Inset shows energy positions for the D^0X and BSF lines with respect to temperature.

Figure 68(a) and (b) show PL transients measured from ^+c and ^-c -wings of $(1\bar{1}01)$ GaN/Si structures in 2 ns and 10 ns time windows at room temperature, respectively. The PL transients exhibit biexponential decays. However, the fast decay component representing nonradiative recombination has substantially larger contribution for the ^-c -wings, while the PL transients measured on the ^+c -wing are dominated by the slow decay component. It is also worth noting that the time constant of the fast decay component (0.11 ns) is shorter for the ^-c -wing as compared to 0.21 ns for the ^+c -wing. This finding is in good agreement with the room temperature NSOM measurements, which will be given in Chapter 7, indicating weak optical emission from the ^-c -

wings due to the presence of high density of nonradiative centers associated with dislocations and stacking faults. The slow decay constants (1.70 ns) corresponding to radiative recombination were found to be similar for the \bar{c} - and ^+c -wings.

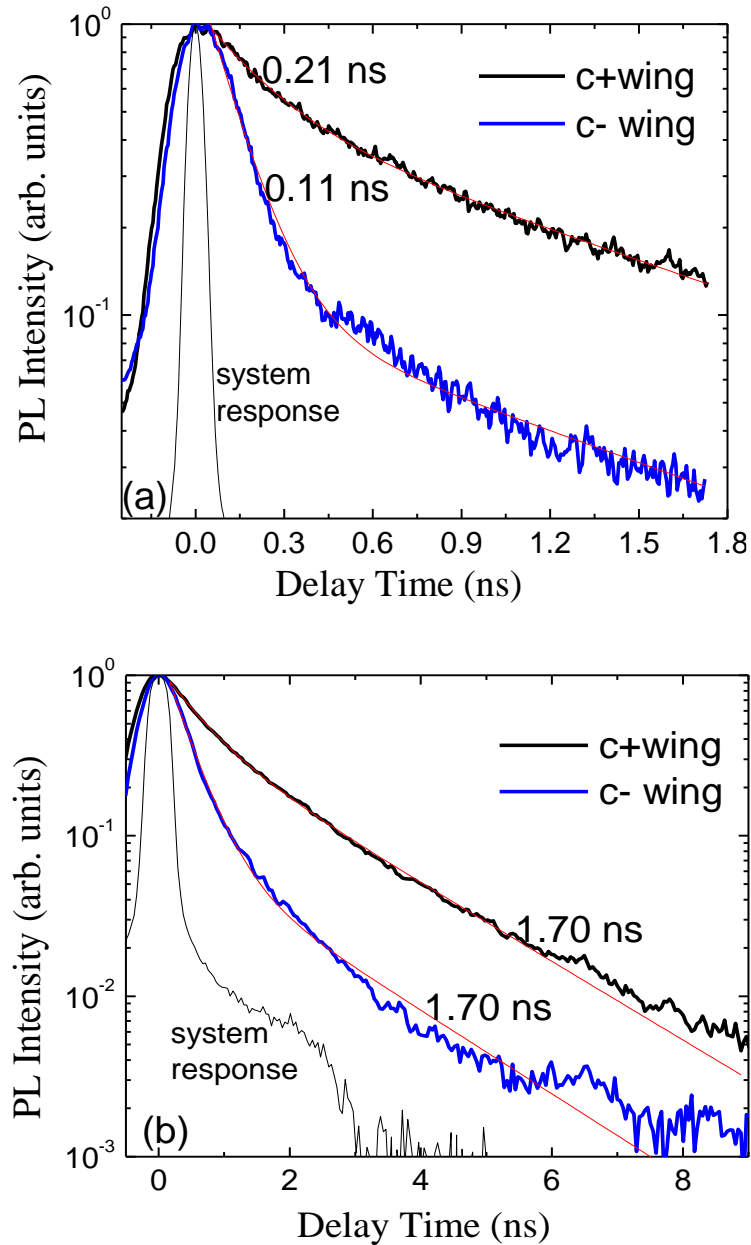


Figure 68. PL transients for NBE peak measured on ^+c - and \bar{c} -wings of $(1\bar{1}01)$ GaN/Si. Red curves represent biexponential fits. The PL decay was measured at room temperature with excitation wavelength of 355 nm: (a) 2 ns and (b) 10 ns time windows.

In order to better understand the effect of defects on the recombination dynamics, low temperature (15 K) excitation power dependent TRPL measurements were performed for the semipolar GaN sample. As shown in Figure 69, PL transients for BSF and PSF related emission lines showed no dependence on the excitation power density within the range employed (5 - 420 W/cm²). On the other hand, D⁰X emission exhibited a much faster and excitation power dependent PL decay (0.13 ns at 5 W/cm² and 0.22 ns at 420 W/cm²). Among the stacking faults, higher PL intensity and faster decay times for BSFs compared to PSFs indicate that BSFs have larger density and larger contribution to recombination dynamics. It should also be noted that the recombination dynamics are affected not only by stacking faults, but by point defects and threading dislocations as well. High optical quality of the (1 $\bar{1}$ 01) GaN layers and degradation of optical quality by coalescence were revealed by room temperature TRPL in a previous study.¹²⁶ PL decay time for the semipolar GaN sample at 295 K was 2 ns longer than that for the state-of-the-art nano-ELO GaN layer (1.16 ns).¹²⁶

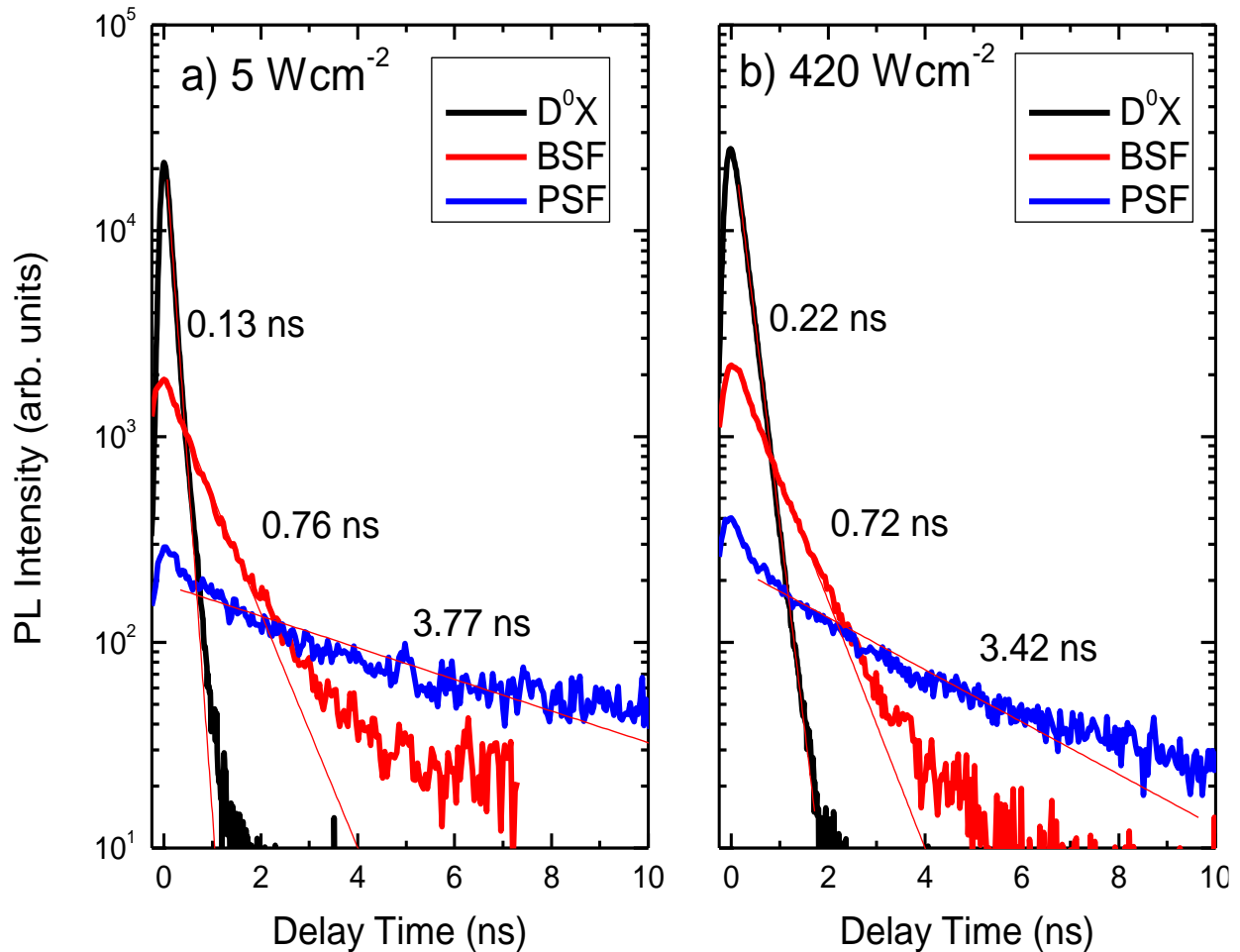


Figure 69. PL transients for D^0X , BSF, and PSF spectral lines measured at 15 K and excitation densities of (a) 5 W/cm^2 and (b) 420 W/cm^2 .

Another important feature of semipolar GaN is that the emission normal to the sample plane is polarized as the optical axis has a nonzero in-plane projection. Effects of stacking faults on optical quality can therefore be further investigated through polarization resolved PL. Figure 70 shows the normalized polarization resolved PL intensity on a polar plot for band edge and BSF emission peaks of the semipolar GaN sample. The directions of the excitation light wave vector k and the electric field E with respect to selected crystallographic directions in a wurtzite structure are indicated on the same figure. A linear polarization analyzer was used to resolve the polarization state of the PL with the light collected always normal to the sample. 90° for the polarizer

corresponds to polarization parallel to the $(1\bar{1}\bar{2}0)$ GaN axis. The polarization degree of PL is defined as $\rho = (I_h - I_l) / (I_h + I_l)$, where I_h and I_l represent the highest and the lowest PL intensities resolved, respectively. Polarization degree for the D^0X line at 15 K is 0.35, almost twice the room temperature value of 0.19 for the near band-edge emission. At 15 K, the polarization degree for the BSF peak is 0.22, lower than that for the D^0X line. It is therefore clear that polarization diminishes when carriers recombine through the BSFs, which can be considered as one of the negative effects of stacking faults on the optical quality of the semipolar $(1\bar{1}01)$ GaN layers.

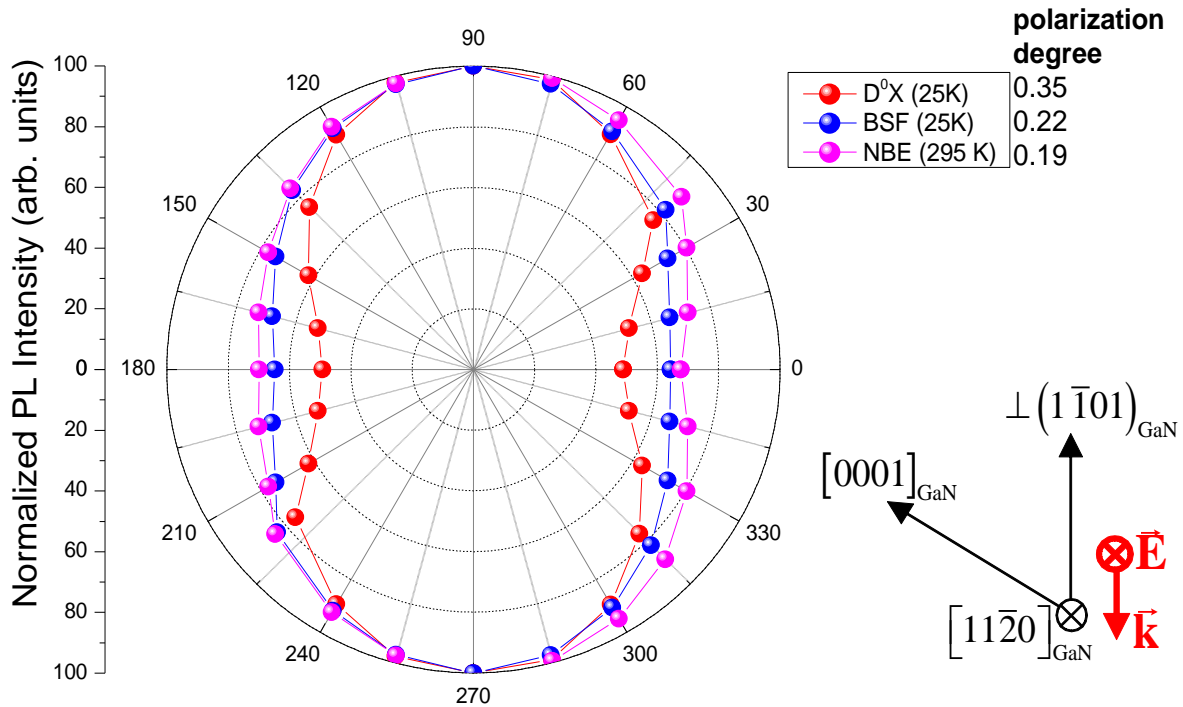


Figure 70: Normalized polarization resolved PL intensity for the semipolar GaN sample for 420 W/cm^2 for the spectral lines D^0X , BSF at low temperature and NBE at room temperature.

In summary, semipolar $(1\bar{1}01)$ GaN template grown on a Si(001) 7° offcut substrate with $3 \mu\text{m} \times 10 \mu\text{m}$ groove patterns was studied by steady-state PL, time- and polarization-resolved PL. Steady-state PL and TRPL results indicated that inferior optical quality for the \bar{c} -wings of

semipolar GaN layers compared to ^+c -wings originate not only from the point defects and threading dislocations, but also from basal plane and prismatic stacking faults. It is found in TRPL results that fast decay component representing the nonradiative recombination has substantially larger contribution for the ^-c -wings, while the PL transients measured on the ^+c -wing are dominated by the slow decay component, mostly of radiative origin. Higher PL intensity and faster PL decay times for BSFs (0.8 ns) compared to PSFs (3.5 ns) suggest larger density and larger contribution to carrier recombination dynamics of BSFs compared to PSFs. BSF emission further exhibited lower polarization degree than the donor bound exciton at low temperatures, which is considered to be a negative effect on the optical quality of the semipolar $(1\bar{1}01)$ GaN layers as well.

4.4. Strong carrier localization in basal plane and prismatic stacking faults in semipolar $(11\bar{2}2)$ GaN

Lower crystal quality of semipolar and nonpolar GaN layers¹²⁸ still lag the efficiency behind that of the polar GaN substrates.⁴⁹ High density of extended defects, threading dislocations and stacking faults (SFs) emerge during the semipolar/nonpolar GaN growth.^{50,51} In general, stacking faults are regarded as an interrupted sequence in the stacking of closely-packed planes in the crystal, and they form on (0001) basal plane and on $(11\bar{2}0)$ prismatic planes, and develop by slip. The stacking sequence of the (0001) basal plane in wurtzite crystals is “ABABABABA...” where the letters A and B denote lattice structures consisting of atomic Ga-N bilayers. SFs are terminated by free surfaces or heteroepitaxial interfaces, and propagated by dislocations within a crystal. I_1 -type basal plane stacking fault (BSF) is the most common type observed in semipolar/nonpolar GaN templates which has the lowest formation energy compared to I_2 -, I_3 - and E-type basal plane stacking faults. It has recently been shown that the formation of I_1 type BSF is

related to the coalescence of islands in the Volmer-Weber growth mode.¹²⁹ Prismatic stacking fault (PSF)¹³⁰ is attached to basal plane stacking faults and propagates in the growth direction. The sequential termination of the prismatic faults along the growth direction usually folds into basal-plane faults. The atomic configuration of the PSFs are reported in high-resolution transmission electron studies.⁵⁴ PSFs always connect two I₁-type BSF with stair-rod dislocations forming at the intersections, leading to step-like features and loops.

The alignment of the conduction and valence bands is very important for heterostructures. The conduction and valence band offsets have opposite signs for type-I alignment, whereas type-II alignment has band offsets in the same sign. Both electrons and holes are confined in the QW for a type-I alignment, while the holes reside outside the QW for a type-II alignment. In a wurtzite GaN, BSFs are regarded as thin zinc-blend segments in wurtzite matrix, which are under high uniaxial compressive strain shifting the conduction band to form a potential well in the band diagram.⁵³ At low temperatures, the free exciton emission is found to be placed at 3.478 eV¹³¹ and at 3.276 eV¹³² for a wurtzite and zinc blende GaN, respectively. The wurtzite phase creates a significant spontaneous polarization compared to zinc blend phase, which leads to electric fields across the SF quantum wells. In literature, the debate still continues about whether the band alignment for wurtzite/zinc blende heterostructure in GaN is type-I¹³³ or type-II.¹³⁴ In a recent study, Lähnemann et al compared a type-I band alignment with a type-II band alignment taking the polarization field of 2.5 MVcm⁻¹ ($P_{sp} = -0.022 \text{ Cm}^{-2}$) into account for up to 3 nm thick cubic segments (BSFs) in a wurtzite GaN matrix. They carried out the calculations using an effective-mass approach through a self-consistent solution of the one-dimensional Poisson and Schrodinger equations.⁵² They observed small differences in transition energies with increasing cubic segment thickness in the wurtzite matrix confirming similar behavior of a type-I band alignment and a type-

II alignment due to the fact that the spontaneous polarization dominates the emission energy change, and holes are confined in the triangular valence bands regardless of the actual band alignment.⁵² Microscopic mechanisms governing the stacking fault formation as well as their effects on the optical quality are not well understood yet. There are limited studies in literature regarding recombination dynamics associated with basal plane stacking faults^{135,136,137,138} and no studies are dedicated to recombination dynamics associated with the prismatic stacking faults. Therefore, comprehensive studies for the defects in nonpolar and semipolar nitrides and their influence on the optical quality through the recombination dynamics are required to be investigated in order to improve the material quality and thus device performance for optoelectronic device applications.

Various optical techniques such as photoluminescence (PL), time- and polarization-resolved PL (TRPL and PRPL) were used to investigate the influence of stacking faults on optical performance and recombination dynamics of semipolar (11 $\bar{2}2$) GaN. Semipolar (11 $\bar{2}2$) GaN layer was grown on m-plane sapphire substrate using metal-organic chemical vapor deposition (MOCVD) using trimethylgallium (TMGa) and NH₃ as Ga and N sources, respectively. First, 500 nm thick GaN layer was grown on m-plane sapphire substrate with mass flow rates of 17 sccm and 9 L for TMGa and NH₃, respectively, at a temperature of 1090 °C and a chamber pressure of 200 Torr. Then, a very thin noncoalesced SiN_x layer was deposited in a SiH₄ flow, followed by a 800 nm thick GaN growth at chamber pressure 200 Torr with mass flow rates of 17 sccm and 9 L for TMGa and NH₃, respectively, at a temperature of 1100 °C. The process is known as in situ nanoELO where SiN_x layer helps to improve structural quality in addition to surface morphology. **Figure 71(a)** shows the growth schematic of the sample while **Figure 71(b)** shows the crystallographic directions in wurtzite GaN. Photoluminescence measurements were performed using frequency-tripled Ti:Sapphire laser excitation (267 nm) with a pulse width of 150 fs. For

temperature dependent measurements, the sample was mounted on a closed-cycle He-cooled cryostat where emission was collected from the cryostat window using an optical fiber focused into a spectrometer. The collected PL was analyzed by a liquid nitrogen cooled charge couple device (CCD) which was connected to the spectrometer. Time-resolved photoluminescence (TRPL) was measured between a temperature range of 15 K and 295 K to investigate the effects of defects on the carrier dynamics. Hamamatsu streak camera was used in order to analyze the time-resolved data. In polarization-dependent PL measurements, a linear polarization analyzer was used to resolve the polarization state of the PL and collected signal was analyzed using CCD.

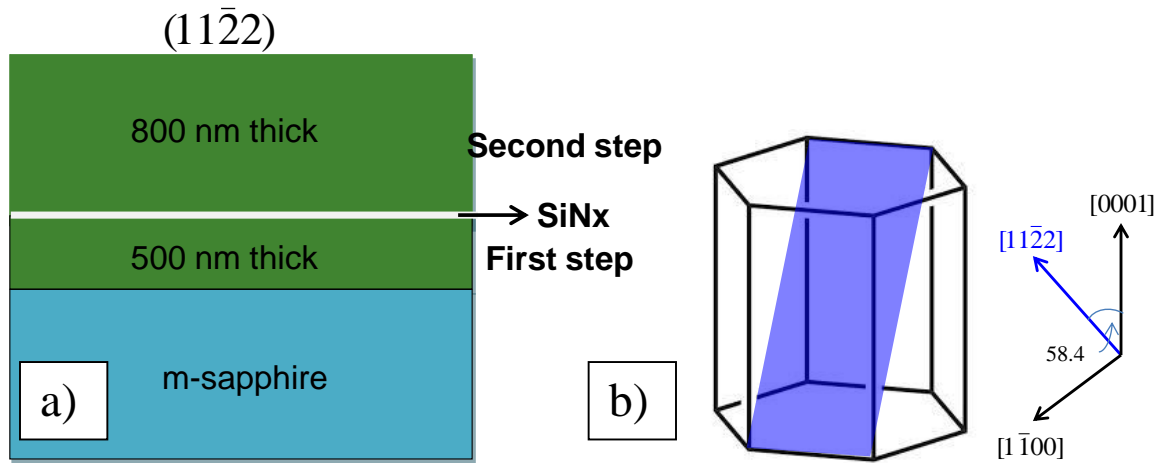


Figure 71: Schematic representation of growth procedure for $(11\bar{2}2)$ GaN (a) and Crystallographic directions in wurtzite GaN structure (b).

Only a few studies reported BSF related emission from GaN templates at room temperature.^{139,140} In these studies, BSF lines were observed to be quenching with increasing temperature and shifting together with the near band edge line. In order to explore the optical behavior of stacking faults in detail, free exciton (FX), basal plane stacking faults emission were evaluated in temperature dependent steady-state PL measurements. **Figure 72** shows PL spectra for the semipolar $(11\bar{2}2)$ GaN sample collected a set of different temperature levels (from 15 to 295 K). The transitions from the stacking faults are clearly observed at 15 K PL spectra for the

(11 $\bar{2}2$) GaN template, and indicated with different colored lines for their temporal evolution in **Figure 72**. These transitions at energies changing between 3.31 eV and 3.43 eV at 15 K. The I₁-type BSF (3.43 eV at 15 K) is found to have highest PL intensity for the given temperature range in the semipolar GaN compared to other types. Comparing the reported peak emission for the stacking faults it can be said that the stacking faults in this semipolar (11 $\bar{2}2$) GaN layer are under compressive strain which shifts their emission about 1-2 meV towards blue. The emission energies for the I₁, I₂ and E-type (or PSF) BSFs at room temperature are found to be 3.38, 3.30 and 3.24 eV, respectively, which are in a very agreement with Lähnemann et al.⁵² One should note that the BSF related emissions quenched at room temperature indicating that nonradiative recombination paths become dominant with increasing the temperature. These nonradiative recombination centers are believed to be mainly Frank and Shackley dislocations surrounding the basal plane stacking faults.

The binding energy of an electron at a basal plane stacking fault is estimated to be nearly 25 meV from a solution of one-dimensional Schrodinger equation for a square quantum well.¹⁴¹ The calculation is obtained for the case of δ -potential well approximation where the binding energy is defined as $E_e = m_e (\Delta E_c L)^2 / 2\hbar^2$. The length of the basal plane stacking fault is taken as L=1 nm and the electron effective mass as $m_e = 0.2m_0$. It is believed that the binding energy of an exciton bound to a stacking fault must be higher since the hole effective mass is much higher than a free electron's. Supporting this argument, the binding energy of a free exciton at a stacking fault is found to be 45 meV based on the theoretical calculations given in Rebane et al.¹⁴¹ According to the discussion one can say that electrons can even bind to basal plane stacking fault at room temperature in either free or excitonic forms which is very consistent with the steady-state PL results shown in **Figure 72(a)** where the BSF emission is clearly observed at room temperature.

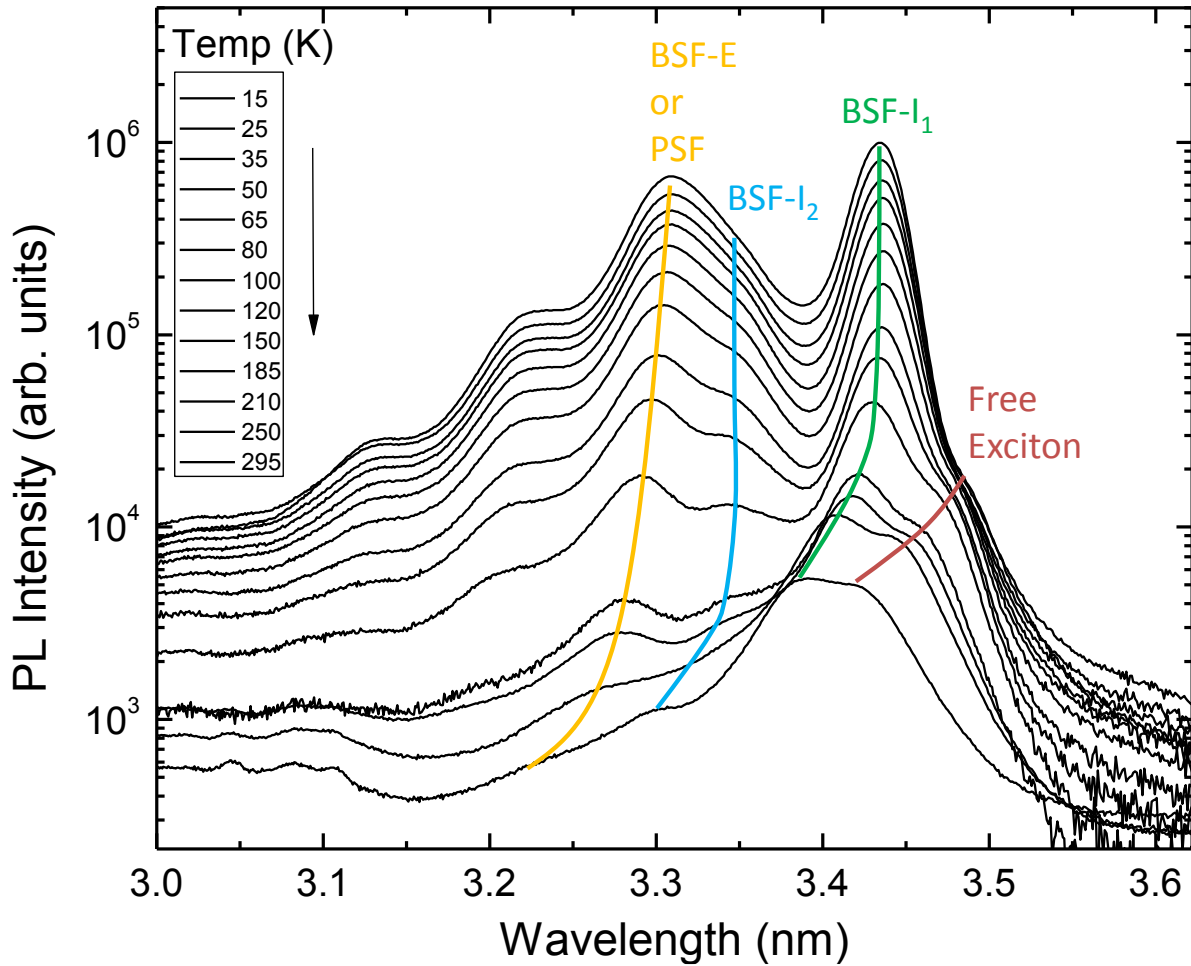


Figure 72: Temperature-dependent PL spectra for the semipolar $(11\bar{2}2)$ GaN layer.

Evaluating earlier reports, it is found that 3.31 eV emission in PL spectrum obtained at 15 K can be either from E-type basal plane stacking fault or prismatic stacking fault shows, which has PL intensities similar to I_1 -type BSF at low temperatures. Due to high density of I_1 -type BSF in the semipolar $(11\bar{2}2)$ GaN layer 3.31 eV is likely belong to PSF since PSF are always associated with I_1 -type BSF. However, transmission electron microscopy study is needed in order to say if the emission from E-type BSF or PSF. Both PL intensities for I_1 -type BSF and 3.31 eV emission show slight decrease up to 80 K following with a drastic drop as can be seen in **Figure 73(a)**. It is believed that this behavior is closely related to donors which are acting as exciton capture sides

up to 80 K. Excitons are fully delocalized from donors after 80 K (localization energy of the donors is 7 meV (~80K)).¹³⁷ PL ratio of these stacking faults showed slight increase from 15 K to 80 K (**Figure 73(b)**). However, the ratio significantly decreased by increasing the temperature above 80 K. The slight increase in the ratio up to 80 K might be due to either the carrier transfer between the stacking faults or different radiative recombination efficiency of carriers in different type of stacking faults since they have different polarization in their QW-like band gaps. Latter is supported by time-resolved PL results that will be discussed later. The fast decrease in the PL ratio after 80 K is a clear indication of which carriers has lower binding energy at 3.31 eV SF compared to I₁-type BSF. One can assume that an electron bound to a 3.31 eV SF can either bind to a basal plane stacking fault or become a free electron when the substrate temperature is increased above 80 K. However, the effect of the nonradiative centers cannot be neglected in all processes affecting intensity of all stacking fault related emissions via carrier capture. This is very plausible considering that the donors cannot prevent excitons from nonradiative recombination since excitons are fully ionized from donors at high temperature levels.

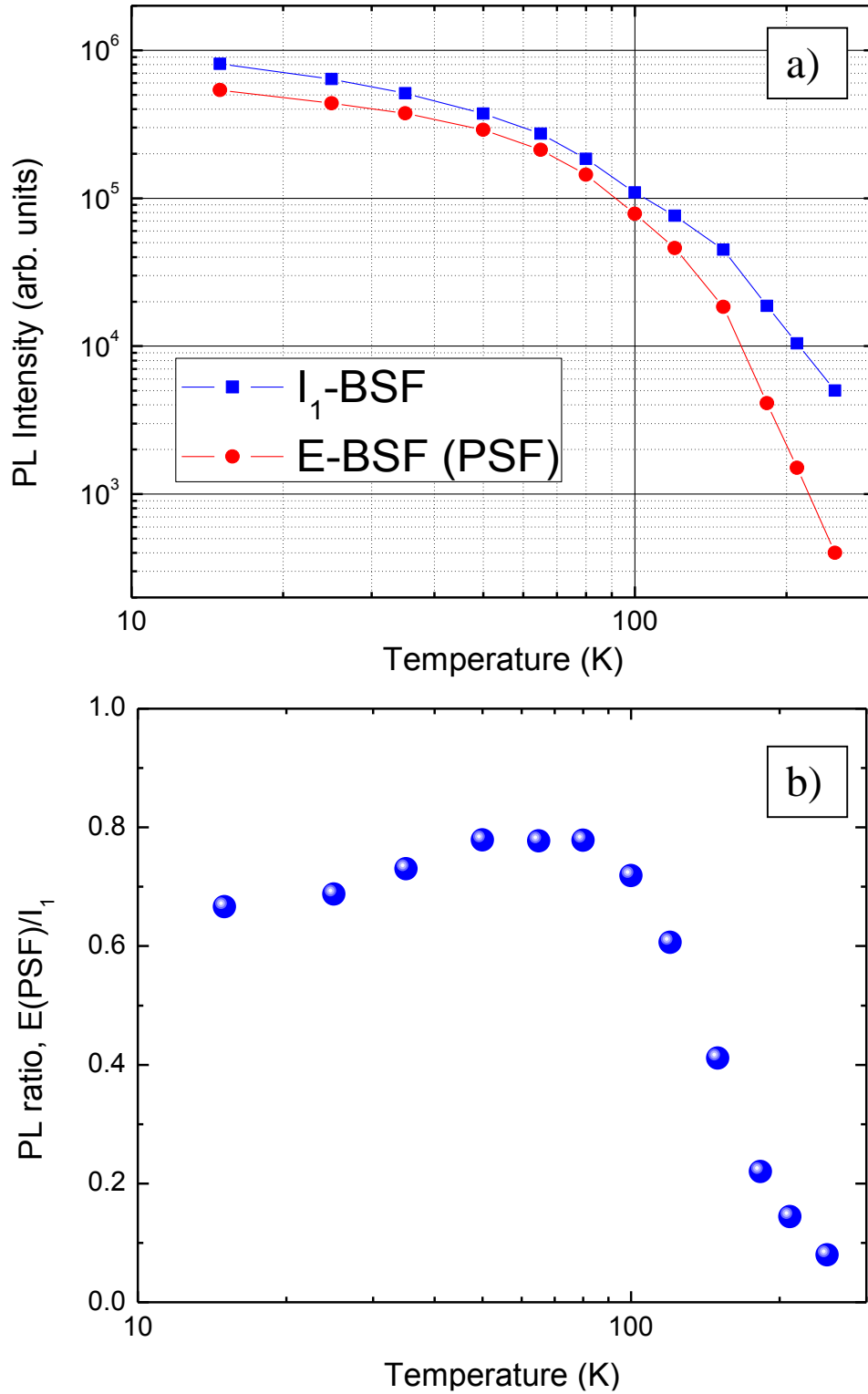


Figure 73: (a) PL intensity and (b) PL intensity ratio of 3.31 eV SF and I_1 -type BSF with respect to temperature.

Temperature dependent TRPL measurements were performed to better understand the effect of stacking faults on recombination dynamics. **Figure 74** shows PL decay times obtained from biexponential fitting of PL transients for I₁-type BSF and 3.31 eV SF related emissions. Longer decay times are taken as characteristic PL decay times since initial fast decays in transients are related to the carrier diffusion away from the surface deeper into the sample.¹⁴² Among the stacking faults, higher PL intensity and faster decay times for I₁-type BSF compared to other stacking faults indicate that I₁-type BSF has larger density and larger contribution to overall recombination dynamics. It should be also mentioned here that recombination dynamics are affected by not only stacking faults, but also point defects and threading dislocations. However, the discussion here is limited to effects of stacking faults on the recombination dynamics deduced from their temperature dependent PL decay profiles. PL decay times of both I₁-type BSF and 3.31 eV SF do not show temperature dependence up to 80 K. After 80 K, PL decay times decreased by power of ~ -2 and ~ -1 for I₁-type BSF and 3.31 eV SF, respectively. One may conclude that the carrier delocalization with respect to increasing temperature is higher in I₁-type BSF compared to 3.31 eV SF. This is consistent considering the stacking faults' energy levels where the I₁-type BSF energy level is closer to conduction band level compared to 3.31 eV SF, which makes the carriers in 3.31 eV SF to be trapped by either other basal plane stacking faults or conduction band by giving additional thermal energy. However, one should also consider the temperature effects where the probability for the dissociation of excitons into free carriers increases by increasing the temperature. It must be also taken into account that the carrier localization will be different for the free excitons and donor bound excitons in addition to free electrons. For example, when free excitons are around the vicinity of a BSF line, the probability of their capture by the BSF will be higher than that by donors. This is more effective up to 80 K since the excitons localized in donors

cannot bind to donors anymore after this temperature. Another mechanism related to electron localization in basal stacking faults was investigated by Confdir et. al.¹⁴³ They theoretically showed that presence of a donor in the vicinity of an I₁-type basal stacking fault localizes the electrons along the plane of the basal plane stacking fault. The localization gets stronger when the distance between the donor and the basal stacking fault gets closer, and reaches its maximum when the donor is placed inside the basal stacking fault.¹⁴³ Nevertheless, the most effective process for the dramatic decrease in PL decay time for both the stacking fault after 80 K is related to nonradiative recombination since increasing the temperature increases the nonradiative channels and delocalize carriers from either donors or stacking faults moving to these channels. It can be understood from above discussion that the processes associated with the carrier recombination dynamics together with stacking faults are quite complicated and it is indeed difficult to distinguish all effects one by one using optical techniques. But optical techniques give strong evidence about the dominating mechanisms on the carrier recombination dynamics when temporal evolution of PL intensity and PL decay times for the stacking faults are investigated. One may conclude that exchange of carriers between the energy levels (conduction band, donor bound, and stacking faults) takes place via carrier trapping/detrapping processes and affects the carrier dynamics in addition to nonradiative recombination centers.

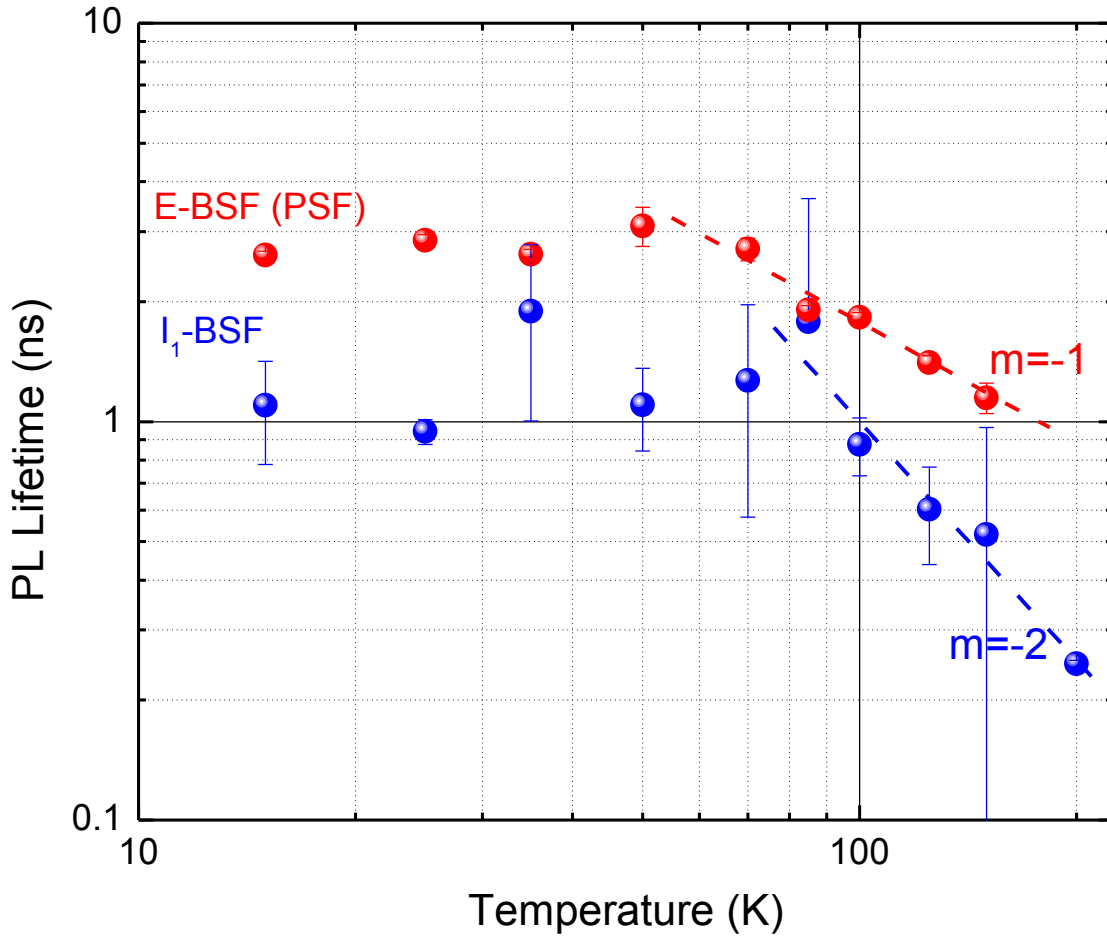


Figure 74: PL decay times for I₁-type BSF and 3.31 eV SF obtained from biexponential fits of the transients.

The temperature-dependent PL lifetimes and PL intensity ratios were used to separate the radiative and nonradiative lifetimes for both I₁-type BSF and 3.31 eV SF emissions based on the technique given in Appendix C. **Figure 75** shows extracted radiative and nonradiative lifetimes. As can be seen from **Figure 75** the radiative lifetime dominates the PL decay time at low temperatures and increases with temperature. The theoretical value for radiative decay time versus temperature is 1.5 for bulk samples, and 1 for two-dimensional structures shown in **Figure 75**. However, the slopes obtained for these stacking faults differs substantially from the theory as the stacking faults are expected to show two-dimensional character. This strongly implies that other

mechanisms are affecting the radiative recombination dynamics. The slope for 3.31 eV SF is found to be steeper compared I₁-type BSF indicating that the density of carriers, which contribute the radiative recombination, in 3.31 eV SF decreases much faster with increasing the temperature compared to I₁-type BSF. As can be seen in **Figure 75**, the radiative lifetime at 200 K is ~20 ns and ~100 ns for I₁-type BSF and 3.31 eV SF, respectively. Assuming a radiative recombination coefficient $B = 5 \times 10^{-11} \text{ cm}^3/\text{s}$ and using the $\tau_{\text{Rad}} = 1/BN$ one can find the carrier density. The carrier densities for I₁-type BSF and 3.31 eV SF at 200 K are calculated to be 10^{18} cm^{-3} and $2 \times 10^{17} \text{ cm}^{-3}$, respectively. The radiative decay times for the I₁-type BSF and 3.31 eV SF at room temperature will be ~40 ns and ~300 ns, respectively, based on the slopes. As noticed the radiative decay gets slower twice at room temperature for the I₁-type BSF compared to 200 K, while the decay slowed down three times for 3.31 eV SF. Therefore, the carrier densities at room temperature will be $5 \times 10^{17} \text{ cm}^{-3}$ and $6.6 \times 10^{16} \text{ cm}^{-3}$ for the I₁-type BSF and 3.31 eV SF, respectively. This clearly shows that the escape rate of the carriers from the 3.31 eV SF are much faster than the I₁-type BSF supporting the earlier arguments and data. The electron bound to these stacking faults can either bind to another stacking fault or become a free electron when the substrate temperature is increased. However, the effect of the nonradiative centers, surrounding the stacking faults, should not be neglected in all processes.

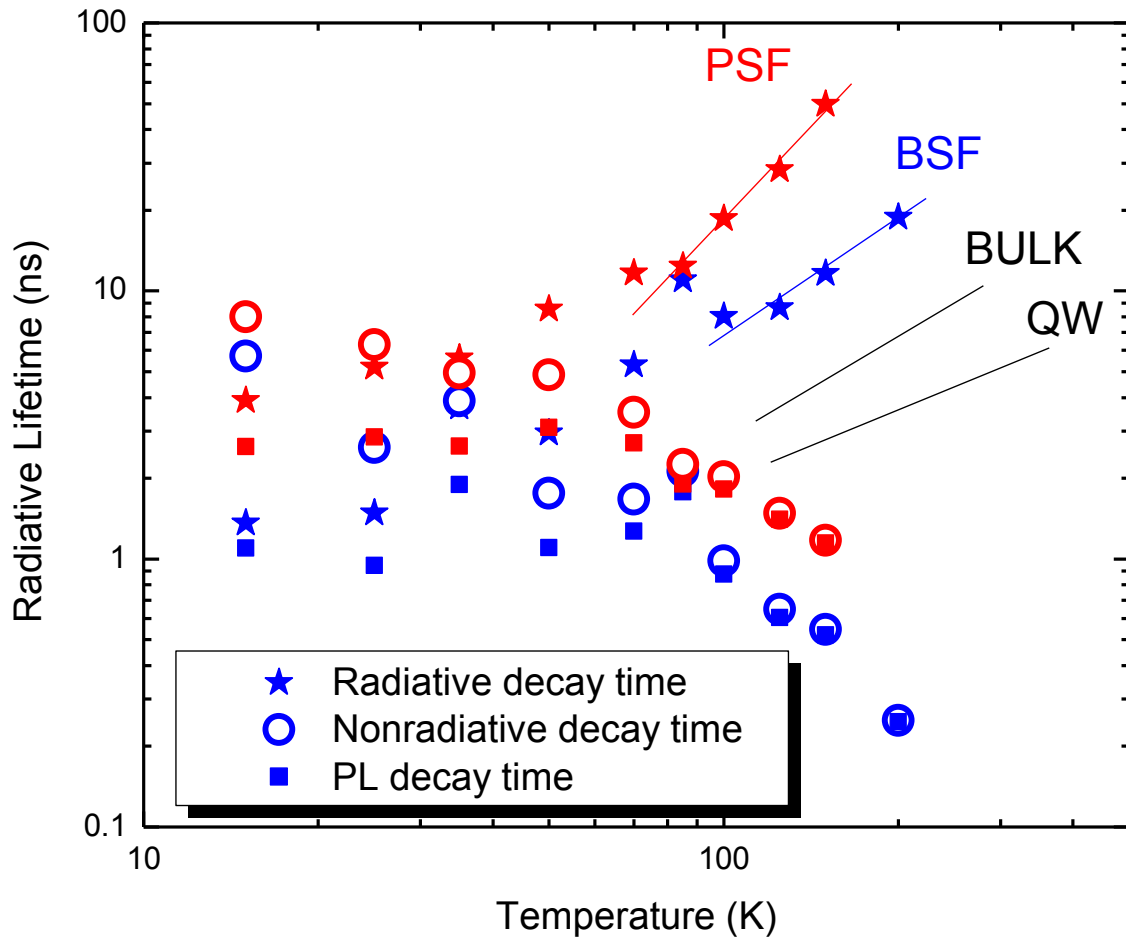


Figure 75: Temperature-dependent radiative and nonradiative decay times extracted from PL decay times. Stars, open circle and full square show radiative, nonradiative and PL decay times, respectively.

Effects of stacking faults on optical processes are further investigated using polarization-resolved PL (PRPL) technique. Figure 76 shows the normalized PL intensity on a polar plot for I_1 -type BSF and 3.31 eV SF emission of the semipolar GaN sample measured at 15 K. The directions of the excitation light wave vector k and the electric field E with respect to selected crystallographic directions in a wurtzite structure are indicated in the same figure. A linear polarization analyzer was used to resolve the polarization state of the PL with the light collected always normal to the sample. 90° for the polarizer corresponds to polarization parallel to the $[11\bar{2}0]$ GaN axis. The

degree of polarization is defined as $\rho = (I_h - I_l)/(I_h + I_l)$, where I_h and I_l represent the highest and the lowest PL intensities resolved, respectively. The degree of polarization is found to be 0.30 and 0.15 at 15 K for the I_1 -type BSF and 3.31 eV SF lines, respectively. Polarization may seem to diminish when carriers recombine through the 3.31 eV SF compared to I_1 -type BSF. However, the two times decrease in degree of polarization arises from different orientations of the stacking faults. This results is quite different from the PRPL results given in Okur et al¹⁴⁴ where the degree of polarization clearly diminishes when carriers recombine through basal plane stacking faults affecting adversely the optical quality of semipolar $(1\bar{1}01)$ GaN layers.

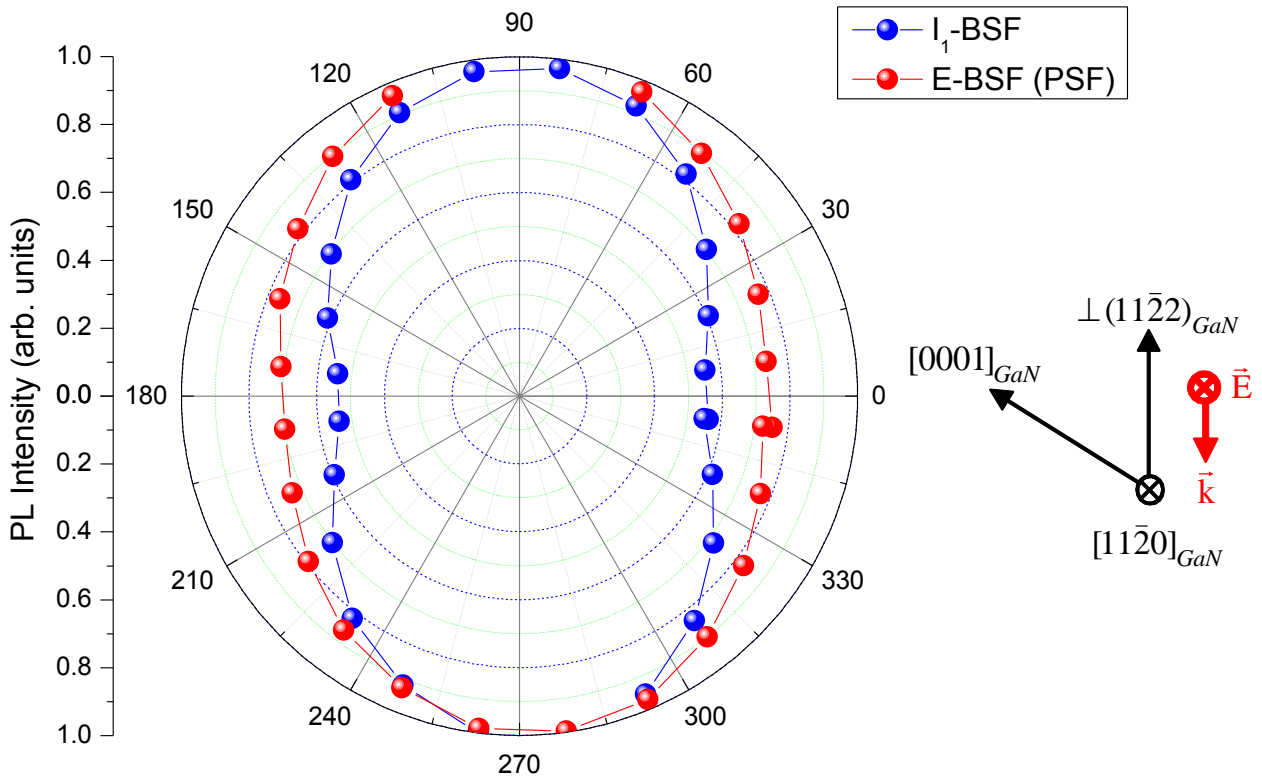


Figure 76: Normalized polarization-resolved PL intensity plot for the I_1 -type BSF and 3.31 eV SF at 15 K together with directions for the excitation light wave vector \vec{k} and the electric field \vec{E} with respect to selected crystallographic directions in the wurtzite structure.

In summary, the stacking faults in semipolar $(1\bar{1}\bar{2}2)$ GaN are investigated using various optical characterization techniques. Stacking faults are found to be actively involved in optical processes substantially influencing the carrier dynamics. In addition to nonradiative recombination centers, carrier trapping/detrapping by stacking faults and carrier transfer between stacking faults and donor energy levels are found to be among those processes affecting the carrier recombination processes at different temperature levels. Temperature dependent steady-state PL results showed that carriers are loosely localized in 3.31 eV SF compared to I_1 -type BSF. This is evidenced by strong I_1 -type BSF PL appearing at room temperature while the 3.31 eV SF PL dies around 250 K. Temperature has a strong influence on the PL intensity ratio of those two which is believed to be closely related to exciton localization energy to donors (7 meV) where excitons are fully delocalized from donors after 80 K. Higher PL intensity and much faster radiative recombination decay times of I_1 -type BSF compared to 3.31 eV SF showed that I_1 -type BSF has larger density and larger contribution to recombination dynamics.

4.5. Microscopic distribution of stacking faults in semipolar $(1\bar{1}01)$ GaN substrates revealed from spatially resolved photoluminescence

In addition, spatially and spectrally-resolved cathodoluminescence (CL) measurements at low temperature (5.8 K) and room temperature spatially-resolved near-field scanning optical microscopy (NSOM) were used to investigate the defect distributions, and consequently the optical quality of the semipolar $(1\bar{1}01)$ GaN layers whose PL and TRPL results were presented in Chapter 6. CL measurements¹⁴⁵ were conducted by Dr. Sebastian Mentzner from University of Magdeburg, Germany. For NSOM measurements, HeCd laser (325 nm wavelength) excitation through a Cr-Al coated optical fiber probe with a 100 nm. A band-pass filter (350-370 nm) was used to measure

the GaN near bandedge emission. In addition, steady-state PL measurements were performed at low and room temperature to compare the optical performance and defect related PL lines.

The NSOM and CL data for the wide-groove pattern sample are summarized in Figure 77. The atomic force microscopy (AFM) image in Figure 77(a) and the corresponding NSOM near-band edge emission (NBE) intensity map (integrated between 350-370 nm) in Figure 77(b) for the wide-groove pattern sample show that NBE originates mainly from the ^+c -sides of the stripes. Figure 77(c) shows the steady-state PL spectra for the wide- and narrow-groove pattern samples collected at 15 K and 295 K. At 15 K the intensities of the donor-bound exciton (D^0X) emission for both samples are comparable to that for a state-of-the-art polar GaN template ($\sim 10 \mu\text{m}$ thick) grown on sapphire using *in situ* epitaxial lateral overgrowth (ELO) with a SiN_x nano-network mask.⁸⁰ The relatively high BSF and PSF¹²⁷ PL intensities (3.416 eV and 3.336 eV, respectively), are indicative of a large density of stacking faults in the semipolar ($1\bar{1}01$) GaN samples. The presence of a high density of defects is also evidenced by the rapid decrease of the internal quantum efficiency (IQE) from the assumed 100% at 15 K to 4% at 100 K and 1% at room temperature for the wide-groove pattern sample. The distinction between the ^+c and ^-c -sides in terms of the defect densities and the optical quality deduced from NSOM data is confirmed from the SEM and the corresponding 5.8 K CL intensity (integrated between 350-380 nm) and CL peak wavelength images shown in Figure 77(d), (e), and (f), respectively. The CL NBE (~ 3.47 eV or ~ 357 nm) mainly originates from the ^+c -sides, and the overall emission from the ^-c -sides is significantly weaker. Additional nonradiative centers due to threading dislocations (TDs) and associated point defects are also manifested as dark regions in NSOM-PL and CL images. The dark patterns elongated normal to the stripes correspond to TDs that originate from the Si interface and reach the ($1\bar{1}01$) GaN surface mainly in the ^-c sides.

In order to further understand the distribution of TDs in the wide-groove pattern sample, cross-sectional CL measurements were performed. As seen in Figure 78(a), CL intensity diminishes at the GaN/Si interface where the growth initiates, and therefore, a high density of TDs exists. During the initial stages of growth, the TDs propagate along the ^+c -direction. However, as the growth proceeds the TDs which propagate in the vicinity of $(1\bar{1}01)$ growth fronts bend toward them under the action of image forces¹⁴⁶ as schematically shown in Figure 78(b). Gradeèaka *et al.*¹⁴⁶ demonstrated that a significant portion of the TDs bend by 90° (depending on the type of dislocation and the associated Burger's vector, intermediate bending angles of $\sim 45^\circ$ and $\sim 60^\circ$ have also been observed.^{146,147} and then propagate in the basal plane, *i.e.* in the direction perpendicular to major progressing growth front for our geometry, as illustrated in Figure 78(b). The rest of TDs propagate in the ^+c -direction perpendicular to the growing (0001) front and terminate at the lower $(1\bar{1}01)$ facets. As a result, a relatively narrow slice of the defective material (referred to here as the ^-c -side) forms adjacent to the ^-c -wing of the stripe (appearing as a dark region on the top-view and cross-sectional CL and NSOM images shown in Figure 77 and Figure 78).

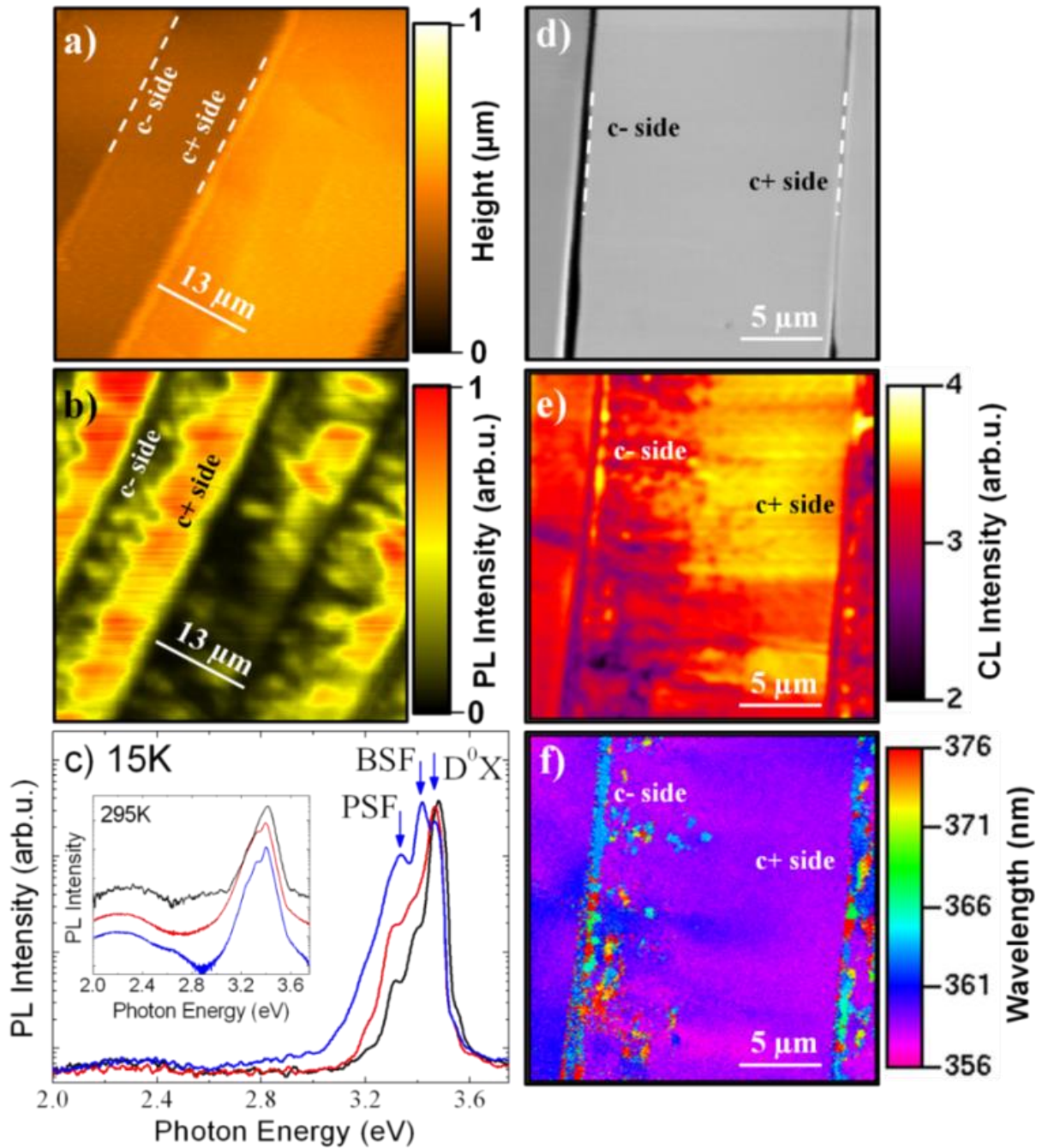


Figure 77: Top-view (a) AFM and (b) the corresponding room temperature near-band edge emission (integrated between 350-370 nm) NSOM images, (c) 15 K and room temperature PL spectra (red), (d) SEM, and the corresponding 5.8 K (e) CL intensity (integrated between 350-380 nm) and (f) CL peak wavelength images of the wide-groove pattern ($1\bar{1}01$) GaN sample. In (c) the PL spectra for the narrow-groove pattern ($1\bar{1}01$) GaN sample (blue) and a c-plane GaN reference sample (black) are also shown.

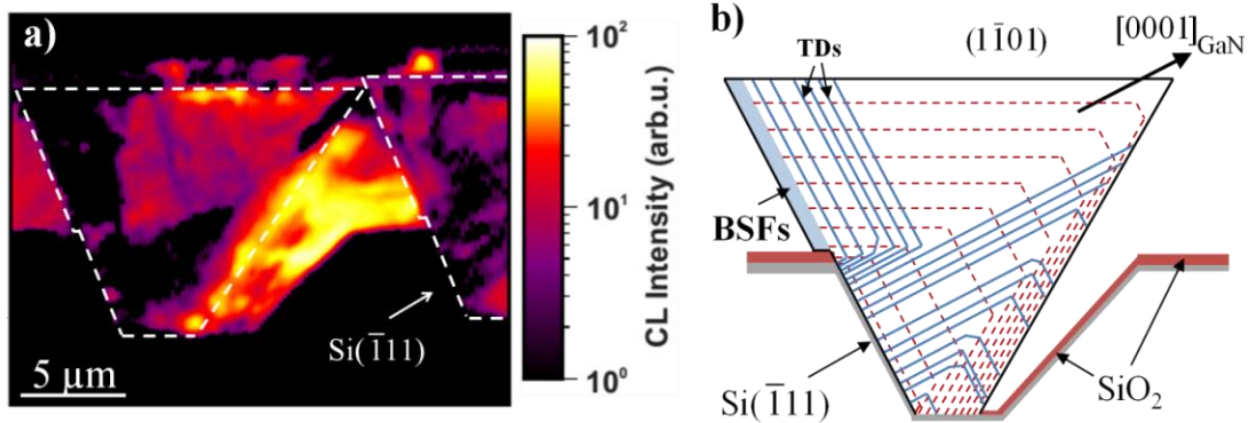


Figure 78: (a) Cross-sectional integrated CL intensity image (350–380 nm) for the wide-groove pattern sample. The dashed lines represent GaN growth boundaries. (b) Cross-sectional schematic of GaN growth from Si($\bar{1}11$) sidewall showing TD propagation (blue lines) and the growth fronts (dashed lines). Note that propagation of the bottom ($1\bar{1}01$) front is the slowest because of limited material supply.

The distribution of defects is found to be quite different in the narrow-groove pattern layer as seen in Figure 79. The BSF and PSF densities are significantly higher in the narrow-groove pattern sample compared to the wide-groove pattern sample. Moreover, the narrow-groove pattern sample exhibited nearly 30 times lower NBE at room temperature than the wide-groove pattern sample due to a significantly higher density of extended defects inclusive of threading dislocations and the associated point defects. This is why the patterning geometry caused more TDs in addition to extra BSF rows¹²⁶ formed where the growing ^+c -fronts of GaN made contact with the SiO₂ masking layer on the opposite side of the groove in the Si substrate (Figure 80).

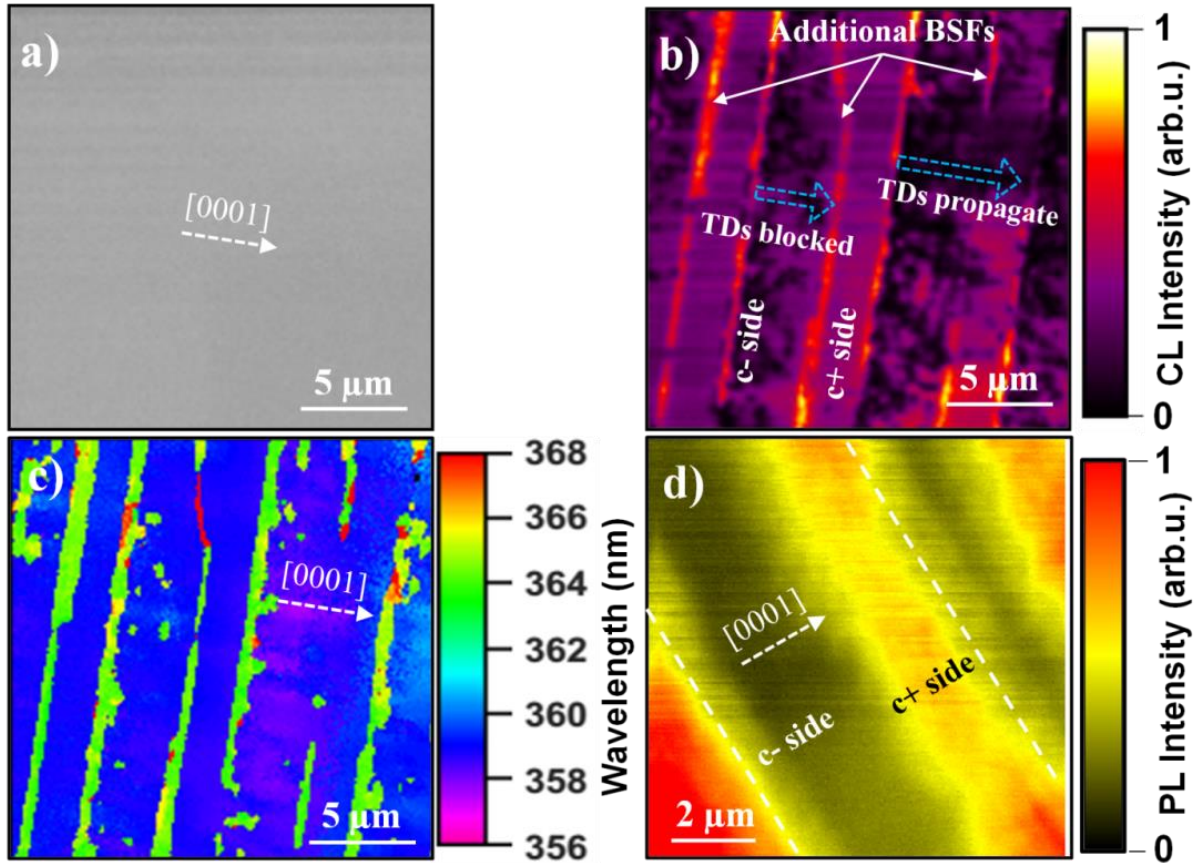


Figure 79: Plan-view (a) SEM and the corresponding 5.8 K (b) CL intensity (350–380 nm) and (c) CL peak wavelength images, and (d) room temperature near-band edge emission NSOM image of the narrow-groove pattern ($1\bar{1}01$) GaN sample. The projection of the c-axis is also indicated on the images.

The regions with high density of BSFs are manifested as high brightness rows in plan-view [Figure 79(b)] and cross-sectional [Figure 80(a)] CL intensity images. The CL peak wavelength image in Figure 79(c) confirmed the presence of BSFs (~ 364 nm emission) in the ^-c -wings as well as within the ^+c -wings. Additional BSF rows are also observable in Figure 80. Concentration of strain near the region in contact with SiO_2 and/or oxygen and/or silicon out-diffusion from SiO_2 followed by surface migration of the species have been proposed as possible causes.¹²⁶ These additional BSF rows within the ^+c -sides are found to play a critical role for the material quality in the narrow-groove pattern sample. As evident from the plan-view [Figure 79(b)] and cross-

sectional CL intensity [Figure 80(a)] and CL peak wavelength [Figure 80(b)] images, the TDs, manifested as dark spotty patterns along the c -direction, are blocked by the additional BSF rows. Some of the TDs initially propagating along the c -direction are bent into the basal plane with further growth as in the narrow-groove pattern sample, and those continuing along the c -direction are terminated if they encounter an additional BSF row. This is illustrated in the schematic of Figure 80(c). As a result of this interaction between the TDs and the BSFs, the regions between the two BSF rows are virtually free of TDs [see the bright regions between two BSF rows in Figure 79(b) and Figure 80(a)]. This is also confirmed by the NSOM NBE intensity image of Figure 79(d), which shows periodic high brightness stripes representing the high quality regions between the two BSF rows. The effective blocking of TDs by the additional BSFs in the narrow-groove pattern sample can be beneficial to further reduce the TD density without the need for a two-step selective growth technique.¹⁴⁸

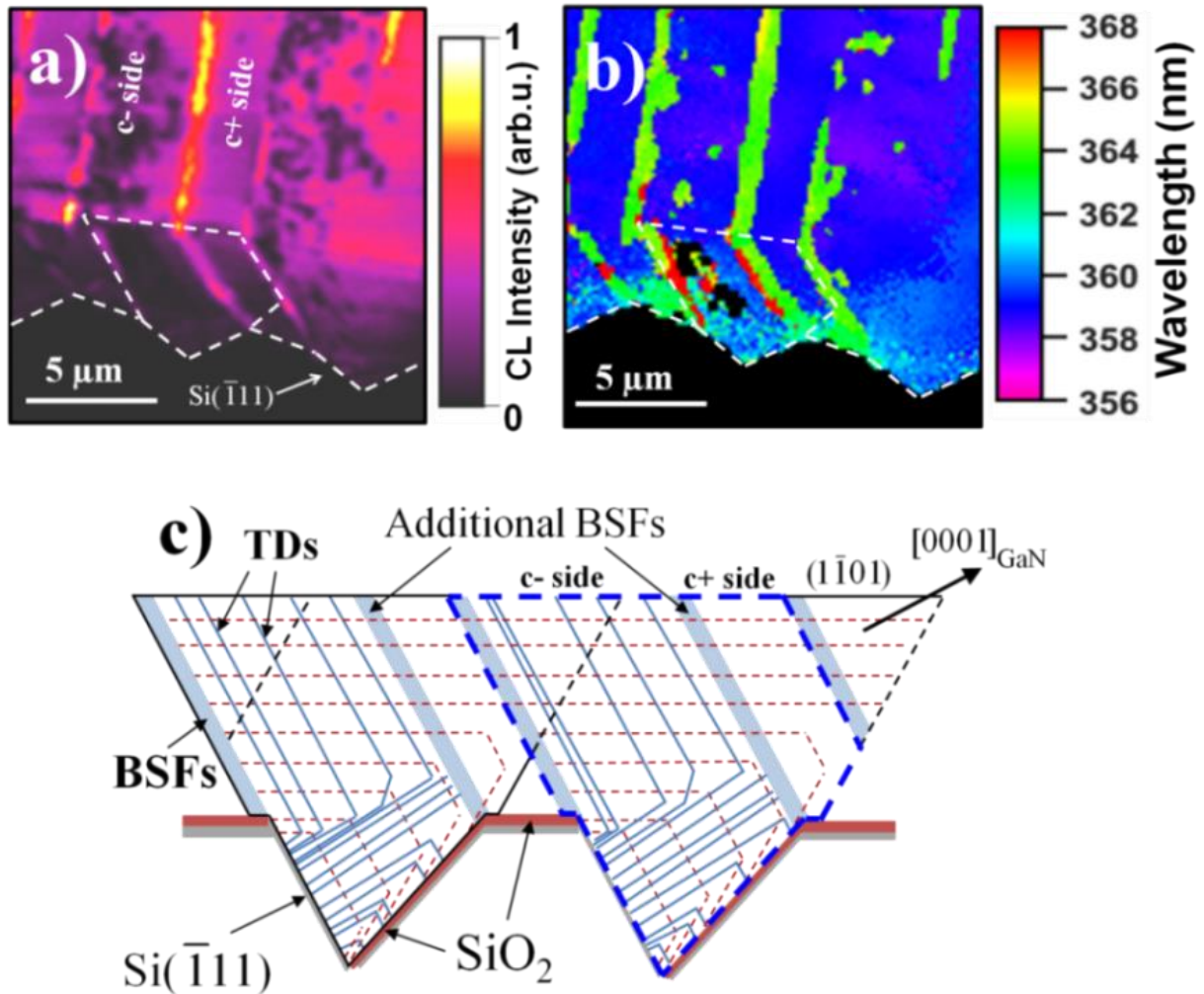


Figure 80: CL intensity (350–380 nm) and (b) CL peak wavelength images for the narrow-groove pattern sample (1̄101) GaN sample. The solid and dashed lines indicate the Si substrate surface and the GaN stripe cross section, respectively. (c) Cross-sectional schematic of GaN growth from Si(1̄11) sidewall showing threading dislocation propagation (blue solid lines) and the growth fronts (red dashed lines).

In summary, semipolar (1̄101) GaN layers were studied by steady-state PL and spatially resolved NSOM and CL with emphasis on the distribution of defects and their effects on the optical quality. The PL from the near surface ⁺c-sides of the semipolar (1̄101) GaN layers are found to be mainly dominated by the strong near bandedge emission; however, emission from the ⁻c-sides is substantially weaker due to high density of threading dislocations and stacking faults. By entirely

optical means, without the need for any structural microscopy analysis, it was revealed that some TDs bend toward the surface. Additional stacking faults formed in the narrow-groove pattern sample when the growing ^+c fronts made contact with the SiO₂ masking layer were found to block TD propagation along the ^+c -direction. These results indicate that, for proper Si(001) substrate patterning geometry, high quality (1 $\bar{1}$ 01) GaN free from extended defects can be obtained using a single ELO step.

4.6. Optical performance of nonpolar m -plane (1 $\bar{1}$ 00) GaN layers grown using two-step growth technique

As explained before, the reactor pressure during MOCVD growth have a dramatic effect on the optical properties of m -plane (1 $\bar{1}$ 00) GaN layers. Therefore, the nonpolar GaN layers are grown on Si (112) substrates patterned to form grooves aligned parallel to the $\langle 110 \rangle$ Si direction at high pressure to achieve high optical quality, similar to that of semipolar (1 $\bar{1}$ 01) GaN films which are successfully grown at high pressure of 200 Torr (as discussed above, the optical quality of (1 $\bar{1}$ 01) GaN is comparable to that of state-of-art c -plane GaN; see **Figure 59**). However, for the formation of the nonpolar m -plane (1 $\bar{1}$ 00) GaN facets, a low reactor pressure of 30 Torr required.¹⁴⁹ Therefore, m -plane GaN developed by two-stage growth procedure, in which low-pressure (30 Torr) first stage is used to ensure formation and lateral expansion of m -facet until coalescence and high-pressure stage (200 Torr) is employed for improvement of optical quality. A reference nonpolar (1 $\bar{1}$ 00) GaN sample also was grown in one step at a pressure of 30 Torr (low pressure) for comparison. M -plane (1 $\bar{1}$ 00) GaN samples were characterized by scanning electron microscopy (SEM), steady-state photoluminescence (PL), and near-field scanning optical

microscopy (NSOM). HeCd laser excitation (325 nm wavelength) was used for the excitation source in the PL measurements.

Figure 81 shows a cross-sectional SEM image of non-coalesced GaN stripes grown on the patterned Si substrate. GaN growth started on the vertical sidewalls and then advanced laterally first along the GaN [0001] +*c* direction (+*c* wing) and then, once the vertical growth had advanced above the Si(112) substrate surface, also along the [000 $\bar{1}$] -*c* direction (-*c* wing). The growth rate of GaN in the +*c* direction is much higher than that in -*c* direction; therefore, the +*c* wing is wider than the -*c* wing, as seen from **Figure 81**.

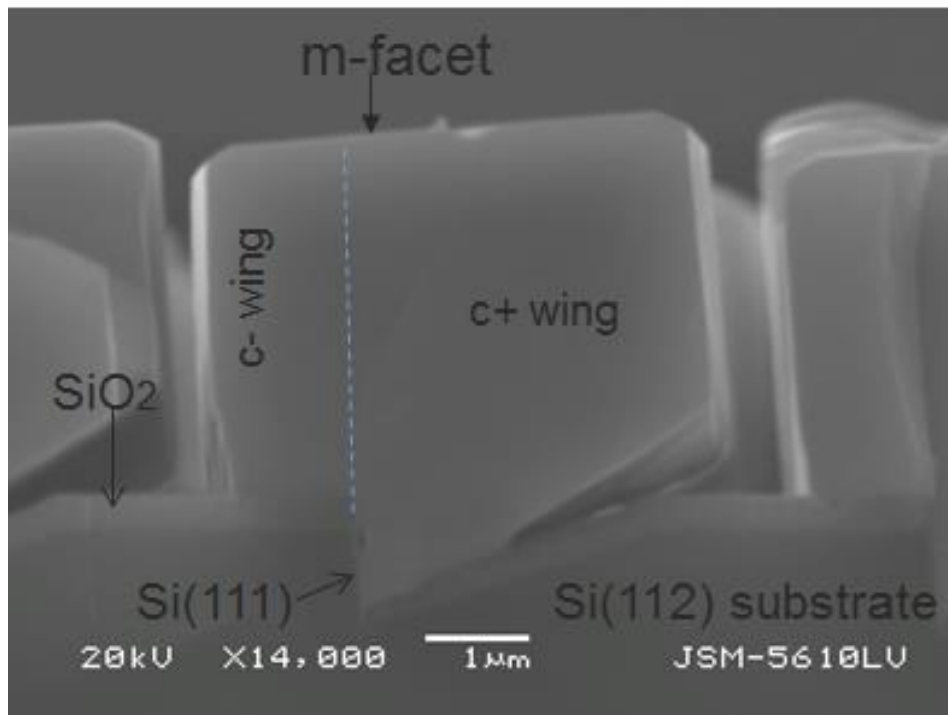


Figure 81: Cross-sectional SEM images of nonpolar m-plane GaN on patterned Si(112) substrate.

Figure 82(a) compares room-temperature PL spectra from two m-plane GaN samples: one grown in two steps (30 + 300 Torr) and another grown at a low pressure of 30 Torr. The spectra from semipolar ($1\bar{1}01$)GaN sample grown on patterned Si(001) substrate at 200 Torr and polar c-plane GaN layer grown on the state-of-the-art GaN templates using in situ epitaxial lateral

overgrowth (ELO) with a SiNx nano-network mask are also shown for comparison. One can see that the m-plane GaN sample grown at low pressure shows rather weak near band edge emission (NBE) with a strong defect-related deep emission band around 550 nm. The sample grown in two steps shows improvement of the optical quality: the PL intensity for this sample is about 3 times higher than that for the layer grown at 30 Torr in a single step and the intensity of the deep emission is considerably lower. However, the emission from m-plane GaN is still more than an order of magnitude lower than that of the semipolar GaN grown under the same conditions. **Figure 82(b)** presents 15-K PL spectra measured for the low-pressure sample and the sample grown in two steps. In addition to narrow donor-bound exciton emission line (D^0X) at 357.6 nm, the low-pressure sample shows a strong peak at 380 nm related to PSFs and its phonon replicas at longer wavelengths. A shoulder of the D^0X line at about 362 nm can be assigned to basal stacking faults. A broad NBE line at 356.4 nm is observed in the spectrum of the two-step-grown sample, while PSF-related emission is seen only as a weak shoulder. One can see that emission from nonpolar *m*-GaN is still lower than that of the semipolar GaN grown under the similar conditions. For further improvement of the nonpolar material quality, deeper understanding of mechanisms of defect formation is essential.

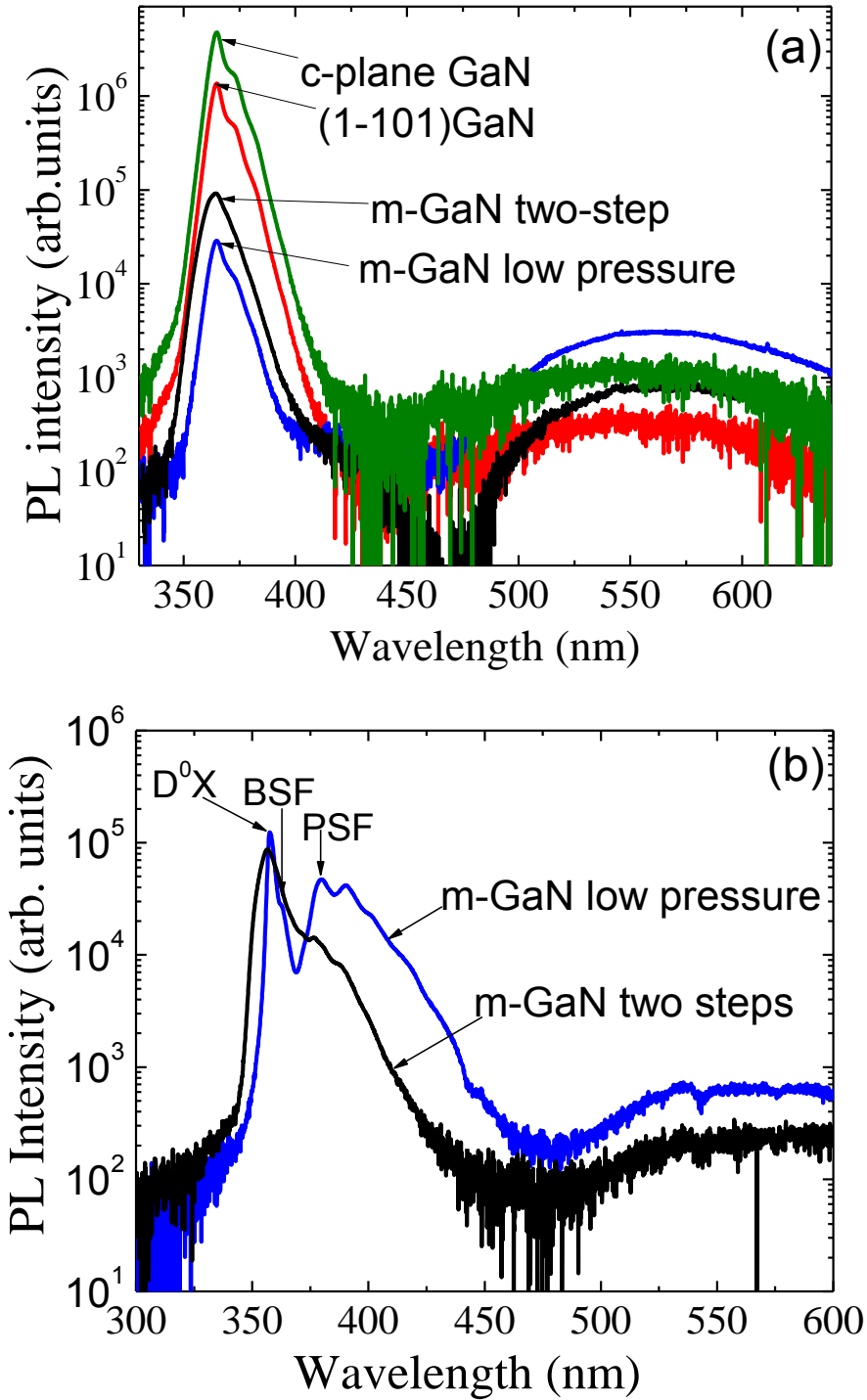


Figure 82: (a) Room-temperature steady-state PL spectra for m-plane GaN layers grown at 30 Torr (blue) and in two steps (30 + 200 Torr) (black). The spectra from polar c-plane GaN nano-ELO sample (green) and $(1\bar{1}01)$ GaN semipolar sample (red) are shown for comparison. (b) Low-temperature (15 K) PL spectra for m-plane GaN samples grown at 30 Torr (blue) and in two steps (black).

To study PL intensity distribution among the $+c$ and $-c$ wings, NSOM measurements were performed. **Figure 83(a)** shows the micro PL spectra from $+c$ and $-c$ wings of the m -plane GaN sample grown in two steps, where the intensity of PL emission from $+c$ and $-c$ wing regions is virtually the same. **Figure 83(b)** and (c) present the NSOM map, i.e. spatial distribution of intensity of near band edge emission and yellow emission, respectively, over the surface of m -plane GaN sample grown in two steps. The results of NSOM mapping are consistent with the micro PL data: PL intensity distribution shows no apparent difference between the $+c$ and $-c$ wings. The strong yellow emission from the near surface regions suggests a high density of point defects in these regions.

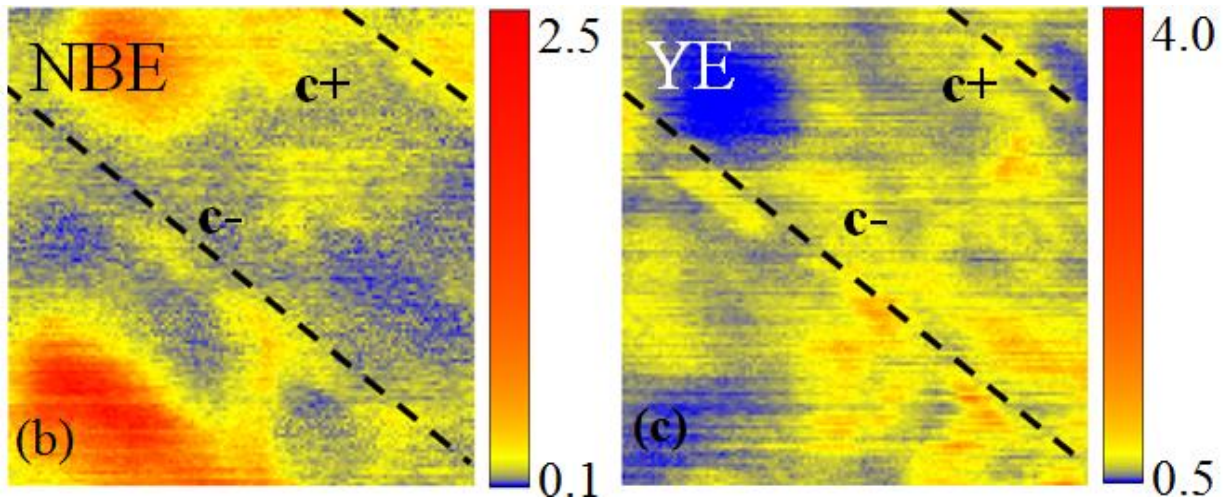
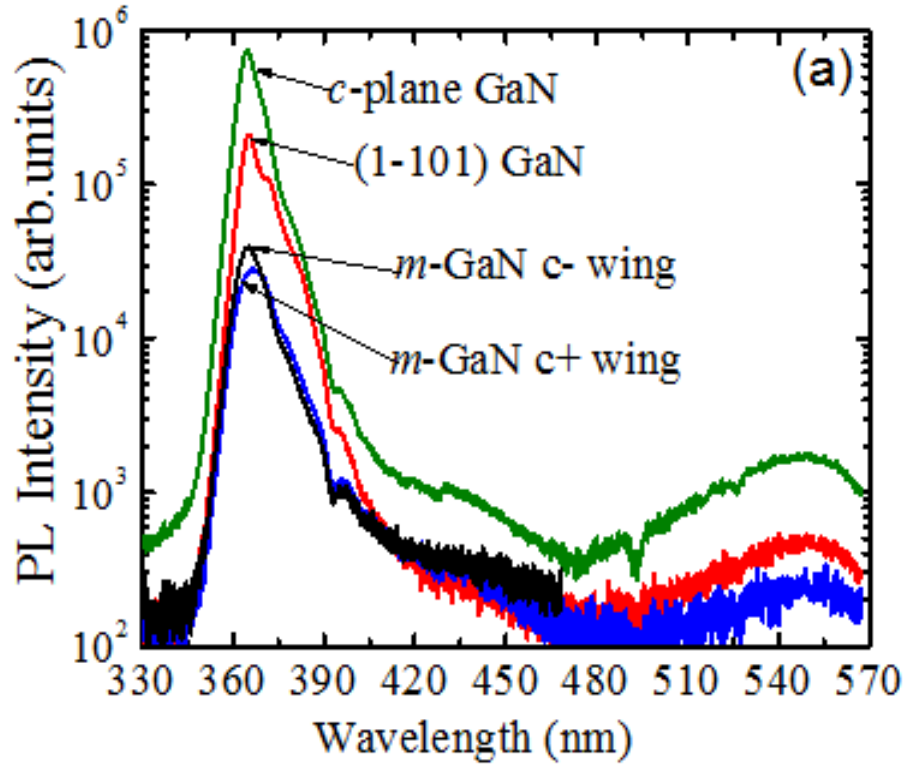


Figure 83: NSOM maps for (a) near-band edge and (c) yellow emissions. Dashed lines show the boundaries of GaN stripes. The scan area is $20 \times 20 \mu\text{m}$. The spectra were integrated between 350–370 nm for the near bandedge (NBE) intensity maps and above 450 nm for the yellow emission (YE) intensity maps.

Nonpolar m-plane GaN layers were grown on patterned Si (112) substrates by MOCVD using a two-step approach to improve their optical quality. The two-stage growth procedure involving a low-pressure (30 Torr) first stage to ensure formation of the m-plane facet and a high-pressure

stage (200 Torr) for improvement of optical quality was employed. Two-stage growth for the m-plane GaN growth resulted in higher optical quality layers compared to m-plane layers grown only at low reactor pressures (30 Torr), but still lower than that of semipolar ($1\bar{1}01$)GaN layers which were grown in similar conditions. Compared to the layers grown at low pressure in a single step, the near band edge PL intensity was ~ 3 times higher and the deep emission was considerably weaker. Optical emission over the c^- and c^+ wings of the nonpolar GaN/Si was found to be similar in terms of PL intensity confirmed by both spatially resolved NSOM and microPL measurements.

4.7. Semipolar ($1\bar{1}01$) and ($11\bar{2}2$) InGaN LED performance

An InGaN LED structure is grown on a semipolar ($1\bar{1}01$) GaN. LED design optimized for polar c -plane LEDs on sapphire in our laboratory were employed for this sample.¹⁵⁰ As shown schematically in Figure 84, the LED active region consists of six 3 nm $\text{In}_{0.16}\text{Ga}_{0.84}\text{N}$ layers separated by 3 nm $\text{In}_{0.01}\text{Ga}_{0.99}\text{N}$ barriers. Situated below the active region is a two-layer staircase electron injector (SEI)³⁰ grown on a 60 nm n -type ($2 \times 10^{18} \text{ cm}^{-3}$) $\text{In}_{0.01}\text{Ga}_{0.99}\text{N}$ underlying layer that was employed to reduce the probability of strain relaxation in the active region owing to its compliance action warranted by its softer lattice compared to GaN. The SEI consists of $\text{In}_{0.04}\text{Ga}_{0.96}\text{N}$ and $\text{In}_{0.08}\text{Ga}_{0.92}\text{N}$ layers of the same thickness of 16 nm grown in the given order. The LED structures were completed with 100 nm-thick Mg-doped p -GaN layers having approximately $5 \times 10^{17} \text{ cm}^{-3}$ hole density (calibration was done for c -plane structures by using Hall effect measurements). Spatial distribution of extended defects in the structure was studied at room temperature using a Cryoview 2000 NSOM system (Nanonics Imaging Ltd). HeCd laser (325 nm wavelength) excitation through a Cr-Al coated optical fiber probe with a 100 nm aperture was used for NSOM measurements.

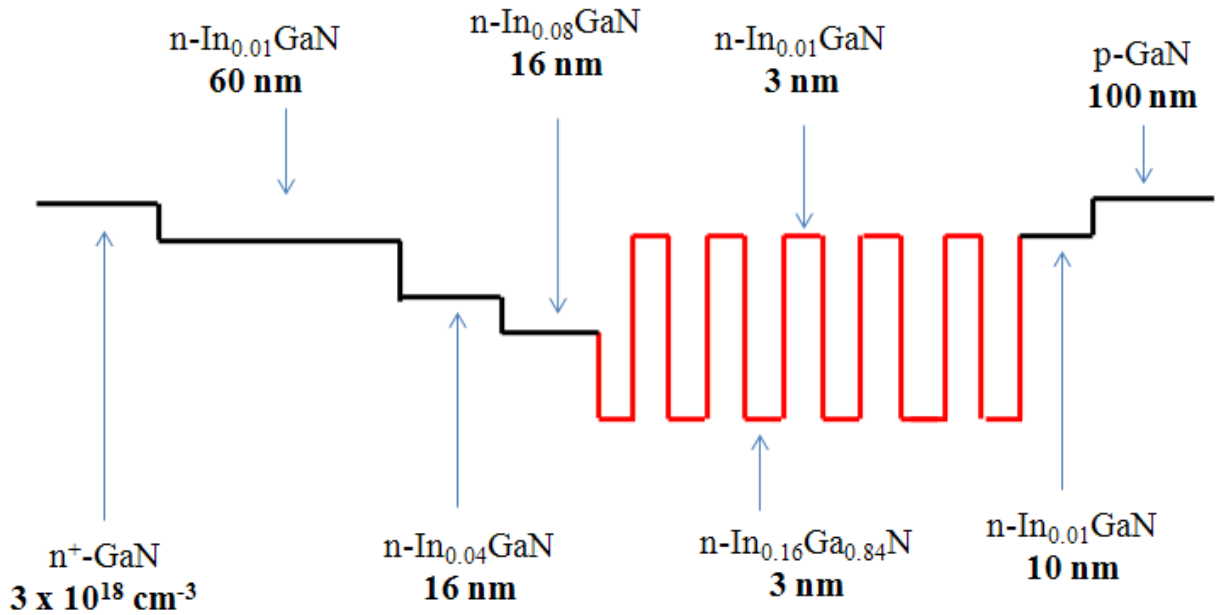


Figure 84: Conduction band schematic structure of LED active region grown on $(1\bar{1}01)$ GaN templates on patterned Si substrates (flat band conditions). The underlying In_{0.01}GaN layer is used to improve the active region material quality. Similar LED structures were grown on *c*-plane GaN for comparison.

Figure 85 compares the PL intensity from the semipolar $(1\bar{1}01)$ LED structure on patterned Si with that from a highly optimized polar *c*-plane LED structure having a high internal quantum efficiency of about 80%. To avoid influence from the top *p*-GaN layer, the InGaN active regions were excited with below GaN bandgap excitation (385 nm wavelength). One can see that the PL intensity from the semipolar InGaN/GaN structures on patterned Si is comparable to that from the polar LED structure grown on sapphire. These findings indicate that semipolar $(1\bar{1}01)$ -oriented material with optical quality required for light emitting devices can be achieved on patterned Si substrates.

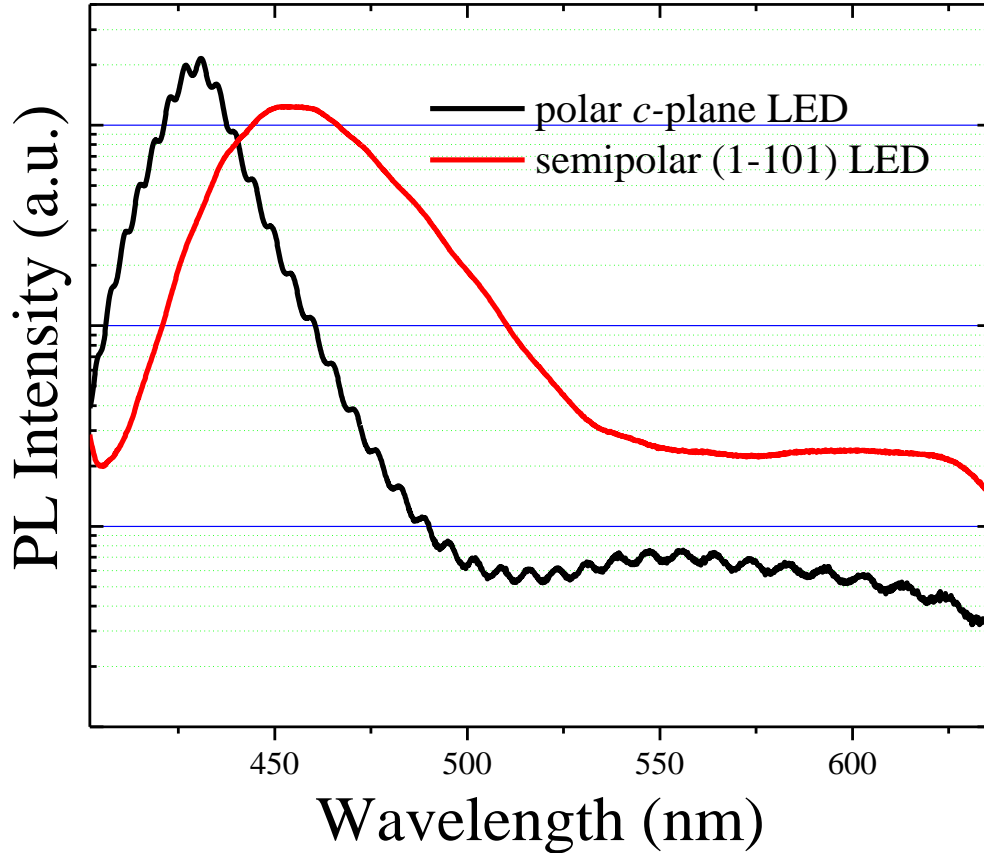


Figure 85: PL spectra for semipolar $(1\bar{1}01)$ InGaN LED structure grown on $(1\bar{1}01)$ GaN on stripe patterned Si substrate measured with an excitation wavelength of 385 nm. PL spectrum for a highly optimized polar c -plane LED structure with 80% internal quantum efficiency is shown for comparison.

Figure 86 presents the room temperature NSOM reflection (325 nm incident wavelength) and InGaN band-edge PL intensity maps of semipolar $(1\bar{1}01)$ InGaN/GaN LED structures. To block the short-wavelength emission from GaN, a 400 nm high-pass filter was used. One can see that the \bar{c} -wing regions appear as dark areas in the PL map due to the presence of large density of stacking faults (acting as nonradiative recombination channels at room temperature) and threading dislocations. The emission from the ^+c -wings is very bright and relatively uniform across the sample, which is indicative of homogeneous In distribution.

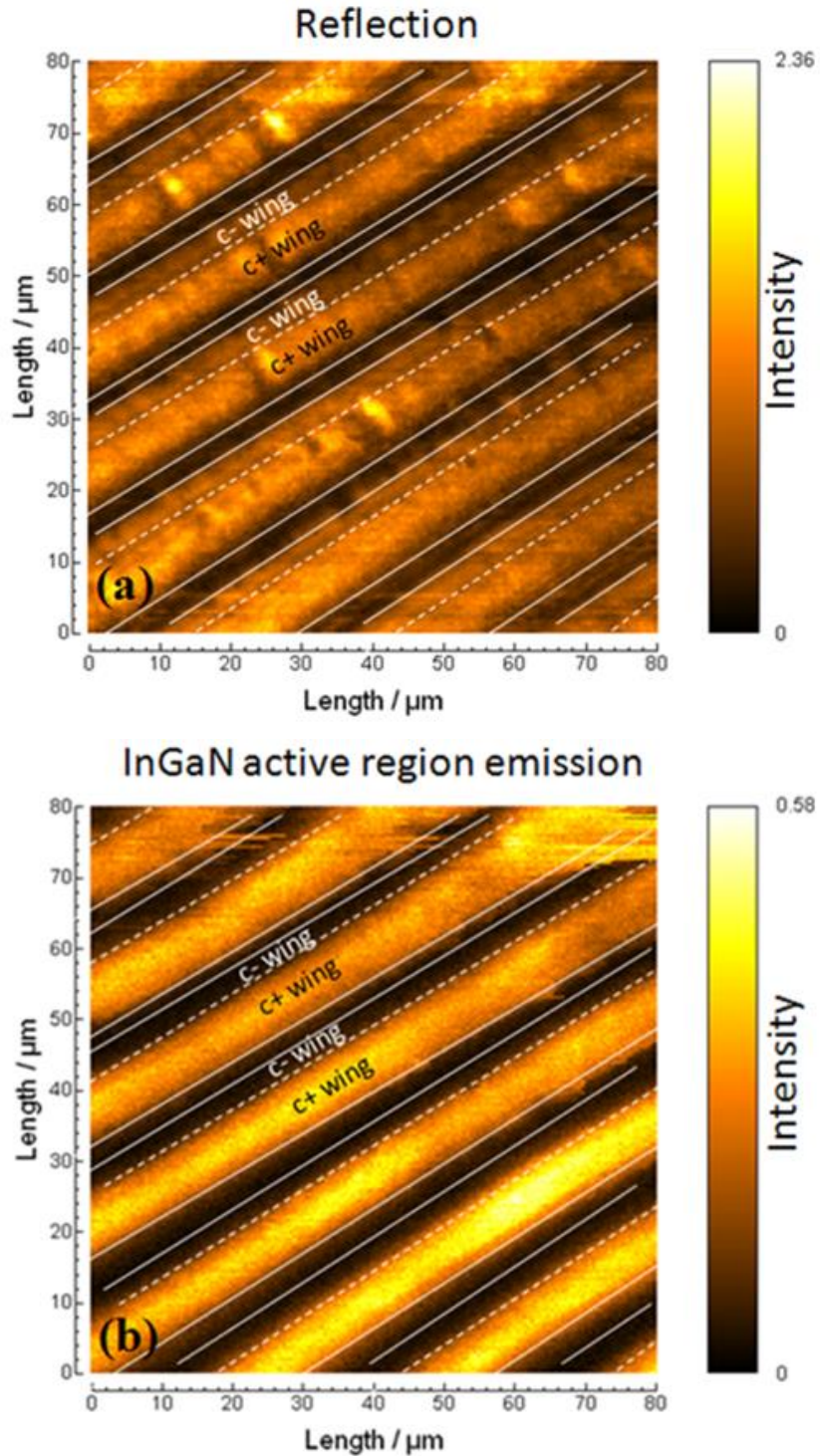


Figure 86: Room temperature NSOM maps of semipolar $(1\bar{1}01)$ InGaN/GaN LED structure grown on $(1\bar{1}01)$ GaN templates on stripe patterned Si substrates. (a) Optical reflection image (325 nm wavelength), (b) PL intensity distribution measured with 400 nm high-pass filter. Boundaries of ^+c - and ^-c -wings are indicated with dashed lines.

The PL from the near surface ^+c -sides of the semipolar $(1\bar{1}01)$ InGaN LED is found to be mainly dominated by the strong active region emission; however, emission from the ^-c -sides is substantially weaker due to high density of threading dislocations and stacking faults as revealed in NSOM measurements.

Another InGaN LED structure is grown on a semipolar $(11\bar{2}2)$ GaN on m-sapphire substrate, which is schematically similar to Figure 84, but with active region consisting of four 3 nm $\text{In}_{0.16}\text{Ga}_{0.84}\text{N}$ layers instead of six in the case of $(1\bar{1}01)$ LED structure. **Figure 87** compares the PL intensity from the semipolar $(11\bar{2}2)$ LED structure with that from a highly optimized polar c -plane LED structure having a high similar active region. The InGaN active regions were excited with 325 nm HeCd laser excitation. One can see that the PL intensity from the semipolar InGaN/GaN structures on m-sapphire substrate is substantially lower than that from the polar LED structure grown on c-sapphire. These results indicate that semipolar $(11\bar{2}2)$ -oriented material quality requires to be improved for light emitting devices.

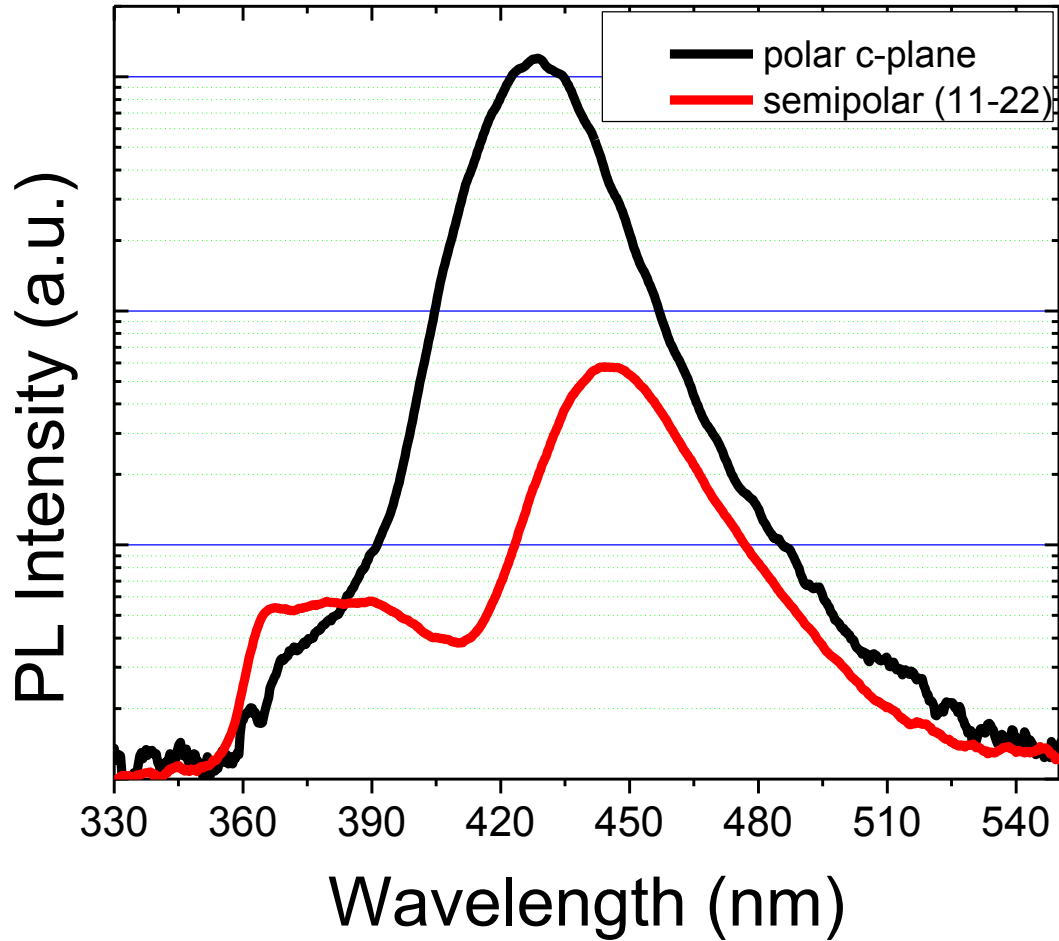


Figure 87: PL spectra for semipolar $(11\bar{2}2)$ InGaN LED structure grown on m-sapphire substrate measured with an excitation wavelength of 325 nm. PL spectrum for a highly optimized polar c-plane LED structure with 80% internal quantum efficiency is shown for comparison.

In summary, semipolar $(1\bar{1}01)$ InGaN LED structure grown on Si(001) 7° offcut substrate with $3\ \mu\text{m} \times 10\ \mu\text{m}$ groove pattern and $(11\bar{2}2)$ InGaN LED structure grown on m-sapphire substrate were studied by photoluminescence measurements in addition to spatially-resolved NSOM with emphasis on the distribution of defects and their effects on the optical quality for $(1\bar{1}01)$ InGaN LED structure. PL measurements showed a promising optical quality of $(1\bar{1}01)$ InGaN LED structure which has a similar PL peak intensity to an optimized c-plane polar LED structure. However, PL results support the argument that structural quality of $(11\bar{2}2)$ InGaN LED

needs to be improved for better optical quality. NSOM results indicate inferior optical quality for the \bar{c} -wings of semipolar $(1\bar{1}01)$ InGaN layers compared to ^+c -wings originate not only from the point defects and threading dislocations, but also from basal plane and prismatic stacking faults.

Chapter 5. Summary and Conclusions

A set of optical techniques have been used to explore the major challenges during the development of a new type blue InGaN-based vertical cavity structure grown on nearly defect free epitaxial lateral overgrown (ELO) GaN layers employed with bottom and top dielectric DBRs. The vertical cavity structure provided solutions to narrow stop-band bottom DBR and their integration with cavity active region, high quality GaN substrate and InGaN active regions, and cumbersome substrate removal process after top dielectric DBR deposition. In the context of enhancement of active region quality, DH active regions are investigated in addition to nonpolar and semipolar GaN substrates.

Rabi splitting of 75 meV at low temperature (45 meV at room temperature) was obtained for the cavity using InGaN MQW (6 x 2nm well) active region grown on a free-standing GaN substrate confirming strong exciton-photon coupling being one of the largest in the literature, which is very promising for ideally thresholdless polariton lasers. Substantial increase in quality factors (from 300 to 1300) was obtained for the vertical cavity structure grown on a sapphire substrate with dual hex 3 nm DH active region compared to the vertical cavity with MQW on free-standing GaN. In order to achieve the vertical cavity structure, MOCVD growth parameters also studied for higher lateral to vertical (L/V) growth ratio ELO-GaN wings. In addition, the etching parameters for ELO wings using inductively coupled plasma (ICP) etching technique investigated to obtain desired vertical cavity lengths on the ELO wings. Final cavity structure was obtained after the lithography techniques used following with e-beam deposition for the electrical contacts.

The relative roles of radiative and nonradiative processes and the polarization field on the light emission from the single and multiple DH active designs have been studied. Experimental

results supported by theoretical and numerical studies that injection dependent electron and hole wavefunction overlap and the corresponding radiative recombination coefficients suggest to employ multiple InGaN DH structures separated by thin and low barriers for better optical performance. Time-resolved photoluminescence measurements also revealed higher radiative recombination rates with increasing excitation due to screening of the internal field and enhanced electron and hole overlap at higher injection levels. It is also shown that a good design of SEI may play an important role for the efficiency improvement of LEDs. It is found that the integrated PL intensity of LEDs employed with 20+20 nm SEI are nearly 10 times higher than that of 5+5 nm at low injection levels. Most importantly, the increased SEI thickness boosted the electron cooler potential and substantially reduced the electron overflow for the DH LEDs. Among the efforts to enhance the quantum efficiency at elevated injection levels, MDH designs constituted a viable approach to achieve high efficiency and high power LEDs.

Nonpolar and semipolar GaN substrates have been investigated using temperature dependent photoluminescence, time-resolved photoluminescence and near-field scanning optical microscopy techniques, which provided many insightful information about the optical and material quality of these layers. First of all, it is found that one can successfully measure the contributions of free carriers and excitons to recombination process and quantify them at different excitation densities and temperatures for the mixed exciton-free carrier system if TRPL and PRPL techniques are employed together. Based on the results, free carrier population increases by increasing both excitation density (by screening the excitons) and temperature (by dissociation of excitons) radiative recombination rate and degree of polarization are strongly affected. Stacking faults (basal-plane and prismatic) are shown to be actively involved in optical processes substantially influencing the carrier dynamics in semipolar $(1\bar{1}01)$ and $(11\bar{2}2)$ GaN layers grown on silicon and

sapphire substrate, respectively. Steady-state PL and TRPL results indicated inferior optical quality of \bar{c} -wings of semipolar $(1\bar{1}01)$ GaN layers compared to c -wings originating not only from the point defects and threading dislocations, but also from basal plane and prismatic stacking faults. Higher PL intensity and faster PL decay times for BSFs (0.8 ns) compared to PSFs (3.5 ns) suggested larger density and larger contribution to carrier recombination dynamics of BSFs compared to PSFs in semipolar $(1\bar{1}01)$ GaN layers. Their presence are also evidenced from spatially and spectrally resolved near-field scanning optical microscopy (NSOM) and cathodoluminescence (CL) measurements and showed very good agreement with PL and TRPL results. In addition to nonradiative recombination centers, carrier trapping/detrapping by stacking faults and carrier transfer between stacking faults and donor energy levels are found to be among those processes affecting the carrier recombination dynamics at different temperature levels. Temperature dependent steady-state PL results showed that carriers are loosely localized in prismatic stacking faults compared to basal stacking faults. Nevertheless, optical studies conclude that nonradiative recombination is still the most effective process for the carrier recombination dynamics for these layers.

Semipolar $(1\bar{1}01)$ InGaN LED structure grown on Si(001) 7° offcut substrate with $3\ \mu\text{m} \times 10\ \mu\text{m}$ groove pattern and $(11\bar{2}2)$ InGaN LED structure grown on m-sapphire substrate were studied by photoluminescence measurements PL measurements showed a promising optical quality of $(1\bar{1}01)$ InGaN LED structure which has a similar PL peak intensity to an optimized c -plane polar LED structure. However, PL results supports the argument that structural quality of $(11\bar{2}2)$ InGaN LED needs to be improved for better optical quality.

Chapter 6. Outlook

InGaN active regions were evaluated using a set of optical techniques to obtain the most efficient structural design for light emitting devices, LEDs and vertical cavities. Among the efforts to enhance the quantum efficiency at elevated injection levels, MDH designs constituted a viable approach to achieve high efficiency and high power LEDs. On the other hand, it was found that a good design of SEI might have played an important role for the efficiency improvement of LEDs. The LEDs employed with 20+20 nm SEI increased the PL intensities and substantially reduced the electron overflow for the LEDs. It is suggested that LEDs with active regions with MDH and 20+20 nm SEI should be investigated more using time-resolved techniques to obtain more information about the radiative and nonradiative recombination processes and should be compared to LEDs with different active regions. These investigations would pave for further optimization of the active regions used in LEDs and vertical cavity lasers.

Chapter 3 examines the hybrid vertical cavities (bottom semiconductor and top dielectric DBR) and a vertical cavity with full dielectric DBRs. A hybrid vertical cavity with MQW active region showed a strong coupling behavior with 75 meV Rabi splitting, which is very promising for ideally thresholdless polariton lasers. This cavity structure should be investigated more with optical techniques using high power lasers to obtain the threshold lasing value. Excitation power dependent PL measurements would also help to find the β coefficient (the fraction of spontaneous emission that seeds the lasing process). Eventually, photolithography and deposition techniques should be employed to constitute the electrical contacts to test this sample under electrical injection.

A vertical cavity structure grown on nearly defect free epitaxial lateral overgrown (ELO) GaN layers employed with bottom and top dielectric DBRs. The vertical cavity structure provided solutions to narrow stop-band bottom DBR and their integration with cavity active region, high quality GaN substrate and InGaN active regions, and cumbersome substrate removal process after top dielectric DBR deposition. However, fabrication issues having to do with the full contiguity of the metal layer are at least partially, if not nearly fully, responsible for not observing the lasing at electrical injection. Further reduction of the p-GaN layer thickness in addition to improving the fabrication procedures may lead to lasing in these devices under electrical injection.

As stated in Chapter 4, nonpolar and semipolar GaN substrates are promising for light emitting device applications mainly due to the lack of polarization-induced electric field compared to its widely used c-plane counterpart. Demonstration of their growth on patterned Si substrates shows great promise for obtaining low-cost large-area GaN substrates for the optoelectronic device applications. In this thesis, the studies focused on achieving high-quality non-polar m-plane and semipolar $(1\bar{1}01)$ and $(11\bar{2}2)$ GaN layers and investigating them using various optical techniques. Semipolar $(1\bar{1}01)$ GaN layers showed better performance in terms of structural and optical quality, while nonpolar m-plane and semipolar $(11\bar{2}2)$ GaN layers were found to be in need of further structural improvements for better quality. Consequently, $[1\bar{1}01]$ -orientated GaN surface should be pursued to construct LEDs and vertical cavities for better device performance in short term. It is believed that nonpolar m-plane and semipolar $(11\bar{2}2)$ GaN substrates will also take their place in light emitting device applications in near future when their quality are improved. In addition to engineering side, physics also benefit from these substrates due to their rich nature for optical investigations. Contrary to polar c-plane substrates, nonpolar and semipolar orientations allow one to study polarization-resolved recombination dynamic thanks to the polarization selection rules.

For this reason, temperature and excitation power dependent PL and TRPL measurement techniques should be employed with polarization dependent PL measurements to gain insights about the nature of the particles as well as defects which are actively involved in radiative and nonradiative recombination processes.

References

- ¹ I. Vurgaftman and J. R. Meyer, *Journal of Applied Physics* **94** (6), 3675 (2003).
- ² Hadis Morkoç, *Handbook of Nitride Semiconductors and Devices*. (Wiley-VCH, Weinheim, 2008).
- ³ T. Someya, K. Tachibana, J. Lee, T. Kamiya, and Y. Arakawa, *Japanese Journal of Applied Physics Part 2-Letters* **37** (12A), L1424 (1998).
- ⁴ H. L. Zhou, M. Diagne, E. Makarona, A. V. Nurmikko, J. Han, K. E. Waldrip, and J. J. Figiel, *Electronics Letters* **36** (21), 1777 (2000).
- ⁵ Y. K. Song, H. Zhou, M. Diagne, A. V. Nurmikko, R. P. Schneider, C. P. Kuo, M. R. Krames, R. S. Kern, C. Carter-Coman, and F. A. Kish, *Applied Physics Letters* **76** (13), 1662 (2000).
- ⁶ R. Butte, E. Feltn, J. Dorsaz, G. Christmann, J. F. Carlin, N. Grandjean, and M. Ilegems, *Japanese Journal of Applied Physics Part 1-Regular Papers Brief Communications & Review Papers* **44** (10), 7207 (2005).
- ⁷ Jung-Tang Chu, Tien-Chang Lu, Min You, Bor-Jye Su, Chih-Chiang Kao, Hao-Chung Kuo, and Shing-Chung Wang, *Applied Physics Letters* **89** (12) (2006).
- ⁸ T. Tawara, H. Gotoh, T. Akasaka, N. Kobayashi, and T. Saitoh, *Applied Physics Letters* **83** (5), 830 (2003).
- ⁹ L. E. Cai, J. Y. Zhang, B. P. Zhang, S. Q. Li, D. X. Wang, J. Z. Shang, F. Lin, K. C. Lin, J. Z. Yu, and Q. M. Wang, *Electronics Letters* **44** (16), 972 (2008).
- ¹⁰ J. Y. Zhang, L. E. Cai, B. P. Zhang, S. Q. Li, F. Lin, J. Z. Shang, D. X. Wang, K. C. Lin, J. Z. Yu, and Q. M. Wang, *Journal of Lightwave Technology* **27** (1-4), 55 (2009).
- ¹¹ Tien-Chang Lu, Chih-Chiang Kao, Hao-Chung Kuo, Gen-Sheng Huang, and Shing-Chung Wang, *Applied Physics Letters* **92** (14) (2008).
- ¹² Tien-Chang Lu, Tzeng-Tsong Wu, Shih-Wei Chen, Po-Min Tu, Zhen-Yu Li, Chien-Kang Chen, Cheng-Hung Chen, Hao-Chung Kuo, Shing-Chung Wang, Hsiao-Wen Zan, and Chun-Yen Chang, *Ieee Journal of Selected Topics in Quantum Electronics* **17** (6), 1594 (2011).
- ¹³ Y. Higuchi, K. Omae, H. Matsumura, and T. Mukai, *Applied Physics Express* **1** (12) (2008).

- ¹⁴ Daiji Kasahara, Daisuke Morita, Takao Kosugi, Kyosuke Nakagawa, Jun Kawamata, Yu Higuchi, Hiroaki Matsumura, and Takashi Mukai, *Applied Physics Express* **4** (7) (2011).
- ¹⁵ Shing-Chung Wang, Tien-Chang Lu, Chih-Chiang Kao, Jong-Tang Chu, Gen-Sheng Huang, Hao-Chung Kuo, Shih-Wei Chen, Tsung-Ting Kao, Jun-Rong Chen, and Li-Fan Lin, *Japanese Journal of Applied Physics* **46** (8B), 5397 (2007).
- ¹⁶ T. Someya, R. Werner, A. Forchel, M. Catalano, R. Cingolani, and Y. Arakawa, *Science* **285** (5435), 1905 (1999).
- ¹⁷ Chih-Chiang Kao, Y. C. Peng, H. H. Yao, J. Y. Tsai, Y. H. Chang, J. T. Chu, H. W. Huang, T. T. Kao, T. C. Lu, H. C. Kuo, S. C. Wang, and C. F. Lin, *Applied Physics Letters* **87** (8), 081105 (2005).
- ¹⁸ Jiang-Yong Zhang, Li- E. Cai, Bao-Ping Zhang, Shui-Qing Li, Feng Lin, Jing-Zhi Shang, Du-Xiang Wang, Ke-Chuang Lin, Jin-Zhong Yu, and Qi-Ming Wang, *Applied Physics Letters* **93** (19), 191118 (2008).
- ¹⁹ W. J. Liu, S. Q. Chen, X. L. Hu, Z. Liu, J. Y. Zhang, L. Y. Ying, X. Q. Lv, H. Akiyama, Z. P. Cai, and B. P. Zhang, *Ieee Photonics Technology Letters* **25** (20), 2014 (2013).
- ²⁰ Umit Ozgur, Huiyong Liu, Xing Li, Xianfeng Ni, and Hadis Morkoc, *Proceedings of the Ieee* **98** (7), 1180 (2010).
- ²¹ Michael R. Krames, Oleg B. Shchekin, Regina Mueller-Mach, Gerd O. Mueller, Ling Zhou, Gerard Harbers, and M. George Craford, *Journal of Display Technology* **3** (2), 160 (2007).
- ²² N. F. Gardner, G. O. Mueller, Y. C. Shen, G. Chen, S. Watanabe, W. Gotz, and M. R. Krames, *Applied Physics Letters* **91** (24) (2007).
- ²³ Kris T. Delaney, Patrick Rinke, and Chris G. Van de Walle, *Applied Physics Letters* **94** (19) (2009).
- ²⁴ J. Hader, J. V. Moloney, B. Pasenow, S. W. Koch, M. Sabathil, N. Linder, and S. Lutgen, *Applied Physics Letters* **92** (26) (2008).
- ²⁵ J. Lee, X. Li, X. Ni, Ue Oezguer, H. Morkoc, T. Paskova, G. Mulholland, and K. R. Evans, *Applied Physics Letters* **95** (20) (2009).
- ²⁶ I. V. Rozhansky and D. A. Zakheim, *Physica Status Solidi a-Applications and Materials Science* **204** (1), 227 (2007).

- ²⁷ X. Li, X. Ni, J. Lee, M. Wu, U. Ozgur, H. Morkoc, T. Paskova, G. Mulholland, and K. R. Evans, *Applied Physics Letters* **95** (12) (2009).
- ²⁸ Min-Ho Kim, Martin F. Schubert, Qi Dai, Jong Kyu Kim, E. Fred Schubert, Joachim Piprek, and Yongjo Park, *Applied Physics Letters* **91** (18) (2007).
- ²⁹ X. Ni, X. Li, J. Lee, S. Liu, V. Avrutin, Ue Oezguer, H. Morkoc, A. Matulionis, T. Paskova, G. Mulholland, and K. R. Evans, *Physica Status Solidi-Rapid Research Letters* **4** (8-9), 194 (2010).
- ³⁰ X. Ni, X. Li, J. Lee, S. Liu, V. Avrutin, U. Ozgur, H. Morkoc, A. Matulionis, T. Paskova, G. Mulholland, and K. R. Evans, *Applied Physics Letters* **97** (3) (2010).
- ³¹ X. Ni, X. Li, J. Lee, S. Liu, V. Avrutin, U. Ozgur, H. Morkoc, and A. Matulionis, *Journal of Applied Physics* **108** (3) (2010).
- ³² Aurelien David, Michael J. Grundmann, John F. Kaeding, Nathan F. Gardner, Theodoros G. Mihopoulos, and Michael R. Krames, *Applied Physics Letters* **92** (5) (2008).
- ³³ J. P. Liu, J. H. Ryou, R. D. Dupuis, J. Han, G. D. Shen, and H. B. Wang, *Applied Physics Letters* **93** (2) (2008).
- ³⁴ J. H. Zhu, S. M. Zhang, H. Wang, D. G. Zhao, J. J. Zhu, Z. S. Liu, D. S. Jiang, Y. X. Qiu, and H. Yang, *Journal of Applied Physics* **109** (9) (2011).
- ³⁵ X. Li, F. Zhang, S. Okur, V. Avrutin, S. J. Liu, U. Oezguer, H. Morkoc, S. M. Hong, S. H. Yen, T. S. Hsu, and A. Matulionis, *Physica Status Solidi a-Applications and Materials Science* **208** (12), 2907 (2011).
- ³⁶ R. Langer, J. Simon, V. Ortiz, N. T. Pelekanos, A. Barski, R. Andre, and M. Godlewski, *Applied Physics Letters* **74** (25), 3827 (1999).
- ³⁷ T. Deguchi, K. Sekiguchi, A. Nakamura, T. Sota, R. Matsuo, S. Chichibu, and S. Nakamura, *Japanese Journal of Applied Physics Part 2-Letters* **38** (8B), L914 (1999).
- ³⁸ M. Zamfirescu, B. Gil, N. Grandjean, G. Malpuech, A. Kavokin, P. Bigenwald, and J. Massies, *Physical Review B* **64** (12) (2001).
- ³⁹ Jonas Lähnemann, Humboldt-Universität zu Berlin, 2013.
- ⁴⁰ T. Takeuchi, H. Amano, and I. Akasaki, *Japanese Journal of Applied Physics Part 1-Regular Papers Short Notes & Review Papers* **39** (2A), 413 (2000).

- ⁴¹ A. E. Romanov, T. J. Baker, S. Nakamura, J. S. Speck, and Erato Jst Ucsb Group, *Journal of Applied Physics* **100** (2), 023522 (2006).
- ⁴² Nicholas P. Hylton, Philip Dawson, Carol F. Johnston, Menno J. Kappers, Jonathan L. Hollander, Clifford McAleese, and Colin J. Humphreys, *Physica Status Solidi C: Current Topics in Solid State Physics*, Vol 6, Suppl 2 **6**, S727 (2009).
- ⁴³ M. Feneberg, F. Lipski, R. Sauer, K. Thonke, T. Wunderer, B. Neubert, P. Brueckner, and F. Scholz, *Applied Physics Letters* **89** (24) (2006).
- ⁴⁴ Hisashi Masui, Hirokuni Asamizu, Thiago Melo, Hisashi Yamada, Kenji Iso, Samantha C. Cruz, Shuji Nakamura, and Steven P. DenBaars, *Journal of Physics D-Applied Physics* **42** (13) (2009).
- ⁴⁵ F. Scholz, *Semiconductor Science and Technology* **27** (2), 024002 (2012).
- ⁴⁶ T. Zhu and R. A. Oliver, *Physical chemistry chemical physics : PCCP* **14** (27), 9558 (2012).
- ⁴⁷ A. V. Rodina, M. Dietrich, A. Goldner, L. Eckey, A. Hoffmann, A. L. Efros, M. Rosen, and B. K. Meyer, *Physical Review B* **64** (11) (2001).
- ⁴⁸ D. R. Hang, M. M. C. Chou, and J. L. Lin, *J. Korean Phys. Soc.* **55** (1), 250 (2009).
- ⁴⁹ Hisashi Masui, Shuji Nakamura, Steven P. DenBaars, and Umesh K. Mishra, *Ieee Transactions on Electron Devices* **57** (1), 88 (2010).
- ⁵⁰ Z. Liliental-Weber, J. Jasinski, and D. N. Zakharov, *Opto-Electronics Review* **12** (4), 339 (2004).
- ⁵¹ R. M. Farrell, E. C. Young, F. Wu, S. P. DenBaars, and J. S. Speck, *Semiconductor Science and Technology* **27** (2) (2012).
- ⁵² Jonas Lähnemann, Uwe Jahn, Oliver Brandt, Timur Flissikowski, Pinar Dogan, and Holger T. Grahn, *Journal of Physics D: Applied Physics* **47** (42), 423001 (2014).
- ⁵³ C. Stampfl and C. G. Van de Walle, *Physical Review B* **57** (24), 15052 (1998).
- ⁵⁴ Dmitri Zakharov, Zuzanna Liliental-Weber, Brian Wagner, Zachary Reitmeier, Edward Preble, and Robert Davis, *Physical Review B* **71** (23) (2005).

- ⁵⁵ J. Mei, S. Srinivasan, R. Liu, F. A. Ponce, Y. Narukawa, and T. Mukai, *Applied Physics Letters* **88** (14) (2006).
- ⁵⁶ C. Weisbuch, M. Nishioka, A. Ishikawa, and Y. Arakawa, *Phys. Rev. Lett.* **69** (23), 3314 (1992).
- ⁵⁷ A. Imamoglu, R. J. Ram, S. Pau, and Y. Yamamoto, *Physical Review A* **53** (6), 4250 (1996).
- ⁵⁸ T. C. H. Liew, I. A. Shelykh, and G. Malpuech, *Physica E-Low-Dimensional Systems & Nanostructures* **43** (9), 1543 (2011).
- ⁵⁹ Hui Deng, Hartmut Haug, and Yoshihisa Yamamoto, *Reviews of Modern Physics* **82** (2), 1489 (2010).
- ⁶⁰ A. Kavokin, *Physica Status Solidi B-Basic Solid State Physics* **247** (8), 1898 (2010).
- ⁶¹ H. Deng, G. Weihs, C. Santori, J. Bloch, and Y. Yamamoto, *Science* **298** (5591), 199 (2002).
- ⁶² M. Richard, J. Kasprzak, R. Andre, R. Romestain, L. S. Dang, G. Malpuech, and A. Kavokin, *Physical Review B* **72** (20) (2005).
- ⁶³ R. Shimada, J. Xie, V. Avrutin, U. Ozgur, and H. Morkoc, *Applied Physics Letters* **92** (1) (2008).
- ⁶⁴ T. Zhu, A. Dussaigne, G. Christmann, C. Pinguier, E. Feltn, D. Martin, R. Butte, and N. Grandjean, *Applied Physics Letters* **92** (6) (2008).
- ⁶⁵ D. G. Lidzey, D. D. C. Bradley, M. S. Skolnick, T. Virgili, S. Walker, and D. M. Whittaker, *Nature* **395** (6697), 53 (1998).
- ⁶⁶ N. Antoine-Vincent, F. Natali, D. Byrne, A. Vasson, P. Disseix, J. Leymarie, M. Leroux, F. Semond, and J. Massies, *Physical Review B* **68** (15) (2003); T. Tawara, H. Gotoh, T. Akasaka, N. Kobayashi, and T. Saitoh, *Phys. Rev. Lett.* **92** (25) (2004).
- ⁶⁷ I. R. Sellers, F. Semond, M. Leroux, J. Massies, P. Disseix, A. L. Henneghien, J. Leymarie, and A. Vasson, *Physical Review B* **73** (3) (2006).
- ⁶⁸ C. Schneider, A. Rahimi-Iman, N. Y. Kim, J. Fischer, I. G. Savenko, M. Amthor, M. Lerner, A. Wolf, L. Worschech, V. D. Kulakovskii, I. A. Shelykh, M. Kamp, S. Reitzenstein, A. Forchel, Y. Yamamoto, and S. Hofling, *Nature* **497** (7449), 348 (2013).

- ⁶⁹ R. Butté, G. Delalleau, A. Tartakovskii, M. Skolnick, V. Astratov, J. Baumberg, G. Malpuech, A. Di Carlo, A. Kavokin, and J. Roberts, *Physical Review B* **65** (20) (2002).
- ⁷⁰ B. Monemar and B. E. Sernelius, *Applied Physics Letters* **91** (18) (2007).
- ⁷¹ Byung-Jun Ahn, Tae-Soo Kim, Yanqun Dong, Moon-Taek Hong, Jung-Hoon Song, Jae-Ho Song, Hwan-Kuk Yuh, Sung-Chul Choi, Duk-Kyu Bae, and Youngboon Moon, *Applied Physics Letters* **100** (3) (2012).
- ⁷² X. F. Ni, Q. Fan, R. Shimada, U. Ozgur, and H. Morkoc, *Applied Physics Letters* **93** (17) (2008).
- ⁷³ Q. Dai, M. F. Schubert, M. H. Kim, J. K. Kim, E. F. Schubert, D. D. Koleske, M. H. Crawford, S. R. Lee, A. J. Fischer, G. Thaler, and M. A. Banas, *Applied Physics Letters* **94** (11) (2009).
- ⁷⁴ Aurelien David and Nathan F. Gardner, *Applied Physics Letters* **97** (19) (2010).
- ⁷⁵ S. Watanabe, N. Yamada, M. Nagashima, Y. Ueki, C. Sasaki, Y. Yamada, T. Taguchi, K. Tadatomo, H. Okagawa, and H. Kudo, *Applied Physics Letters* **83** (24), 4906 (2003).
- ⁷⁶ Ya-Ju Lee, Ching-Hua Chiu, Chih Chun Ke, Po Chun Lin, Tien-Chang Lu, Hao-Chung Kuo, and Shing-Chung Wang, *Ieee Journal of Selected Topics in Quantum Electronics* **15** (4), 1137 (2009).
- ⁷⁷ X. Li, S. Okur, F. Zhang, V. Avrutin, Ue Oezguer, H. Morkoc, S. M. Hong, S. H. Yen, T. S. Hsu, and A. Matulionis, *Journal of Applied Physics* **111** (6) (2012).
- ⁷⁸ P. P. Paskov, T. Paskova, P. O. Holtz, and B. Monemar, *Physical Review B* **70** (3), 4 (2004).
- ⁷⁹ Markus Maier, Thorsten Passow, Michael Kunzer, Wilfried Pletschen, Klaus Koehler, and Joachim Wagner, in *Physica Status Solidi C: Current Topics in Solid State Physics, Vol 7, No 7-8* (2010), Vol. 7.
- ⁸⁰ J. Xie, U. Ozgur, Y. Fu, X. Ni, H. Morkoc, C. K. Inoki, T. S. Kuan, J. V. Foreman, and H. O. Everitt, *Applied Physics Letters* **90** (4) (2007).
- ⁸¹ X. A. Cao, E. B. Stokes, P. M. Sandvik, S. F. LeBoeuf, J. Kretchmer, and D. Walker, *Ieee Electron Device Letters* **23** (9), 535 (2002).
- ⁸² C. H. Kuo, Y. K. Fu, G. C. Chi, and S. J. Chang, *Ieee Journal of Quantum Electronics* **46** (3), 391 (2010).

- ⁸³ M. S. Minsky, S. B. Fleischer, A. C. Abare, J. E. Bowers, E. L. Hu, S. Keller, and S. P. Denbaars, *Applied Physics Letters* **72** (9), 1066 (1998).
- ⁸⁴ J. Hader, J. V. Moloney, and S. W. Koch, *Applied Physics Letters* **96** (22) (2010).
- ⁸⁵ T. Malinauskas, A. Kadys, T. Grinys, S. Nargelas, R. Aleksiejunas, S. Miasojedovas, J. Mickevicius, R. Tomasiunas, K. Jarasiunas, M. Vengris, S. Okur, V. Avrutin, X. Li, F. Zhang, U. Ozgur, and H. Morkoc, *Gallium Nitride Materials and Devices Vii* **8262** (2012).
- ⁸⁶ P. Blood, *Ieee Journal of Quantum Electronics* **36** (3), 354 (2000).
- ⁸⁷ V. I. Litvinov, *Journal of Applied Physics* **88** (10), 5814 (2000).
- ⁸⁸ R. J. Radtke, U. Waghmare, H. Ehrenreich, and C. H. Grein, *Applied Physics Letters* **73** (15), 2087 (1998).
- ⁸⁹ A. Dmitriev and A. Oruzhenikov, *Journal of Applied Physics* **86** (6), 3241 (1999).
- ⁹⁰ F. Della Sala, A. Di Carlo, P. Lugli, F. Bernardini, V. Fiorentini, R. Scholz, and J. M. Jancu, *Applied Physics Letters* **74** (14), 2002 (1999).
- ⁹¹ Lei Wang, Cimang Lu, Jianing Lu, Lei Liu, Ningyang Liu, Yujie Chen, Yanfeng Zhang, Erdan Gu, and Xiaodong Hu, *Optics Express* **19** (15), 14182 (2011).
- ⁹² C. K. Sun, S. Keller, G. Wang, M. S. Minsky, J. E. Bowers, and S. P. Denbaars, *Applied Physics Letters* **69** (13), 1936 (1996).
- ⁹³ G. Franssen, S. Grzanka, R. Czernecki, T. Suski, L. Marona, T. Riemann, J. Christen, H. Teisseyre, P. Valvin, R. Lefebvre, P. Perlin, M. Leszczynski, and I. Grzegory, *Journal of Applied Physics* **97** (10) (2005).
- ⁹⁴ G. Mohs, B. Fluegel, H. Giessen, H. Tajalli, N. Peyghambarian, P. C. Chiu, B. S. Phillips, and M. Osinski, *Applied Physics Letters* **67** (11), 1515 (1995).
- ⁹⁵ J. Piprek, *Physica Status Solidi a-Applications and Materials Science* **207** (10), 2217 (2010).
- ⁹⁶ J. S. Im, A. Moritz, F. Steuber, V. Harle, F. Scholz, and A. Hangleiter, *Applied Physics Letters* **70** (5), 631 (1997).
- ⁹⁷ S. W. Feng, Y. C. Cheng, Y. Y. Chung, C. C. Yang, M. H. Mao, Y. S. Lin, K. J. Ma, and J. I. Chyi, *Applied Physics Letters* **80** (23), 4375 (2002).

- ⁹⁸ M. Furis, F. Chen, A. N. Cartwright, H. Wu, and W. J. Schaff, in *Gan and Related Alloys-2002*, edited by C. Wetzel, E. T. Yu, J. S. Speck et al. (2003), Vol. 743, pp. 689.
- ⁹⁹ Hyunsung Kim, Dong-Soo Shin, Han-Youl Ryu, and Jong-In Shim, *Japanese Journal of Applied Physics* **49** (11) (2010).
- ¹⁰⁰ Pavlos G. Lagoudakis, *Journal of Applied Physics* **95** (5), 2487 (2004).
- ¹⁰¹ G. S. Huang, T. C. Lu, H. H. Yao, H. C. Kuo, S. C. Wang, C. W. Lin, and L. Chang, *Applied Physics Letters* **88** (6) (2006).
- ¹⁰² Zhen-Yu Li, Tien-Chang Lu, Hao-Chung Kuo, Shing-Chung Wang, Ming-Hua Lo, and K. M. Lau, *Journal of Crystal Growth* **311** (10), 3089 (2009).
- ¹⁰³ P. Kelkar, V. Kozlov, H. Jeon, A. V. Nurmikko, C. C. Chu, D. C. Grillo, J. Han, C. G. Hua, and R. L. Gunshor, *Physical Review B* **52** (8), R5491 (1995).
- ¹⁰⁴ S. I. Tsintzos, P. G. Savvidis, G. Deligeorgis, Z. Hatzopoulos, and N. T. Pelekanos, *Applied Physics Letters* **94** (7) (2009).
- ¹⁰⁵ Ü Özgür, X. Ni, Y. Fu, H. Morkoç, and H. O. Everitt, *Applied Physics Letters* **89** (26), 262117 (2006).
- ¹⁰⁶ Chih-Chiang Kao, H. W. Huang, J. Y. Tsai, C. C. Yu, C. F. Lin, H. C. Kuo, and S. C. Wang, *Materials Science and Engineering: B* **107** (3), 283 (2004).
- ¹⁰⁷ P. Scajev, K. Jarasiunas, S. Okur, U. Ozgur, and H. Morkoc, *Journal of Applied Physics* **111** (2) (2012).
- ¹⁰⁸ H. Yang, S. J. Xu, Q. Li, and J. Zhang, *Applied Physics Letters* **88** (16) (2006).
- ¹⁰⁹ Y. Honda, N. Kameshiro, M. Yamaguchi, and N. Sawaki, *Journal of Crystal Growth* **242** (1-2), 82 (2002).
- ¹¹⁰ T. Hikosaka, T. Narita, Y. Honda, M. Yamaguchi, and N. Sawaki, *Applied Physics Letters* **84** (23), 4717 (2004).
- ¹¹¹ P. P. Paskov, T. Paskova, P. O. Holtz, and B. Monemar, *Phys. Status Solidi A-Appl. Res.* **201** (4), 678 (2004).
- ¹¹² A. Toropov, Yu Kitaev, T. Shubina, P. Paskov, J. Bergman, B. Monemar, and A. Usui, *Physical Review B* **77** (19) (2008).

- ¹¹³ P. Scajev, K. Jarasiunas, Ue Oezguer, H. Morkoc, J. Leach, and T. Paskova, *Applied Physics Letters* **100** (2) (2012).
- ¹¹⁴ Sandip Ghosh, P. Waltereit, O. Brandt, H. T. Grahn, and K. H. Ploog, *Applied Physics Letters* **80** (3), 413 (2002).
- ¹¹⁵ Kazunobu Kojima, Masaya Ueda, Mitsuru Funato, and Yoichi Kawakami, *physica status solidi (b)* **244** (6), 1853 (2007).
- ¹¹⁶ S. F. Chichibu, H. Yamaguchi, L. Zhao, M. Kubota, K. Okamoto, and H. Ohta, *Applied Physics Letters* **92** (9), 091912 (2008).
- ¹¹⁷ N. Peyghambarian, H. M. Gibbs, J. L. Jewell, A. Antonetti, A. Migus, D. Hulin, and A. Mysyrowicz, *Phys. Rev. Lett.* **53** (25), 2433 (1984).
- ¹¹⁸ B. Monemar, P. P. Paskov, J. P. Bergman, A. A. Toropov, T. V. Shubina, T. Malinauskas, and A. Usui, *physica status solidi (b)* **245** (9), 1723 (2008).
- ¹¹⁹ P. Scajev, K. Jarasiunas, S. Okur, U. Ozgur, and H. Morkoc, *Physica Status Solidi B-Basic Solid State Physics* **249** (3), 503 (2012).
- ¹²⁰ Kestutis Jarasiunas, Patrik Scajev, Saulius Nargelas, Ramunas Aleksiejunas, Jacob Leach, Tania Paskova, Serdal Okur, Uemit Oezguer, and Hadis Morkoc, *Gallium Nitride Materials and Devices VII* **8262** (2012).
- ¹²¹ A. Dadgar, R. Ravash, P. Veit, G. Schmidt, M. Muller, A. Dempewolf, F. Bertram, M. Wieneke, J. Christen, and A. Krost, *Applied Physics Letters* **99** (2) (2011).
- ¹²² N. Suzuki, T. Uchida, T. Tanikawa, T. Hikosaka, Y. Honda, M. Yamaguchi, and N. Sawaki, *Journal of Crystal Growth* **311** (10), 2875 (2009).
- ¹²³ X. Ni, Y. Fu, Y. T. Moon, N. Biyikli, and H. Morkoc, *Journal of Crystal Growth* **290** (1), 166 (2006).
- ¹²⁴ Tasuku Murase, Tomoyuki Tanikawa, Yoshio Honda, Masahito Yamaguchi, and Hiroshi Amano, *Physica Status Solidi C: Current Topics in Solid State Physics, Vol 8, No 7-8* **8** (7-8) (2011).
- ¹²⁵ C. H. Chiu, D. W. Lin, C. C. Lin, Z. Y. Li, W. T. Chang, H. W. Hsu, H. C. Kuo, T. C. Lu, S. C. Wang, W. T. Liao, T. Tanikawa, Y. Honda, M. Yamaguchi, and N. Sawaki, *Applied Physics Express* **4** (1) (2011).

- ¹²⁶ N. Izyumskaya, F. Zhang, S. Okur, T. Selden, V. Avrutin, Ü Özgür, S. Metzner, C. Karbaum, F. Bertram, J. Christen, and H. Morkoç, *Journal of Applied Physics* **114** (11), 113502 (2013).
- ¹²⁷ R. Liu, A. Bell, F. A. Ponce, C. Q. Chen, J. W. Yang, and M. A. Khan, *Applied Physics Letters* **86** (2), 021908 (2005).
- ¹²⁸ S. Okur, S. Metzner, N. Izyumskaya, F. Zhang, V. Avrutin, C. Karbaum, F. Bertram, J. Christen, H. Morkoc, and U. Ozgur, *Applied Physics Letters* **103** (21) (2013).
- ¹²⁹ P. Vennegues, J. M. Chauveau, Z. Bougrioua, T. Zhu, D. Martin, and N. Grandjean, *Journal of Applied Physics* **112** (11) (2012).
- ¹³⁰ J. Mei, S. Srinivasan, R. Liu, F. A. Ponce, Y. Narukawa, and T. Mukai, *Applied Physics Letters* **88** (14), 141912 (2006).
- ¹³¹ K. P. Korona, *Physical Review B* **66** (16) (2002).
- ¹³² J. Menniger, U. Jahn, O. Brandt, H. Yang, and K. Ploog, *Physical Review B* **53** (4), 1881 (1996).
- ¹³³ A. Belabbes, L. C. de Carvalho, A. Schleife, and F. Bechstedt, *Physical Review B* **84** (12) (2011).
- ¹³⁴ M. Murayama and T. Nakayama, *Physical Review B* **49** (7), 4710 (1994).
- ¹³⁵ A. Dussaigne, P. Corfdir, J. Levrat, T. Zhu, D. Martin, P. Lefebvre, J. D. Ganière, R. Butté, B. Deveaud-Plédran, N. Grandjean, Y. Arroyo, and P. Stadelmann, *Semiconductor Science and Technology* **26** (2), 025012 (2011).
- ¹³⁶ T. J. Badcock, M. J. Kappers, M. A. Moram, P. Dawson, and C. J. Humphreys, *physica status solidi (b)* **249** (3), 498 (2012).
- ¹³⁷ P. Corfdir, P. Lefebvre, J. Levrat, A. Dussaigne, J. D. Ganière, D. Martin, J. Ristić, T. Zhu, N. Grandjean, and B. Deveaud-Plédran, *Journal of Applied Physics* **105** (4), 043102 (2009).
- ¹³⁸ P. Corfdir, J. Ristić, P. Lefebvre, T. Zhu, D. Martin, A. Dussaigne, J. D. Ganière, N. Grandjean, and B. Deveaud-Plédran, *Applied Physics Letters* **94** (20), 201115 (2009).
- ¹³⁹ P. P. Paskov, R. Schifano, B. Monemar, T. Paskova, S. Figge, and D. Hommel, *Journal of Applied Physics* **98** (9) (2005).

- ¹⁴⁰ P. P. Paskov, R. Schifano, T. Malinauskas, T. Paskova, J. P. Bergman, B. Monemar, S. Figge, D. Hommel, B. A. Haskell, P. T. Fini, J. S. Speck, and S. Nakamura, in *Physica Status Solidi C - Current Topics in Solid State Physics, Vol 3, No 6*, edited by S. Hildebrandt and M. Stutzmann (Wiley-Vch, Inc, New York, 2006), Vol. 3, pp. 1499.
- ¹⁴¹ Y. T. Rebane, Y. G. Shreter, and M. Albrecht, *Phys. Status Solidi A-Appl. Res.* **164** (1), 141 (1997).
- ¹⁴² Patrik Ščajev, Kęstutis Jarašiūnas, Serdal Okur, Ümit Özgür, and Hadis Morkoç, *Journal of Applied Physics* **111** (2), 023702 (2012).
- ¹⁴³ P. Corfdir, P. Lefebvre, J. Ristić, J. D. Ganière, and B. Deveaud-Plédran, *Physical Review B* **80** (15) (2009).
- ¹⁴⁴ S. Okur, N. Izyumskaya, F. Zhang, V. Avrutin, S. Metzner, C. Karbaum, F. Bertram, J. Christen, H. Morkoc, and U. Ozgur, *Gallium Nitride Materials and Devices IX* **8986** (2014).
- ¹⁴⁵ F. Bertram, T. Riemann, J. Christen, A. Kaschner, A. Hoffmann, C. Thomsen, K. Hiramatsu, T. Shibata, and N. Sawaki, *Applied Physics Letters* **74** (3), 359 (1999).
- ¹⁴⁶ S. Gradecak, P. Stadelmann, V. Wagner, and M. Ilegems, *Applied Physics Letters* **85** (20), 4648 (2004).
- ¹⁴⁷ P. Gibart, *Reports on Progress in Physics* **67** (5), 667 (2004).
- ¹⁴⁸ Tasuku Murase, Tomoyuki Tanikawa, Yoshio Honda, Masahito Yamaguchi, Hiroshi Amano, and Nobuhiko Sawaki, *Japanese Journal of Applied Physics* **50**, 01AD04 (2011).
- ¹⁴⁹ N. Izyumskaya, S. J. Liu, V. Avrutin, X. F. Ni, M. Wu, U. Ozgur, S. Metzner, F. Bertram, J. Christen, L. Zhou, D. J. Smith, and H. Morkoc, *Journal of Crystal Growth* **314** (1), 129 (2011).
- ¹⁵⁰ V. Avrutin, S. D. A. Hafiz, F. Zhang, U. Ozgur, H. Morkoc, and A. Matulionis, *J. Vac. Sci. Technol. A* **31** (5) (2013).

Appendices

Appendix A: Determination of IQE from excitation density dependent photoluminescence measurement

It is assumed that at steady state the total generation rate (G) is equal to the total recombination rate (R) which includes Shockley-Read-Hall nonradiative recombination (An), bimolecular radiative recombination (Bn²), and Auger recombination (Cn³) if any, where n is the carrier concentration, i.e.

$$G = An + Bn^2 + Cn^3 \quad \text{Equation 16}$$

When the generated steady-state carrier density n is relatively low (in the range 10¹⁶ - 10¹⁸ cm⁻³), the Auger recombination term is very weak as compared to the radiative recombination term. In other words, the Cn³ term becomes much smaller than An + Bn². Then Equation 16 can be simplified to:

$$G = An + Bn^2 \quad \text{Equation 17}$$

Fortunately G could also be calculated separately from experimental parameters:

$$G = \frac{P_{laser}(1-R)\alpha}{A_{spot}h\nu} \quad \text{Equation 18}$$

where P_{laser} is the optical power incident on the sample, R is the Fresnel reflection at the sample surface, spot A is the laser spot size, hν is the energy of a photon from laser source, α is the absorption coefficient of the InGaN active layers at the laser wavelength. The absorption coefficient for InGaN can be obtained by⁷³

$$\alpha = \alpha_0 \sqrt{\frac{E - E_g}{E_g}} \quad \text{Equation 19}$$

where α_0 is the absorption coefficient at $h\nu = 2E_g$, which is obtained by linear interpolation between of GaN and InN ($2.0 \times 10^5 \text{ cm}^{-1}$ for GaN, $1.2 \times 10^5 \text{ cm}^{-1}$ for InN) values.⁷³

The measured PL intensity could be represented as

$$I_{PL} = \eta_c B n^2 \quad \text{Equation 20}$$

where I_{PL} is the integrated PL intensity, the collection factor η_c includes escape efficiency of photons as well as the collection efficiency of luminescence by the optics/detector, which is constant during a given measurement but different from measurement to measurement even though attempts are made to keep the collection geometry the same.

By eliminating n from Equation 17 and Equation 20, one can obtain

$$G = \frac{A}{\sqrt{\eta_c B}} \sqrt{I_{PL}} + \frac{1}{\eta_c} I_{PL} = P_1 \sqrt{I_{PL}} + P_2 I_{PL} \quad \text{Equation 21}$$

where G is obtained as a function of I_{PL} . By fitting the plot of G versus I_{PL} , one could obtain the three fitting coefficients. Then the IQE could be calculated by

$$IQE = \frac{B n^2}{A n + B n^2} = \frac{B n^2}{G} \quad \text{Equation 22}$$

As an example, **Figure 88** shows the fitting of the generation rate G as a function of the integrated PL intensity I_{PL} for a c-plane LED active layer (with low barrier MQW) on sapphire (the reference sample used in Figure 17 in section 2.1. During the calculation of G values, a diameter of $100 \mu\text{m}$ has been used to estimate the laser spot size. Measurement was carried out on the LED active layer sample at room temperature using a frequency-doubled 80 MHz repetition rate femtosecond Ti:Sapphire laser. The excitation laser wavelength was 385 nm, below the bandgap of the quantum barriers and top GaN.

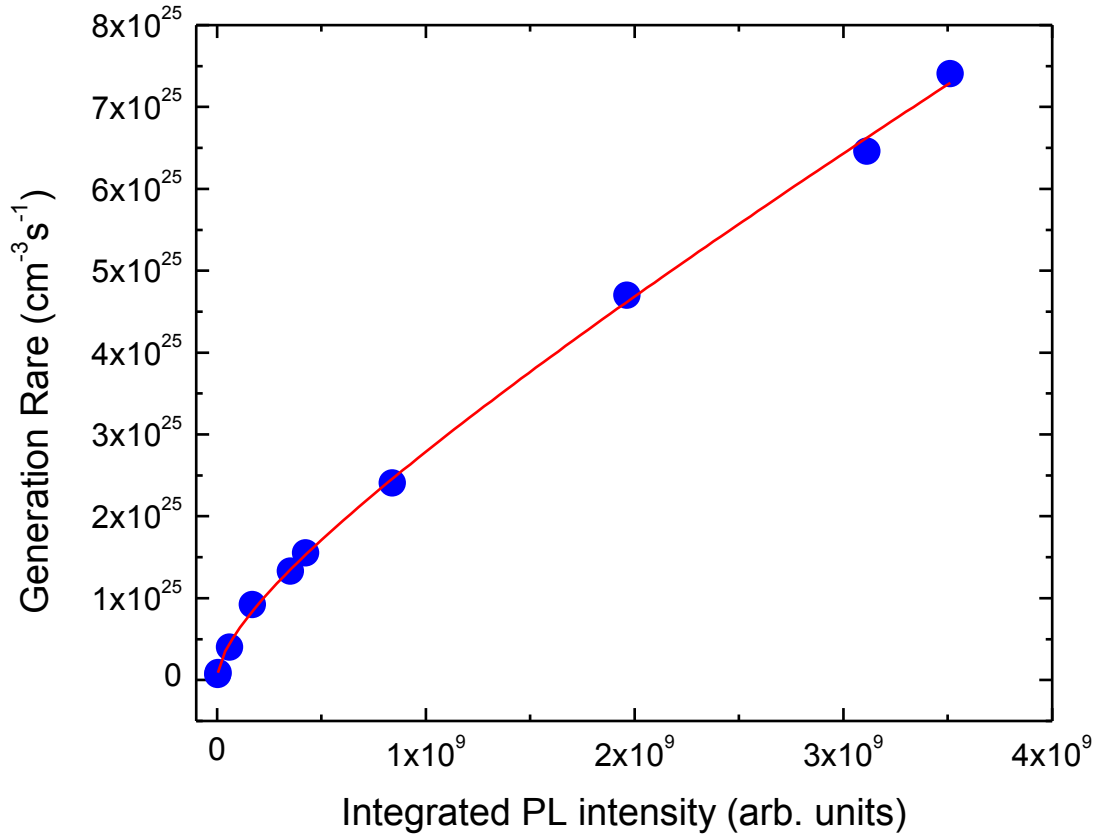


Figure 88: Curve fitting results of the generation rate as a function of integrated PL intensity for a c-plane LED active layer (with low barrier MQW) on sapphire. The red curve represents the fits obtained using Equation 25.

After obtaining fitting one can reach the IQE values with as a function of generation rate (i.e. laser excitation powers) without knowing the values of A and B coefficients. After assuming (or measuring) a value for B coefficient ($1 \times 10^{-11} \text{ cm}^3 \text{ s}^{-1}$ used here), one could obtain the steady-state carrier density n by thereby the IQE values as a function of the generated carrier density n .

Appendix B: Working principle of a Streak Camera

The streak camera is an ultra high-speed detector which captures extremely short time period light emission. Figure 83 shows its working principle. The light pulse to be measured is projected onto the slit and is focused by a lens into an optical image on the photocathode, able to

cover a wavelength range between 300 nm and 1500 nm. Here, the photons are converted into a stream of electrons proportional to the intensity of the incident light. As the electron stream created from the light pulse passes between a pair of sweep electrodes, a time-varying voltage is applied to the electrodes, resulting in a high-speed sweep. This means that the early part of the pulse is deflected less than the later part of the pulse, so that different parts of the pulse strike the micro channel plate (MCP) at different positions. Thus the temporal structure of the pulse is converted into a spatial distribution, or ‘streak’, pattern. As the electrons pass the MCP, they are multiplied several thousands of times and are then bombarded against the phosphor screen, where they are converted back into light. The fluorescence image corresponding to the early part of the incident light pulse is positioned at the top of the phosphor screen, with later parts positioned in descending order; in other words, the axis in the perpendicular direction on the phosphor screen serves as the temporal axis. The brightness of the fluorescence image is proportional to the intensity of the corresponding incident light pulses and the position in the horizontal direction on the phosphor screen corresponds to the wavelength of the incident light.

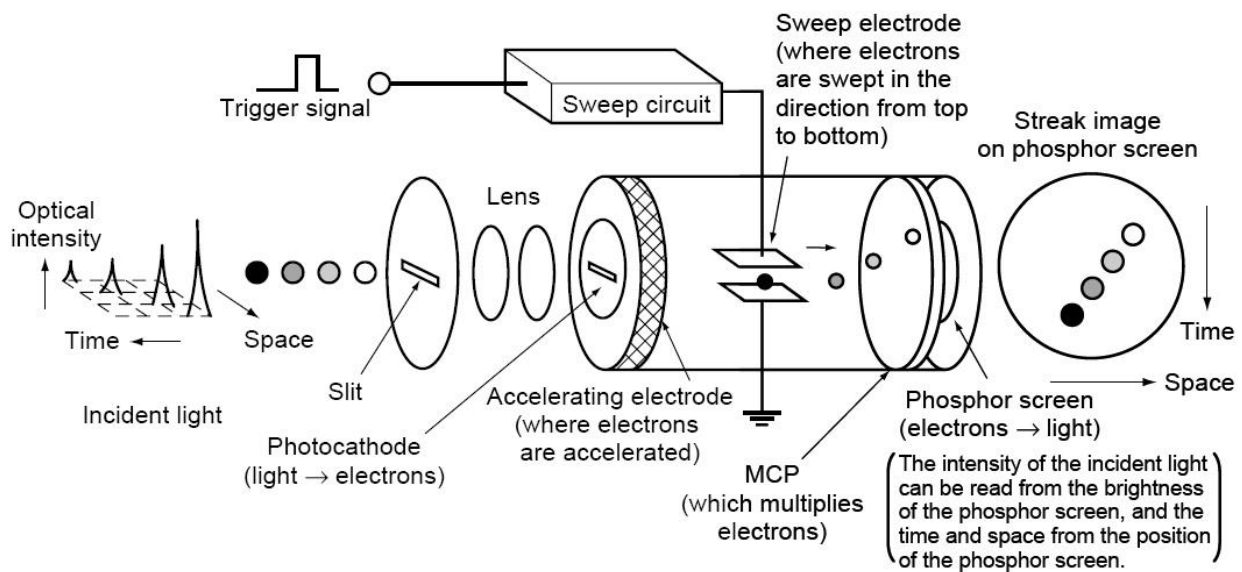


Figure 89: Schematic illustration of a Streak camera components and working principle.

Appendix C: Calculation of temperature dependent radiative and nonradiative lifetimes

Temperature dependent PL intensity in terms of radiative and nonradiative PL decay times is defined as

$$I(T) = I(0) \frac{1}{1 + \tau_r / \tau_{nr}} \quad \text{Equation 23}$$

where one can obtain the ratio of radiative and nonradiative lifetimes as

$$\frac{\tau_r}{\tau_{nr}} = \frac{I(0)}{I(T)} - 1 \quad \text{Equation 24}$$

where the radiative and nonradiative lifetimes characterize the PL lifetime through the relation

$$\frac{1}{\tau_{PL}} = \frac{1}{\tau_r} + \frac{1}{\tau_{nr}} \Rightarrow \frac{1}{\tau_{PL}} = \frac{\tau_r + \tau_{nr}}{\tau_r \tau_{nr}} \quad \text{Equation 25}$$

writing the radiative lifetime from the Eq. 25 one get

$$\tau_r = \tau_{PL} \frac{\tau_r + \tau_{nr}}{\tau_{nr}} \Rightarrow \tau_r = \tau_{PL} \left(1 + \frac{\tau_r}{\tau_{nr}} \right) \quad \text{Equation 26}$$

After evaluating Eq. 25 and Eq. 26 one get the temperature dependent radiative lifetime in terms of PL lifetime and PL intensity ratio.

$$\tau_r = \tau_{PL} \frac{I(0)}{I(T)} \quad \text{Equation 27}$$

It can be understood from the Eq. 27 one can easily measure radiative and nonradiative lifetimes at different temperatures through the temperature dependent PL and TRPL measurements which PL lifetime and PL intensity ratio are obtained, respectively.

Curriculum Vitae

Serdal Okur

DOB : May 26, 1983

Nationality: Turkey

Email: okurs@vcu.edu, serdalokur@gmail.com

Education:

2014 Ph.D., Virginia Commonwealth University / Electrical and Computer Engineering

2010 M.Sc., Izmir Institute of Technology / Physics

2005 B.Sc., Ondokuz Mayıs University / Physics

Publication List (in chronological order):

Peer-reviewed journal papers:

- 1) D Rosales, B Gil, T Bretagnon, B Guizal, N Izyumskaya, M Monavarian, F Zhang, **S Okur**, V Avrutin, Ü Özgür, H Morkoç “Recombination dynamics of excitons with low non-radiative component in semi-polar (10-11)-oriented GaN/AlGaIn multiple quantum wells” *Journal of Applied Physics* 116 (2014) 093517
- 2) M. Toporkov, V. Avrutin, **S. Okur**, N. Izyumskaya, D. Demchenko, J. Volk, D. J. Smith, H. Morkoç, and Ü. Özgür “Enhancement of Be and Mg incorporation in wurtzite quaternary BeMgZnO alloys with up to 5.1 eV optical bandgap” *Journal of Crystal Growth* 402 (2014) 60-64
- 3) D Rosales, B Gil, T Bretagnon, B Guizal, F Zhang, **S Okur**, M Monavarian, N Izyumskaya, V Avrutin, Ü Özgür, H Morkoç, JH Leach “Excitonic recombination dynamics in non-polar GaN/AlGaIn quantum wells” *Journal of Applied Physics* 115 (2014) 073510
- 4) **S. Okur**; S. Metzner; N. Izyumskaya; F. Zhang; V. Avrutin; Ü. Özgür; C. Karbaum; F. Bertram; J. Christen; D. J. Smith; H. Morkoç “Microscopic distribution of extended defects

and blockage of threading dislocations by stacking faults in semipolar (1-101) GaN revealed from spatially resolved luminescence” *Applied Physics Letters* 103 (2013) 211908

- 5) N. Izyumskaya; F. Zhang; **S. Okur**; V. Avrutin; Ü. Özgür; S. Metzner; C. Karbaum; F. Bertram; J. Christen; D. J. Smith; H. Morkoç “Optical studies of strain and defect distribution in semipolar (1-101) GaN on patterned Si substrates” *Journal of Applied Physics* 114 (2013) 113502
- 6) F. Zhang, X. Li, **S. Okur**, V. Avrutin, Ü. Özgür, and H. Morkoç “The effect of stair case electron injector design on electron overflow in InGaN light emitting diodes” *Applied Physics Letters* 103 (2013) 051122
- 7) **Serdal Okur**, Ryoko Shimada, Fan Zhang, Shopan Din Ahmad Hafiz, Jaesoong Lee, Vitaliy Avrutin, Ümit Özgür, Hadis Morkoç, Alexander Franke, Frank Bertram, and Juergen Christen “GaN-Based Vertical Cavities with All Dielectric Reflectors by Epitaxial Lateral Overgrowth” *Japanese Journal of Applied Physics* 52 (2013) 08JH03
- 8) K. Jarasiunas, S. Nargelas, R. Aleksiejunas, S. Miasojedovas, M. Vengris, **S. Okur**, H. Morkoc, U. Ozgur, C. Giesen, O. Tuna, and M. Heuken “Spectral distribution of excitation-dependent recombination rate in In_{0.13}Ga_{0.87}N epilayer” *Journal of Applied Physics* 113 (2013) 093103
- 9) X. Li, **S. Okur**, F. Zhang, S. A. Hafiz, V. Avrutin, Ü. Özgür, H. Morkoç, and K. Jarašiūnas, “Improved quantum efficiency in InGaN light emitting diodes with multi-double-heterostructure active regions” *Applied Physics Letters* 101 (2012) 041115
- 10) Xing Li, **Serdal Okur**, Fan Zhang, Vitaliy Avrutin, Ümit Özgür, Hadis Morkoç, Steve M. Hong, Sheng-Hong Yen, Ta-Cheng Hsu, Arvydas Matulionis “Impact of active layer design on InGaN radiative recombination coefficient and LED performance” *Journal of Applied Physics* 111 (2012) 063112
- 11) Lidia Tarnawska, Peter Zaumseil, Markus Andreas Schubert, **Serdal Okur**, Umit Ozgur, Hadis Morkoc, Regina Paszkiewicz, Peter Storek, Thomas Schroeder, “Structural and optical quality of GaN grown on Sc₂O₃/Y₂O₃/Si(111)” *Journal of Applied Physics* 111 (2012) 073509
- 12) Scajev P., Jarasiunas K, Okur S., Ozgur, U., Morkoc, H. “Carrier dynamics in bulk GaN” *Journal of Applied Physics* 111 (2012) 023702
- 13) Scajev P., Jarasiunas K., Okur S., Ozgur U., Morkoc H. “Carrier dynamics under two- and single-photon excitation in bulk GaN” *Physics. Status Solidi B* 249, No. 3 (2012) 503-506
- 14) X. Li, F. Zhang, **S. Okur**, V. Avrutin, S. J. Liu, U. Ozgur, H. Morkoc, S. M. Hong, S. H. Yen, T. S. Hsu, A. Matulionis “On the quantum efficiency of InGaN light emitting diodes: Effects of active layer design, electron cooler, and electron blocking layer” *Physics Status Solidi A* 208, No. 12 (2011) 2907–2912

- 15) Ü. Özgür, X. Ni, X. Li, J. Lee, S. Liu, **S. Okur**, V. Avrutin, A. Matulionis and H. Morkoç “Ballistic transport in InGaN-based LEDs: impact on efficiency” *Semiconductor Science and Technology* 26 (2011) 014022
- 16) O. Öztürk, **S. Okur**, L. Pichon, M.O. Liedke, J.P. Riviere “Magnetic layer formation on plasma nitrided CoCrMo alloy” *Surface & Coatings Technology* 205 (2011) S280–S285
- 17) L. Pichon, **S. Okur**, O. Öztürk, J.P. Riviere, M. Drouet “CoCrMo alloy treated by floating potential plasma assisted nitriding and plasma based ion implantation: Influence of the hydrogen content and of the ion energy on the nitrogen incorporation” *Surface & Coatings Technology* 204 (2010) 2913–2918
- 18) O. Öztürk, **S. Okur**, J.P. Riviere “Structural and magnetic characterization of plasma ion nitride layer on 316L stainless steel alloy” *Nuclear Instruments and Methods in Physics Research B* 267 (2009) 1540–1545

Peer-reviewed proceeding papers:

- 19) **Serdal Okur**, Natalia Izyumskaya, Fan Zhang, Vitaliy Avrutin, Sebastian Metzner, Christopher Karbaum, Frank Bertram, Jürgen Christen, Hadis Morkoç, Ümit Özgür “Impact of extended defects on optical properties of (1-101)GaN grown on patterned Si” *Proc. SPIE* 8986 (2014) 89860L
- 20) Natalia Izyumskaya, **Serdal Okur**, Fan Zhang, Morteza Monavarian, Vitaliy Avrutin, Ümit Özgür, Sebastian Metzner, Christopher Karbaum, Frank Bertram, Jürgen Christen, Hadis Morkoç “Optical properties of m-plane GaN grown on patterned Si(112) substrates by MOCVD using a two-step approach” *Proc. SPIE* 8986 (2014) 898628
- 21) Daniel Rosales, Bernard Gil, and Thierry Bretagnon, Fan Zhang, **Serdal Okur**, Shopan din Ahmad Hafiz, Natalia Izyumskaya, Vitaliy Avrutin, Ümit Özgür, and Hadis Morkoç “Polarized time-resolved photoluminescence measurements of m-plane AlGaN/GaN MQWs” *Proc. SPIE* 8986 (2014) 89860L
- 22) Shopan Hafiz, Fan Zhang, Morteza Monavarian, **Serdal Okur**, Vitaliy Avrutin, Hadis Morkoç, Ümit Özgür “Estimation of carrier leakage in InGaN light emitting diodes from photocurrent measurements” *Proc. SPIE* 9003 (2014) 90031R
- 23) **Serdal Okur**, Kęstutis Jarašiūnas, Shopan din Ahmed Hafiz, J. Leach, T. Paskova, Ü. Özgür, and H. Morkoç “Recombination dynamics in non-polar m-plane GaN investigated by time- and polarization-resolved photoluminescence” *Proc. SPIE* 8625 (2013) 82252D
- 24) N. Izyumskaya; **S. Okur**; F. Zhang; V. Avrutin; Ü. Özgür; S. Metzner; C. Karbaum; F. Bertram; J. Christen; H. Morkoç “Depth distribution of carrier lifetimes in semipolar (1-101)GaN grown by MOCVD on patterned Si substrates” *Proc. SPIE* 8625 (2013) 86252G

- 25) F. Zhang; S. A. Hafiz; **S. Okur**; V. Avrutin; Ü. Özgür; H. Morkoç “InGaN based multi-double heterostructure light emitting diodes with electron injector layers” *Proc. SPIE 8625 (2013) 82251J*
- 26) F. Zhang; **S. Okur**; S. A. Hafiz; V. Avrutin; Ü. Özgür; H. Morkoç “GaN-based vertical cavity lasers with semiconductor/dielectric and all dielectric reflectors” *Proc. SPIE 8625 (2013) 86252F*
- 27) F. Zhang; X. Li; **S. Okur**; V. Avrutin; Ü. Özgür; H. Morkoç; S. M. Hong; S. H. Yen; T. S. Hsu; A. Matulionis “The impact of active layer design on quantum efficiency of InGaN light emitting diodes” *Proc. SPIE 8262 (2012) 82621G*
- 28) N. Izyumskaya; S. J. Liu; V. Avrutin; **S. Okur**; F. Zhang; Ü. Özgür; S. Metzner; C. Karbaum; F. Bertram; J. Christen; D. J. Smith; H. Morkoç “Effect of MOCVD growth conditions on the optical properties of semipolar (1-101) GaN on Si patterned substrates” *Proc. SPIE 8262 (2012) 826224*
- 29) Kęstutis Jarašiūnas; Patrik Ščajev; Saulius Nargelas; Ramūnas Aleksiejūnas; Jacob Leach; Tania Paskova; **Serdal Okur**; Ümit Özgür; Hadis Morkoç “Recombination and diffusion processes in polar and nonpolar bulk GaN investigated by time-resolved photoluminescence and nonlinear optical techniques” *Proc. SPIE 8262 (2012) 82620G*
- 30) T. Malinauskas, A. Kadys, T. Grinys, S. Nargelas, R. Aleksiejūnas, S. Miasojedovas, J. Mickevičius, R. Tomašiūnas, K. Jarašiūnas, M. Vengris, **S. Okur**, X. Li, F. Zhang, Ü. Özgür, and H. Morkoç “Impact of carrier localization, recombination, and diffusivity on excited state dynamics in InGaN/GaN quantum wells” *Proc. SPIE 8262 (2012) 82621S*
- 31) N. Izyumskaya, S. J. Liu, **S. Okur**, M. Wu, V. Avrutin, Ü. Özgür, and H. Morkoç “Optical properties of nonpolar (1-100) and semipolar (1-101)GaN grown by MOCVD on Si patterned substrates” *Proc. SPIE 7939 (2011) 79391W*
- 32) F. Zhang, X. Li, S. Liu, **S. Okur**, V. Avrutin, Ü. Özgür, and H. Morkoç “Impact of ballistic electron transport on efficiency of InGaN based LEDs” *Proc. SPIE 7939 (2011) 793917*